

MASARYKOVA UNIVERZITA  
Přírodovědecká fakulta  
Ústav fyzikální elektroniky

Laserová a elektrická diagnostika neizotermického  
plazmatu

Laser and electric diagnostics of non-isothermal plasma

Pavel Dvořák

Habilitační práce  
Obor: Fyzika plazmatu

Brno, 2017



**Poděkování**

Děkuji kolegům, kteří okolo mne vytvořili tvůrčí a přátelské prostředí. Děkuji také rodině, na prvním místě manželce Katce, přátelům a blízkým, kteří obohacují můj život a v mnohém mě podpořili. Největší dík bych rád vyjádřil Bohu za vše.



## Abstrakt

Předložená habilitační práce shrnuje výsledky získané v oboru fyzika plazmatu zejména pomocí diagnostiky plazmatu, která ale byla v některých případech provázaná s modelováním příslušného výboje. Práce se omezuje na dvě hlavní témata mého výzkumu a to na fluorescenční diagnostiku výbojů buzených za atmosférického tlaku a na projevy nelineárních elektrických vlastností kapacitně vázaných výbojů. Na poli fluorescenčních měření se podařilo metodu rozvinout tak, že umožnila např. i měření jednoatomových radikálů vodíku v povrchových výbojích, které kladou diagnostice nejednu překážku. S takovouto metodou jsme pak mohli zjistit chování různých reaktivních radikálů v dielektrických bariérových výbojích, potvrdit roli radikálových reakcí v tzv. atomizátorech (zařízeních používaných v analytické chemii), získat mapy rozložení rotačních stavů v plazmatu nebo najít vztah mezi mícháním plynů a koncentrací radikálů v atmosférických plazmových tryskách. Na poli kapacitních výbojů se podařilo postoupit v sondové diagnostice vysokofrekvenčních složek potenciálu plazmatu, vytvořit teoretický model popisující vznik vyšších harmonických frekvencí a tyto frekvence využít k citlivému monitorování depozičních procesů.



## Abstract

This habilitation work summarizes results obtained in the field of plasma physics, namely by means of plasma diagnostics, that was in some cases combined with modelling of examined discharge. The work is restricted to the two main fields of my research: to the laser-induced fluorescence (LIF) of discharges ignited at atmospheric pressure and to the nonlinear electric properties of capacitively coupled discharges. The LIF method was developed so that we were able e.g. to measure the concentration of atomic hydrogen radicals in surface discharges, that present a challenge for any laser-based diagnostics. With such a tool we were able to discover behaviour of reactive radical species in various dielectric barrier discharges, confirm the role of radical reactions in so-called atomizers (devices used in analytical chemistry), obtain maps of the distribution function of rotational states in plasmas or find the relation between gas mixing and concentration of radicals in atmospheric-pressure plasma jets. In the field of capacitively coupled discharges a progress was made of probe diagnostics of high-frequency components of plasma potential, a theoretical model was developed that describes the generation of higher harmonic frequencies of discharge current and voltages and these higher harmonics were used for sensitive monitoring of deposition processes.



# Obsah

<b>1</b>	<b>Úvod</b>	<b>1</b>
<b>2</b>	<b>Nelineární elektrické vlastnosti kapacitních výbojů</b>	<b>3</b>
2.1	Úvod do problematiky . . . . .	3
2.2	Sondová diagnostika . . . . .	4
2.3	Vyšší harmonické frekvence v depozičních a leptacích procesech . . . . .	9
2.4	Modelování elektrické nelinearity výbojů . . . . .	12
<b>3</b>	<b>Fluorescenční měření v plazmatu</b>	<b>17</b>
3.1	Úvod do problematiky . . . . .	17
3.2	Metoda fluorescenčních měření . . . . .	18
3.2.1	Základní vztahy . . . . .	18
3.2.2	Parazitní signály . . . . .	19
3.2.3	Saturační efekty . . . . .	21
3.2.4	Spektrální překryv . . . . .	22
3.2.5	Trojčásticové srážky excitovaných částic . . . . .	22
3.2.6	Srážková přeuspořádání excitovaného stavu . . . . .	23
3.3	Objemový dielektrický bariérový výboj . . . . .	24
3.4	Koplanární dielektrický bariérový výboj . . . . .	26
3.5	Atmosférické plazmové trysky . . . . .	29
<b>4</b>	<b>Shrnutí</b>	<b>33</b>
<b>5</b>	<b>Přiložené komentované práce</b>	<b>41</b>



# Kapitola 1

## Úvod

Neizotermické nízkoteplotní plazma je nerovnovážený stav látky, ve kterém probíhá pestrá paleta fyzikálních a chemických procesů. Většina z nich je iniciovaná elektrony, které v elektrickém poli vloženém na plazma zvenčí mohou získat vysokou energii a tu pak využít k ionizaci přítomných atomů a molekul, jejich disociaci či excitaci. V plazmatu pak existuje množství reaktivních částic, jejichž doby života sahají od desítek pikosekund pro rychle zhasené excitované částice po například sekundy u některých metastabilních částic, a fotonů včetně agresivního hlubokého UV záření. Připočteme-li k rozmanitosti částic v plazmatu ještě značnou nehomogenitu některých výbojů, jejich rychlý časový vývoj na úrovni piko- a nanosekund a skutečnost, že zároveň může probíhat několik různých mechanismů dodávání energie do plazmatu, dostáváme pestrou podívanou na poměrně složité prostředí. Moje práce se snaží přispět k popsání a pochopení tohoto prostředí, zejména prostřednictvím diagnostiky plazmatu, místy také pomocí teoretického modelu.

Práce je dělená na dvě nezávislé části. První se věnuje elektrickým vlastnostem kapacitních výbojů s důrazem na jejich nelineární charakter projevující se generováním vyšších harmonických frekvencí napětí a proudu. Druhá část studuje plazma atmosférických výbojů pomocí fluorescenčních měření. Další témata, jako např. problematika difúzního  $\alpha$ -režimu kapacitních výbojů iniciovaných za atmosférického tlaku [1, 2], diagnostika HI-PIMS výboje [3], měření Langmuirovou sondou v kapacitním výboji [4], spektroskopická analýza fotochemických problémů [5, 6], fluorescenční studium plamene, starší témata výzkumu a témata vzdálená od fyziky plazmatu nejsou v práci obsažena.

Práce je psaná formou komentáře vybraných článků. Všechny důležitější vlastní publikace, které jsou v habilitační práci citovány, jsou přiloženy. Proto je jejich komentář stručný a jen občas je dokumentován obrazově – příslušné podrobnosti a grafy lze najít v přílohách. Obrázky proto jen volně doprovázejí text, který se odkazuje pouze na příslušné publikace. V textu jsem se snažil dát jednotlivé publikace do souvislostí a někdy

ukázat cesty, kterými se náš výzkum ubíral. Proto občas zmiňuji i některé z aktuálně řešených problémů, které se popisované problematiky týkají, i když ještě nebyly dotaženy k přijaté publikaci.

Samozřejmě jsem spolupracoval s mnoha kolegy, jejichž jména jsou většinou uvedena v autorství jednotlivých publikací. Zde zmiňme alespoň Jana Voráče, Vojtěcha Procházku, Martinu Mrkvičkovou a Marka Talábu, s nimiž jsme společně realizovali fluorescenční měření, Petra Vašinu, se kterým jsme detekovali vyšší harmonické frekvence v reaktivním magnetronovém naprašování, Vilmu Buršíkovou a Radka Žemličku, se kterými jsem sledoval tyto harmoniky při PECVD, Adama Obrusníka, jenž naše fluorescenční měření doplnil modely, skupinu Jiřího Dědiny z Ústavu analytické chemie, která nejen iniciovala výzkum atomizátorů, nebo Jozefa Ráhela, jednoho z hybatelů měření v koplanárním DBD. Ke jmenovaným ale patří mnoho dalších, jejichž přínosu si jsem vědomý a bez kterých by uplynulé roky byly chudší. Řadu z jmenovaných i nejmenovaných jsem v minulých letech vedl při jejich bakalářských, magisterských nebo doktorských pracích. V textu se zaměřuji na výsledky, na kterých jsem se přímo podílel, i když někdy bylo potřeba okrajově zmínit souvislost s prací kolegů a leckdy, zejména v případě vedených studentských prací, není možné některé zásluhy striktně rozdělit.

Přeji příjemné čtení.

# Kapitola 2

## Nelineární elektrické vlastnosti kapacitních výbojů

### 2.1 Úvod do problematiky

V uplynulých letech se naše znalosti o kapacitních výbojích téměř skokově prohloubily. Díky dostupné diagnostické technice i pokroku teoretického modelování jsme získali např. mnohem přesnější obraz o způsobech dodávání energie do výboje. Novým rozměrem fyziky kapacitních výbojů, který byl vytažen na světlo, je přítomnost nečekaně silných složek napětí a proudů s frekvencemi několikanásobně vyššími než je frekvence napětí dodávaná do plazmatu z vnějšího zdroje. Tyto plazmatem spontánně generované signály zpestřují pohled na kapacitní výboje, ovlivňují plazma a mohou být s překvapivou citlivostí využity i pro diagnostické účely. Pojdme si ale nejdřív shrnout některé charakteristiky kapacitních výbojů.

O vysokofrekvenčním kapacitně vázaném výboji mluvíme tehdy, když frekvence elektrického pole budícího výboj je podstatně nižší než plazmová frekvence elektronů v plazmatu, ale vyšší než plazmová frekvence iontů. Zatímco elektrony tedy stíhají reagovat na vf. elektrické pole, průměrná rychlost iontů uvnitř plazmatu je malá a ionty získávají vyšší kinetickou energii jen na rozhraní mezi plazmatem a elektrodami. U vf. kapacitního výboje také očekáváme, že vzdálenost elektrod nebo charakteristická délka plazmatu je podstatně menší než vlnová délka elektrického pole. Aby šlo o kapacitní výboj, musí mít dominantní vliv elektrické pole vytvořené přímo napětím mezi elektrodami, narozdíl od induktivního výboje, kde dominuje vliv elektrického pole indukovaného změnou magnetického pole.

Oblast kapacitně vázaného výboje můžeme rozdělit na vlastní plazma a stěnové vrstvy kladného prostorového náboje, které vlastní plazma oddělují od povrchů předmětů, jež jsou v kontaktu s plazmatem, zejména elektrod. Díky prostorovému náboji málo po-

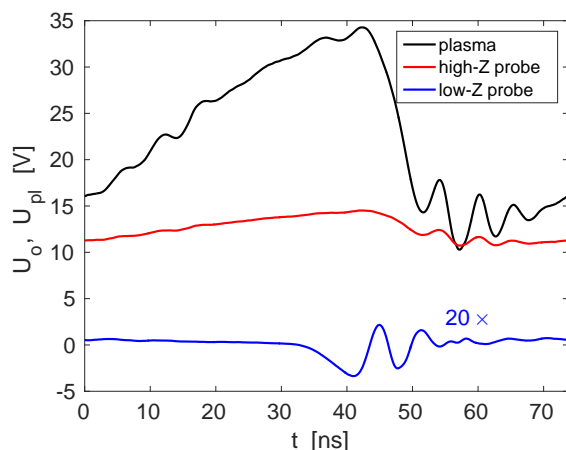
hyblivých iontů je uvnitř stěnových vrstev silné stejnosměrné elektrické pole. Zatímco z hlediska elektrických vlastností má vlastní plazma induktivní charakter, stěnové vrstvy vykazují kapacitní a, protože jejich tloušťka se ve vysokofrekvenčním elektrickém poli rychle mění, silně nelineární charakter [7]. Nelinearita stěnových vrstev se projevuje zejména tvorbou vyšších harmonických frekvencí napětí a proudu [7, 8]. Za nízkého tlaku nejsou vzniklé oscilace příliš tlumeny srážkami elektronů s neutrálními částicemi a jejich amplitudy mohou dosahovat vysokých hodnot, dokonce mohou přerůst přes amplitudu základní frekvence dodávané z vf. generátoru [9, 10, 11]. Amplituda buzených oscilací může být velká zejména tehdy, když jejich frekvence leží blízko frekvence tzv. sériové rezonance plazmatu, při které je induktivní plazma v rezonanci s kapacitními stěnovými vrstvami [12]. Vliv na sériovou rezonanci mají i další části vf. obvodu [13, 14]. Protože základní vlastnosti kapacitních výbojů vč. koncentrace elektronů jsou silně závislé na frekvenci elektrického pole [15, 16], může mít přítomnost vybuzených oscilací velký vliv na charakter plazmatu.

I opačně platí, že parametry plazmatu mají velký vliv na chování vyšších harmonických frekvencí. Výše uvedený text už naznačil, že jejich chování závisí na tlaku, koncentraci elektronů a srážkové frekvenci elektronů [17, 9, 12]. Dalšími důležitými parametry působícími na vyšší harmoniky jsou napětí na stěnových vrstvách [7, 14], nesymetrie výboje, pozice ve výbojovém reaktoru a vzdálenost mezi elektrodami [12, 18]. Amplitudy vyšších harmonik ovšem závisejí na elektrických vlastnostech celého vf. obvodu, včetně uspořádání přizpůsobovacího členu [19, 14] a impedance reaktoru s plazmatem [20]. Jejich chování proto může být značně komplikované. Protože však vyšší harmonické frekvence mohou citlivě reagovat i na drobné změny plazmatu včetně vzniku deponované vrstvy na některé z elektrod [20, 21, 22] nebo vzniku prachu v objemu plazmatu [23, 24], jsou vhodným nástrojem pro monitorování praktických plazmových procesů, jak bude více popsáno v kpt. 2.3.

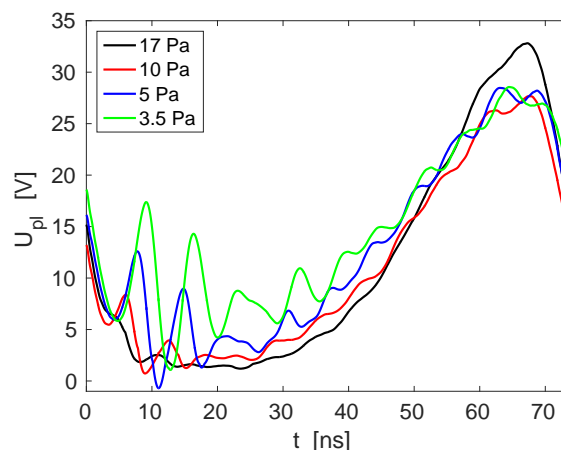
Přestože vyšší harmonické frekvence mohou silně ovlivňovat plazma kapacitních výbojů a jsou citlivým nástrojem pro diagnostiku a monitorování plazmatu, stály dlouho na okraji zájmu vědecké komunity. Nedostatečná pozornost se věnuje jak jejich měření, zejména potřebné sondové diagnostice uvnitř plazmatu, tak i teoretickému modelování. Následující kapitoly shrnují pokroky učiněné na poli elektrických vlastností a nelinearity kapacitních výbojů na našem pracovišti v posledních několika letech.

## 2.2 Sondová diagnostika

Ačkoli elektrické vlastnosti plazmatu lze měřit na různých částech reaktoru a přítomnost vyšších harmonických frekvencí byla sledována na přívodu vf. napětí [20, 26, 27]



Obr. 2.1: Příklad jedné periody potenciálu plazmatu spolu s průběhem napětí vysoko- a nízko-impedanční sondy. Napětí nízkoimpedanční sondy je v obrázku  $20\times$  zvětšeno. Publikováno v [25].



Obr. 2.2: Průběh potenciálu plazmatu během jedné periody kapacitního výboje iniciovaného v dusíku za čtyřech různých tlaků. Publikováno v [25].

a na proudu tekoucím segmentem stěny reaktoru [17] nebo zemněnou elektrodou [27], výsadní postavení mají sondová měření [27, 11, 28], která jediná umožňují relativně přímá a prostorově rozlišená měření potenciálu plazmatu. Nicméně i okolo sondy ponořené do plazmatu vzniká tenká stěnová vrstva prostorového náboje, která odděluje sondu od plazmatu, což znemožňuje skutečně přímé měření potenciálu plazmatu. Vysokofrekvenční vlastnosti této stěnové vrstvy není jednoduché přesně určit, navíc má tato vrstva obecně opět nelineární charakter. Snad právě přítomnost stěnové vrstvy okolo sondy způsobila, že zatímco stejnosměrná složka potenciálu plazmatu je rutinně měřena pomocí kompenzované Langmuirovy sondy, vysokofrekvenční průběh potenciálu plazmatu měřilo jen pár autorů [28, 27, 11], přestože vf. složky potenciálu plazmatu mají minimálně stejný význam pro fyziku vf. výbojů jako složka stejnosměrná.

Předchozí autoři se snažili omezit vliv stěnové vrstvy okolo sondy minimalizací vf. proudu tekoucí sondou a aby byli schopni vyhodnotit vliv vrstvy na měření, modelovali její chování jednoduchým kondenzátorem. Tloušťku vrstvy a tedy i její kapacitu odhadli pomocí Child-Langmuirova zákona [28] nebo pomocí srovnání měření se zatíženou a nezatíženou sondou [27]. Protože skutečné chování stěnové vrstvy je značně pestřejší, věnují se následující odstavce rozvoji sondové metody měření vf. složek potenciálu plazmatu vč. jeho vyšších harmonických frekvencí.

První nekompenzovaná sonda pro měření časového průběhu potenciálu plazmatu, kte-

rou jsem sestrojil, sledovala technicky nejjednodušší řešení. Šlo prakticky o částečně stíněný drátek, který byl vně reaktoru, těsně za vakuovou průchodkou, připojen na padesátiohmový koaxiální kabel [29]. Pro omezení proudu tekoucího na sondu byl koaxiální kabel připojen k osciloskopu se vstupním odporem  $1\text{ M}\Omega$ . Na spojení drátu s koaxiálním kabelem a zejména na vstupu osciloskopu docházelo samozřejmě k odrazům vř. signálu, a proto byla provedena kalibrace vlastní sondy, jejímž výstupem byla kaskádní matice popisující přenos signálu sondou. Všechny prvky matice byly frekvenčně závislé. Tento postup byl sice funkční, ale vyžadoval měření kaskádní matice sondy pro mnoho frekvencí, což ovšem přidává zdroje neurčitosti výsledků.

Rozhodl jsem se proto pro alternativní postup, kdy jsem neomezoval proud tekoucí sondou, ale minimalizoval rozdíl mezi průběhem napětí na hrotu a výstupu sondy a především jsem se pokusil realisticky modelovat chování stěnové vrstvy okolo sondy. Konstrukce nové sondy, model stěnové vrstvy i test metody jsou posány v [11]. Zde stručně shrnu, že sonda byla tvořena koaxiálním kabelem uvnitř vakuového vedení, jehož jedno vlákno centrálního vodiče přesahovalo vakuové vedení a tvořilo vlastní válcovou sondu zanořenou do plazmatu. Druhý konec koaxiálního kabelu byl přiveden na vstup osciloskopu, tentokrát s přizpůsobeným vstupním odporem. Bylo otestováno, že průběh vř. napětí na hrotu a na výstupu sondy jsou prakticky identické.

Těžiště práce leželo ve výpočtu napětí na stěnové vrstvě. Byl vytvořen model vrstvy založený na následujících předpokladech:

- Elektrický proud vrstvou je složen z proudu neseného elektrony, konstantního iontového proudu a Maxwellova posuvného proudu.
- Maxwellův posuvný proud ( $I_d$ ) lze popsat pomocí efektivní tloušťky stěnové vrstvy:

$$I_d = en \frac{S}{r_p} s \frac{ds}{dt}, \quad (2.1)$$

kde  $e$  je elementární náboj,  $n$  koncentrace elektronů,  $S$  plocha povrchu sondy,  $r_p$  poloměr sondy,  $s$  vzdálenost vnější hranice stěnové vrstvy od osy sondy a  $t$  je čas.

- Napětí na stěnové vrstvě lze spočítat pomocí efektivní tloušťky stěnové vrstvy vztahem

$$U = \frac{en}{4\epsilon_0} \left( 2s^2 \ln \frac{s}{r_p} - s^2 + r_p^2 \right), \quad (2.2)$$

kde  $\epsilon_0$  je permitivita vakua. Tento vztah odpovídá napětí na válcové stěnové vrstvě s tloušťkou  $s - r_p$  a konstantní hustotou náboje  $ne$ .

Aby střední tloušťka stěnové vrstvy a tím i stejnosměrné napětí na vrstvě byly určeny dobře, byla stejnosměrná složka potenciálu plazmatu změřena vysokofrekvenčně kompenzovanou Langmuirovou sondou. Model stěnové vrstvy okolo sondy byl pak řešen s požadavky, aby střední hodnota spočítaného potenciálu plazmatu odpovídala hodnotě změřené Langmuirovou sondou a aby časový průběh potenciálu plazmatu byl periodický. Takovýto model již realisticky popsal chování stěnové vrstvy, jejíž tloušťka se během periody vf. napětí radikálně mění, a umožnil tak z měřeného průběhu napětí na sondě věrohodně spočítat průběh potenciálu plazmatu.

Test věrohodnosti metody byl proveden tak, že na sondu bylo přivedeno externí záporné stejnosměrné napětí v rozsahu od 0 do -40 V a průběh potenciálu plazmatu byl změřen pro několik různých předpětí sondy. Snížením stejnosměrného napětí sondy bylo dosaženo zvětšení tloušťky stěnové vrstvy okolo sondy a bylo možné testovat, zda tato různá měření poskytnou stejné průběhy potenciálu plazmatu. Přestože při tomto testu byla násobně zvětšena tloušťka stěnové vrstvy, byly získané průběhy potenciálu plazmatu v dobré vzájemné shodě.

Realizovaná měření potvrdila, že potenciál plazmatu kapacitního výboje obsahuje vysoký podíl vyšších harmonických frekvencí, jejichž amplituda může být za tlaku několika pascalů srovnatelná s amplitudou základní frekvence dodávané z vysokofrekvenčního generátoru. Oscilace plazmatu na frekvenci sériové rezonance, jež jsou především zodpovědné za vznik vyšších harmonik, byly vybudeny zejména během expanze stěnové vrstvy u buzené elektrody. Ukázalo se také, že výbojový proud je silně korelován s napětím měřeným sestavenou nízkoimpedanční (50  $\Omega$ ) sondou.

Ze studovaných závislostí amplitudy vyšších harmonik na parametrech plazmatu byly dva příklady uveřejněny v [30]. Závislost na tlaku a na složení plynu byla použita k demonstraci vlivu koncentrace elektronů na vyšší harmoniky. Na jedné straně jsem pozoroval rezonanční zesílení některých harmonik v souladu s teorií, chování jiných harmonik ale nebylo možné vysvětlit jejich zesílením při sériové rezonanci plazmatu. Pro vysvětlení je zde potřeba použít i vzájemnou vazbu vyšších harmonických frekvencí, kterou popisuje model uvedený v kpt. 2.4.

Jako příklad studovaných závislostí vyšších harmonik na parametrech výbojové aparatury uveďme závislosti na nastavení přízpůsobovacího členu [14]. Při změně jeho nastavení se sice může měnit hodnota frekvence sériové rezonance plazmatu, dominantní vliv na vyšší harmonické frekvence ale v použitém experimentálním uspořádání měla skutečnost, že rozladění přízpůsobovacího členu snižuje velikost napětí na stěnové vrstvě u buzené elektrody. Toto pozorování ve shodě s teoretickým modelem popsaným v kpt. 2.4 říká, že stejnosměrné napětí (a zároveň amplituda základní harmoniky) na stěnové vrstvě je jednou z klíčových veličin řídících vyšší harmoniky.

## 8KAPITOLA 2. NELINEÁRNÍ ELEKTRICKÉ VLASTNOSTI KAPACITNÍCH VÝBOJŮ

Sestavená nekompensovaná sonda s nízkou impedancí a analýza jejího chování pomocí zmíněného modelu stěnové vrstvy sice přinesly věrohodná data a byly úspěšně použity pro diagnostiku a monitorování plazmatu, nicméně zřetelně existoval prostor pro další zpřesnění metody, a to kombinace sestaveného modelu stěnové vrstvy s vysokoimpedanční sondou, která minimalizuje vř. proud tekoucí na sondu. Proto byla sestavena nekompensovaná sonda s nízkou kapacitou vůči zemi (0.9 pF), jejíž napětí bylo měřeno vysokoimpedanční (3 pF,  $10^8 \Omega$ ) vstupní sondou rychlého osciloskopu a napětí na této sondě bylo analyzováno pomocí modelu (2.1)–(2.2) [25].

Sestavená vysokoimpedanční nekompensovaná sonda opět úspěšně prošla testem založeným na měření průběhu potenciálu plazmatu při různých stejnosměrných předpětích sondy, navíc obstála i v podobném testu, při kterém byla zatížena dodatečným kondenzátorem. Analýza nové sondy [25] také uvádí rozbor citlivosti sondy na hodnoty vstupních parametrů (střední hodnota potenciálu plazmatu, koncentrace a teplota elektronů). Ukázalo se, že pro přibližná měření lze sondu použít dokonce i bez znalosti uvedených vstupních parametrů, neboť záporným předpětím sondy lze vyloučit vliv teploty elektronů na měření, střední hodnotu potenciálu plazmatu je možné odhadnout i pomocí této nekompensované sondy a citlivost metody na hodnotu koncentrace elektronů je malá. Nová metoda byla dále srovnána se staršími metodami založenými buď na aproximaci stěnové vrstvy okolo sondy kondenzátorem [27, 28] nebo na použití nízkoimpedanční sondy [11]. Přestože starší metody často dávaly podobné výsledky jako popisovaná nová metoda, byly v některých případech pozorovány i podstatné odchylky starších metod od výsledků věrohodnější nové metody, takže pro měření průběhu potenciálu plazmatu lze jednoznačně doporučit popsanou novou metodu.

V závěru práce [25] byla nekompensovaná sonda využita k měření průběhu potenciálu plazmatu v kapacitních výbojích zapalovaných v různých plynech (Ar, N<sub>2</sub>, O<sub>2</sub>, H<sub>2</sub>) a za různých výbojových podmínek. V souladu s teorií a s předchozím textem bylo pozorováno, že potenciál plazmatu obsahuje značný podíl vyšších harmonických frekvencí, které citlivě reagují na hodnotu koncentrace elektronů a které dosahují vysokých amplitud zejména za nízkého tlaku, vysoké koncentrace elektronů a při dosažení sériové rezonance plazmatu.

Další logický krok ve vývoji nekompensovaných sond je zobecnění modelu stěnové vrstvy okolo sondy tak, aby věrohodně popsala i situace, kdy stěnová vrstva kolabuje a potenciál sondy se (krátkodobě) dostane nad potenciál plazmatu. Lze očekávat, že s takovýmto modelem bude možno nekompensovanou sondu využít i k měření koncentrace a teploty elektronů, tedy veličin, které jsou doposud měřeny vysokofrekvenčně kompenzovanými Langmuirovými sondami. Elektrické pole okolo válcové sondy jsme proto popsali

pomocí realističtější rovnice

$$\frac{d^2\varphi}{dr^2} + \frac{1}{r} \frac{d\varphi}{dr} + \frac{en}{\varepsilon_0} \left[ 1 - e^{-\frac{\varphi - \varphi_{pl}}{kT_e}} \right] = 0, \quad (2.3)$$

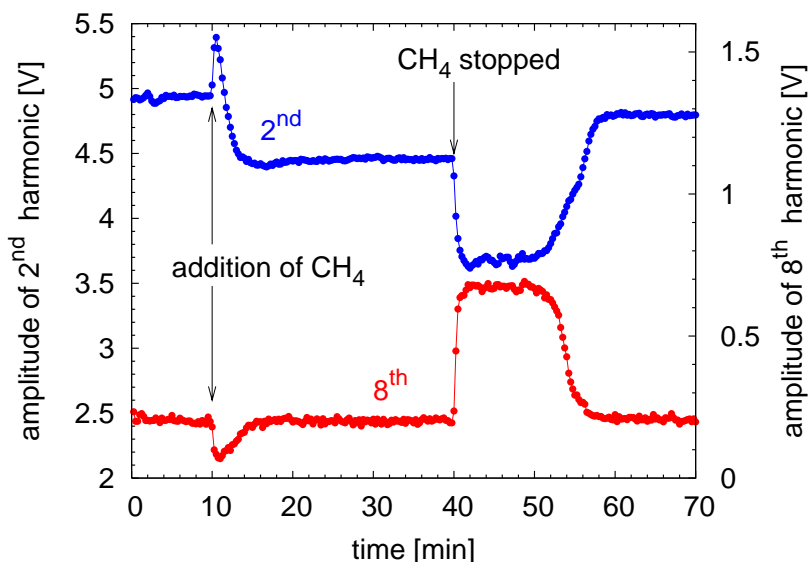
kde  $\varphi$  je potenciál v okolí sondy,  $\varphi_{pl}$  aktuální potenciál plazmatu,  $r$  vzdálenost od osy sondy a  $T_e$  teplota elektronů. Tuto rovnici jsme spolu s Jurajem Páleníkem numericky vyřešili a použili při zpracování měřených dat [31]. Měření, při kterých byl potenciál sondy vždy pod potenciálem plazmatu, podle očekávání potvrdila platnost předchozí metody popsané výše. Podrobná analýza měření realizovaných i pro vyšší potenciály sondy včetně testování možnosti určit např. teplotu nebo koncentraci elektronů je ale teprve před námi.

Analogické nekompensované sondy jsme dále použili při monitorování depozičních a leptacích procesů. Hlavním výsledkům této oblasti se věnuje následující kpt. 2.3.

## 2.3 Vyšší harmonické frekvence v depozičních a leptacích procesech

Protože vyšší harmonické frekvence generované plazmatem citlivě reagují i na drobné změny v plazmatu, mohou být vhodným nástrojem pro monitorování depozičních a leptacích procesů. Je známo, že amplitudy některých vyšších harmonik se mohou výrazně změnit při odleptání tenké vrstvy přítomné na elektrodě, a proto je možné vyšší harmoniky použít k detekci konce leptacího procesu [20, 21]. Důvod pro reakci na tak malou změnu výbojových podmínek ale nebyl jasný.

Protože při leptacím procesu má přítomnost vrstvy vliv na vyšší harmonické frekvence, rozhodli jsme se vyzkoušet, jestli je možné vyšší harmoniky použít na monitorování jiného procesu, a to vysokofrekvenčního reaktivního magnetronového naprašování. Magnetronové naprašování je založeno na rozprašování a následné depoziaci materiálu elektrody (terče) energetickými ionty extrahovanými z plazmatu hořícího v magnetickém poli, většinou v argonu. Při reaktivním magnetronovém naprašování se do aparatury přidává i reaktivní plyn, např. dusík nebo kyslík, který reaguje s materiálem rostoucí vrstvy a vytváří např. nitridy nebo oxidy. Reaktivní plyn ovšem nereaguje pouze s rostoucí vrstvou, ale i s materiálem terče. Je-li koncentrace reaktivního plynu malá, stíhá se povrch terče čistit rozprašováním a proces běží v tzv. kovovém režimu. Při vyšší koncentraci reaktivního plynu se ale projeví skutečnost, že vzniklé sloučeniny se zpravidla rozprašují pomaleji než čistý materiál terče. Vznik sloučeniny na terči tedy vede ke snížení rozprašovací, a tím i depoziční rychlosti. Pomaleji rostoucí vrstva ovšem spotřebuje menší množství reaktivního plynu, takže parciální tlak reaktivního plynu vzroste a s ním i rychlost jeho reakce s povrchem terče. Tato kladná zpětná vazba vede ke skokovému otrávení povrchu terče



Obr. 2.3: Vývoj amplitudy druhé a osmé harmoniky výbojového napětí během růstu a leptání tenké DLC vrstvy. Depozice začala v desáté minutě přidáním metanu do vodíkového výboje a skončila ve čtyřicáté minutě zastavením metanu. Od čtyřicáté do přibližně 56-té minuty docházelo k leptání vrstvy. Přidání a zastavení metanu se projevilo prakticky skokovou změnou měřených amplitud díky změně tlaku a složení plynu. Reakce na vznik a zánik vrstvy jsou vidět od desáté do patnácté a od padesáté do 56-té minuty. Publikováno v [22].

sloučeninou reaktivního plynu, snížení depoziční rychlosti a změně složení deponované vrstvy. Tento skok má hysteretní charakter a otrávení terče má proto podstatný vliv na další průběh depozice. Protože kvalitní materiály s požadovanou stechiometrií vznikají často za podmínek blízkých přechodu mezi kovovým a otráveným režimem, nebo dokonce uvnitř hysteretní křivky přechodu, vyžaduje tento depoziční proces citlivé monitorování.

Chování vyšších harmonických frekvencí jsme studovali ve vf. reaktivním magnetronovém naprašování oxidů a nitridů titanu. Do argonového výboje zapáleného v blízkosti titanového terče jsme připouštěli dusík nebo kyslík a kromě tlaku plynu, intenzity vybraných spektrálních čar a stejnosměrného předpětí na terči jsme sledovali i amplitudy jednotlivých frekvenčních komponent napětí na jednoduché válcové sondě vložené do plazmatu a na vedení k rozprašovanému terči, který byl zároveň živou elektrodou výboje [32].

Na napětí terče i sondy jsme skutečně pozorovali přítomnost vyšších harmonických frekvencí, velkých amplitud dosahovaly zejména na sondě. Většina vyšších harmonik při přechodu mezi kovovým a otráveným režimem výboje zřetelně měnila svoji amplitudu.

### 2.3. VYŠŠÍ HARMONICKÉ FREKVENCE V DEPOZIČNÍCH A LEPTACÍCH PROCESECH 11

Zatímco stejnosměrné předpětí terče, které se tradičně používá k monitorování procesu, se při přechodu měnilo jen o několik procent, amplitudy některých vyšších harmonických frekvencí se měnily dokonce o stovky procent. Amplitudy vyšších harmonických frekvencí se tedy staly nejcitlivější známou elektrickou metodou monitorování stavu vf. reaktivního magnetronového naprašování.

S objevem této nové metody monitorování se ovšem vynořila otázka, na co konkrétně vyšší harmonické frekvence reagují. V úvahu připadaly dvě příčiny: Buď je chování harmonik způsobené změnou složení a celkového tlaku plynu při přechodu mezi kovovým a otráveným režimem, nebo změnou složení povrchu terče. Oba jmenované faktory by mohly hrát roli. Změna složení plynu bývá provázena změnou koncentrace a srážkové frekvence elektronů, což obojí má na chování vyšších harmonických frekvencí vliv. Změna povrchu terče ale také působí na koncentraci elektronů např. prostřednictvím potenciálové emise elektronů při dopadu iontu.

Položená otázka byla analyzována ve člancích [26, 22]. Povrch titanového terče byl nejprve zcela otráven výbojem ve směsi argonu se značným množstvím reaktivního plynu ( $N_2$  nebo  $O_2$ ). Plyny byly poté z výbojové komory odčerpány a výboj byl znovu zapálen v čistém argonu. Ukázalo se, že amplitudy harmonik byly před a po odčerpání reaktivního plynu prakticky stejné, nezávisely tedy příliš na celkovém tlaku ani přítomnosti reaktivního plynu v objemu plazmatu. Nitridová nebo oxidová vrstva na povrchu terče ale byla v argonovém výboji postupně odprašována, takže při tomto experimentu jsme mohli sledovat reakci vyšších harmonických frekvencí na změnu složení povrchu terče při zachování téměř nezměněné čisté argonové atmosféry. Stav povrchu terče jsme sledovali také pomocí intenzity spektrálních čar titanu. Ve chvíli, kdy došlo k očištění povrchu terče od nitridu nebo oxidu, došlo k prudké změně vyšších harmonických frekvencí a jejich amplitudy se vrátily z hodnot odpovídajících otrávenému režimu na hodnoty odpovídající kovovému režimu výboje. Tím bylo prokázáno, že citlivá reakce vyšších harmonických frekvencí na přeskok mezi kovovým a otráveným režimem reaktivního magnetronového naprašování není způsobena změnou tlaku ani složení plynu v objemu plazmatu, ale změnou složení povrchu magnetronového terče.

Zjištění, že vyšší harmonické frekvence reagují právě na stav povrchu terče mj. znamená, že navržená metoda monitorování sleduje přímo přítomnost tenké vrstvy na elektrodě, což je ideální jak pro monitorování reaktivního vf. magnetronového naprašování, tak i jiných leptacích či depozičních procesů.

Ve zmíněném článku [22] jsme se zaměřili na chování Fourierových složek (tedy vyšších harmonických frekvencí ale i základní frekvence a stejnosměrného předpětí) výbojového i sondového napětí nejenom v magnetronovém naprašování, ale také při PECVD depoziční a leptání tenkých diamantu podobných (DLC) vrstev. Abychom mohli rozlišit vliv různých

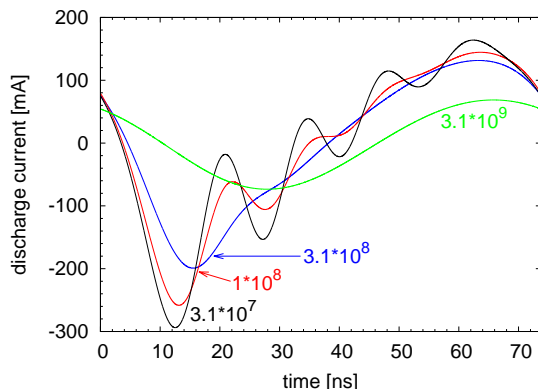
ných jevů na chování měřených Fourierových složek, provedli jsme sadu experimentů, ve kterých jsme se drželi následujícího postupu: Výboj byl nejprve zapálen v čistém vodíku. Po několika minutách jsme do hořícího vodíkového výboje začali pouštět i metan, což vedlo k depozici DLC vrstvy, zejména na buzené elektrodě. Po půlhodině depozice jsme tok metanu zastavili a v následujících desítkách minut tedy výboj hořel opět v čistém vodíku, ve kterém se DLC vrstva po nějakém čase odleptala. Tento postup umožnil srovnat hodnoty výbojových napětí ve všech kombinacích výboje s i bez reaktivního plynu a s i bez deponované vrstvy, sledovat reakce na změnu tloušťky vrstvy a zároveň kontrolovat, zda se výboj po odčerpání reaktivního plynu a odleptání vrstvy vrátil do původního stavu. Popsané experimenty proběhly pro depozici/leptání na vodivých i nevodivých substrátech a byl také sledován vliv tlaku vodíku. Ukázalo se, že prostá přítomnost vrstvy má na měřené amplitudy napětí často větší vliv než přidání poměrně velkého množství metanu. Tento vliv byl navíc leckdy i opačný, např. přidání metanu vedlo ke zvýšení amplitudy druhé harmonické frekvence výbojového napětí, zatímco vznik vrstvy na elektrodě vedl ke snížení této amplitudy. Reakce jednotlivých frekvenčních složek napětí na přítomnost vrstvy tedy opět nebyla způsobena ovlivněním plazmatu odleptávaným materiálem, a protože jsme vyloučili i vliv vodivosti vrstvy, reagovaly jednotlivé harmoniky i zde na stav povrchu buzené elektrody, nejspíš na pravděpodobnost emise elektronů z povrchu. Skutečnost, že chování frekvenčních složek nezáviselo na vodivosti povrchu elektrody, umožňuje zavést monitorování založené na sledování základní či vyšších harmonických frekvencí do plazmových procesů používajících jak vodivé, tak i nevodivé vrstvy či substráty.

Navržené vysvětlení, podle kterého je reakce (vyšších) harmonických frekvencí na přítomnost tenké vrstvy způsobena rozdílnými hodnotami pravděpodobnosti emise elektronu z povrchu tenké vrstvy a substrátu, předpovídá, že při odleptání tenké vrstvy se musí změnit koncentrace elektronů v plazmatu. Tuto předpověď jsme ověřili měřením koncentrace elektronů vf. kompenzovanou Langmuirovou sondou.

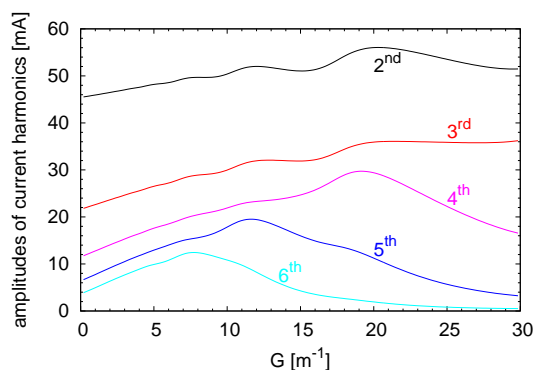
## 2.4 Modelování elektrické nelinearity výbojů

Pro porozumění nelineárním vlastnostem kapacitních výbojů bylo potřeba vytvořit teoretický model elektrického chování plazmatu včetně chování vyšších harmonických frekvencí. Stávající modely řešily buď jen symetrický výboj se shodnými plochami elektrod [33, 16], kde je generování vyšších harmonických frekvencí potlačeno, nebo extrémně nesymetrický případ [34, 35, 17], kde byl zcela zanedbán vliv nelineární stěnové vrstvy u zemněné elektrody.

Proto jsem vytvořil model, který bere v potaz nelineární vlastnosti kapacitního výboje a který lze použít k popisu symetrických i nesymetrických výbojů s jakýmkoli stupněm



Obr. 2.4: Spočítaný průběh proudu nesy-metrickým kapacitním výbojem pro různé hodnoty srážkové frekvence elektronů. Zejména při expanzi stěnové vrstvy u živé elektrody se vybudí vlastní kmity plazmatu, které jsou tlumeny díky srážkám elektronů s neutrály. Publikováno v [18].



Obr. 2.5: Vzájemná vazba mezi vyššími harmonickými frekvencemi nízkotlakého kapacitního výboje. Zesílení čtvrté až šesté harmoniky při sériové rezonanci se projeví i na ostatních harmonikách. Veličina  $G$  vyjadřuje podíl vzdálenosti a plochy elektrod. Publikováno v [18].

nesymetrie [18]. V tomto elektrickém modelu je vodivost vlastního „bulkového“ plazmatu popsána vztahem

$$\sigma = \frac{ne^2}{m(\nu + i\omega)} + i\omega\epsilon_0, \quad (2.4)$$

kde  $\nu$  je srážková frekvence pro přenos hybnosti elektronu a  $\omega$  je úhlová frekvence elektrického pole. Protože proudy stěnovými vrstvami dominuje Maxwellův posuvný proud, bylo jejich elektrické chování vyjádřeno vztahy

$$U_s = \frac{ne}{2\epsilon_0} s^2 \quad (2.5)$$

$$I = \pm Sne \frac{ds}{dt}, \quad (2.6)$$

kde  $U_s$  označuje napětí na stěnové vrstvě a  $I$  proud stěnovou vrstvou,  $S$  je plocha příslušné elektrody a  $s$  tloušťka stěnové vrstvy. Uvedené vztahy byly odvozeny pro stěnovou vrstvu s konstantní koncentrací iontů a nulovou koncentrací elektronů. Vytvořil jsem proto i model jedné stěnové vrstvy s nehomogenní koncentrací náboje a ověřil, že pro V-A charakteristiku vrstvy dává výsledky velmi podobné jednoduchému modelu (2.5)–(2.6). Model (2.4)–(2.6) byl poté doplněn o generátor vf. napětí a jeho výstupní impedanci a byl řešen numericky.

Protože kapacitní výboje generují jen omezený počet vyšších harmonických frekvencí, bylo výhodné provést Fourierův rozklad rovnic modelu a řešit rovnice Fourierova obrazu sestaveného modelu. K rovnicím byla přidána podmínka nulového stejnosměrného proudu výbojem, která zajistila správné počítání stejnosměrných napětí stěnových vrstev a tedy i stejnosměrného předpětí na živé elektrodě. Potřeba takovéto podmínky byla zdůvodněna v [36]. Byla nalezena vhodná numerická metoda řešení vzniklého systému rovnic a byly sestaveny funkce pracující v prostředí Matlab, které tento model řeší. Sestavené funkce byly popsány a poskytnuty k volnému stažení [37].

Část výsledků modelu je publikovaná ve článku [18]. Předpověď modelu byla úspěšně srovnána s měřením časového průběhu potenciálu plazmatu nekompensovanou sondou (kpt. 2.2) a model pak byl využit ke studiu nelineárních vlastností plazmatu. Například byl pozorován vliv srážkové frekvence elektronů, jejíž růst vede k útlumu vyšších harmonických frekvencí i snižování základní frekvence výbojového proudu. Ukázalo se ale, že díky vlivu vyšších harmonik nemusí být pokles výbojového proudu monotónní (může tedy dojít i k omezenému nárůstu proudu) a že díky Maxwellově posuvnému proudu, který může plazmatem téct i při jakkoli vysoké srážkové frekvenci, nedojde k úplnému vymizení vyšších harmonických frekvencí ani ve výbojích iniciovaných za atmosférického tlaku. Předpovězenou existenci vyšších harmonických frekvencí v kapacitních výbojích buzených za atmosférického tlaku jsme poté experimentálně potvrdili v práci [2], kde jsme také pozorovali snížení amplitudy sudých harmonik díky opačnému působení stěnových vrstev u živé a zemněné elektrody. Jiným příkladem využití modelu je pozorování vlivu koncentrace elektronů, jehož výpočet názorně demonstroval vliv rezonancí jednotlivých harmonik jak s plazmovou frekvencí vlastního plazmatu, tak se sériovou („*plasma-sheath*“) rezonancí. Hodnota sériové rezonance byla mírně ovlivněna i amplitudou přivedeného napětí a poměrem ploch obou elektrod [36]. Model dále ukázal, že amplituda přivedeného v.f. napětí má vliv na efektivní nesymetrii i nelinearitu výboje, a to navzdory skutečnosti, že geometrická asymetrie, tj. poměr ploch elektrod, zůstával konstantní. Byl pozorován i opačný efekt, kdy vyšší harmonické frekvence generované díky nelinearitě výboje ovlivňovaly nesymetrii výboje a tím i předpětí na živé elektrodě. Nelinearita stěnových vrstev dále vedla i ke vzájemné vazbě mezi jednotlivými vyššími harmonikami, což souhlasí s pozorováním zmíněným v kpt. 2.2.

Zmíněný vliv vyšších harmonických frekvencí na stejnosměrná napětí na stěnových vrstvách [18] byl motivací ke studiu vlivu vyšších harmonických frekvencí na tzv. elektrický asymetrický efekt, ke kterému dochází ve dvoufrekvenčních kapacitních výbojích [38, 39]. Při tomto efektu se využívá interakce mezi dvěma přivedenými napětími, přičemž frekvence jednoho napětí je sudým násobkem frekvence druhého napětí, a změnou fáze mezi přivedenými napětími se ladí velikost stejnosměrného napětí na jednotlivých

stěnových vrstvách. Proto byl model (2.4)–(2.6) využit i ke studiu takovýchto dvoufrekvenčních výbojů [40]. Studium dvoufrekvenčního výboje ukázalo, že elektrický asymetrický efekt lze využít i v nesymetrických výbojích. Situace je ovšem komplikovanější díky vyšším harmonickým frekvencím, které skutečně ovlivňují hodnoty stejnosměrných napětí na stěnových vrstvách. Většina výsledků analýzy modelu dvoufrekvenčního výboje se teprve připravuje k publikaci.

Doposud popisovaný model ovšem platí pouze v  $\alpha$ -režimu výboje, ve kterém elektrony emitované z elektrod hrají jen vedlejší roli. Naopak v  $\gamma$ -režimu hrají emise elektronů z elektrod s následující lavinovou ionizací ve stěnové vrstvě roli zásadní a právě  $\gamma$ -režim je nejčastější stabilní formou kapacitních výbojů hořících za atmosférického tlaku. Model stěnové vrstvy (2.5)–(2.6) jsem tedy obohatil o elektronový a iontový proud a o ionizaci ve stěnové vrstvě. Tato snaha byla motivována spektrálními měřeními elektrických polí ve stěnové vrstvě atmosférického  $\gamma$ -režimu kapacitního výboje realizovaných kolegy [41]. Jejich měření nečekaně ukázala téměř pravoúhlý časový průběh intenzity elektrického pole ve stěnové vrstvě, přestože výboj byl buzen vf. proudem se sinovým průběhem. Tento měřený průběh se mi podařilo velmi dobře reprodukovat vytvořeným modelem stěnové vrstvy [41]. Ukázalo se, že při zvýšení napětí na stěnové vrstvě dochází díky zintenzivnění lavinové ionizace k prudkému zvýšení vodivosti stěnové vrstvy, takže od jisté úrovně intenzity elektrického pole ve vrstvě už zvyšování výbojového proudu vede jen k velmi malému nárůstu napětí na vrstvě a proto se prakticky zastaví i růst intenzity elektrického pole.



# Kapitola 3

## Fluorescenční měření v plazmatu

### 3.1 Úvod do problematiky

Mezi nejdůležitější reaktivní částice v plazmatu patří jedno- i víceatomové radikály vzniklé disociací molekul plynu (při nárazu elektronu nebo vlivem metastabilu), iontovými reakcemi nebo disociativní rekombinací, reakcí jiných radikálů, disociací vysoce vibračně excitovaných stavů, příp. dopravené do plazmatu desorpcí z blízkého pevného nebo kapalného povrchu. Právě vysoké reaktivitě radikálů plazma vděčí za mnoho svých vlastností, většina modifikací povrchů plazmatem je založena na účincích těchto částic a velká část plazmochemie popisuje radikálové reakce.

Je proto žádoucí mít vhodný nástroj pro měření koncentrací radikálových částic včetně jejich prostorového rozložení i časového vývoje. Diagnostické metody jsou ale omezené: naprostá většina radikálů je v základním elektronovém stavu, a proto spontánně nezáří, krátká doba života radikálů omezuje možnosti jejich transportu mimo plazma a následnou analýzu standardními chemickými metodami, absorpční měření nepřinášejí informaci o prostorovém rozložení a bývají málo citlivá. Navíc mnohé metody použitelné za nízkého tlaku naráží na mnoho komplikací, pokud mají být aplikované na plazma iniciované za atmosférického tlaku. V současnosti nejvhodnější způsob detekce radikálů (a metastabilů) je proto založen na fluorescenci [42, 43, 44] – buď prosté laserem indukované fluorescenci (LIF, *laser-induced fluorescence*) nebo fluorescenci indukované dvoufotonovou absorpcí laserového záření (TALIF, *two-photon absorption laser-induced fluorescence*), která umožňuje excitaci i lehkých jednoatomových částic (H, C, N, O) bez použití VUV laseru.

I fluorescenční metody ovšem mají své komplikace a zejména za atmosférického tlaku nejsou ještě zcela standardní metodou. Proto se následující kapitola věnuje způsobu měření a vyhodnocení fluorescenčních metod s důrazem na několik problematických bodů,

u kterých jsem se podílel na hledání jejich korektních řešení. Teprve potom se zaměřím na konkrétní typy výbojů, které jsme pomocí fluorescence studovali. I když jsme detekovali i jiné částice, omezím se v této práci na diskuzi měření jednoatomových radikálů vodíku, kyslíku a dusíku a molekulového hydroxylového radikálu (OH).

## 3.2 Metoda fluorescenčních měření

### 3.2.1 Základní vztahy

Protože přesné určení absolutní citlivosti měření (TA)LIF je problematické, kalibrují se tyto metody pomocí měření jiných signálů se známou intenzitou. Jako nejvhodnější a námi používané se jeví měření Rayleigha rozptylu pro kalibraci jednofotonové LIF a měření TALIF signálu vzácného plynu (Kr, Xe) se známou koncentrací pro kalibraci TALIF. Při použití těchto kalibračních metod získáváme pro koncentraci částic hydroxylových radikálů měřených jednofotonovou LIF [45] vztah

$$N_{OH} = \frac{S_f}{S_r} N_r \frac{1}{f} \frac{c 4\pi \frac{d\sigma_r}{d\Omega}}{\kappa_f B h\nu_r} \frac{E_{lr}}{E_{lf}} \cdot \frac{1}{\tau^{(1)}} \frac{C_r}{\sum_{ij} F_{ij}^{(1)} C_{ij}^{(1)} A_{ij}^{(1)} f_i^{(1)}(T) + V\tau^{(0)} \sum_{ij} F_{ij}^{(0)} C_{ij}^{(0)} A_{ij}^{(0)} f_i^{(0)}(T)} \quad (3.1)$$

a pro koncentraci jednoatomových radikálů měřených metodou TALIF [46] vztah

$$N_X = N_K \frac{S_X \kappa_K}{S_K \kappa_X} \left( \frac{E_K}{E_X} \right)^2 \left( \frac{\nu_X}{\nu_K} \right)^2 \frac{\sigma_K^{TA}}{\sigma_X^{TA}} \frac{A_K \tau_K}{A_X \tau_X} \frac{F_K C_K}{F_X C_X}, \quad (3.2)$$

kde  $N$  označuje koncentraci,  $S$  měřený (TA)LIF signál,  $\kappa$  faktor spektrálního překryvu absorpční a laserové čáry,  $\nu$  frekvenci laserového záření,  $E$  energii laserových pulzů,  $\sigma$  účinný průřez pro dvoufotonovou absorpci nebo Rayleigha rozptyl,  $A$  Einsteinův koeficient spontánní emise,  $B$  Einsteinův koeficient absorpce záření radikálem OH,  $\tau$  dobu života excitovaných stavů,  $F$  propustnost použitého interferenčního filtru,  $C$  kvantovou účinnost detektoru (ICCD kamery) pro příslušnou vlnovou délku,  $f$  Boltzmannův faktor a  $V$  rychlost vibračního přenosu energie mezi prvním a základním vibračním stavem elektronově excitovaného radikálu OH. Indexy  $f$ ,  $r$ ,  $X$  a  $K$  rozlišují veličiny vztahující se k fluorescenci OH radikálu ( $f$ ), Rayleigha rozptylu ( $r$ ), TALIF měření jednoatomových radikálů ( $X$ ) nebo kalibračního TALIF měření vzácného plynu ( $K$ ). Indexy  $^{(0)}$  a  $^{(1)}$  odlišují základní a excitovaný vibrační stav elektronově excitovaného OH radikálu, index  $ij$  označuje konkrétní rotační čáru detekovaného vibračního pásu radikálu OH. Vztah (3.1) platí pro případ, kdy OH radikály excitujeme do prvního vibračně excitovaného stavu. V případě excitace

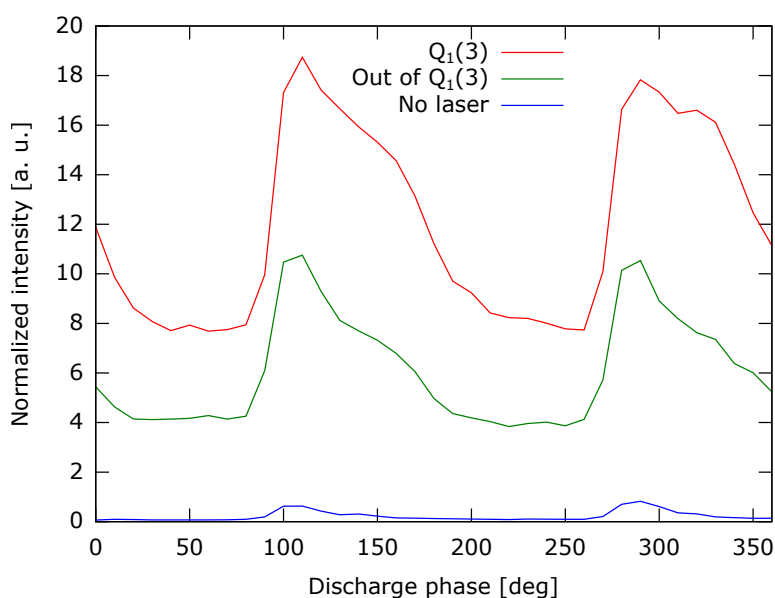
do základního vibračního stavu platí o něco jednodušší varianta tohoto vztahu [47, 48]. Korektní určení některých veličin vystupujících v základních vztazích (3.1) a (3.2) není zcela triviální a několika z nich se proto věnují následující řádky.

### 3.2.2 Parazitní signály

I když je fluorescenční signál snímán přes interferenční filtr, mohou k měřenému signálu kromě vlastní fluorescence zkoumaných částic ( $S$  v předchozích vzorcích) přispět i různé nechtěné efekty. Některé je snadné očekávat, např. temný signál detektoru, jiné mohou být překvapivější. Parazitní signály mohou vzniknout při rozptylu laseru na povrchu pevných předmětů nebo kapalin a při fluorescenci těchto látek. K tomuto jevu dochází často při diagnostice povrchových výbojů, kde se nelze zcela vyhnout kontaktu laserového svazku s povrchem blízkého předmětu, většinou dielektrika. Zejména při kontaktu laseru s dielektrickou bariérou hrozí také ovlivnění výboje laserovým pulzem [49], hlavně nastartování výboje a zesílení jeho záření v momentu, kdy chceme měřit fluorescenční signál [50]. A nakonec laser sám může způsobit fotodisociaci molekul ve výboji a tím uměle zvýšit koncentraci měřených částic.

Po analýze chování vyjmenovaných parazitních signálů v různých typech výboje jsme doporučili eliminovat jejich vliv na získané hodnoty koncentrací měřených částic pomocí následujících bodů:

- Minimalizace kontaktu laserového svazku s okolními povrchy [50], a to i odražených a rozptýlených částí svazku, např. pomocí přesného nastavení svazku, použití clonek, zastínění aparatury a sklonění případných okének v laserové dráze pod Brewsterovým úhlem [51]. Pokud to situace umožňuje, je výhodné mít v kontaktu se svazkem pouze nefluoreskující materiály s hladkým povrchem a vhodnou geometrií [51].
- Ověření, že prostřednictvím fotodisociace laserem neprodukuje fluorescenční signál při vypnutém výboji [52, 43] (nebo těsně po výboji). Pokud ano, je potřeba snížit energii laserových pulzů tak, aby tento signál vymizel.
- Měření a odečtení nejen signálu zaznamenaného při vypnutém laseru, ale také signálu detekovaného se zapnutým laserem, který ale má vlnovou délku rozladěnou mimo absorpční čáry částic přítomných v plazmatu. Takovéto měření totiž obsahuje případné vlivy rozptýleného laseru, fluorescence povrchů a ovlivnění výboje laserem [50]. Při odečtení parazitních signálů je potřeba vzít v úvahu, že nikdy nebyly měřeny při zcela stejných energiích laserových pulzů [51, 45].
- Časová synchronizace laseru s výbojem a naměření různých signálů (s naladěnou i rozladěnou vlnovou délkou laseru, bez laseru) v závislosti na fázi budicího napětí



Obr. 3.1: Časově rozlišené měření LIF OH v koplanárním povrchovém DBD iniciovaném v čisté vodní páře za atmosférického tlaku (za teploty  $120^{\circ}\text{C}$ ) v závislosti na fázi vf. napětí přivedeného na elektrody [45]. Od měřené intenzity už je odečten temný signál detektoru. Červená křivka ukazuje časový vývoj signálu měřeného s laserem naladěným na střed absorpční čáry OH. Modrá křivka prezentuje měření bez laseru, tedy spontánní záření výboje, které by před vyhodnocením koncentrace OH mělo být odečteno od červené křivky. Překvapením může být vysoká intenzita signálu měřeného s laserem, který měl vlnovou délku rozladěnou mimo absorpční čáru OH a nemohl proto způsobit fluorescenci OH (zelená křivka). Měření s rozladěným laserem odhaluje nejenom parazitní fluorescenci dielektrika či rozptyl laseru na dielektriku, ale také zesílení „spontánního“ záření výboje vlivem laseru. Kdyby zelená křivka nebyla odečtena od červené, vedlo by zpracování ke zcela špatnému časovému vývoji OH a k předeměření koncentrace OH o víc než 100 %.

výboje. Následné měření v takové fázi výboje, kdy elektrické pole ve výbojce je slabé a kdy tedy laser nemůže iniciovat výboj [50, 51].

- Naměření závislosti měřeného signálu na energii laserových pulzů (v případě TALIF na její druhé mocnině) a kontrola, že tato křivka nemá konkávní tvar (což by pravděpodobně bylo způsobeno produkcí reaktivních částic laserem) a že protíná počátek souřadnic [50]. Před vyhodnocením může být vhodné od uvedené křivky odečíst analogickou křivku měřenou s rozladěnou vlnovou délkou laseru. Následně je vhodné měřit při nízké energii laserových pulzů, ideálně v lineární části diskutované křivky.

Ovšem i uvedené parazitní signály mohou být užitečné: Časoprostorové rozložení spontánního záření výboje samozřejmě o plazmatu vypovídá a to i tehdy, byl-li výboj uměle nastartován laserem v přesně definované fázi budicího napětí. Signál rozptýleného laseru jsme využili k detekci kapek v koplanárním DBD iniciovaném ve vodních parách [45]. A původně nechtěnou fotodisociativní produkci radikálů laserem lze od fluorescence originálně přítomných částic odlišit díky odlišné závislosti na energii laserových pulzů a následně ji využít k detekci plazmatem produkovaných molekul, např.  $O_3$  nebo  $H_2O_2$  [53].

### 3.2.3 Saturační efekty

Tradiční měření LIF probíhá v lineárním režimu, tedy při tak slabém laserovém záření, kdy je závislost intenzity fluorescence přímo úměrná energii laserových pulzů. Nízká energie laseru ale často vede k nedostatečnému poměru signálu a šumu, takže by bylo žádoucí mít možnost realizovat kvantitativní LIF měření i při vyšších energiích, kdy ovšem dochází k částečné saturaci fluorescence. Proto jsme analyzovali procesy probíhající při LIF včetně saturačních jevů (ochuzení základního stavu, stimulovaná emise) a dospěli jsme k závěru, že slabou saturaci lze popsat vztahem

$$S_{sat} = \frac{\alpha E_l}{1 + \beta E_l}, \quad (3.3)$$

kde  $S_{sat}$  je měřený signál,  $\alpha$  a  $\beta$  jsou parametry fluorescenčního procesu, které lze získat fitem rovnice (3.3) na měřenou závislost fluorescenčního signálu na energii laserových pulzů ( $E_l$ ) [50]. Hodnota  $\alpha E_l$  udává hypotetickou intenzitu fluorescence, kdyby nedocházelo k saturaci, hodnota  $\beta E_l$  nese informaci o síle saturace. Uvedenou rovnici lze použít pro  $\beta E_l \leq 0.4$ . Jakmile stanovíme hodnotu parametru  $\beta$ , můžeme vyhodnocovat i částečně saturovaná měření tak, že měřenou (saturací ovlivněnou) intenzitu vynásobíme faktorem  $1 + \beta E_l$  a tak získáme hodnotu hypotetického nesaturovaného signálu  $S_f$ , kterou můžeme dosadit do rovnice (3.1).

### 3.2.4 Spektrální překryv

Při výpočtu koncentrace detekovaných částic je ovšem potřeba znát fluorescenční signál integrovaný přes celou excitační (absorpční) čáru sledované částice. V prvním přiblížení je možné naměřit profil excitační čáry přeladováním vlnové délky laseru a v následujících měřeních, která z důvodů času a stability experimentů bývají provedena jen s laserem naladěným do centra excitační čáry, vynásobit měřenou intenzitu poměrem měřeného integrálu celé excitační čáry ku signálu měřenému v maximu. Tento přístup by ale byl přesný pouze kdyby laser měl nekonečně úzkou spektrální čáru. Proto jsem odvodil faktor spektrálního překryvu excitační a laserové čáry

$$\kappa_f = \int_0^{\infty} l(\nu) a(\nu) d\nu, \quad (3.4)$$

kde  $l$  a  $a$  představují spektrální profily laserové a excitační čáry normované na jedničku a tento faktor jsme použili ve vyhodnocení fluorescenčních experimentů [47].

Ukázalo se ovšem, že faktor  $\kappa_f$  (stejně jako zmíněný jednodušší poměr maximálního signálu a integrální intenzity) je značně citlivý na saturaci, protože saturace může výrazně změnit tvar excitační čáry v okolí jejího maxima. Proto je potřeba měřit profily excitačních čar při dostatečně nízké energii laserových pulzů, příp. saturaci korigovat nebo naměřit hodnoty  $\kappa_f$  pro různé hodnoty energie laseru a měřenou závislost extrapolovat k nulové energii [47].

### 3.2.5 Trojčásticové srážky excitovaných částic

Při vyhodnocení (TA)LIF experimentů je důležité znát dobu života excitovaných stavů. Ta ovšem za atmosférického tlaku může být neměřitelně krátká a pak je nutné ji spočítat pomocí známých rychlostních konstant zhášení a zářivé deexcitace. Za atmosférického tlaku ale existuje riziko, že doba života je zkrácena i vlivem tříčásticových srážek [44], jejichž rychlostní konstanty jsou většinou neznámé. Z tohoto důvodu jsme všude, kde to bylo možné, doby života měřili (např. [52, 47, 48, 45, 54]) a potvrdili, že v námi studovaných prostředích je vliv tříčásticových srážek na zhášení studovaných excitovaných částic zanedbatelný.

Stejný problém ale nastává i při kalibraci TALIF, která je založena na TALIF signálu kryptonu nebo xenonu. Pro jednoduchost a eliminaci potenciálních systematických chyb (plynoucích z umístování výbojky během kalibračních měření do vakuové aparatury) jsme začali kalibraci provádět za atmosférického tlaku v proudu argonu, do kterého bylo přidáno zhruba 1 % Kr nebo Xe. Pak ale bylo nutné vyloučit nebo kvantifikovat vliv tříčásticového zhášení, což ovšem nešlo přímým měřením doby života, která se pohybovala

v řádu 100 ps. Provedli jsme proto různá měření závislosti TALIF signálu Kr a Xe na tlaku (vč. měření excitačních profilů čar), využili známé koncentrace Kr/Xe v aparatuře i závislosti TALIF signálu na době života a určili tak tlakovou závislost doby života na tlaku směsi Ar + Kr/Xe [52, 46]. Ukázalo se, že v použitých směsích hrají tříčásticové srážky zanedbatelnou roli, což zjednodušuje a umožňuje zavedení jednoduché kalibrace TALIF přímo za atmosférického tlaku.

### 3.2.6 Srážková přeuspořádání excitovaného stavu

Přestože při laserem indukované fluorescenci excitujeme částici do jednoho konkrétního stavu, může se na fluorescenčním procesu podílet mnohem více excitovaných stavů, a to hlavně tehdy, když je stav částice měněn srážkami s okolními molekulami. Tento jev je důležitý zejména u víceatomových částic, u kterých vstupují do hry různé vibrační a rotační stavy. Kromě zhášení excitovaného stavu tedy může při srážkách dojít i k rotačnímu a vibračnímu přenosu energie, a proto jsme tuto problematiku podrobně studovali při fluorescenci OH radikálů.

Za atmosférického tlaku jsou srážková přeuspořádání velmi rychlá. To lze doložit např. naším měřením fluorescenčního spektra v plazmové tužce (kpt. 3.5), kde excitovaný stav  $A^2\Sigma^+$  ( $v' = 0$ ) byl během celého procesu prakticky v rotační rovnováze [55, 47], docházelo tedy k extrémně rychlému přeuspořádání desítek různých rotačních stavů. Výhodou situace s extrémně rychlým rotačním přeuspořádáním je to, že celý vibronický stav se všemi jeho rotačními hladinami můžeme považovat za jeden efektivní excitovaný stav OH radikálů. Efektivní Einsteinův koeficient fluorescenčního záření jsme potom počítali jako vážený součet Einsteinových koeficientů všech více než sto emisních čar celého vibračního pásu.

V prostředí s vodní parou (viz kpt. 3.4) bylo ale zhášení tak rychlé, že se excitovaný stav nestihl dostat do rotační rovnováhy [45]. Navíc jsme v tomto případě OH excitovali do prvního vibračně vzbuzeného stavu, takže zde kromě rotačního přeuspořádání hrálo roli i vibrační přeuspořádání. Elektronově excitovaný stav OH jsme proto modelovali jako soustavu tří stavů – efektivního stavu ( $v' = 0$ ) zahrnujícího všechny příslušné rotační hladiny s rozdělením odpovídajícím teplotě plynu, analogického vibračně excitovaného efektivního stavu ( $v' = 1$ ) a laserem přímo čerpané rotační hladiny, která byla po větší část fluorescence populovaná více, než by odpovídalo rotační teplotě plynu.

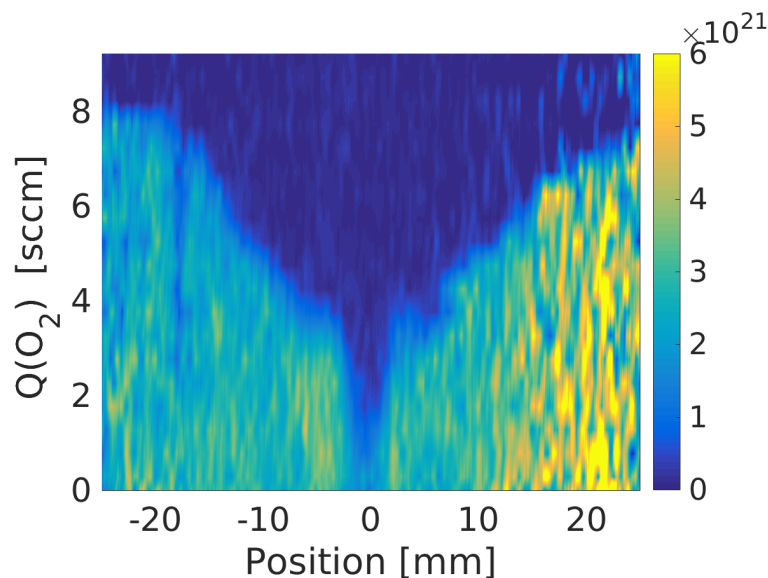
Ani toto ovšem v některých případech není zcela věrný popis reality. Jak se ukázalo na fluorescenčním spektru OH radikálů v objemovém dielektrickém bariérovém výboji (kpt. 3.3), které vyhodnotil Vojtěch Procházka [56], nemusí se do rotační rovnováhy dostat nejen rotačním přenosem energie populované hladiny pásu ( $v' = 1$ ), ale ani hladiny

nižšího vibračního pásu ( $v' = 0$ ). Při vibračním přechodu se totiž přebytečná energie může přenést právě do rotační excitace, takže výsledná rotační teplota vibračního pásu  $0-0$  může být vyšší než rotační teplota základního vibronického stavu  $X^2\Pi (v'' = 0)$ , která odpovídá skutečné translační teplotě neutrálního plynu. Při počítání efektivního Einsteinova koeficientu jednotlivých vibračních pásů je proto korektnější použít jejich vlastní rotační teploty, které se mohou od translační teploty plynu lišit.

### 3.3 Objemový dielektrický bariérový výboj

Jedním z typu výbojů, které pomocí (TA)LIF metod analyzujeme, je objemový dielektrický bariérový výboj (DBD) zapalovaný v tzv. atomizátoru ve směsích Ar, H<sub>2</sub> a příp. O<sub>2</sub>. Tento atomizátor je jednoduché plazmové zařízení tvořené pravoúhloú křemennou trubicí, do jejíhož středu proudí uvedená směs plynů a ve které je zapálen DBD. Takovéto atomizátory se využívají v analytické chemii pro účely citlivé a jednoduché detekce hydridotvorných prvků jako jsou As, Te, Se, Pb, Bi, Sn nebo Sb [57]. Tyto prvky jsou do plazmatu přivedeny ve formě plynného hydridu, který je ve výboji rozložen a volné atomy analytu jsou následně detekovány pomocí absorpce nebo fluorescence. V současnosti se předpokládá, že žádaný rozklad hydridu je způsoben reakcemi s jednoatomovými vodíkovými radikály. V DBD zapáleném pouze v argonu s příměsí hydridu totiž signál analytu pozorován nebyl, signál se objevil až v přítomnosti vodíku. Vodíkové radikály mohou v atomizátoru vznikat vlivem plazmatu ale také hořením, je-li kromě vodíku přítomen i kyslík. Pro potvrzení uvedené teorie, pochopení procesů v atomizátorech a snad i jejich zdokonalení bylo tedy žádoucí naměřit koncentrace reaktivních radikálů, zejména atomárního vodíku, který ale do té doby nebyl nikým ve výbojích za atmosférického tlaku metodou TALIF měřen.

Proto jsme provedli sérii (TA)LIF měření v uvedeném atomizátoru [46, 52], při kterých jsme se nejdříve zaměřili na radikály H a O ve směsích Ar + H<sub>2</sub> nebo Ar + O<sub>2</sub>. Ukázalo se, že koncentrace těchto radikálů je v řádu  $10^{21} \text{ m}^{-3}$ , je homogenní podél atomizátoru a prakticky konstantní během celé periody budicího napětí. Uvedená koncentrace atomů (H, O) je řádově větší než koncentrace hydridů a je tedy dost velká, aby vysvětlila pozorovaný rozklad hydridů ve směsi s vodíkem a pozorovaný záchyt analytu na stěnách atomizátoru (spojený pravděpodobně s jeho oxidací) ve směsi s kyslíkem. Zatímco ve směsi Ar + O<sub>2</sub> rostla koncentrace O s parciálním tlakem O<sub>2</sub> podle odmocninové závislosti, což odpovídá zániku O rekombinací uvnitř plazmatu, ve směsi Ar + H<sub>2</sub> při zvyšování parciálního tlaku H<sub>2</sub> koncentrace H klesala. To lze vysvětlit nižší disociační efektivitou výboje v prostředí s nízkou koncentrací Ar a toto vysvětlení bylo i potvrzeno chováním výboje ve směsi s přidaným O<sub>2</sub>. Uvedeným pozorováním se vysvětlil fakt, že za nižšího průtoku H<sub>2</sub> bývají



Obr. 3.2: Prostorové rozložení koncentrace vodíkových radikálů ( $\text{m}^{-3}$ ) v objemovém DBD v atomizátoru v závislosti na průtoku kyslíku pro konstantní průtok vodíku 16 sccm.

atomizátory více citlivé, a zároveň se tím nastiňuje jedna z možností zlepšení atomizátoru dalším snížením průtoku  $\text{H}_2$ . To za běžného provozu atomizátoru sice není triviální, protože vodík vzniká jako boční produkt hydridizace analytu, ale možné to je např. pomocí zadržení hydridů ve vymrazovací pasti a následného rozkladu v přítomnosti nižší koncentrace  $\text{H}_2$ . (V jiném typu atomizátoru jsme nedávno skutečně pozorovali zvýšení citlivosti detekce olova při snížení parciálního tlaku vodíku, šlo ale o zařízení jiného typu, a proto nelze tímto pozorováním potvrdit uvedenou hypotézu.) Po výměně argonu za helium klesla koncentrace obou jednoatomových radikálů, čímž lze opět vysvětlit skutečnost, že při použití He místo Ar jsou atomizátory méně citlivé. Nakonec zbývá zmínit, že závislost koncentrace jednoatomových radikálů na výkonu dodávaném do DBD se dobře shodla s výkonovou závislostí citlivosti atomizátoru. Všechna naše měření tak jsou v souladu s předpokladem, že za atomizaci hydridů jsou v DBD zodpovědné vodíkové radikály.

Ve směsi  $\text{Ar} + \text{H}_2 + \text{O}_2$  jsme kromě uvedených jednoatomových radikálů měřili i radikál OH. V této směsi už byla koncentrace radikálů nehomogenní a vykazovala následující strukturu: V centru atomizátoru, tedy blízko vtoku plynů, se objevila oblast s nízkou koncentrací H-radikálů a s poměrně vysokou koncentrací O-radikálů. Tato oblast byla ostře ohraničena úzkou zónou s vysokou koncentrací OH a s prudkým nárůstem koncentrace H. Ve vnějších oblastech atomizátoru pak dominovaly vodíkové radikály s již homogenní koncentrací prakticky neovlivněnou přítomností kyslíku, který zde byl téměř

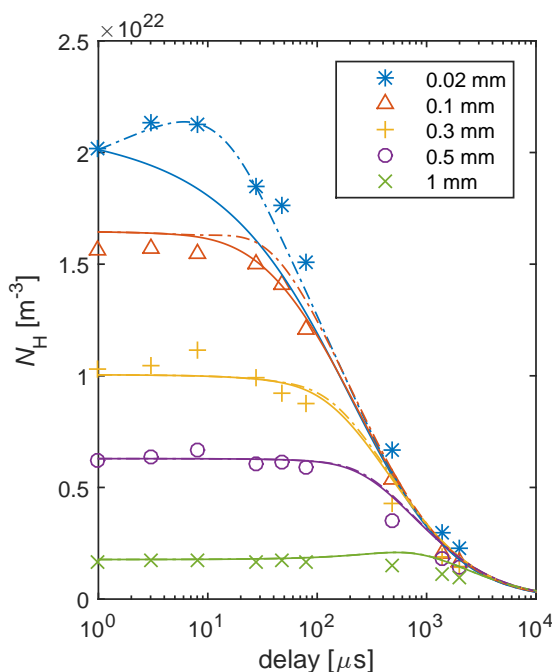
všechny zreagovaný na vodu. Zvyšování poměru průtoků  $H_2/O_2$  vedlo k rozšiřování centrální oblasti s nízkou koncentrací H, až při stochiometrickém poměru vzhledem k vodě se tato oblast roztáhla po celé délce atomizátoru. Na její šířku měl při malých průtocích  $O_2$  viditelný vliv i vír vznikající u vtoku plynů do atomizátoru. I silně podstechiometrické množství kyslíku mělo velký vliv na složení radikálů v centrální oblasti, kde koncentrace atomárního kyslíku převýšila koncentraci atomárního vodíku. Tím byl vysvětlen známý fakt, že i malé množství  $O_2$  stačí na utlumení signálu analytu v atomizátoru a k jeho zachycení na stěnu, kde tímto způsobem může být zakoncentrován a později bez přítomnosti kyslíku znovu převeden do plynné formy a detekován s lepším detekčním limitem. Experimentální data se stala podkladem pro teoretický model Adama Obrusníka, který se s měřeními průběhy dobře shodl a který vnesl světlo do chemických reakcí a proudění plynu v atomizátoru. Měření LIF OH bylo také použito ke stanovení teploty plynu (okolo 500 K).

### 3.4 Koplanární dielektrický bariérový výboj

Bariérový výboj ovšem nemusí být zapálen pouze v objemové variantě. Ve spolupráci Masarykovy Univerzity (Brno) a Univerzity Komenského v Bratislavě byl vyvinut tzv. koplanární DBD, který vytváří tenkou ( $\sim 0,3$  mm) vrstvu plazmatu u povrchu dielektrika [58] a který je schopný vytvářet plazma s vysokým podílem difúzní složky v běžných pracovních plynech jako jsou vzduch nebo dusík bez potřeby používat vzácné plyny. Stažení výboje do tenké vrstvy vedlo k rekordní hustotě dodávaného výkonu a očekávalo se, že vysoká hustota výkonu povede k vysoké koncentraci reaktivních částic. Tento předpoklad byl spolu s otázkou, jestli povrch dielektrika znatelně ovlivní chování radikálů, samozřejmě motivací pro (TA)LIF měření v koplanárním DBD. Takováto měření byla zároveň i diagnostickou výzvou, protože právě blízkost povrchu musela vést k téměř všem parazitním jevům popsaným v kpt 3.2.2.

První větší fluorescenční měření v koplanárním DBD jsme realizovali ve směsi argonu a vodíku, kde jsme metodou TALIF sledovali jednoatomové vodíkové radikály [51]. Vliv parazitních signálů byl měřen a korigován, ale abychom tento vliv minimalizovali, byl výboj zapálen na vnějším povrchu hladké křemenné trubice, což umožnilo minimalizovat kontakt laseru s dielektrikem, rozptýl záření směrem k detektoru i fluorescenci dielektrika. Abychom mohli sledovat vývoj koncentrace H v delším časovém úseku, byl výboj přerušován s frekvencí v řádu stovek Hz. Časové pulzování výboje vedlo spolu s jednofilamentní konfigurací aparatury k prostorové stabilizaci výboje, takže jsme mohli realizovat časově i prostorově rozlišená měření s prostorovým rozlišením v řádu  $10 \mu\text{m}$ .

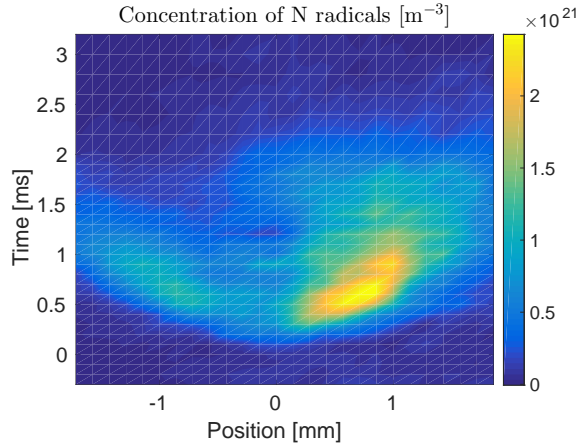
Měření potvrdila vysokou koncentraci vodíkových radikálů v řádu  $10^{22} \text{ m}^{-3}$ , tedy řá-



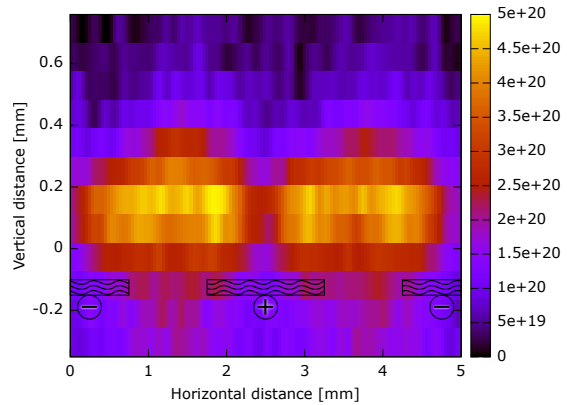
Obr. 3.3: Časový vývoj koncentrace atomárního vodíku během dohasínání koplanárního DBD. Měřeno v různých vzdálenostech od povrchu dielektrika. Křivky znázorňují výsledky modelu, který předpokládá (čerchované křivky) nebo nepředpokládá (souvislé křivky) zdroj atomů vodíku na povrchu dielektrika. Publikováno v [51].

dově vyšší než v objemovém DBD. Atomy H měly vysokou koncentraci ve vrstvě tlusté zhruba 0,3 mm, což odpovídá viditelné tloušťce koplanárního DBD, a pomocí difúze pronikaly zhruba 1 mm od výboje. Časový vývoj koncentrace H po vypnutí výboje vykazoval poměrně dlouhé časové plató a až po něm nastal očekávaný pokles. Doba zachování konstantní koncentrace závisela na vzdálenosti od povrchu dielektrika – od přibližně 10  $\mu$ s těsně u dielektrika po téměř milisekundu ve vzdálenosti 1 mm. Existence plató byla vysvětlena difúzně-rekombinačním modelem vytvořeným Davidem Truncem, který předvedl, že dlouhé udržení vysoké koncentrace je způsobeno difúzí atomů vodíku z oblastí blíž k dielektriku, tedy z oblastí s ještě vyšší koncentrací. Existence plató v těsné blízkosti dielektrika pak naznačila, že povrch dielektrika způsobuje nejenom ztráty reaktivních radikálů povrchovou rekombinací, ale že může sloužit i jako zdroj nebo rezervoár radikálů, které mohou z povrchu desorbovat a zvyšovat koncentraci reaktivních částic v plynu.

V téměř stejné aparatuře jsme metodou TALIF měřili také koncentraci atomárního dusíku ve výboji buzeném v dusíkové atmosféře a ve směsích dusíku s kyslíkem nebo vo-



Obr. 3.4: Časoprostorový vývoj koncentrace atomárního dusíku u povrchu dielektrika koplánárního DBD. Počátek časové osy odpovídá zapálení výboje, úbytek dusíkových atomů po 2 ms je způsoben vypnutím výboje. Nulová pozice označuje centrum filamentu. Obrázek demonstruje difúzi atomů dusíku z filamentu, ale také přesun maximální koncentrace  $N$  mimo výbojový filament.



Obr. 3.5: Prostorové rozložení koncentrace  $OH$  v koplánárním DBD ve vodní páře. Vlnkované obdélníky znázorňují polohu páskových elektrod ukrytých v keramice.  $OH$  radikály jsou koncentrovány v tenké vrstvě nad povrchem dielektrika na obloukových drahách výbojů přemostujících mezielektrodový prostor. Publikováno v [45].

díkem. Hlavní důraz jsme položili na časový vývoj koncentrace dusíkových atomů během zapalování výboje v čistém dusíku [59]. Opět jsme stanovili vysokou koncentraci radikálů v řádu  $10^{22} \text{ m}^{-3}$ . Časoprostorový vývoj koncentrace dusíkových atomů umožňuje pozorovat tvorbu, difúzi a zánik těchto radikálů. Vývoj během zapalování výboje obsahoval dva zvláštní rysy: Prvním byla skutečnost, že koncentrace  $N$  prošla během zapalování výboje maximem, pak výrazně poklesla a její hodnota v ustáleném výboji byla výrazně nižší než v maximu během zapalování. Toto pozorování lze vysvětlit počáteční nepřítomností reaktivních částic podílejících se na destrukci atomárního dusíku nebo vysokou teplotou elektronů v prvních fázích výboje. Nabízí se proto zkusit zvýšit efektivitu koplánárního DBD pomocí jeho pulzování. Druhý zvláštní rys spočíval v dočasném prostorovém posunu maxima koncentrace dusíkových atomů mimo oblast aktivního výboje. Toto pozorování zatím nedokážeme vysvětlit a před jeho analýzou plánujeme provést další série obdobných měření.

Za účelem vytvoření plazmatu se silným oxidačním účinkem a s jednoduchým, dobře definovaným působením na opracovávané povrchy, byl na Univerzitě Komenského v Bra-

tislavě sestaven mnohaelektrodový koplanární DBD pracující v čistých vodních parách. Aby za atmosférického tlaku nedocházelo k nadměrné koncentraci vody, je celý reaktor vyhříván na teplotu 120 °C. Očekávalo se, že takovýto výboj bude produkovat vysokou koncentraci OH radikálů, které patří mezi nejsilnější oxidační činidla vůbec, a proto jsme realizovali OES a LIF diagnostiku tohoto výboje [45]. Kromě mnoha parazitních jevů jsme ovšem ve vodní páře museli čelit extrémně rychlému zhášení, které snižovalo fluorescenční signál a způsobovalo nerovnovázné rotační rozložení excitovaných stavů.

První otázkou bylo, jestli výboj produkuje zejména oxidační OH radikály, nebo jestli je v něm i velké množství redukčních atomů vodíku, které také vznikají při disociaci molekul vody. Optická emisní spektroskopie naznačila, že plazmatu zapálenému ve vodní páře skutečně dominují OH radikály (a že jejich excitované stavy jsou extrémně vibračně a rotačně excitované), ale tuto skutečnost musela potvrdit fluorescence, která dokáže detekovat základní elektronové stavy částic. Nejprve jsme se pokoušeli detekovat vodíkové atomy pomocí TALIF. Přestože ve výboji zapáleném ve vzduchu jsme fluorescenční signál H okamžitě našli, přidání vodní páry rychle utlumilo signál pod měřitelnou úroveň a v čisté vodní páře byla koncentrace atomů H bezpečně pod detekčním limitem metody (zde  $10^{18} - 10^{19} \text{ m}^{-3}$ ) díky reakci  $\text{H} + \text{H}_2\text{O} \rightleftharpoons \text{H}_2 + \text{OH}$  [60]. Nemusíme se proto obávat, že redukční reakce vodíku budou konkurovat oxidačnímu účinku OH radikálů a také vidíme, že ošetřované povrchy budou vystaveny prakticky pouze jednomu typu jednoduchých radikálů, což je důležité pro dobře definovanou úpravu povrchů.

Fluorescence OH radikálů v koplanárním DBD ve vodní páře ukázala, že jejich koncentrace je v řádu  $10^{20} \text{ m}^{-3}$ , což je  $10\times$  více než ve stejném výboji iniciovaném ve vzduchu, takže výměna vzduchu za vodní páru vedla kromě zjednodušení spektra reaktivních radikálů i ke zvýšení koncentrace OH. Během periody budicího napětí výboje koncentrace OH radikálů silně kolísala, doba života radikálů byla ve vodní páře i ve vzduchu přibližně  $10 \mu\text{s}$ . I prostorové rozložení OH radikálů bylo značně nehomogenní a dobře korelovalo s prostorovým rozložením záření viditelného výboje. Zatímco ve vzduchu ležela maxima koncentrace OH nad hranami anody a nad centrem momentální katody, ve vodní páře tvořily koncentrace OH i viditelný výboj obloukové dráhy přemostující oblast nad mezielektrodovým prostorem.

### 3.5 Atmosférické plazmové trysky

Atmosférické plazmové trysky, tedy výboje zapálené většinou ve vzácném plynu proudícím do okolní atmosféry, lze dělit podle frekvence použitého elektrického pole [61]: výboje využívající frekvence v řádu kHz mívají charakter dielektrického bariérového výboje, trysky s frekvencí v řádu MHz jsou většinou kapacitně vázanými výboji a gigahertzové

frekvence budí některý typ mikrovlnného výboje.

Nejvíce jsme se věnovali LIF hydroxylových radikálů v tzv. plazmové tužce, tedy jednopólové argonové plazmové trysce buzené frekvencí 13,56 MHz uvnitř křemenné trubičky, ze které plazma proniká do okolí. První bodová měření ukázala, že maximum koncentrace OH leží blízko špičky viditelného výboje [47]. Následující měření jsme na základě nápadu Jana Voráče provedli s laserovým svazkem, který byl v jednom směru zúžený a v druhém roztažený, takže jsme skrz plazma posílali rovinu laserového záření [48]. Osa výboje ležela v této laserové rovině, takže jsme jedním experimentem získali obrázek s prostorovým rozložením koncentrace OH v celém řezu výboje „vyfukovaného“ z plazmové tužky. Zjistili jsme, že koncentrace OH je poměrně nízká v centru viditelného výboje a relativně vysokých hodnot dosahuje na okraji proudu argonu, kde se do argonu přimíchává okolní vlhký vzduch, jehož vodní pára je zdrojem OH radikálů. Maximum koncentrace OH leželo blízko špičky viditelného výboje, tedy v místě se silným elektrickým polem, nezanedbatelným množstvím přimíchaného vlhkého vzduchu a prostě také v místě, kde plyn měl za sebou cestu celým výbojem.

Fluorescenční měření jsme zároveň použili i ke studiu proudění argonu. Doba života excitovaných OH radikálů totiž závisí na složení okolních molekul, takže jsme z naměřených map dob života mohli spočítat mapy množství vzduchu přimíchaného do proudu argonu. Změřené množství přimíchaného vzduchu dobře souhlasilo s hodnotami předpovězenými modelem proudění. Měření přimíchaného vzduchu potvrdilo výše uvedené vysvětlení, proč je koncentrace OH vysoká po bocích výboje. Dále se ukázalo, že viditelný výboj hoří pouze v oblasti s téměř čistým argonem. Jednotky procent přimíchaného vzduchu stačily na to, aby zamezily protažení výboje do sledované oblasti. S rostoucím průtokem Ar se proto výboj protahoval, dokud nedošlo k přechodu z laminárního do turbulentního proudění, které způsobilo intenzivnější promíchávání plynů a zkrácení výboje. Přirozeně i rozložení koncentrace OH záviselo na průtoku Ar – protahování výboje s rostoucím průtokem posouvalo pozici maxima koncentrace do oblastí vzdálenějších od křemenné trysky a přechod do turbulentního režimu proudění přivodil pokles koncentrace OH. Třetí sadou map, kterou jsme pomocí fluorescenčních měření získali, byla prostorová rozložení rotační teploty OH. Také teplota dosahovala maxima na špičce viditelného výboje nebo dokonce v její blízkosti vně výboje a i na ni měl vliv průtok argonu – vyšší průtok přirozeně vedl k nižší teplotě plynu.

V DBD plazmové trysce budící 80 kHz výboj v heliu jsme studovali vliv vlhkosti helia na formování rychlých streamerů, tzv. *plasma bullets*, a na koncentraci OH radikálů. Ukázalo se, že vlhkost He má zásadní vliv na vzhled těchto streamerů a že při nízké vlhkosti (20–30 ppm) ztrácejí svůj kulový tvar a získávají difuznější charakter [62]. Naopak při vysoké vlhkosti (1000 ppm) přestával za daného výkonu výboj hořet. Většina těchto

měření je aktuálně předmětem zpracování.

I třetí typ plazmové trysky – mikrovlnný výboj – jsme studovali pomocí LIF OH radikálů a TALIF atomárního kyslíku. Koncentrace kyslíkových i hydroxylových radikálů zde dosahovala poměrně vysoké koncentrace  $10^{22} \text{ m}^{-3}$ . Mapa koncentrace OH radikálů opět ukázala hlavní maximum blízko špičky výboje, v některých případech se ale objevilo i druhé maximum 6 mm za výbojem, kam sice už nedosahoval viditelný aktivní výboj, ale kam mohou dospět argonové metastability a kde se argon intenzivněji promíchával s okolním vlhkým vzduchem laboratoře. Pulzování výboje mělo vliv na koncentraci OH – modulace výboje s frekvencí 80 Hz vedla ke zvýšení koncentrace a zániku druhého maxima [54], což pravděpodobně souvisí se změnou proudění plynu při jeho střídavé expanzi a kompresi způsobené pulzováním teploty.



# Kapitola 4

## Shrnutí

Vysokofrekvenční elektrické kmity samovolně generované plazmatem kapacitního výboje mohou tento výboj znatelně ovlivnit a přispívají k jeho zajímavosti i použitelnosti. Na poli vývoje sondové diagnostiky se podařilo nejenom zpřesnit metodu měření průběhu potenciálu plazmatu i s jeho vyššími harmonickými frekvencemi, ale dotýkáme se i cíle získat pomocí sondy bez vf. kompenzace údaje, které doposud vyžadovaly kompenzovanou Langmuirovu sondu. Naměřené chování v nízkotlakém i atmosférickém kapacitním výboji souhlasí s vytvořenými teoretickými modely, které lze použít k vysvětlení pozorovaného chování i k dalším předpovědím, např. k popisu dvou- a vícefrekvenčních výbojů. Ukázali jsme, že vyšší frekvence mohou být použity k citlivému monitorování vf. reaktivního magnetronového naprašování a že ve všech zkoumaných procesech (reaktivní naprašování, PECVD depozice a leptání uhlíkových vrstev) reagovaly vyšší harmoniky na stav povrchu elektrody, tedy právě na klíčový objekt mnoha depozičních a leptacích procesů.

Fluorescenční měření se stalo základní metodou diagnostiky reaktivních radikálů v plazmatu. Tuto techniku se nám podařilo zpřesnit a využít na studium řady výbojů buzených za atmosférického tlaku, včetně diagnostiky náročných prostředí jako např. povrchový výboj v čisté vodní páře. Jako příklady potvrzující sílu této diagnostické metody mohou posloužit vysvětlení role jednoatomových radikálů v tzv. atomizátorech využívaných v analytické chemii, potvrzení vysoké koncentrace reaktivních částic v koplánárních DBD, stanovení, že atmosférický výboj ve vodní páře je čistým zdrojem jen jednoho typu reaktivních radikálů, nebo nalezení souvislostí mezi mícháním plynu, koncentrací reaktivních částic, teplotou a délkou výboje atmosférických plazmových trysek.



# Literatura

- [1] R. JOSEFSON, Z. NAVRÁTIL, L. DOSOUDILOVÁ, P. DVOŘÁK, and D. TRUNEC, *IEEE Transactions on Plasma Science* **42**, 2348 (2014).
- [2] Z. NAVRÁTIL, L. DOSOUDILOVÁ, R. JOSEFSON, P. DVOŘÁK, and D. TRUNEC, *Plasma Sources Sci. Technol.* **23**, 042001 (2014).
- [3] P. VAŠINA, M. FEKETE, J. HNILICA, P. KLEIN, L. DOSOUDILOVÁ, P. DVOŘÁK, and Z. NAVRÁTIL, *Plasma Sources Sci. Technol.* **24**, 065022 (2015).
- [4] Z. NAVRÁTIL, P. DVOŘÁK, O. BRZOBOHATÝ, and D. TRUNEC, *J. Phys. D: Appl. Phys.* **43**, 505203 (2010).
- [5] V. LADÁNYI, P. DVOŘÁK, J. A. ANSHORI, Ľ VETRÁKOVÁ, J. WIRZ, and D. HEGGER, *Photochemical and Photobiological Sciences*, *accepted* (2017).
- [6] Ľ VETRÁKOVÁ, V. LADÁNYI, J. A. ANSHORI, P. DVOŘÁK, J. WIRZ, and D. HEGGER.
- [7] M. A. LIEBERMAN, *IEEE Transactions on Plasma Science* **16**, 638 (1988).
- [8] M. KLICK, *Journal of Applied Physics* **79**, 3445 (1996).
- [9] U. CZARNETZKI, T. MUSSENBRÖCK, and R. BRINKMANN, *Physics of Plasmas* **13**, 123503 (2006).
- [10] T. MUSSENBRÖCK and R. BRINKMANN, *Applied Physics Letters* **88**, 151503 (2006).
- [11] P. DVOŘÁK, *Plasma Sources Sci. Technol.* **19**, 025014 (2010).
- [12] V. P. T. KU, B. M. ANNARATONE, and J. E. ALLEN, *Journal of Applied Physics* **84**, 6536 (1998).

- [13] Y. YAMAZAWA, M. NAKAYA, M. IWATA, and A. SHIMIZU, *Japanese Journal of Applied Physics* **46**, 7453 (2007).
- [14] P. DVOŘÁK and Z. MORAVEC, *Chem. Listy* **102**, s1356 (2008).
- [15] M. LIEBERMAN and A. LICHTENBERG, *Principles of plasma discharges and materials processing*, John Wiley & sons, inc., New Plasma Sources SciYork, 1994.
- [16] P. CHABERT and N. BRAITHWAITE, *Physics of Radio-Frequency Plasmas*, Cambridge University Press, 2011.
- [17] M. KLICK, W. REHAK, and M. KAMMEYER, *Japanese Journal of Applied Physics* **36**, 4625 (1997).
- [18] P. DVOŘÁK, *Plasma Sources Sci. Technol.* **22**, 045016 (2013).
- [19] S. RAUF and M. J. KUSHNER, *Journal of Applied Physics* **83**, 5087 (1998).
- [20] V. J. LAW, A. J. KENYON, N. F. THORNHILL, V. SRIGENGAN, and I. BATTY, *Vacuum* **57**, 351 (2000).
- [21] V. LISOVSKIY, J.-P. BOOTH, K. LANDRY, D. DOUAI, V. CASSAGNE, and V. YEGORENKOV, *Vacuum* **82**, 321 (2007).
- [22] P. DVOŘÁK, P. VAŠINA, V. BURŠÍKOVÁ, and R. ŽEMLIČKA, *Plasma Phys. Control. Fusion* **52**, 124011 (2010).
- [23] L. BOUFENDI, J. GAUDIN, S. HUET, G. VIERA, and M. DUDEMAINE, *Applied Physics Letters* **79**, 4301 (2001).
- [24] J.-C. SCHAUER, S. HONG, and J. WINTER, *Plasma Sources Science and Technology* **13**, 636 (2004).
- [25] P. DVOŘÁK, M. TKÁČIK, and J. BÉM, *Plasma Sources Sci. Technol.* **26**, 055022 (2017).
- [26] P. DVOŘÁK and P. VAŠINA, *Plasma Sources Sci. Technol.* **19**, 055016 (2010).
- [27] M. A. SOBOLEWSKI, *IEEE Transactions on Plasma Science* **23**, 1006 (1995).
- [28] M. YATSUZUKA, K. MORISHITA, K. SATOH, and S. NOBUHARA, *Japanese Journal of Applied Physics* **24**, 1724 (1985).

- [29] P. DVOŘÁK, *Komplexní diagnostika reaktivního plazmatu doutnavého výboje*, PhD thesis, Masarykova Univerzita v Brně, 2005.
- [30] P. DVOŘÁK, V. BURŠÍKOVÁ, P. VAŠINA, and R. ŽEMLIČKA, Higher harmonic frequencies in capacitive discharges, in *Conference Proceedings of ICRP-6*, 2010.
- [31] J. PÁLENÍK, *Elektrická sonda bez vysokofrekvenční kompenzace v plazmatu kapacitního výboje* – bakalářská práce, Masarykova univerzita, Brno, 2017.
- [32] P. VAŠINA and P. DVOŘÁK, *EPL (Europhysics Letters)* **85**, 15002 (2009).
- [33] K. NAGAYAMA, B. FAROUK, and Y. LEE, *IEEE Transactions on Plasma Science* **26**, 125 (1998).
- [34] T. MUSSENBROCK, D. ZIEGLER, and R. BRINKMANN, *Physics of Plasmas* **13**, 083501 (2006).
- [35] T. MUSSENBROCK and R. BRINKMANN, *Plasma Sources Science and Technology* **16**, 377 (2007).
- [36] P. DVOŘÁK and R. ŽEMLIČKA, in *Conference Proceedings of PASNPG*, p. 41, 2012.
- [37] P. DVOŘÁK, Harmonics, <http://is.muni.cz/repo/1092071/cs/Dvorak/Harmonics?lang=cs;lang=cs>, 2013.
- [38] U. CZARNETZKI, B. HEIL, J. SCHULZE, Z. DONKÓ, T. MUSSENBROCK, and R. BRINKMANN, *Journal of Physics: Conference Series* **162**, 012010 (2009).
- [39] Z. DONKÓ, *Plasma Sources Science and Technology* **20**, 024001 (2011).
- [40] P. DVOŘÁK, Calculation of higher harmonic frequencies generated in capacitively coupled discharges, in *Conference Proceedings of 31<sup>st</sup> ICPIG*, 2013.
- [41] Z. NAVRÁTIL, R. JOSEFSON, N. CVETANOVIĆ, B. OBRADOVIĆ, and P. DVOŘÁK, *Plasma Sources Sci. Technol.* **25**, 03LT01 (2016).
- [42] J. AMORIM, G. BARAVIAN, and J. JOLLY, *Journal of Physics D: Applied Physics* **33**, R51 (2000).
- [43] K. NIEMI, V. S. VON DER GATHEN, and H. DÖBELE, *Plasma Sources Sci. Technol.* **14**, 375 (2005).
- [44] A. F. H. VAN GESSEL, S. C. VAN GROOTEL, and P. J. BRUGGEMAN, *Plasma Sources Science and Technology* **22**, 055010.

- [45] V. PROCHÁZKA, Z. TUČEKOVÁ, P. DVOŘÁK, D. KOVÁČIK, P. SLAVÍČEK, A. ZAHORANOVÁ, and J. VORÁČ, *Plasma Sources Sci. Technol.*, *accepted* (2017).
- [46] P. DVOŘÁK, M. TALÁBA, A. OBRUSNÍK, J. KRATZER, and J. DĚDINA, *Plasma Sources Sci. Technol.* **26**, 085002 (2017).
- [47] J. VORÁČ, P. DVOŘÁK, V. PROCHÁZKA, J. EHLBECK, and S. REUTER, *Plasma Sources Sci. Technol.* **22**, 025016 (2013).
- [48] J. VORÁČ, A. OBRUSNÍK, V. PROCHÁZKA, P. DVOŘÁK, and M. TALÁBA, *Plasma Sources Sci. Technol.* **23**, 025011 (2014).
- [49] P. F. AMBRICO, M. AMBRICO, M. ŠIMEK, A. COLAIANNI, G. DILECCE, and S. DE BENEDICTIS, *Applied Physics Letters* **94** (2009).
- [50] J. VORÁČ, P. DVOŘÁK, V. PROCHÁZKA, T. MORÁVEK, and J. RÁHEL, *Eur. Phys. J. Appl. Phys.* **71**, 20812 (2015).
- [51] M. MRKVIČKOVÁ, J. RÁHEL, P. DVOŘÁK, D. TRUNEC, and T. MORÁVEK, *Plasma Sources Sci. Technol.* **25**, 055015 (2016).
- [52] P. DVOŘÁK, M. MRKVIČKOVÁ, A. OBRUSNÍK, J. KRATZER, J. DĚDINA, and V. PROCHÁZKA, *Plasma Sources Sci. Technol.* **26**, 065020 (2017).
- [53] P. DVOŘÁK, V. PROCHÁZKA, R. KRUMPOLEC, and T. HOMOLA, *proposed to Plasma Sources Sci. Technol.* .
- [54] J. VORÁČ, J. HNILICA, V. KUDRLE, and P. DVOŘÁK, *Open Chemistry* **13**, 193 (2015).
- [55] J. VORÁČ, V. PROCHÁZKA, and P. DVOŘÁK, *Chem. Listy* **106**, S1504 (2012).
- [56] V. PROCHÁZKA, *Diagnostika plazmatu pomocí laserových a optických metod*, PhD thesis, Masarykova Univerzita, Brno, 2017.
- [57] J. DĚDINA and D. L. TSALEV, *Hydride Generation Atomic Absorption Spectrometry*, Wiley, Chichester, 1995.
- [58] M. ŠIMOR, J. RÁHEL, P. VOJTEK, A. BRABLEC, and M. ČERNÁK, *Applied Physics Letters* **81**, 2716 (2002).
- [59] M. MRKVIČKOVÁ, J. RÁHEL, and P. DVOŘÁK, in *Proceedings of XII Frontiers in Low Temperature Plasma Diagnostics, Zlatibor, Serbia*, p. 32, 2017.

- [60] D. R. JENKINS and T. M. SUGDEN, *Flame Emission and Atomic Absorption Spectrometry, Volume 1-Theory*, chapter Radicals and molecules in flame gases, pp. 151–187, Marcell Dekker, New York, 1971.
- [61] X. LU, G. V. NAIDIS, M. LAROUSSE, S. REUTER, D. B. GRAVES, and K. OSTRIKOV, *Physics Reports* **630**, 1 (2016).
- [62] N. SELAKOVIĆ, J. VORÁČ, N. PUAC, G. MALOVIĆ, P. DVOŘÁK, and Z. L. PETROVIĆ, in *XXXIII International Conference on Phenomena in Ionized Gases – Conference proceedings*, p. 239, Portugal, 2017.



# Kapitola 5

## Přiložené komentované práce

V následující části jsou přiložené práce [11, 18, 22, 25, 26, 41, 45, 46, 48, 50, 51, 52].

# Measurement of plasma potential waveforms by an uncompensated probe

P Dvořák

Department of Physical Electronics, Masaryk University, Kotlářská 2, Brno 611 37, Czech Republic

E-mail: [pdvorak@physics.muni.cz](mailto:pdvorak@physics.muni.cz)

Received 25 August 2009, in final form 10 February 2010

Published 8 March 2010

Online at [stacks.iop.org/PSST/19/025014](http://stacks.iop.org/PSST/19/025014)

## Abstract

A method is presented that enables measurement of plasma potential waveforms. The method consists of measurement by an uncompensated probe and analysis of the measured waveforms by means of a model of the sheath around the probe. The method was successfully tested in a nitrogen capacitively coupled discharge. The strong influence of the sheath around the probe on the probe voltage and the correlation between the probe current waveform and the discharge current are shown. At low pressures, the plasma potential waveform contains a large amount of higher harmonic frequencies whose amplitudes are comparable to the amplitude of the fundamental frequency.

(Some figures in this article are in colour only in the electronic version)

## 1. Introduction

The nonlinear nature of the VA characteristics of sheaths results in the production of higher harmonic frequencies of discharge voltage and current in capacitively coupled discharges [1]. Since sheaths are in contact with the plasma, the nonlinear signal produced in sheaths induces electric oscillations in the system of inductive plasma and capacitive sheaths [2]. These oscillations have their eigenfrequency approximately equal to the frequency of the so-called plasma-sheath (series) resonance [3] and they amplify the amplitude of higher harmonic frequencies produced by sheaths. Higher harmonics are strong particularly at low pressures where electric oscillations are not significantly damped by electron–neutral collisions. Moreover, the plasma-sheath resonance frequency is relatively low at low pressures and can be easily induced by the nonlinear sheath oscillation. At pressures below 10 Pa the ohmic heating caused by higher harmonic frequencies may even be the dominant heating process in capacitive discharges [4].

The significance of higher harmonics is not only based on the fact that they influence the plasma. Since higher harmonics are very sensitive functions of plasma parameters [5–7] and discharge parameters [8, 9], they are a suitable tool for diagnostic and monitoring purposes. Higher harmonics are used for the end-point detection of etching processes [5], sensitive monitoring of reactive magnetron sputtering [7], monitoring of dust growth [10] and the measurement of electron concentration and collisional frequency [6].

Higher harmonics can be measured by means of an uncompensated probe immersed in the plasma or a segment of the reactor wall that collects a part of the discharge current. A third possibility is to provide a measurement of RF voltage and/or current on the line between the power generator and the powered electrode. However, none of these methods gives direct information concerning the plasma potential waveform since the measurement points are separated from the bulk plasma, at least by a sheath. While the mean (dc) value of the plasma potential is routinely measured by compensated Langmuir probes, there is a lack of data describing changes in plasma potential during the RF period. For the measurement of plasma potential waveforms an uncompensated probe has been chosen in this work since it is a very sensitive sensor of higher harmonics, it is in closest contact with the bulk plasma, and it is the only method suitable for space-resolved measurements. Despite these facts, the relationship between the signal measured by the uncompensated probe and the plasma potential waveform has not, as yet, been clarified, since the measured probe voltage waveform is affected by a thin nonlinear sheath around the probe. The sheath influence can be reduced when such a probe is used that minimizes the RF current flowing to the probe and the RF voltage on the sheath around the probe. This can be achieved by means of a high-impedance probe [11–15]. Some of the cited works neglect the sheath effect, others calculate the effect of the sheath around the probe as though it was a capacitor. The

sheath capacity was estimated in [12] by means of the Child–Langmuir law, whereas the work [11] uses a comparison of measurements with probe terminated by various impedances. These approaches are valid when the nonlinear sheath effects are negligible. In general, the sheath around the probe should be modelled as an element that has a specific nonlinear current–voltage characteristic. Alternatively, the active compensation of a Langmuir probe [16, 17] could be, in principle, used for the measurement of plasma potential waveform. The active compensation removes the RF voltage between the probe and the plasma by driving the probe externally with the RF voltage identical to the RF variation of plasma potential. The right driving can be searched by tuning the amplitude and phase of all frequencies that are externally driven to the probe and looking for conditions that lead to the highest value of the measured dc floating potential. However, the plasma potential frequently contains more than ten harmonic frequencies with high amplitude. Therefore, proper tuning of amplitudes and phases of all the harmonics is highly problematic due to the number of tuned parameters.

In this work, the nonlinear response of the sheath around the probe is calculated. As a result, a method for the evaluation of the plasma potential waveform by means of an uncompensated probe is presented that takes into account the complicated character of the sheath. Consequently, it is not necessary to use a high-impedance probe or an active compensation and the behaviour of an uncompensated probe terminated with a low impedance is analysed.

## 2. Experimental arrangement

The experiments were carried out in a spherical (i.d. 33 cm) stainless steel reactor with two horizontally mounted, parallel, stainless steel electrodes of 80 mm diameter. The upper electrode, embedded in a grounded ring, was driven at a frequency of 13.56 MHz. The bottom electrode was grounded. Their distance was 40 mm. The reactor was evacuated by a turbomolecular pump with a membrane pump. The pressure was varied within the range 0.5–23 Pa, dc self-bias on the powered electrode varied within  $-140$  to  $-200$  V showing an asymmetry of the discharge. The value of the RF power delivered to the discharge was 40 W. The RF voltage, RF current and dc self-bias on the powered electrode were measured on the coaxial cable between the matching unit and the reactor. Plasma parameters, i.e. electron concentration, mean electron energy and mean (dc) plasma potential, were measured by a compensated Langmuir probe (ESPion, Hidden Analytical).

The plasma potential waveforms were measured by means of an uncompensated probe made from a 10 cm long metallic wire with diameter 0.21 mm. This wire was immersed in the plasma and connected by a  $50\ \Omega$  coaxial cable to an oscilloscope with an input impedance of  $50\ \Omega$ . An example of the waveform measured by the uncompensated probe is shown in figure 1, which clearly demonstrates a high proportion of higher harmonics in the probe waveform. In the same figure, there is a comparison with an uncompensated probe waveform measured by an oscilloscope with an input impedance of  $1\ \text{M}\Omega$

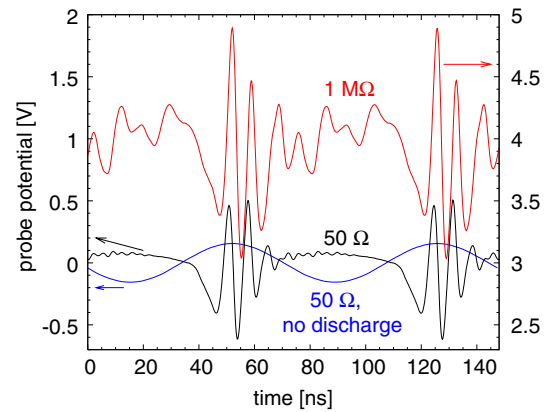


**Figure 1.** Voltage measured by the uncompensated probe terminated with impedance  $50\ \Omega$  (black curve) and  $1\ \text{M}\Omega$  (red) and probe voltage measured when no discharge was present (blue).

showing a strong influence of the oscilloscope input impedance on the measured data. This comparison demonstrates the necessity to have equal values of the coaxial cable and oscilloscope input impedance. In addition, figure 1 contains the signal measured by the probe when no plasma is present showing the monofrequency sinusoidal signal coming from the power generator. Higher harmonic frequencies are present in the probe waveform only when the plasma with its nonlinear sheaths is ignited. A final analysis of the presented data showed that this 10 cm long probe terminated with  $50\ \Omega$  may collect a substantial part of the discharge current (see figure 5) and thereby influence the discharge. Therefore, it is recommended to use a shorter probe in order to reduce the effect on the discharge. Moreover, a shorter probe will enhance possibilities of space-resolved measurements.

## 3. Sheath model

Since the probe tip and the plasma are separated by a sheath, the waveform of the probe voltage and the plasma potential differ. Consequently, it is necessary to solve a model of the sheath in order to obtain the plasma potential waveform. For this purpose, a model was developed that takes into account the nonlinear nature of the sheath. The model takes into account three ways by which electric current can flow through the sheath:

$$I(t) = I_d(t) + I_e(t) + I_i, \quad (1)$$

where  $I$  represents the total current flowing to the probe,  $I_d$  the displacement current,  $I_e$  the electron current and  $I_i$  the ion current. The ion current is assumed to be constant during the whole RF period. For the electron current the formula

$$I_e(t) = -\frac{enS}{4} \sqrt{\frac{8kT_e}{\pi m_e}} \exp\left\{-\frac{eU(t)}{kT_e}\right\} \quad (2)$$

is used where  $e$  represents the elementary charge,  $n$  the electron concentration in the bulk plasma,  $S$  the probe surface area,  $k$  the Boltzmann constant,  $T_e$  the electron temperature,  $m_e$  the electron mass and  $U$  is the probe sheath voltage, i.e.

$U(t) = U_{\text{pl}}(t) - U_o(t)$ , where  $U_{\text{pl}}$  denotes the instantaneous plasma potential and  $U_o$  the probe voltage. In order to calculate the displacement current some assumptions concerning the sheath structure must be made. The model assumes that the concentration of ions is constant in the sheath and equal to the electron concentration in the undisturbed plasma ( $n$ ). In addition, the electron concentration inside the sheath is assumed to be small enough to have only a negligible effect on the space charge. These assumptions lead to the formula

$$I_d(t) = en \frac{S}{r_p} s(t) \frac{ds(t)}{dt}, \quad (3)$$

where  $r_p$  denotes the probe radius and  $s$  the time-varying radius of the sheath, i.e.  $s - r_p$  represents the instantaneous sheath width. The supposed sheath structure leads to the following formula for the sheath voltage:

$$U = \frac{en}{4\epsilon_0} \left( 2s^2 \ln \frac{s}{r_p} - s^2 + r_p^2 \right) \quad (4)$$

and its derivative

$$\frac{dU}{dt} = I_d \frac{r_p}{\epsilon_0 S} \ln \frac{s}{r_p}. \quad (5)$$

The presented model assumes that the probe potential is less than the plasma potential during the whole RF period. In rare situations when the probe potential exceeds the plasma potential, an equation describing the current flowing to a probe at  $U < 0$  should be added to the model. Eventually, the probe could be biased negatively in order to prevent this situation.

The probe current flows through the coaxial cable to the input impedance of the oscilloscope where it causes the measured voltage  $U_o = I \cdot Z_0$  ( $Z_0 = 50 \Omega$ ). Therefore, the probe current waveform is known and it is possible to use this known quantity in the calculation of changes in the sheath voltage. At the beginning of the procedure, the displacement current should be calculated by means of equations (1) and (2). Then, equation (3) enables one to get the derivation of the sheath radius which can be used for the calculation of sheath voltage derivation by means of equation (4). Afterwards, the sheath voltage waveform during the whole RF period can be obtained by numerical integration when at each step the actual sheath voltage derivation must be calculated by means of equations (1)–(4). Finally, the plasma potential waveform can be calculated as a sum of the sheath voltage and the measured probe voltage:

$$U_{\text{pl}}(t) = U(t) + U_o(t). \quad (6)$$

However, the value of the ion current that is included in equation (1) and the initial sheath voltage needed in equation (2) are not known. The ion current value can be obtained by means of the fact that the sheath voltage is a periodical function of time with a known period. Therefore, the displacement current value averaged during a RF period is zero which leads to the value of the ion current  $I_i = \langle I \rangle - \langle I_e \rangle$ . Consequently, the ion current value can be fitted so that the calculated sheath voltage (or plasma potential) was a periodical

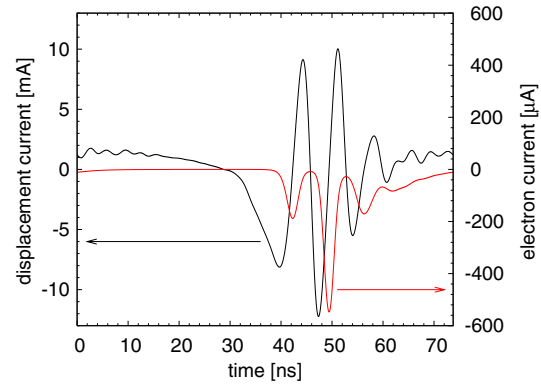


**Figure 2.** Calculated displacement (black curve) and electron (red) currents flowing to the uncompensated probe at nitrogen pressure 6 Pa.

function of time or, equivalently, so that the sum  $I_i + \langle I_e \rangle + \langle I_d \rangle$  was equal to the mean value of the total measured current  $\langle I \rangle$ . The initial sheath voltage can be fitted so that the mean value of the calculated plasma potential was equal to the value obtained by another measurement technique, for example by means of a compensated Langmuir probe. It is advisable to provide the compensated Langmuir probe measurements also in order to get the values of electron concentration and temperature that should be used in equations (2)–(4). Unfortunately, fitting the two parameters (ion current and initial sheath voltage) somewhat complicates the numerical procedure.

Figure 2 shows the calculated waveforms of displacement and electron currents flowing to the uncompensated probe. The figure demonstrates that the displacement current usually dominates the probe current. Consequently, the presented method is not sensitive to errors made by the estimation of plasma parameters (electron concentration and temperature) that are necessary for the evaluation of the electron current. In our case, even neglecting electron and ion currents did not cause any visible change in the calculated plasma potential waveform. Therefore, in some cases model (1)–(4) can be simplified and only the equations (4), (5) and  $I_d \approx I$  must be taken into account. Moreover, fitting of the ion current does not occur in this simplified case. Nevertheless, all results shown in this work were calculated by the complete model (1)–(4). The fact that the electron current is usually an almost negligible part of the probe current complicates the possible effort of using an uncompensated probe for the estimation of electron concentration and temperature. However, this subject lies outside the topic of this paper.

#### 4. Test of the method

In order to test the described model the probe was externally biased to various dc potentials which lead to significant changes in the probe sheath thickness. In this series of measurements the oscilloscope impedance was set to 1 M $\Omega$  and the coaxial cable was terminated by a 50  $\Omega$  terminator with a capacitor which blocked the dc current, as depicted in figure 3(b). Its capacity had a high value in order to short

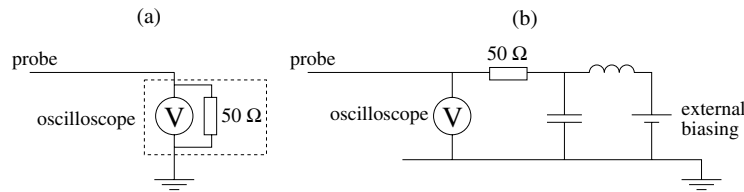


**Figure 3.** Schema of the uncompensated probe circuit. Usually, the probe is connected via a coaxial cable directly to an oscilloscope with input impedance  $50\ \Omega$  (a). In order to test the method the probe was externally biased (b).

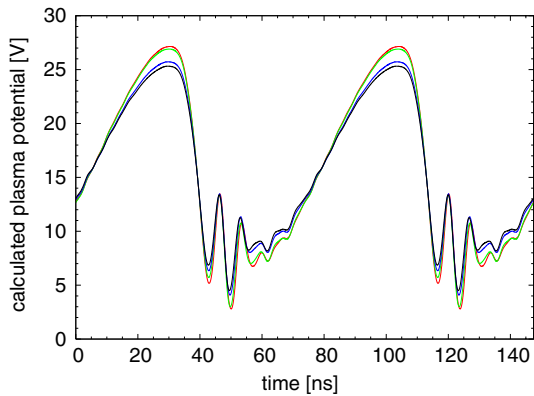


**Figure 4.** Plasma potential waveforms obtained at various biasing of the uncompensated probe at nitrogen pressure 6 Pa. Red, green, blue and black curves represent waveforms obtained by means of probe biased to 0 V,  $-10$  V,  $-20$  V and  $-40$  V, respectively.

out RF current and it was connected to a dc source via a coil that prevented the RF current from flowing to the dc source. (Except for this test, the coaxial cable was connected directly to the oscilloscope with an input impedance of  $50\ \Omega$ .) The dc voltage of the capacitor was set to various values in the range from  $-40$  V. The measured signal differed for various bias voltages having its maximum amplitude at dc bias equal to the ‘floating’ potential of the uncompensated probe, i.e. to the dc potential of the uncompensated probe connected to an oscilloscope with a high input impedance (approximately  $4$  V, see figure 1). A biasing voltage higher than this value led to a short collapse of the probe sheath ( $U \leq 0$ ) during each RF period, which could not be described by model (1)–(4).

The model was applied to this series of measurements performed at various biasing of the probe and a series of plasma potential waveforms was obtained. Since the probe is small enough not to influence the plasma significantly, all the obtained plasma potential waveforms should be identical in an ideal case. Even if the sheath voltage was varied by more than 200% during this test, the calculated plasma potential waveforms were approximately identical as is shown in figure 4. Consequently, the presented method can be considered to be reliable.

The plasma potential waveform calculated in the presented test varied by a maximum of 8% when the mean sheath voltage was changed by 100%. Since 100% is a strong change, we can conclude that the uncertainty of the presented method is lower than 8%. This uncertainty visible in figure 4 could be caused by many effects. The first is a possible

perturbation of the plasma by the probe current that was described in section 2. We can exclude this possibility since a decrease in probe current by increasing the probe sheath thickness would lead to less perturbation, i.e. to an increase in plasma potential amplitude. However, the opposite effect was observed. Further, it was checked that a deviation of probe termination impedance depicted in figure 3(b) from  $50\ \Omega$  had no notable effect on the measurement. Finally, it was checked that voltage waveforms on the probe tip are identical to the waveforms measured by the oscilloscope, i.e. that the finite impedance between the probe and the ground had almost a nonmeasurable effect on the measurement. Consequently, the relatively small differences between the curves in figure 4 seem to be caused by simplifications in model (1)–(4), namely by the assumption of constant ion density in the sheath.

## 5. Plasma potential waveforms

A strong difference between the measured probe voltage waveform and the plasma potential waveform is clearly visible in figures 1 and 4. Also the measurement performed with a high input impedance of the oscilloscope (figure 1) significantly differs from the plasma potential waveform. These differences demonstrate that the sheath around the probe has a high influence on the measurement of plasma potential and that it is necessary to use model (1)–(4). Increasing the impedance between the probe and the ground can reduce this drastic influence of the sheath around the probe [11].

The obtained plasma potential waveform was used for the calculation of discharge current which was then compared with the measured probe voltage. In order to get the discharge current waveform a simplified model of the sheath at the grounded electrode was made which supposed a constant ion density in the sheath. This model neglected the electron and ion current and took into account only the displacement current flowing to the electrode. The current flowing to the grounded reactor walls was neglected. These assumptions led to a rough estimation of the discharge current:

$$I_{\text{disch}} = S_E \sqrt{\frac{ne\epsilon_0}{2U_{\text{pl}}}} \frac{dU_{\text{pl}}}{dt}, \quad (7)$$

where  $S_E$  is the electrode area. This estimation of the discharge current is compared with the uncompensated probe current in figure 5 clearly demonstrating a strong correlation between these two quantities.

The plasma potential waveforms obtained at nitrogen pressures 3 Pa, 6 Pa and 18 Pa are shown in figures 6, 4 and 7,

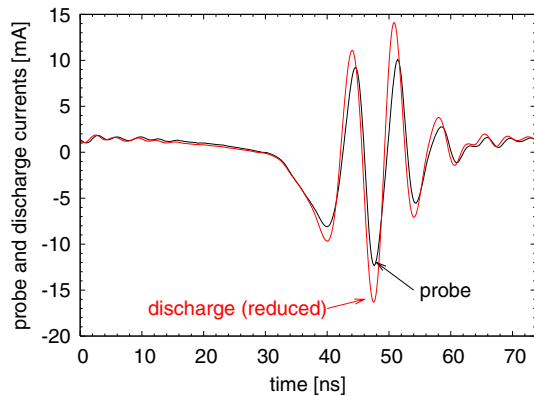


**Figure 5.** Waveform of the probe current (black) and a rough estimation of the discharge current (red,  $10\times$  reduced).

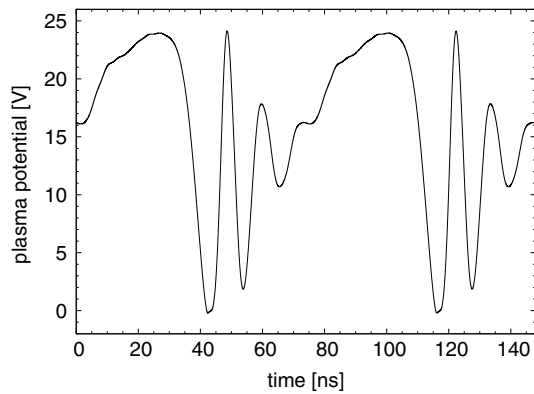


**Figure 6.** Two periods of plasma potential at nitrogen pressure 3 Pa.

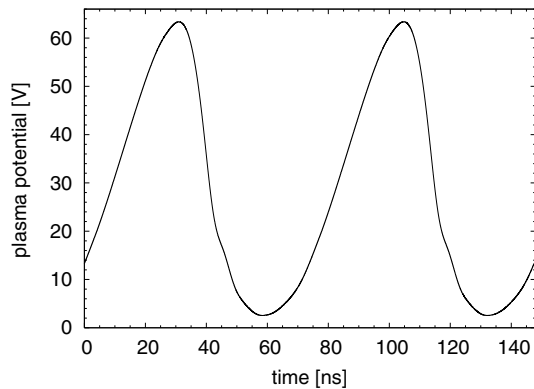


**Figure 7.** Two periods of plasma potential at nitrogen pressure 18 Pa.

respectively. A large amount of higher harmonic frequencies is evident, particularly at low pressures, since they are not significantly damped by electron–neutral collisions and are amplified by plasma–sheath resonance. At pressure 3 Pa the amplitude of higher harmonic frequencies is even comparable to the amplitude of the fundamental frequency (13.56 MHz). As can be seen in figures 6 and 4 the oscillation of the system of plasma glow and sheaths is ignited, namely during the

fast decrease in the plasma potential which is related to the time of expansion of the sheath at the powered electrode. On the other hand, at a higher pressure (18 Pa, figure 7) the oscillation of the system is effectively damped by collisions of electrons with neutrals and the amplitudes of higher harmonics are relatively small when compared with the situation at a lower pressure. However, a significant deviation from a monofrequency sinusoidal waveform is still present.

## 6. Conclusion

A method was developed that enables the measurement of plasma potential waveforms. The method consists of measurement by an uncompensated probe and analysis of the measured waveform by means of a model that calculates the voltage of the nonlinear sheath around the probe. The model requires a knowledge of plasma parameters (dc plasma potential, electron concentration and temperature) that can be measured by means of a compensated Langmuir probe. However, the method is not very sensitive to errors made by the estimation of these parameters, since the electron and ion currents flowing to the probe are usually negligible when compared with the displacement current. In addition, the dominance of the displacement current enables the modification of the presented model to a simpler numerical form that does not depend on the electron temperature at all. The presented method was successfully tested in a nitrogen capacitively coupled discharge.

It was shown that the waveforms of plasma potential and voltage measured by the probe differ significantly, which demonstrates a strong influence of the sheath around the probe on the measured data. The waveform measured by the probe was strongly correlated with the discharge current. At low pressures, the plasma potential waveform contained a large amount of higher harmonic frequencies that were ignited, namely during the fast expansion of the sheath at the powered electrode.

## Acknowledgments

This work has been supported by the Czech Ministry of Education, contract MSM0021622411.

## References

- [1] Lieberman M A 1988 *IEEE Trans. Plasma Sci.* **16** 638
- [2] Czarnetzki U, Mussenbrock T and Brinkmann R P 2006 *Phys. Plasmas* **13** 123503
- [3] Ku V P T, Annaratone B M and Allen J E 1998 *J. Appl. Phys.* **84** 6536
- [4] Mussenbrock T and Brinkmann R P 2006 *Appl. Phys. Lett.* **88** 151503
- [5] Law V J, Kenyon A J, Thornhill N F, Srigengan V and Batty I 2000 *Vacuum* **57** 351
- [6] Klick M, Rehak W and Kammeyer M 1997 *Japan. J. Appl. Phys.* **36** 4625
- [7] Vašina P and Dvořák P 2009 *Europhys. Lett.* **85** 15002
- [8] Rauf S and Kushner M J 1998 *J. Appl. Phys.* **83** 5087
- [9] Dvořák P and Moravec Z 2008 *Chem. Listy* **102** S1356

- [10] Boufendi L, Gaudin J, Huet S, Viera G and Dudemaine M 2001 *Appl. Phys. Lett.* **79** 4301
- [11] Sobolewski M A 1995 *IEEE Trans. Plasma Sci.* **23** 1006
- [12] Yatsuzuka M, Morishita K, Satoh K and Nobuhara S 1985 *Japan. J. Appl. Phys.* **24** 1724
- [13] Benjamin N 1982 *Rev. Sci. Instrum.* **53** 1541
- [14] Savas S E and Donohoe K G 1989 *Rev. Sci. Instrum.* **60** 3391
- [15] Gagné R R J and Cantin A 1972 *J. Appl. Phys.* **43** 2639
- [16] Braithwaite N St J, Benjamin N M P and Allen J E 1987 *J. Phys. E: Sci. Instrum.* **20** 1046
- [17] Dyson A, Bryant P and Allen J E 2000 *Meas. Sci. Technol.* **11** 554

# Modelling of electric characteristics of capacitively coupled discharges including nonlinear effects of sheaths

P Dvořák

Department of Physical Electronics, Faculty of Science, Masaryk University, Kotlářská 2, Brno 611 37, Czech Republic

E-mail: [pdvorak@physics.muni.cz](mailto:pdvorak@physics.muni.cz)

Received 11 February 2013, in final form 16 May 2013

Published 5 July 2013

Online at [stacks.iop.org/PSST/22/045016](http://stacks.iop.org/PSST/22/045016)

## Abstract

Electric characteristics of capacitively coupled discharges were calculated, including their nonlinear behaviour and generation of higher harmonic frequencies of discharge current and voltage. The discharge was modelled as a series combination of the bulk plasma, two nonlinear sheaths and a radio frequency generator. Comparison of the results of the model with an experiment is discussed. The model was used for studying the waveforms of discharge current and sheath voltages and generation of higher harmonic frequencies at a wide range of discharge parameters. Coupling of higher harmonic frequencies, discharge asymmetry and discharge voltage was demonstrated. The effects of plasma–sheath resonance and other phenomena on the discharge behaviour were shown.

(Some figures may appear in colour only in the online journal)

## 1. Introduction

Capacitively coupled discharges have been widely used for numerous decades for plasma deposition, etching, surface treatment, dust formation, etc. Therefore, much effort has been devoted to the theoretical modelling of these discharges, which resulted in the development of the so-called global model (see, e.g., [1]) or Monte Carlo–particle-in-cell (PIC) simulations (see, e.g., [2–4]). However, most of these works did not take into account the nonlinear nature of capacitive discharges or were restricted to symmetric discharges with equal electrode areas, where the nonlinear behaviour of the plasma is suppressed.

The nonlinear nature of capacitive discharges is caused by sheaths, areas with a high spatial charge, that spontaneously develop between the bulk plasma and electrodes. Their nonlinear character leads to the production of higher harmonic frequencies of discharge current and sheath voltages [5]. Amplitudes of higher harmonic frequencies can be very high [6, 7], even higher than the amplitude of the fundamental frequency supplied by the radio frequency (RF) generator [8]. Higher harmonics reach high amplitudes usually at a low pressure, where they are not significantly damped by collisions between electrons and neutrals, especially if they reach the

(series) plasma–sheath resonance [9, 10]. The plasma–sheath resonance occurs if the inductance of the bulk plasma resonates with the capacitance of sheaths, i.e. approximately at the angular frequency of the electric field:

$$\omega = \frac{\omega_{pe}}{\sqrt{1 + L/t_s}}, \quad (1)$$

where  $\omega_{pe}$  is the plasma frequency of electrons,  $L$  is the length of the bulk plasma and  $t_s$  is the total thickness of both sheaths. Consequently, higher harmonic frequencies can have a significant influence on the plasma. They contribute to plasma heating [8] and ionization [11] (higher frequencies are more effective in ionization than the fundamental frequency [1]), and they can produce a spontaneous electrical asymmetric effect [12, 13], which influences the ratio of sheath voltages. The time-dependent capacity of the sheath and the resulting generation of higher harmonics were also observed at higher pressures close to 1 kPa [14].

Since higher harmonics sensitively react to plasma parameters such as electron concentration and collision frequency or discharge asymmetry, they can be used for monitoring plasma processes. They are used, e.g., for monitoring the end-point detection of etching processes [15, 16], monitoring the compound layer on magnetron targets

[17, 18] or dust growth [19–21] and for the measurement of electron concentration and collision frequency [22].

Efforts were made to calculate the nonlinear behaviour of capacitive plasmas and the production of higher harmonic frequencies [22–25]. Some of the models reached good agreement with experiments but they were restricted to extremely asymmetric discharges where the influence of the sheath at the grounded electrode was neglected, eventually to purely symmetric discharges that do not describe the real situation in most of the experiments. Some of the models expected only a monofrequency waveform of the voltage at the powered electrode neglecting higher harmonic frequencies of the discharge voltage. Therefore, this work deals with modelling of capacitively coupled discharges with various levels of discharge asymmetry and focuses on the behaviour of higher harmonic frequencies produced by the discharge.

## 2. Description of the model

### 2.1. Basic model equations

In this model, the discharge is described as a series combination of two nonlinear sheaths, the bulk plasma and an RF generator with  $50 \Omega$  output (figure 1). The bulk plasma conductivity ( $\sigma$ ) is given by the equation

$$\sigma = \frac{ne^2}{m(\nu + i\omega)} + i\omega\varepsilon_0, \quad (2)$$

where  $n$  is the electron concentration,  $e$  is the elementary charge,  $m$  is the electron mass,  $\nu$  is the momentum-transfer collision frequency of electrons,  $\omega$  is the angular frequency of the electric field and  $\varepsilon_0$  is the vacuum permittivity. The term  $ne^2/[m(\nu + i\omega)]$  describes the electron motion, and the term  $i\omega\varepsilon_0$  describes the displacement current flowing through the space. Equation (2) can be used for the estimation of bulk plasma impedance:

$$Z_{\text{bulk}} = \frac{G}{\frac{ne^2}{m(\nu + i\omega)} + i\omega\varepsilon_0} = \frac{G}{\varepsilon_0} \frac{\nu + i\omega}{\omega_{\text{pe}}^2 - \omega^2 + i\nu\omega}, \quad (3)$$

$$\omega_{\text{pe}}^2 = \frac{e^2 n}{m\varepsilon_0}, \quad (4)$$

where  $\omega_{\text{pe}}$  is the electron plasma frequency and  $G$  is a geometrical factor that would be in a homogeneous bulk plasma with length  $L$  and cross section area  $S$  equal to  $G = L/S$ . The real geometry of the bulk plasma and spatial variations of electron concentration can lead to a more complicated relation for  $G$  and eventually to a more complicated relation for  $Z_{\text{bulk}}$ .

The sheaths are treated as areas with constant concentration of positive ions equal to  $n$ . The spatial distribution of electrons is treated as stepwise, i.e. the electron concentration at the sheath edges is  $n$  and there are no electrons inside the sheaths. The intensity of the electric field at the plasma–sheath edges is assumed to be negligible when compared with the electric field inside the sheaths. In the sheaths, only a displacement current is taken into account

in the basic model equations. These assumptions lead to the following relations between sheath voltage ( $u_s$ ), sheath thickness ( $x$ ) and electric current ( $i$ ):

$$u_s = \frac{ne}{2\varepsilon_0} x^2, \quad (5)$$

$$i = \pm neS_s \frac{dx}{dt}, \quad (6)$$

where  $S_s$  is the sheath (or electrode) area and  $t$  is the time. The sign in equation (6) is positive when the current direction is chosen from the plasma to the electrode. The nonlinear VA sheath characteristics (5)–(6) is the source of higher harmonic frequencies of discharge current and voltage.

In this work, the powered electrode is connected to an RF voltage generator with frequency 13.56 MHz and output impedance  $Z_g = 50 \Omega$ . However, this model can be used for the solution of double [12, 13, 26] or multifrequency [27, 28] discharges as well if the higher frequencies are integer multiples of the lowest frequency. For simplicity, the influence of the transition line between the RF generator and the powered electrode including the matching box, cabling, powered electrode geometry and capacitive current flowing to the grounded ring around the powered electrode is not taken into account. It is expected that the dc current is blocked by a capacitor, but the influence of this capacitor on the RF components of the discharge current is neglected. The RF voltage produced by the generator  $u_g$  is the sum

$$u_g = u_B + u_{\text{bulk}} - u_A + Z_g i, \quad (7)$$

where  $u_A$  and  $u_B$  are the sheath voltages at the powered and grounded electrodes, respectively, and  $u_{\text{bulk}}$  is the bulk plasma voltage. The relation between the bulk plasma voltage and the discharge current is described by the bulk plasma impedance (3). Equation (7) is also valid for dc components with the exception that the dc bias  $u_{\text{bias}} = \langle u_B \rangle - \langle u_A \rangle$  at the powered electrode must be used instead of the dc component of the generator voltage since the dc current is blocked by the blocking capacitor.

### 2.2. Fourier transform of model equations

Since capacitively coupled discharges are known to produce only a limited number of higher harmonic frequencies, the model equations were transformed by the discrete Fourier transform, which is defined by the following relations between  $N$  values of the equidistantly sampled quantity  $\{y_j\}$  and its Fourier picture  $\{Y_k\}$ :

$$y_j = \frac{1}{N} \sum_{k=1}^N Y_k e^{i2\pi \frac{(k-1)(j-1)}{N}}, \quad (8)$$

$$Y_k = \sum_{j=1}^N y_j e^{-i2\pi \frac{(k-1)(j-1)}{N}}. \quad (9)$$

In order to describe the dc component and  $H$  harmonic frequencies (including the fundamental frequency 13.56 MHz) of discharge characteristics, it is necessary to sample one RF

period by  $N = 2H + 1$  points. It is advantageous to use the fact that all the physical quantities used in equations (5)–(7) have real values. For real  $\{y_j\}$  it can be shown that  $H$  of  $\{Y_k\}$  elements are only complex conjugates of other  $\{Y_k\}$  elements:

$$Y_k = Y_{N+2-k}^*, \quad \text{for } k = H + 2, \dots, N. \quad (10)$$

This will reduce the number of model equations that have to be solved from  $2H + 1$  to  $H + 1$ . From the  $\{Y_k\}$  values the mean value of the quantity  $y$  can be found as  $\langle y \rangle = Y_1/N$  and for  $2 \leq k \leq H + 1$  the amplitude of the signal with angular frequency  $\omega_{k-1} = 2\pi(k-1)/T$  can be found as  $2\sqrt{Y_k Y_k^*}/N$ , where  $T$  denotes the RF period.

In order to transform equation (7), it is necessary to express the square  $x^2$  in equation (5) and the derivative in equation (6) into their Fourier pictures, which leads to

$$\frac{2\varepsilon_0}{ne} NU_{sk} = \sum_{l=1}^N X_l X_p, \quad (11)$$

$$p = \begin{cases} k + 1 - l, & \text{for } k \geq l, \\ k + 1 - l + N, & \text{for } k < l \end{cases}$$

and

$$I_k = \pm i(k-1) \frac{2\pi}{T} S_s ne X_k, \quad (12)$$

where  $\{U_{sk}\}$ ,  $\{X_l\}$  and  $\{I_k\}$  are the Fourier pictures of the sheath voltage  $u_s$ , sheath thickness  $x$  and discharge current  $i$ , respectively, and  $T$  is the RF period. Furthermore, the model treats the discharge with two sheaths  $A$  and  $B$  that are developed at electrodes with areas  $S_A$  and  $S_B$ , respectively. The current continuity leads to

$$S_A \frac{dx_A}{dt} = -S_B \frac{dx_B}{dt}, \quad (13)$$

$$X_{Bk} = -\frac{S_A}{S_B} X_{Ak}, \quad \text{for } k \neq 1, \quad (14)$$

where indices  $A$  and  $B$  denote the thicknesses of the corresponding sheaths.

Now, equation (7) can be transformed by means of equations (11), (12) and (14) to the system of equations

$$NU_{Gk} \frac{2\varepsilon_0}{ne} = -2X_{Ak} \left( X_{A1} + \frac{S_A}{S_B} X_{B1} \right) + \left[ \left( \frac{S_A}{S_B} \right)^2 - 1 \right] \times \sum_{\substack{l=2 \\ l \neq k}}^N X_{Al} X_{Ap} - iN \frac{4\pi\varepsilon_0}{T} S_A (Z_{\text{bulk}k} + Z_g) (k-1) X_{Ak}, \quad \text{for } k = 2, \dots, H+1, \quad (15)$$

$$NU_{G1} \frac{2\varepsilon_0}{ne} = -X_{A1}^2 + X_{B1}^2 + \left[ \left( \frac{S_A}{S_B} \right)^2 - 1 \right] \sum_{l=2}^N X_l X_{N+2-l}, \quad (16)$$

where

$$p = \begin{cases} k + 1 - l, & \text{for } k \geq l, \\ k + 1 - l + N, & \text{for } k < l, \end{cases}$$

$$X_{Aj} = X_{A(N+2-j)}^*, \quad \text{for } j = H+2, \dots, N$$

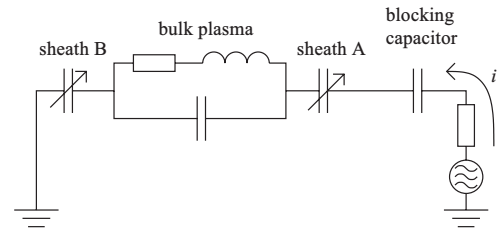


**Figure 1.** Electric schema of the discharge circuit that is solved in the model.

and  $\{U_{Gk}\}$  is the Fourier picture of the generator voltage with the exception of the dc component  $U_{G1}$  that is connected to the dc bias by the relation  $U_{G1} = Nu_{\text{bias}}$ . The system of  $H + 1$  equations (15) and (16) contains  $H + 3$  unknown variables  $X_{A1}, \dots, X_{A(H+1)}, X_{B1}$  and  $U_{G1}$ . The remaining two equations can be obtained from features of the two sheaths, as is described in the next section. The system of equations (15) together with the two remaining equations (21) were numerically solved by means of the optimization toolbox in Matlab. The code can be downloaded from [29].

### 2.3. Mean values of sheath voltages

The model described by the schema in figure 1 cannot give equations for dc values of sheath voltages. Therefore, there are two excess unknown variables in equations (15) and (16). When the model (15)–(16) is compared with an experiment, the dc values of sheath voltages  $\langle u_A \rangle$  and  $\langle u_B \rangle$  can be inserted into the model from Langmuir probe measurements and the unknown variables  $X_{A1}$  and  $X_{B1}$  can be obtained by means of equations

$$U_{A1} N \frac{2\varepsilon_0}{ne} = X_{A1}^2 + \sum_{l=2}^N X_{Al} X_{A(N+2-l)}, \quad (17)$$

$$U_{B1} N \frac{2\varepsilon_0}{ne} = X_{B1}^2 + \left( \frac{S_A}{S_B} \right)^2 \sum_{l=2}^N X_{Al} X_{A(N+2-l)}, \quad (18)$$

where  $U_{A1} = N\langle u_A \rangle$  and  $U_{B1} = N\langle u_B \rangle$ . However, for the application of the model it would be useful to predict these values theoretically.

A possible solution could be obtained by means of an approximate assumption that the minimum thicknesses (or voltages) of both sheaths are zero, i.e. that during each RF period the bulk plasma touches both electrodes. This assumption was tested but it led to strong disagreement both with an experiment and with the requirement of zero dc current flowing through the discharge.

A better possibility is to use the mentioned requirement that there is no dc current flowing through sheaths. The mean electron ( $j_-$ ) and ion ( $j_+$ ) current densities through a sheath can be estimated by

$$j_- = \frac{1}{4} ne \sqrt{\frac{8kT_c}{\pi m}} \exp\left(-\frac{eu_s}{kT_c}\right), \quad (19)$$

$$j_+ = nev_B = ne \sqrt{\frac{kT_c}{m_+}}, \quad (20)$$

where  $k$  is the Boltzmann constant,  $T_e$  is the electron temperature,  $v_B$  is the Bohm velocity and  $m_+$  is the ion mass. The requirements for zero dc currents in both sheaths leads to the two desired equations

$$\left\langle \exp\left(-\frac{eu_A}{kT_e}\right) \right\rangle = \left\langle \exp\left(-\frac{eu_B}{kT_e}\right) \right\rangle = \sqrt{\frac{2\pi m}{m_+}}. \quad (21)$$

Therefore, the values of  $X_{A1}$  and  $X_{B1}$  were numerically fitted so that equation (21) was fulfilled for both sheaths. Equations (19)–(21) are valid if the electron energy distribution function (EEDF) is Maxwellian. The real EEDF shape can deviate from Maxwellian, as discussed, e.g., in [30].

### 3. Comparison with an experiment

The results of the model were compared with plasma potential waveforms measured in a low-pressure capacitively coupled discharge ignited in nitrogen at pressures between 0.5 and 25 Pa. The experiments were carried out in a spherical (i.d. 33 cm) stainless steel reactor with two horizontally mounted, parallel, stainless steel electrodes of 80 mm diameter. The upper electrode, embedded in a grounded ring, was driven at a frequency of 13.56 MHz. The bottom electrode was grounded. Their distance was 40 mm. The value of the RF power delivered to the discharge was 40 W. The dc bias on the powered electrode varied within  $-140$  to  $-200$  V showing an asymmetry of the discharge. The RF voltage, RF current and dc bias were measured on the coaxial cable between the matching unit and the reactor.

The plasma potential waveforms were measured by means of a low-impedance uncompensated probe made from a 10 cm long metallic wire with diameter 0.21 mm, which was connected by a coaxial cable to an oscilloscope. Construction details and the evaluation method of uncompensated probe measurements are described in [7]. The electron concentration, mean electron energy and mean (dc) plasma potential were measured by a compensated Langmuir probe (ESPion, Hidden Analytical).

Unfortunately, not all of the model parameters were known from the experiment. Whereas the area of the powered electrode ( $S_A$ ) is known, it is difficult to determine the effective area of the grounded electrode ( $S_B$ ) since other grounded reactor parts contribute by an unknown value to the area of the grounded electrode. Moreover, the spread of the discharge to these grounded reactor parts makes it practically impossible to determine the geometrical factor  $G$  in equation (3). Finally, the cascade matrix of the electric cabling between the RF generator and the powered electrode was not determined in the experiment. Consequently, there can be a significant difference between the RF voltage amplitude measured on the coaxial cable and the real voltage amplitude on the powered electrode. Therefore, the quantities  $S_B$ ,  $G$  and  $U_{G2}$  were obtained by fitting the model results to the measured plasma potential waveform.

A fit of the model to experimental results is shown in figure 2. The model agrees well with experiments performed at pressures above 10 Pa but there is only partial agreement at

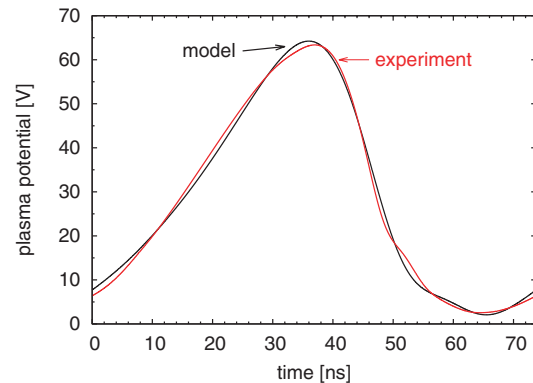


Figure 2. Measured and calculated waveforms of plasma potential in a capacitive discharge ignited in nitrogen at 18 Pa.

lower pressures. It was found recently that at pressures below 10 Pa there is serious disagreement between plasma potential measurements made by various types of uncompensated probes. Therefore, the model cannot be compared with reliable experimental data at these pressures. Efforts are made to improve methods of plasma potential waveform measurements but they lie outside the scope of this work.

Since the agreement of the model with an experiment was confirmed in the case of pressures above 10 Pa, most of the results presented in the next section were calculated under conditions related to the fit in figure 2, i.e. for nitrogen pressure 18 Pa, momentum-transfer collision frequency of electrons  $\nu = 3.1 \times 10^8 \text{ s}^{-1}$ , measured electron concentration  $5.4 \times 10^{14} \text{ m}^{-3}$  and fitted values  $S_B/S_A = 2.97$ ,  $G = 11.8 \text{ m}^{-1}$  and  $U_{G2} = 229 \text{ V}$ .

The ion concentration profile in sheaths strongly influences the sheath thickness and electron heating but it has a smaller effect on the VA characteristics of sheaths. For electric behaviour of sheaths the used assumption of constant ion concentration is equivalent to an assumption of linear increase in the electric field inside a sheath, which agrees relatively well with both PIC simulations [2] and measurements [10]. In order to test the assumption of constant ion concentration, a single sheath model was made that calculated the displacement current flowing through a sheath from a known sheath voltage waveform and that enabled us to work with various more realistic spatial ion concentration profiles. The displacement current flowing through a sheath in the fitted solution of equations (15), (16) and (21) was compared with this model of a single sheath with decreasing ion concentration and good agreement was observed. Consequently, the assumption of the constant ion concentration did not lead to a significant distortion of the model.

Finally, it was tested that the measured dc sheath voltages were in agreement with equation (21).

## 4. Results and discussion

### 4.1. Calculated discharge characteristics

The model enables us to study the waveforms of the discharge current, sheath voltages, plasma bulk voltage or plasma

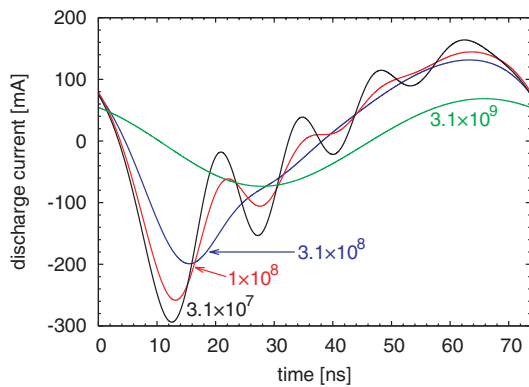


**Figure 3.** Waveforms of the discharge current at various electron collision frequencies  $3.1 \times 10^7 \text{ s}^{-1}$  (black),  $1 \times 10^8 \text{ s}^{-1}$  (red),  $3.1 \times 10^8 \text{ s}^{-1}$  (blue) and  $3.1 \times 10^9 \text{ s}^{-1}$  (green).

potential and their dependences on various plasma parameters such as electron concentration or collision frequency, discharge voltage, electrode distance, etc. The model enables us to study the reaction of plasma upon a change in a single parameter, which cannot usually be achieved by an experiment, where a change in one parameter leads to spontaneous changes of other parameters (e.g. an increase in discharge voltage leads to an increase in electron concentration). Most of the dependences presented in this work are connected to the fit shown in figure 2, i.e. nearly all of the parameters correspond to the nitrogen discharge ignited at pressure 18 Pa and RF power 40 W (see section 3) and only one selected parameter is varied.

Typical calculated waveforms of the discharge current are shown in figure 3. During the expansion of the sheath at the powered electrode (sheath A), eigen-oscillations of the system of bulk plasma and sheaths are ignited, which have the frequency of the series plasma–sheath resonance [9]. Since these oscillations are damped by electron collisions, they are strong at a low electron collision frequency (i.e. at low pressure) and weak at a high collision frequency. Typical waveforms of sheath voltages are shown in figure 4. At a low electron collision frequency the sheath voltage waveforms include visible eigen-oscillations of the plasma–sheath system, but also at high collision frequencies the sheaths show deviations from sinusoidal waveforms, as will be discussed in section 4.3.

It is known (e.g. [1]) that models of a geometrically symmetric discharge with constant ion concentration in sheaths do not lead to the generation of higher harmonics of discharge current even if the sheath voltages and plasma potential include the second harmonic frequency. An increase in the geometric asymmetry of the discharge (i.e. ratio of electrode areas) leads to higher production of higher harmonics, which is demonstrated in figure 5.

#### 4.2. Plasma and plasma–sheath resonances

Discharge impedance strongly depends on electron concentration. The primary effect of an increase in electron concentration is an increase in the first term in the bulk plasma

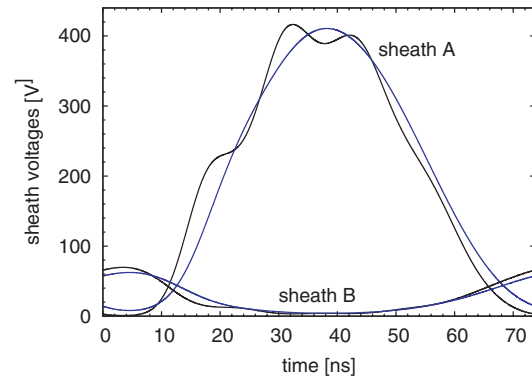


**Figure 4.** Waveforms of sheath voltages at electron collision frequencies  $3.1 \times 10^7 \text{ s}^{-1}$  (black) and  $3.1 \times 10^8 \text{ s}^{-1}$  (blue).

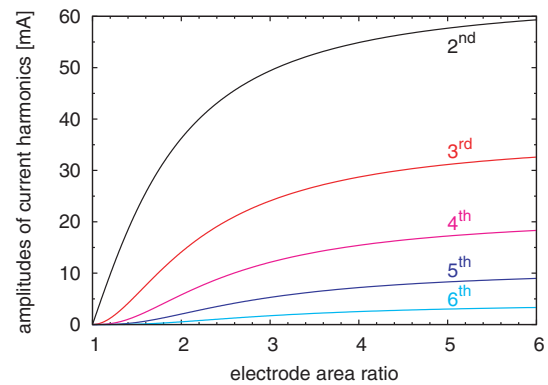


**Figure 5.** Amplitudes of higher harmonic frequencies of discharge current as a function of the electrode area ratio  $S_B/S_A$ .

conductivity equation (2). However, during the change in electron concentration two resonance phenomena can occur, which can significantly affect the plasma impedance. The first phenomenon is the increase in bulk plasma impedance when the angular frequency of the electric field is close to the plasma frequency  $\omega_{pe}$ . This bulk plasma impedance increase is limited due to collisions between electrons and neutrals, but it can effectively reduce the discharge current. The consequent decrease in RF modulation of sheath voltages leads to a drop in the generation of higher harmonic frequencies, as will be shown in section 4.4. The resulting decrease in the higher harmonic frequencies of the discharge current is demonstrated in the left part of figure 6.

When the electron concentration is increased and the resonance with the plasma frequency is left, higher harmonics of the discharge current strongly increase. The increase is supported by the second resonance phenomenon, the (series) plasma–sheath resonance. According to equation (1), harmonics with higher order resonate at a higher electron concentration than harmonics with lower order. For example, the fourth harmonic frequency resonates in our case at an electron concentration of  $3 \times 10^{14} \text{ m}^{-3}$ . It can be seen in figure 6 that its amplitude increases approximately 300 times before this concentration. Whereas amplitudes of higher harmonics of sheath voltages or plasma potential reach clear maxima at

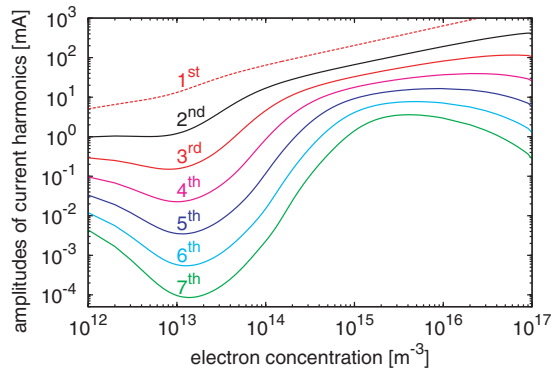


**Figure 6.** Amplitudes of harmonic frequencies of discharge current as a function of electron concentration. The 1st frequency is the fundamental frequency 13.56 MHz; the other curves represent higher harmonic frequencies.

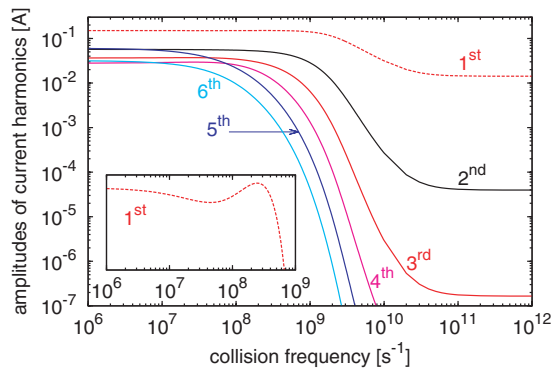


**Figure 7.** Amplitudes of several harmonic frequencies of discharge current as a function of the electron collision frequency.

the plasma–sheath resonance, amplitudes of current harmonics continue to grow even at electron concentrations above the plasma–sheath resonance. The growth of current is caused by both an increase in bulk plasma conductivity and a decrease in sheath widths. At a very high electron concentration the growth of the current is limited by the  $50\ \Omega$  resistor ( $Z_g$ ).

#### 4.3. Effects of momentum-transfer collision frequency of electrons on the discharge

When the electron collision frequency is lower than the angular frequency of the electric field, the effect of  $\nu$  in equation (2) is small when compared with the term  $i\omega$  and the collision frequency does not have high influence on the plasma behaviour. For this reason, there are only small changes in the current or sheath voltage at  $\nu < 10^8\ \text{s}^{-1}$  in figures 7 and 8. When the collision frequency is increased above this value, the bulk plasma conductivity and the discharge current strongly decrease, as shown in figure 7. The fast attenuation of discharge oscillations is visible in figure 3 as well. The increase in bulk plasma impedance (see figure 9) is followed by a decrease in RF voltage modulation of sheaths that leads to a decrease in the generation of higher harmonics of sheath voltage, as shown in figure 8 and further discussed in section 4.4.

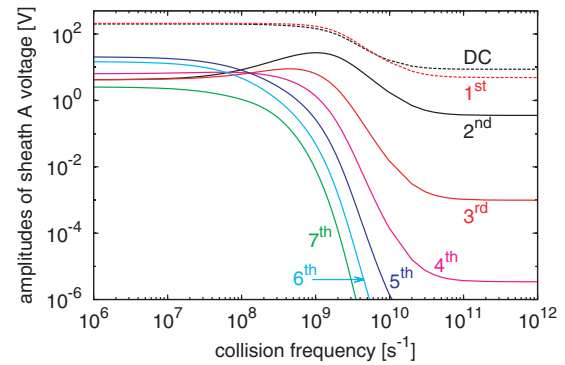


**Figure 8.** Amplitudes of several harmonic frequencies of sheath A voltage as a function of the electron collision frequency.

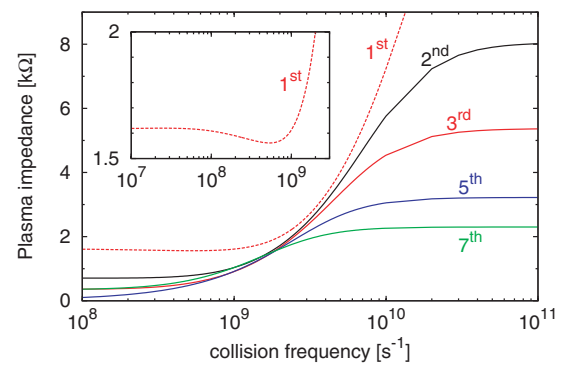


**Figure 9.** Norm of impedance of bulk plasma and sheaths as a function of the electron collision frequency for several frequencies of the electric field. The 1st frequency is the fundamental frequency 13.56 MHz; the other curves represent higher harmonic frequencies.

However, the decrease in bulk plasma conductivity is limited by the capacitive term  $i\omega\epsilon_0$ . At high collision frequencies (in our case above approximately  $2 \times 10^{10}\ \text{s}^{-1}$ ) the capacitive term dominates, and the collision frequency ceases to decrease the plasma conductivity and amplitudes of discharge current and sheath voltages reach an approximately constant value. The model predicts that due to the nonlinearity of equations (5) and (6), higher harmonic frequencies of the discharge current and voltages do not disappear at any value of collision frequency and should be present even in discharges ignited at atmospheric pressure. This fact could be useful in monitoring various plasma processes carried out in atmospheric-pressure discharges.

The decrease in discharge current is not necessarily a monotonic function of the electron collision frequency. As shown in the enlarged section of figure 7, the fundamental harmonic of the discharge current can reach a maximum close to the edge of the following decrease. The current maximum corresponds to the minimum of discharge impedance shown in the enlarged section of figure 9. The values of discharge impedance shown in figure 9 were calculated as a series combination of bulk plasma described by equation (3) and two sheaths. The impedance of each sheath was estimated as an impedance of a capacitor with thickness equal to the mean sheath width. In order to explain the minimum of

discharge impedance for the fundamental frequency, it is useful to mention the fact shown in figure 9 that the discharge impedance for harmonics with higher order starts to grow already at lower collision frequencies than the impedance for harmonics with lower order. The reason is that the capacitive term  $i\omega\epsilon_0$  in equation (2) reduces the effect of the decrease in the term  $ne^2/m(\nu + i\omega)$  on the bulk plasma impedance. Consequently, higher harmonics of the discharge current are attenuated at a lower collision frequency than the fundamental harmonic. Attenuation of higher harmonics leads to a decrease in the thickness of both sheaths, which causes a decrease in sheath impedance and an increase in the fundamental current harmonic.

In agreement with section 4.4, it could be expected that a decrease in sheath modulation caused by an increase in collision frequency should lead to a decrease in higher harmonic frequencies of sheath voltages. However, as demonstrated in figure 8, several harmonics (2nd, 3rd and 4th) increase and reach a maximum prior to the expected decrease in spite of the fact that these conditions are far away from resonance conditions. The increase can be mathematically explained by focusing of the 5th harmonic of the sheath voltage. Under our conditions, the 5th harmonic is the strongest higher harmonic at a low collision frequency since it is close to the frequency of the plasma–sheath resonance. During the increase in collision frequency the signal of the 5th harmonic changes from a pure sinusoidal waveform to a sinus function modulated by an exponential decay. However, Fourier transform of exponentially modulated sinus produces other frequencies in accordance with the observed sequential amplification of the 4th, 3rd and 2nd harmonics.

The changes in plasma impedance can be observed on variations of phase shift between the discharge voltage and current. At low values of collision frequency, the phase shift between the fundamental frequency of sheath current and discharge voltage is close to  $-\pi/2$  due to the capacitive nature of sheaths. An increase in collision frequency increases the resistivity of the bulk plasma and decreases the phase shift. At a high collision frequency, the phase shift between the discharge voltage and the electron conduction current tends to zero in agreement with PIC simulations [31] but the phase shift of the total current flowing through the discharge returns to around  $-\pi/2$  at  $\nu > 2 \times 10^{10} \text{ s}^{-1}$  due to the influence of the capacitive displacement current (the term  $i\omega\epsilon_0$ ). Phase shifts of the higher harmonic frequencies of the discharge current vary rapidly since they depend on the moment when the eigenoscillations of the discharge are excited.

#### 4.4. Effect of sheath modulation on discharge nonlinearity and asymmetry

Some characteristics of capacitive discharges can be illustrated when the amplitude of the RF generator voltage is varied. An increase in generator voltage naturally leads to an increase in discharge current. In agreement with the linear theory of capacitive discharges (see, e.g., [1]) the amplitude of the fundamental frequency of the discharge current increases with the square root of the amplitude of the generator voltage.

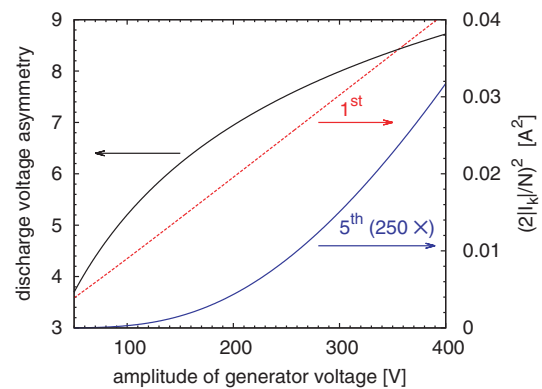


**Figure 10.** Electric asymmetry of the discharge defined as  $\langle u_A \rangle / \langle u_B \rangle$  (black curve, left y-axis) as a function of the generator voltage amplitude. Square of amplitudes of the fundamental (1st, red) and the 5th (blue, 250 × increased) harmonics of the discharge current (depicted on the right y-axis).

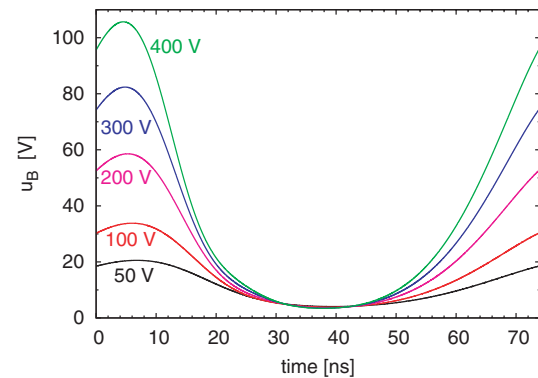


**Figure 11.** Voltage waveforms of the sheath at the grounded electrode ( $u_B$ ) for various amplitudes of RF generator voltage ( $u_g$ ).

However, higher harmonic frequencies of the discharge current do not follow the square root of the generator voltage (see figure 10). Higher harmonics of the discharge current follow a higher power scaling dependence on the generator voltage and the contribution of the higher harmonics to the waveform of the discharge current strongly increases with increasing generator voltage.

Furthermore, the amplitude of the generator voltage influences the value of electric discharge asymmetry, which is defined here as the ratio between the dc components of sheath voltages ( $\langle u_A \rangle / \langle u_B \rangle$ ). As shown in figure 10, the electric discharge asymmetry for a high generator voltage is close to 9, but it decreases with decreasing generator voltage, in spite of the fact that the geometric discharge asymmetry given by the electrode area ratio ( $S_B/S_A$ ) is constant. Examples of sheath voltage waveforms are shown in figure 11. The sheath voltage waveforms have some positive minimum originating from equation (21), which only slightly decreases with increasing generator voltage. Above this minimum the sheath voltage oscillates with an amplitude that naturally grows with increasing generator voltage.

For discussion of the observed results it is valuable to solve the sheath equations (5) and (6) under the assumption of

a simple sheath voltage waveform  $u_s = u_{s1} + u_{s2}(1 + \cos \omega t)$ , where usually  $u_{s1} \geq 0$  due to the requirement of zero dc current flowing through the sheath. It leads to the discharge current

$$i = \pm S_s \sqrt{ne2\varepsilon_0} \frac{d\sqrt{u_s}}{dt} = \mp S_s \sqrt{\frac{ne\varepsilon_0}{2}} \omega \frac{u_{s2} \sin \omega t}{\sqrt{u_{s1} + u_{s2}(1 + \cos \omega t)}}. \quad (22)$$

For low RF modulation of the sheath voltage ( $u_{s2}/u_{s1} \rightarrow 0$ ), the discharge current is proportional to  $\sin \omega t$  and the discharge behaves linearly. However, an increase in the ratio  $u_{s2}/u_{s1}$  increases the effect of the term  $u_{s2}(1 + \cos \omega t)$  inside the square root in equation (22). This leads to a nonlinear sheath behaviour and at the limit of a high RF modulation of the sheath voltage ( $u_{s2}/u_{s1} \rightarrow \infty$ ) the current waveform contains a high content of higher harmonic frequencies, in agreement with the described results of the model.

Equation (22) together with the requirement of current continuity (electric current flowing through both sheaths is identical) can be used for an estimation of the electric discharge asymmetry. For the limit  $u_{s2}/u_{s1} \rightarrow \infty$  (where  $\langle u_s \rangle = u_{s2}/2$ ) it leads to the result

$$\frac{\langle u_A \rangle}{\langle u_B \rangle} = \left( \frac{S_B}{S_A} \right)^2, \quad (23)$$

which is close to 9 under our discharge conditions. This calculation further leads to a decrease in electric discharge asymmetry by a decrease of RF modulation of the sheath voltage, due to the increasing effect of the minimal voltage  $u_{s1}$ , which is in agreement with the calculated behaviour of electric discharge asymmetry shown in figure 10. These illustrative calculations based on equation (22) are only approximate, the whole model (15), (16) and (21) is more accurate since it calculates with more realistic sheath voltage waveforms.

#### 4.5. Effect of nonlinearity on discharge asymmetry

The previous section demonstrated that the amplitude of the fundamental frequency of the discharge voltage influences both the nonlinear plasma behaviour and the discharge asymmetry. This section demonstrates a reverse effect that the nonlinear nature of the plasma influences sheath voltages and discharge asymmetry. Figure 12 shows the changes in mean sheath voltages caused by a change in the geometrical factor  $G$  of the bulk plasma. The geometrical factor can be practically varied, for example, by a change in the electrode distance. The figure shows that an increase in the geometrical factor leads to a decrease in electric discharge asymmetry, which cannot be explained by a change in the amplitude of the fundamental harmonic frequency of sheath voltages.

Since an increase in the geometrical factor increases the bulk plasma impedance, it decreases the frequency of the plasma–sheath resonance and changes the waveform of the discharge current. As a result, the sharpness of the current minimum shown in figure 13, which is formed by means of eigen-oscillations of the plasma–sheath system, decreases with an increase in the geometrical factor. The decrease in the sharpness of the current minimum is connected with a slower

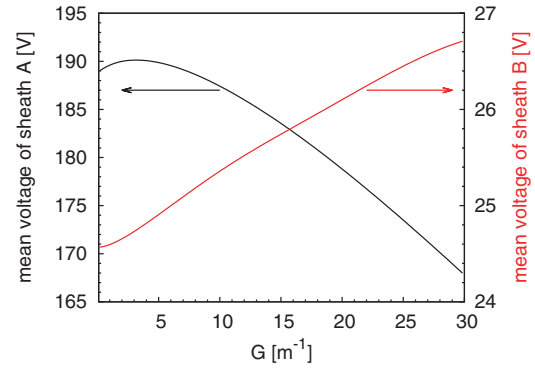


**Figure 12.** Mean sheath voltages as a function of the bulk plasma geometrical factor  $G$ .

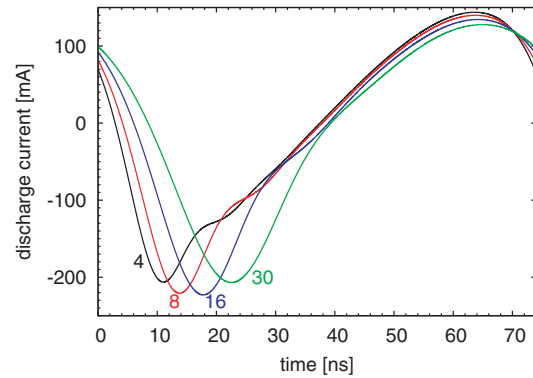


**Figure 13.** Discharge current waveforms at various values of the geometrical factor.  $G = 4 \text{ m}^{-1}$  (black curve),  $8 \text{ m}^{-1}$  (red),  $16 \text{ m}^{-1}$  (blue) and  $30 \text{ m}^{-1}$  (green).

decrease in current prior to this minimum and results in small absolute values of discharge current in the first part of the RF period shown in figure 13.

The current waveform is related to sheath voltages by the relation  $i \propto d\sqrt{u_s}/dt$ . Therefore, a decrease in absolute values of discharge current at the beginning of the RF period influences the temporal derivative of sheath voltages. In the case of the sheath at the powered electrode (sheath A) it results in a slow increase in the sheath voltage, whereas in the case of the sheath at the grounded electrode (sheath B) it results in a slow decrease in the sheath voltage, as shown in figure 14. These facts simply lead to the decrease in mean sheath A voltage, to the increase in mean sheath B voltage and the decrease in electric discharge asymmetry, as shown in figure 12.

#### 4.6. Coupling of higher harmonic frequencies

Equation (15) includes coupling of higher harmonic frequencies. This coupling was studied at a 10 times lower collision frequency ( $\nu = 3.1 \times 10^7 \text{ s}^{-1}$ ) than other results shown in this work, since at a high electron collision frequency the amplitudes of higher harmonics are relatively small and their coupling is weak when compared with coupling to the fundamental frequency. The coupling was demonstrated at

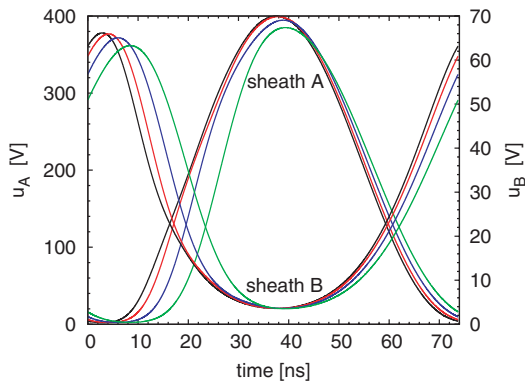


**Figure 14.** Sheath voltage waveforms at various values of the geometrical factor  $G$ . The colours of the curves correspond to the same values of  $G$  as in figure 13.

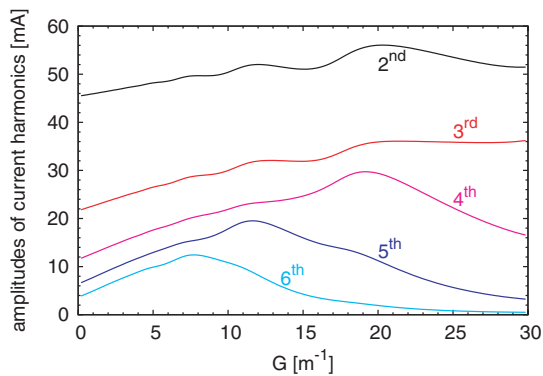


**Figure 15.** Amplitudes of selected higher harmonics of discharge current as a function of the geometrical factor for electron collision frequency  $3.1 \times 10^7 \text{ s}^{-1}$ .

a dependence of the current waveform on the geometrical factor  $G$ , since a change in the geometrical factor enables an amplification of selected harmonics by the plasma–sheath resonance. This fact is shown in figure 15, where the amplification of the 6th, 5th and 4th harmonics of the discharge current by the plasma–sheath resonance is reached at  $G \approx 8 \text{ m}^{-1}$ ,  $12 \text{ m}^{-1}$  and  $19 \text{ m}^{-1}$ , respectively. The coupling of higher harmonic frequencies is demonstrated by the fact that the amplification of a particular harmonic by the plasma–sheath resonance results in the amplification of other harmonics as well.

## 5. Conclusion

Electric characteristics of capacitively coupled discharges were solved by means of a model that describes the discharge as a series combination of the bulk plasma, two nonlinear sheaths and an RF generator with a  $50 \Omega$  input impedance. An assumption of constant ion concentration in sheaths was used. The main aim was modelling of the nonlinear behaviour of the capacitive plasma, which leads to generation of higher harmonic frequencies of discharge current and voltages. The model enables us to study discharges with any

level of asymmetry, from symmetric to extremely asymmetric. Although this work deals only with single-frequency capacitive discharges, the model can be used for studying of two- or multi-frequency discharges at the requirement that the higher frequencies are integer multiples of the fundamental frequency.

The model agreed well with experimental data. A possible limit of the accuracy of the model is the fact that real discharges can have a complex geometry of bulk plasma with a complex spatial profile of electron concentration connected to spatial variations of plasma frequency  $\omega_{pe}$  and that various sheaths in the discharge (i.e. sheaths at the powered electrode, at the grounded electrode and at other grounded reactor parts) can differ in ion concentration. Furthermore, an assumption was made that the electric field at the plasma–sheath interface is negligible. This assumption may decrease the accuracy of the model in discharges with a high electric field inside the bulk plasma, i.e. at high pressures or at plasma–sheath resonance in a discharge with a thin bulk plasma. For simplicity, the present model did not take into account characteristics of the electric line from the RF generator to the powered electrode. For analysis of a plasma in a particular reactor it is recommended to take these parts (including the matching box, cabling and stray capacitance of the powered electrode) into account since they can influence the power consumed by the plasma [32] or shift the frequency of the series plasma–sheath resonance [11]. No significant distortion of the results caused by the assumption of constant ion concentration in sheaths was found.

The model was used for calculation of waveforms of electric discharge quantities (electric current, sheath voltages, etc) and for studying their affect by the (series) plasma–sheath resonance and by resonance of the driving electric field with bulk plasma frequency. Nontrivial effects of the momentum-transfer collision frequency of electrons on the discharge behaviour were discussed and the coupling of higher harmonic frequencies of the discharge current was demonstrated. It was predicted that higher harmonic frequencies are present even in capacitive discharges ignited at atmospheric pressure. Finally, the coupling of discharge voltage, asymmetry and nonlinearity was studied.

## Acknowledgments

The work was supported by the project R&D Center for Low-cost Plasma and Nanotechnology Surface Modifications CZ.1.05/2.1.00/03.0086 (CEPLANT) funding by the European Regional Development Fund and by the Czech Ministry of Education, contract MSM0021622411.S.D.G.

## References

- [1] Chabert P and Braithwaite N 2011 *Physics of Radio-Frequency Plasmas* (Cambridge: Cambridge University Press)
- [2] Nagayama K, Farouk B and Lee Y H 1998 *IEEE Trans. Plasma Sci.* **26** 125
- [3] Donkó Z 2011 *Plasma Sources Sci. Technol.* **20** 024001
- [4] Brzobohatý O, Buršíková V and Trunec D 2004 *Czech. J. Phys.* **54** C527
- [5] Lieberman M A 1988 *IEEE Trans. Plasma Sci.* **16** 638
- [6] Czarnetzki U, Mussenbrock T and Brinkmann R P 2006 *Phys. Plasmas* **13** 123503

- [7] Dvořák P 2010 *Plasma Sources Sci. Technol.* **19** 025014
- [8] Mussenbrock T and Brinkmann R P 2006 *Appl. Phys. Lett.* **88** 151503
- [9] Ku V P T, Annaratone B M and Allen J E 1998 *J. Appl. Phys.* **84** 6536
- [10] Schulze J, Kampschulte T, Luggenhölscher D and Czarnetzki U 2007 *J. Phys.: Conf. Ser.* **86** 012010
- [11] Yamazawa Y 2009 *Appl. Phys. Lett.* **95** 191504
- [12] Schulze J, Schüngel E and Czarnetzki U 2009 *J. Phys. D: Appl. Phys.* **42** 092005
- [13] Schulze J, Schüngel E, Donkó Z and Czarnetzki U 2010 *Plasma Sources Sci. Technol.* **19** 045028
- [14] Belenguer Ph, Guillot Ph and Therese L 2003 *Surf. Interface Anal.* **35** 604
- [15] Law V J, Kenyon A J, Thornhill N F, Srigengan V and Batty I 2000 *Vacuum* **57** 351
- [16] Lisovskiy V, Booth J P, Landry K, Douai D, Cassagne V and Yegorenkov V 2007 *Vacuum* **82** 321
- [17] Vašina P and Dvořák P 2009 *Europhys. Lett.* **85** 15002
- [18] Dvořák P and Vašina P 2010 *Plasma Sources Sci. Technol.* **19** 055016
- [19] Boufendi L, Gaudin J, Huet S, Viera G and Dudemaine M 2001 *Appl. Phys. Lett.* **79** 4301
- [20] Schauer J C, Hong S and Winter J 2004 *Plasma Sources Sci. Technol.* **13** 636
- [21] Hong S, Berndt J and Winter J 2003 *Plasma Sources Sci. Technol.* **12** 46
- [22] Klick M, Rehak A and Kammeyer M 1997 *Japan. J. Appl. Phys.* **36** 4625
- [23] Mussenbrock T, Ziegler D and Brinkmann R P 2006 *Phys. Plasmas* **13** 083501
- [24] Mussenbrock T and Brinkmann R P 2007 *Plasma Sources Sci. Technol.* **16** 377
- [25] Yamazawa Y, Nakaya M, Iwata M and Shimizu A 2009 *Japan. J. Appl. Phys.* **46** 7453
- [26] Boyle P C, Ellingboe A R and Turner M M 2004 *J. Phys. D: Appl. Phys.* **37** 697
- [27] Schulze J, Schüngel E, Donkó Z and Czarnetzki U 2011 *Plasma Sources Sci. Technol.* **20** 015017
- [28] Lafleur T, Delattre P A, Johnson E V and Booth J P 2012 *Appl. Phys. Lett.* **101** 124104
- [29] <http://is.muni.cz/repo/1092071/cs/Dvorak/Harmonics?lang=cs;lang=cs>
- [30] Godyak V A, Piejak R B and Alexandrovich B M 1992 *Plasma Sources Sci. Technol.* **1** 36
- [31] Hemke T, Eremin D, Mussenbrock T, Derzsi A, Donkó Z, Dittmann K, Meichsner J and Schulze J 2013 *Plasma Sources Sci. Technol.* **22** 015012
- [32] Wattieaux G and Boufendi L 2012 *Phys. Plasmas* **19** 033701

# Monitoring of PVD, PECVD and etching plasmas using Fourier components of RF voltage

P Dvořák, P Vašina, V Buršíková and R Žemlička

Department of Physical Electronics, Faculty of Science MU, Kotlářská 2, Brno, Czech Republic

E-mail: [pdvorak@physics.muni.cz](mailto:pdvorak@physics.muni.cz)

Received 10 June 2010, in final form 4 August 2010

Published 15 November 2010

Online at [stacks.iop.org/PPCF/52/124011](http://stacks.iop.org/PPCF/52/124011)

## Abstract

Fourier components of discharge voltages were measured in two different reactive plasmas and their response to the creation or destruction of a thin film was studied. In reactive magnetron sputtering the effect of transition from the metallic to the compound mode accompanied by the creation of a compound film on the sputtered target was observed. Further, deposition and etching of a diamond-like carbon film and their effects on amplitudes of Fourier components of the discharge voltage were studied. It was shown that the Fourier components, including higher harmonic frequencies, sensitively react to the presence of a film. Therefore, they can be used as a powerful tool for the monitoring of deposition and etching processes. It was demonstrated that the behaviour of the Fourier components was caused in both experiments by the presence of the film. It was not caused by changes in the chemical composition of the gas phase induced by material etched from the film or decrease in gettering rate. Further, the observed behaviour was not affected by the film conductivity. The behaviour of the Fourier components can be explained by the difference between the coefficients of secondary electron emission of the film and its underlying material.

(Some figures in this article are in colour only in the electronic version)

## 1. Introduction

Nowadays low temperature plasmas have become a common tool for the deposition of thin films as well as for the surface modification and etching of materials. Their large industrial potential requires the development of efficient and relevant characterization methods providing knowledge about the plasma deposition processes influencing the film properties and taking place in the thin film deposition and etching. Parameter studies providing empirical knowledge about the influence of plasma parameters on the final product of the deposition process are often time consuming and cost-intensive. *In situ* monitoring of the processes taking place during the

deposition or etching offers more effective tools for our understanding of the interrelationship between the plasma process conditions and their influence on the plasma modified material surface.

Plasma processes can be monitored by means of numerous techniques including optical methods, probe measurements, mass spectrometry, etc. Of course, high sensitivity, reliability, simplicity and low price of the monitoring method are often desired. In many cases it is advantageous to use simple electric methods. Traditionally, various plasmas are monitored by the measurement of bias voltage on a powered electrode. The bias voltage is usually strongly correlated with the amplitude of the fundamental frequency of the RF voltage that is used for sustaining the discharge and which can be alternatively used as the monitoring parameter. In the last few years it has been demonstrated that plasma parameters can also be monitored by means of amplitudes of higher harmonic frequencies of discharge voltage or current and that these quantities can be very sensitive markers of plasma processes.

Higher harmonic frequencies are generated due to the nonlinear nature of sheath VA characteristic. Both sheath width and capacity depend on the sheath voltage. Fast variations of sheath capacity during each RF period lead to a nonlinear relation between sheath voltage and displacement current flowing through the sheath [1, 2]. Moreover, sheath expansion produces a current pulse of energetic electrons repelled from the sheath [3], which ignites electric oscillations of the plasma–sheath system. Both these facts lead to the production of higher harmonics. For several reasons amplitude of these harmonics is high in particular at low pressures [4–6], since they are not strongly damped by electron–neutral collisions and they can reach the series plasma–sheath resonance [7] at low pressures. Therefore, higher harmonics can significantly influence plasma at a pressure below 10 Pa [5]. The complex process of creation and damping of higher harmonic frequencies results in a sensitive reaction of higher harmonics to changes in plasma parameters which can be used for diagnostic purposes. They are used for the detection of dust growing in the plasma [8–10], determination of the end of an etching process [11, 12], monitoring of a compound layer on the magnetron target [13, 14] or measurement of electron concentration and collisional frequency [15].

Waveforms of discharge voltages or currents and their Fourier components including higher harmonic frequencies can be measured at various points. From a technical point of view it is simple to perform measurements on the electric line between the RF generator and the reactor [11, 14, 16]. Very sensitive measurements are usually realized by an uncompensated probe [6, 16]. A third possibility is to measure a part of the discharge current flowing to a grounded electrode [16] or to a part of the reactor wall [15]. At all these places it is possible to record and analyse the whole waveform which can give valuable information concerning the plasma. For monitoring purposes it is often sufficient to filter one selected Fourier component and monitor its amplitude.

In numerous plasma processes it is desired to monitor creation or etching of various layers. Both deposition and etching processes can be very complex and it is difficult to make theoretical predictions concerning the complete behaviour of electric parameters of these processes. This work experimentally investigates the behaviour of Fourier components of discharge voltages during the creation and destruction of a layer. Two different processes are used and compared: creation of a compound layer during reactive magnetron sputtering and the deposition of a diamond-like carbon (DLC) film in a capacitively coupled discharge.

In magnetron sputtering films are deposited from atoms that are sputtered from a target by the impact of energetic ions created in a magnetized plasma. Reactive magnetron sputtering enables the deposition of various compound materials by the addition of a reactive gas (e.g. nitrogen or oxygen) into the plasma [17–20]. However, the reactive gas reacts not only with the growing layer but also with the sputtered target, which leads to the creation of a compound

layer on the target and transition between so-called metallic and compound modes [21–23]. This fact causes serious stability problems and leads to the necessity of continuous monitoring of the process. Recently, it has been shown that transitions between the metallic and compound modes can be sensitively monitored by means of higher harmonic frequencies of discharge voltages [13]. Therefore, reactive magnetron sputtering is a process that is suitable for the study of the influence of a compound layer on the Fourier components of RF voltage.

The second investigated process is the deposition of a film growing from dissociated and/or ionized molecules of gases supplied to a capacitively coupled low-pressure discharge. In our case the deposition of amorphous hydrogenated DLC films was studied. These films continue to be at the centre of scientific and industrial interest because they exhibit useful properties for a wide variety of applications; they can be made very hard and chemically inert with low friction coefficient, high wear resistance, good transparency for infrared optics, biocompatibility, etc. Despite their widespread use, deposition and etching mechanism are often not well understood, although it is a fundamental need for the control of film growth with well-defined properties [24, 25]. Development of innovative *in situ* real-time diagnostics using the monitoring of amplitudes of (higher) harmonic frequencies of discharge voltage may provide a scientific basis for optimization and real-time control of film growth and etching.

## 2. Experimental

Experiments were performed in two different plasma reactors. PVD, PECVD and etching of a deposited layer were studied. Reactive magnetron sputtering was studied in the industrial sputtering deposition system Alcatel SCM 650. A cylindrical vacuum chamber, 65 cm in diameter and 35 cm in height, was equipped with a set of four well-balanced magnetron heads, two located on the top and two at the bottom of the deposition chamber. A rotating substrate holder was placed between them. A titanium target of 20 cm diameter and 99.9% purity was mounted on one of the top magnetron heads. RF power was supplied by an Advance Energy Cesar 1.2 kW RF power generator. Prior to the measurement, the chamber was evacuated by a turbomolecular pump backed by a rotary pump. The turbomolecular pump was throttled during the experiment to obtain the desired pumping speed. Argon and the reactive gases (nitrogen or oxygen) were dosed using thermal mass flow regulators. Detailed description of the reactor geometry can be found, e.g., in [14]. The experimental conditions were the following: RF power 1 kW, Ar flow rate 20 sccm and partial pressure of argon 1 Pa. The flow rate of nitrogen or oxygen was varied between 0 and 1.5 sccm.

For the DLC deposition and etching experiments a parallel-plate RF PECVD reactor was used. The reactor chamber consisted of a glass cylinder, inner diameter 28.5 cm and height 19.5 cm, closed by two stainless steel flanges. The bottom duralumin electrode, diameter 14.8 cm, was capacitively coupled to the RF generator working at a frequency of 13.56 MHz. In the standard experimental arrangement the bottom electrode was used as the substrate or the substrate holder and the grounded upper electrode was a graphite target with a diameter of 10 cm. The distance between the electrodes was 10 cm. For the deposition process a mixture of 3 sccm of hydrogen and 1.9 sccm of methane was dosed to the reactor and the deposition took place at a pressure of 19 Pa. The etching of DLC films was performed in a pure hydrogen discharge at a pressure of 13 Pa. The RF power delivered to the discharge was 50 W during both the deposition and the etching. Details of reactor geometry can be found, e.g., in [26].

In both reactors the waveforms of discharge voltages were measured at two places: at a coaxial cable leading from the RF generator to the powered electrode and inside the plasma by means of a home-made uncompensated probe. The probe was a simple steel wire inserted into the plasma that was connected by a coaxial cable to a digital LeCroy Waverunner 6100A

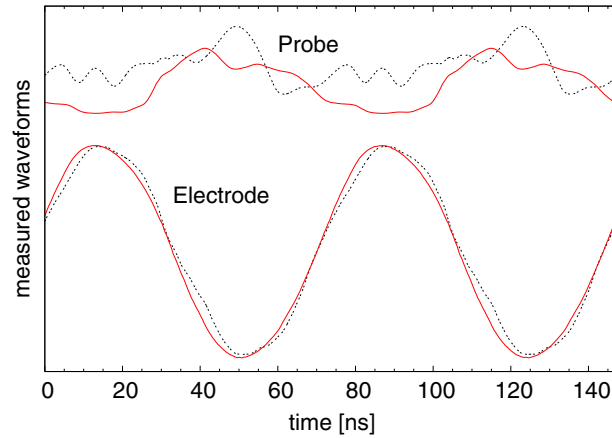


**Figure 1.** Voltage waveforms measured by a probe (upper part of the figure) and at electrodes (bottom part). Black dashed and red solid lines denote measurements in magnetron and PECVD reactors, respectively. Since the waveforms strongly differed in their amplitudes, only their shapes without absolute values are depicted. (Colour online.)

1 GHz oscilloscope with an input impedance of  $1\text{ M}\Omega$ . Examples of measured waveforms are shown in figure 1. Waveforms measured by the probe contained higher amount of higher harmonics than voltage waveforms measured at the electrodes. The amplitudes of dc component, fundamental frequency and higher harmonics were derived from the measured data by Fourier transformation.

### 3. Results and discussion

Addition of a reactive gas into the magnetron plasma is frequently used for the deposition of compound films. However, the presence of the reactive gas leads to the creation of a compound layer on the target resulting in serious stability problems. When the amount of reactive gas is small and target sputtering cleans the target from the compound layer efficiently, a substantial part of the target is not covered by the compound layer and the process runs in a so-called metallic mode. This mode is characterized by fast sputtering, fast deposition and a low partial pressure of the reactive gas which is quickly gettered by the growing film. However, when a large amount of reactive gas is added to the plasma, it cannot be gettered completely; partial pressure of the reactive gas increases which leads to a faster creation of the compound layer on the sputtered target (so-called target poisoning). The sputtering rate of atoms from the compound layer formed on the target surface is usually significantly lower than the sputtering rate of atoms at a clean target surface [27, 28]. Therefore, the poisoning of the target results in a drop in both deposition and gettering rate which leads to a further increase in partial pressure of the reactive gas. This positive feedback leads to a fast poisoning of the whole target and the process jumps into the so-called compound mode characterized by a low deposition rate and a high partial pressure of the reactive gas. Due to the fast creation of a compound film on the sputtered target this transition is suitable for studying the influence of the film on the behaviour of discharge voltage including its higher harmonics.

In this work the influence of mode transition on the behaviour of Fourier components of a discharge voltage was studied by sputtering of a titanium target in argon plasma with

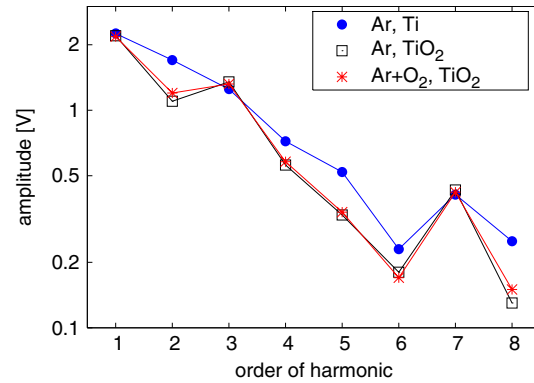


**Figure 2.** Amplitudes of harmonics in metallic mode (full blue circles), pure argon discharge at oxidized target (open black squares) and compound mode (red stars). The metallic mode was ignited in pure argon at a clean titanium target, compound mode in a mixture of argon and oxygen at an oxidized target. Typical standard deviation of the data lies around 1%. Note the semilogarithmic scale. (Colour online.)

an admixture of oxygen or nitrogen. Such a process is routinely used for the deposition of titanium oxides or nitrides. In our experiment the discharge was ignited in pure argon. Then, a reactive gas (nitrogen or oxygen) was added to the discharge until the transition from the metallic to the compound mode occurred. The transition had hysteretic nature, i.e. once the transition to the compound mode occurred, the mode was stable even at lower flow rates of the reactive gas. The reverse transition to the metallic mode occurred at much lower flow rates of the reactive gas than that was necessary for the transition to the compound mode. Waveforms of two voltages were measured during the experiment: voltage of an uncompensated probe immersed in the plasma and voltage on the coaxial cable between the RF generator and the sputtered electrode. The waveforms were analysed by Fourier transformation and the dependence of amplitudes of individual Fourier components on discharge parameters was studied. The amplitudes of the first eight harmonics of the probe voltage in the metallic and in the compound mode measured by the uncompensated probe are depicted in figures 2 and 3. Figure 2 shows the effect of mode transition initialized by oxygen whereas figure 3 shows the effect of nitrogen. Nearly all the harmonics reacted to the transition between the metallic and the compound mode. Their amplitudes changed typically by several per cent or tens of per cent by the mode transition. The harmonics measured on the coaxial cable between the RF generator and the magnetron electrode also reacted to the transition, but were usually less sensitive.

The reaction of harmonics to the transition from the metallic to the compound mode can be caused either by an increase in partial pressure of the reactive gas in the plasma or by the creation of a compound layer on the target surface. In order to distinguish which of these two effects is responsible for the behaviour of the harmonics it was useful to ignite an argon discharge in a reactor with a fully poisoned target as performed in [14], where temporal development of higher harmonics during sputtering of a compound layer on the magnetron target was studied. The state of the target surface in such a discharge was identical with the situation in the compound mode. However, the gas composition was similar to the metallic mode since no reactive gas was added to the reactor at all. The amplitudes of the selected Fourier components of the probe voltage in this discharge are depicted in figures 2 and 3. These figures demonstrate that

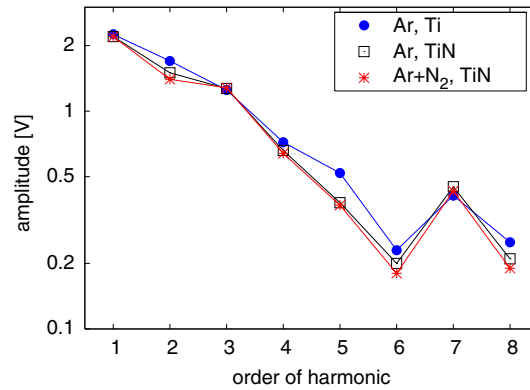


**Figure 3.** Amplitudes of harmonics in metallic mode (full blue circles), pure argon discharge at nitridized target (open black squares) and compound mode (red stars). The metallic mode was ignited in pure argon at a clean titanium target, compound mode in a mixture of argon and nitrogen at a nitridized target. Typical standard deviation of the data lies around 1%. (Colour online.)

the amplitudes measured in the compound mode and the amplitudes measured in a discharge ignited in pure argon at a poisoned target were almost identical. The presence of the reactive gas in the gas phase in the compound mode had almost no influence on the measured harmonics. This observation demonstrates that the changes in harmonics observed by the mode transition are caused by the creation or the removal of the compound layer on the target surface.

A comparison of mode transition in mixtures of argon with nitrogen and oxygen shows that the reaction of Fourier components of discharge voltages to the presence of an oxide or a nitride layer is similar. Usually, changes induced by mode transition in oxygen are a little higher than in nitrogen but the trends are identical. The reaction of higher harmonics to the creation of a nitride or oxide layer on the sputtered target is very similar despite the fact that the two materials differ significantly in electrical conductivity. Titanium nitride has a high electrical conductivity, whereas titanium dioxide is a poor conductor. This is an indication that the conductivity of the compound layer does not have a crucial influence on the behaviour of higher harmonics during the mode transition.

Since the Fourier components of discharge voltages reacted sensitively to the presence of a layer on the magnetron cathode, we extended our research to the PECVD process in order to test the suitability of the presented method for the monitoring of deposition and etching of DLC films in a capacitively coupled discharge. Beyond the monitoring purposes, the relatively simple situation in a capacitive discharge without a magnetic field, without sputtering and in simpler geometry is suitable for the study of reaction of the Fourier components to the presence of a deposited layer.

The DLC films were deposited in a mixture of hydrogen and methane on the powered duralumin electrode. Since the deposition is relatively fast and the effect of film creation combines with the effects of starting the discharge and warming the reactor or addition of methane, the experiments were carried out in the following way. The discharge was started in pure hydrogen supplied with a flow rate of 3 sccm. After several minutes methane was added to the plasma with a flow rate of 1.9 sccm which started the deposition. The deposition took 30 min. Then, methane was stopped and the experiment continued by etching of the deposited film in pure hydrogen. During the whole experiment the discharge was not stopped and the RF power was kept at a constant value of 50 W. This experimental procedure excluded

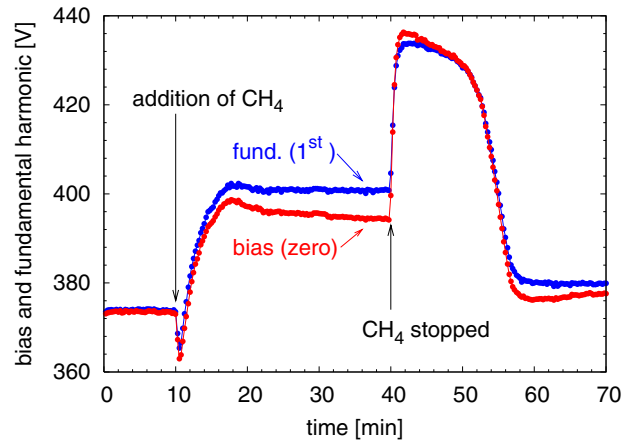


**Figure 4.** Bias and amplitude of the fundamental frequency during deposition and etching of a DLC film.

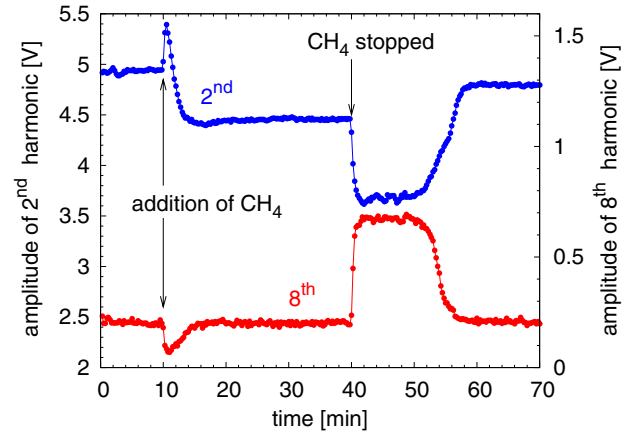


**Figure 5.** Amplitudes of the second and eighth harmonic during deposition and etching of a DLC film.

any influence of transient effects during the start of the discharge since the deposition started several minutes after the discharge ignition. Moreover, it allowed us to distinguish between the effects of methane addition and the presence of the film since the film was etched away much later than the methane was evacuated from the reactor. Again, waveforms of discharge voltages were measured at two points: by an uncompensated probe and on the RF line between the generator and the powered electrode.

The results of the described experiment are shown in figures 4 and 5 where the bias, amplitude of the fundamental frequency and examples of two higher harmonic frequencies are depicted. The addition of methane into the hydrogen discharge in the tenth minute caused a sudden change in the amplitudes of the measured harmonics. This sudden jump is followed by a gradual change which accompanies an initial phase of DLC film deposition. A further

increase in the DLC film thickness does not cause any significant change in amplitudes of the measured harmonics. Then the methane was stopped in order to stop the deposition and to start the etching of the film. The stopping of methane again caused a sudden jump of the measured amplitudes which, however, did not lead to the original values related to a pure hydrogen discharge in a pure reactor without the DLC film at the duralumin electrode. The jump was followed by a ca 10 min long plateau when the film was etched in a hydrogen discharge but the measured amplitudes did not change significantly. The plateau was finished by a fast change in measured amplitudes during which the amplitudes returned to their original values at the beginning of the experiment. After this change there were no visible marks of the DLC film on the electrode. The above described behaviour was observed for almost all the measured Fourier components of the discharge voltage. Better results were obtained for harmonics of low order including the fundamental harmonic (13.56 MHz) and the dc component (bias). This is not surprising since harmonics of low order usually have relatively high amplitude. The Fourier components measured by the uncompensated probe reacted to the addition or stopping of methane and deposition or etching similarly to the Fourier components measured at the powered electrode. Unlike the situation in a magnetron discharge, the sensitivity of harmonics measured at the RF line to the electrode was approximately the same as the sensitivity of harmonics measured by the probe. Therefore, only results measured at the powered electrode are plotted in the graphs. These measurements are more suitable for practical monitoring purposes since they do not require the insertion of any probe into the plasma.

Sudden jumps at 10 and 40 min were evidently caused by the addition or the stopping of methane. The stopping of methane had in all cases an opposite influence than its addition. The amplitude of some harmonics changed during addition and stopping of methane by the same value but in most cases the change by methane addition was relatively low since the influence of methane addition was combined usually with an opposite influence of DLC film deposition that started immediately with methane addition. The addition of methane causes two basic changes in the plasma volume: it increases the pressure and changes the composition of the gas. The influence of pressure is demonstrated in figure 6 where instead of methane addition only hydrogen pressure was increased from 13 to 19 Pa, i.e. to the same value of pressure as in the hydrogen–methane mixture. The pressure was increased in the fifth minute and then decreased back in the twelfth minute of this experiment. The jumps in amplitude of measured harmonics induced by a change in pressure can be compared with the change induced by stopping of methane since this change is not influenced by the deposition of the DLC film. A comparison of figures 4 and 5 with figure 6 demonstrates that stopping of methane or a decrease in hydrogen pressure causes similar changes in the measured amplitudes. Consequently, changes induced by methane addition or stopping are to a large extent caused by changes in pressure. Changes in chemical composition do not have a dominant effect for most of the harmonics. Figure 6 further demonstrates that equilibrium of pressure is reached approximately 1 min after the change in the flow rate, which is useful for understanding the time dependences depicted in figures 4 and 5.

Fast but not so steep changes between 11 and 18 min in figures 4 and 5 and then between 50 and 57 min are caused by the deposition of the DLC film or its etching, respectively. It should be noted that the harmonics reacted to the presence of the film independently on its thickness. The amplitudes of harmonics changed strongly during the initial phase of deposition and then they remained constant, despite the fact that the thickness of the film went on increasing. Analogically, during the etching of the deposited film the amplitudes of harmonics maintained almost constant values until the film was present. Only during the last phase of etching, when the film was totally removed from the electrode surface, the harmonics changed their amplitudes.

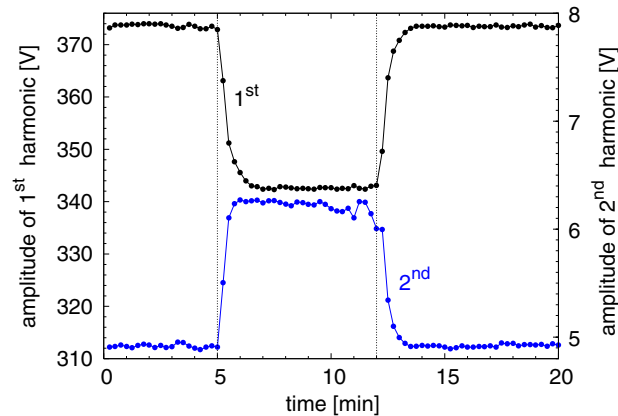


**Figure 6.** Amplitude of fundamental and second harmonics by changes in hydrogen pressure. The dashed vertical lines denote moments of increase or decrease in hydrogen flow rate.

The presence of the DLC film on the powered electrode can influence the discharge voltages in several ways: an insulating material on the conducting electrode can influence the electric parameters of the reactor with the discharge, carbon-containing particles etched from the film influence composition of the plasma and the film differs from the electrode material in coefficient of secondary electron emission which can also influence the harmonics. In order to test the influence of high electric resistivity of the deposited film on the harmonics, the experiment was repeated with a powered electrode covered by a 3 mm thick glass plate. During this experiment the presence of the DLC film did not change the electrical conductivity of the electrode since it was already covered by an insulator before the deposition. The results of this experiment are depicted in figures 7 and 8. The results are similar to the results of the experiment performed without the glass plate (see figures 4 and 5). The time needed for the etching of the film was a little shorter in the case of glass substrate which is in agreement with the fact that the DLC film grows faster on duralumin than on glass. Evidently, changes in amplitudes of the harmonics induced by film deposition or etching are almost identical with the experiment performed without the glass plate at the powered electrode. This demonstrates that film conductivity is not responsible for the behaviour of the harmonics. Therefore, the monitoring method based on the measurement of a selected harmonic is not restricted to the deposition of films with conductivity that differ significantly from the conductivity of a substrate.

After excluding the role of film resistivity on the behaviour of Fourier components of the discharge voltage it should be mentioned that changes in plasma composition caused by the material etched from the film are not responsible for the behaviour of the harmonics. The changes in amplitudes of the harmonics caused by the presence of the DLC film are approximately the same as the changes induced by the addition of methane. The addition of methane added a much higher amount of carbon-containing material to the plasma than it is etched from the film. Therefore, the small amount of material etched from the DLC film cannot cause such a strong change in amplitudes of harmonics as measured in the presented experiments. Moreover, the presence of methane in the plasma and the presence of the DLC film on the electrode have an opposite effect on most of the harmonics. Consequently, the response of harmonics on the presence of the deposited film cannot be caused by the influence of the plasma by the material etched from the film.

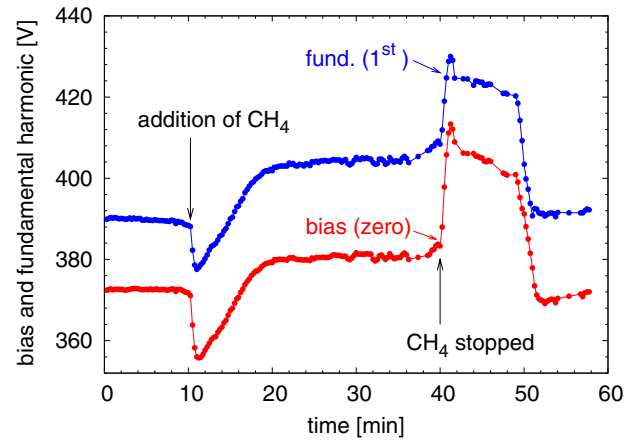


**Figure 7.** Bias and amplitude of the fundamental frequency during deposition and etching of a DLC film on a glass substrate.

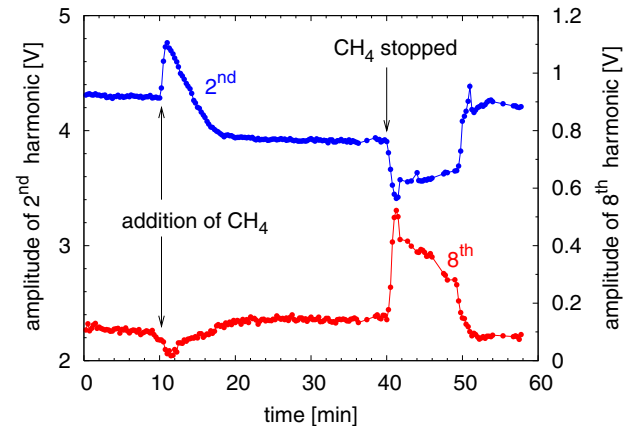


**Figure 8.** Amplitude of the second and eighth harmonic during deposition and etching of a DLC film on a glass substrate.

Since the reaction of the harmonics to the presence of the DLC film is caused neither by the film conductivity nor by the material etched from the film, it seems to be caused by a difference between the coefficients of secondary electron emission of the substrate and the film. Our explanation is supported by earlier findings [26, 29] carried out in the same RF reactor as was used in the case of DLC deposition. It was shown that both the deposition and the etching rates depend strongly on the RF electrode material. In [26] it was demonstrated, using deposition and etching experiments and their computer simulation, that the main source of the electrode material influence consists in its secondary electron yield. The different secondary electron yield of electrode materials can cause a relatively high difference in the plasma density above the different electrodes, since the secondary electron yield is very sensitive to the type of material as well as its surface conditions, morphology, impurities and contamination [30].

This effect influences the deposition and etching rate not only on the RF electrode but also on the opposite grounded electrode. Since the secondary electron yield has a significant influence on the plasma including its density, it is reasonable to expect that it influences also the Fourier components of the discharge voltage that usually react on changes in plasma density very sensitively.

#### 4. Conclusion

Voltages of capacitively coupled discharges include not only fundamental frequency and a dc component but due to a nonlinear nature of plasma they also include higher harmonic frequencies. The reaction of all these Fourier components of discharge voltage to the presence of deposited films was studied in two different plasma processes. In reactive magnetron sputtering a compound film was formed on the magnetron target due to reactions of a reactive gas with the material of the target. In a nonmagnetized capacitively coupled discharge DLC films were deposited from carbon-containing reactive species present in the plasma. In both processes discharge voltages and amplitudes of their Fourier components were measured at two places: at a coaxial cable leading from the RF generator to the powered electrode and by an uncompensated probe immersed directly into the plasma. It was shown that most of the Fourier components sensitively reacted to the creation or destruction of the films. The sensitivity of the Fourier components and simplicity of the measurements make them a powerful tool for monitoring the deposition and etching processes.

It was demonstrated that the behaviour of the Fourier components is not affected significantly by conductivity of the deposited films. Therefore, monitoring based on the measurement of amplitudes of the Fourier components is not restricted to the deposition of conducting or insulating materials. This method can also be used in the case of materials whose conductivity does not differ from the conductivity of the substrate. Further, it was shown that the observed behaviour of the Fourier components was caused by the presence of the film. It was not caused by changes in chemical composition of the gas phase induced by a material etched from the film or decrease in gettering rate. The sensitive reaction of the Fourier components on the presence of the film can be explained by the difference between the coefficients of secondary electron emission of the film and the underlying material.

#### Acknowledgments

This work has been supported by the Czech Ministry of Education, contract MSM0021622411 and by the Czech Science Foundation, contracts GACR202/07/1669 and GA202/08/P038.

#### References

- [1] Lieberman M A 1988 *IEEE Trans. Plasma Sci.* **16** 638
- [2] Klick M 1996 *J. Appl. Phys.* **79** 3445
- [3] Schulze J, Heil B G, Duggenhölscher D, Mussenbrock T, Brinkman R P and Czarnetzki U 2008 *J. Phys. D: Appl. Phys.* **41** 042003
- [4] Czarnetzki U, Mussenbrock T and Brinkmann R P 2006 *Phys. Plasmas* **13** 123503
- [5] Mussenbrock T and Brinkmann R P 2006 *Appl. Phys. Lett.* **88** 151503
- [6] Dvořák P 2010 *Plasma Source Sci. Technol.* **19** 025014
- [7] Ku V P T, Annaratone B M and Allen J E 1998 *J. Appl. Phys.* **84** 6536
- [8] Boufendi L, Gaudin J, Huet S, Viera G and Dudemaine M 2001 *Appl. Phys. Lett.* **79** 4301
- [9] Schauer J C, Hong S and Winter J 2004 *Plasma Source Sci. Technol.* **13** 636
- [10] Hong S, Berndt J and Winter J 2003 *Surf. Coat. Technol.* **174** 754

- [11] Law V J, Kenyon A J, Thornhill N F, Srigengan V and Batty I 2000 *Vacuum* **57** 351
- [12] Lisovskiy V, Booth J P, Landry K, Douai D, Cassagne V and Yegorenkov V 2007 *Vacuum* **82** 321
- [13] Vašina P and Dvořák P 2009 *Europhys. Lett.* **85** 15002
- [14] Dvořák P and Vašina P 2010 *Plasma Sources Sci. Technol.* **19** 055016
- [15] Klick M, Rehak W and Kammeyer M 1997 *Japan. J. Appl. Phys.* **36** 4625
- [16] Sobolewski M A 1995 *IEEE Trans. Plasma Sci.* **23** 1006
- [17] Powell R A and Rossnagel S M 1998 *PVD for Microelectronics* (Boston, MA: Academic)
- [18] Rossnagel S M, Cuomo J J and Westwood W D 1990 *Handbook of Plasma Processing Technology* (New York: Noyes Publications)
- [19] Depla D and Mahieu S 2008 *Reactive Sputter Deposition* (Berlin: Springer)
- [20] Bunshah R F 1994 *Handbook of Deposition Technologies for Films and Coatings* (New Jersey: Noyes Publications)
- [21] Tsiogas C D and Avaritsiotis J N 1992 *J. Appl. Phys.* **71** 5173
- [22] McMahon R, Affinito J and Parsons R R 1982 *J. Vac. Sci. Technol.* **20** 376
- [23] Safi I 2000 *Surf. Coat. Technol.* **127** 203
- [24] Jacob W 1998 *Thin Solid Films* **326** 1
- [25] von Keudell A, Schwarz-Selinger T and Jacob W 1997 *Thin Solid Films* **308–309** 195
- [26] Brzobohatý O, Buršíková V, Nečas D, Valtr M and Trunec D 2008 *J. Phys. D: Appl. Phys.* **41** 035213
- [27] Ranjan R, Allain J P, Hendricks M R and Rujic D N 2001 *J. Vac. Sci. Technol. A* **19** 1004
- [28] Yamamura Y and Tawara H 1996 *Atomic Data and Nuclear Data Tables* vol 62 (New York: Academic) pp 149–253
- [29] Brzobohatý O, Buršíková V and Trunec D 2004 *Czech. J. Phys.* **54** C527
- [30] Lieberman M A and Lichtenberg A J 1994 *Principles of Plasma Discharges and Material Processing* (New York: Wiley)

# Probe technique for measurement of a plasma potential waveform

P Dvořák, M Tkáčik and J Bém

Faculty of Science, Masaryk University, Kotlářská 2, Brno 611 37, Czechia

E-mail: [pdvorak@physics.muni.cz](mailto:pdvorak@physics.muni.cz)

Received 5 October 2016, revised 6 March 2017

Accepted for publication 10 March 2017

Published 18 April 2017



CrossMark

## Abstract

A method for the measurement of plasma potential waveforms is presented that is based on measurement with a high-impedance probe and an electric model of the sheath around the probe. The method was verified and compared with methods that were previously used for measurement of the temporal development of plasma potential during an RF period of capacitive discharges. The sensitivity of the method to the values of required input parameters (mean plasma potential value, electron concentration and temperature) was analyzed and it was found that with a lower precision, the method can be used even without the knowledge of these input parameters. Finally, plasma potential waveforms were measured in a low-pressure capacitively coupled discharge. In agreement with theoretical models, the generation of higher harmonic frequencies of plasma potential and their sensitivity to electron concentration were observed.

Keywords: plasma potential, capacitively coupled discharges, probe, higher harmonic frequencies, sheath

(Some figures may appear in colour only in the online journal)

## 1. Introduction

Plasma potential is one of the fundamental plasma parameters. Its mean (DC) value in low-pressure discharges is usually measured by Langmuir probes. However, alternating or pulsed voltage with a frequency from the kHz–GHz range is used for the excitation of most electric discharges, which lead to substantial variations of plasma potential during each discharge period. Passive [1] or active [2] compensation of a Langmuir probe is therefore used, which prevents the  $V$ – $A$  probe characteristics from distortion caused by alternating currents flowing to the probe. However, the compensation makes the measurement of alternating signals by a compensated probe difficult. Moreover, even when the probe is not compensated, the measurement is complicated by the fact that the alternating components of probe potential can differ significantly from the alternating components of plasma potential, as will be shown below. As a result, while the DC value of the plasma potential is routinely measured by compensated Langmuir probes, there is a lack of data describing the temporal evolution of plasma potential during a discharge period, in spite of the fact that it is a fundamental electric characteristic of plasma. This fact is valid, especially in capacitively coupled discharges where the

plasma potential comprises not only the DC and the one RF component supplied from the RF power generator, but it also includes numerous higher harmonic frequencies created by plasma due to the nonlinear nature of sheaths [3–5].

The complete waveforms of plasma potential can be measured by uncompensated probes that do not suppress the RF signals. However, the analysis of measured data is not straightforward since the probe is separated from the ambient plasma by a sheath. Consequently, the unknown sheath potential must be added to the probe potential in order to obtain the desired plasma potential. Two different approaches were used for the solution of this task. The first is based on the construction of a probe with impedance as high as possible in order to minimize RF current flowing through the sheath around the probe and, consequently, to minimize the RF components of the sheath voltage [6, 7]. The second approach is based on the calculation of the originally unknown sheath voltage [8]. The presented work deals with a combination of these two approaches in order to improve the method of measurement of the complete plasma potential waveforms. A high-impedance uncompensated probe with small dimensions was constructed and the measured data were analyzed by means of a nonlinear model of the sheath

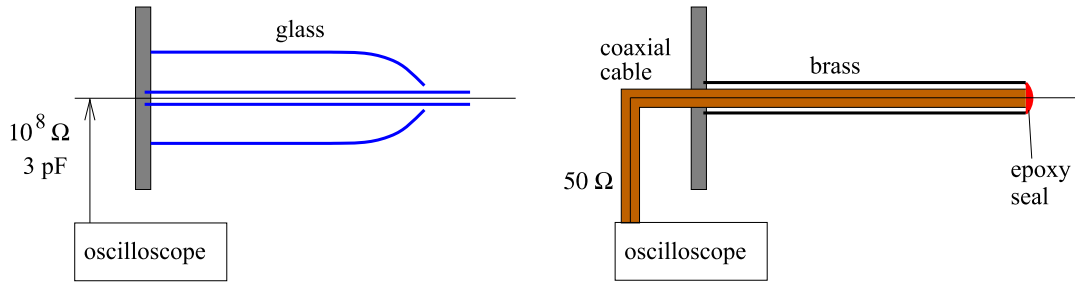


**Figure 1.** Construction of the high-impedance (left) and the low-impedance (right) probes with no RF compensation.

around the probe, which enabled us to measure accurate waveforms of plasma potential with a high spatial resolution. The resulting method is further tested and analyzed in a capacitively coupled RF discharge.

## 2. Experimental

The high-impedance probe with no RF compensation was made of a steel wire with a diameter of 0.27 mm. The 2 cm long tip of this wire was exposed to the plasma, and the rest of the wire was separated from the plasma by two concentric glass tubes (see figure 1). The outer diameter of the inner glass capillary that extended to the probe tip was 1.5 mm. The wire was connected to the oscilloscope (LeCroy WaveRunner 6100A) by a high-voltage oscilloscope probe with input resistance  $10^8 \Omega$  and input capacity 3 pF. The measured total capacity of this uncompensated probe to ground (including the input capacity of the oscilloscope probe) was 3.9 pF.

In order to compare the high-impedance probe with a probe similar to that described in [8], a low-impedance probe with no RF compensation was used simultaneously with the described high-impedance probe. This low-impedance probe was simply made of a 2 cm long bare copper tip of a  $50 \Omega$  coaxial cable that was connected directly to an oscilloscope with an input impedance of  $50 \Omega$  (see figure 1). The probe tip diameter was 0.17 mm.

For the measurements of the mean values of the plasma potential, electron concentration and electron temperature, a Langmuir probe with RF compensation (ESPion, Hiden Analytical) was used. The whole experiment was performed in a low-pressure (0.2–30 Pa) capacitively coupled discharge ignited by RF (13.56 MHz) voltage in various gases (Ar, N<sub>2</sub>, O<sub>2</sub>, H<sub>2</sub>) inside a spherical (i.d. 33 cm) grounded stainless steel reactor with two parallel stainless steel ring electrodes. The diameter of each electrode was 80 mm, and their distance was 40 mm.

## 3. Sheath model

Since bulk plasma is separated from the probe by a sheath, the plasma potential must be calculated as

$$U_{\text{pl}}(t) = U_0(t) + U(t), \quad (1)$$

where  $U_{\text{pl}}$  is the plasma potential,  $U_0$  is the measured probe voltage and  $U$  is the sheath voltage. To calculate the sheath voltage, the model based on the assumptions of constant ion density and stepwise electron density with negligible electron concentration inside the sheath was used. The model is described in [8].

The sheath voltage was expressed by means of the sheath radius ( $s$ )

$$U = \frac{en}{4\epsilon_0} \left( 2s^2 \ln \frac{s}{r_p} - s^2 + r_p^2 \right), \quad (2)$$

where  $e$  is the elementary charge,  $n$  is the electron concentration in the bulk plasma,  $\epsilon_0$  is the vacuum permittivity and  $r_p$  is the probe radius. The derivative of the sheath radius was calculated from the displacement current flowing to the probe ( $I_d$ )

$$I_d(t) = en \frac{S}{r_p} s(t) \frac{ds(t)}{dt}, \quad (3)$$

where  $S$  is the surface area of the probe. The displacement current was obtained by subtraction of the electron ( $I_e$ ) and ion ( $I_i$ ) current from the total current ( $I$ ) flowing to the probe

$$I(t) = I_d(t) + I_e(t) + I_i \quad (4)$$

$$I_e(t) = -\frac{enS}{4} \sqrt{\frac{8kT_e}{\pi m_e}} \exp\left\{-\frac{eU(t)}{kT_e}\right\}, \quad (5)$$

where  $k$  denotes the Boltzmann constant,  $T_e$  is the electron temperature and  $m_e$  is the electron mass. The ion current was assumed to be constant during the whole discharge period, since the ion plasma frequency was significantly smaller than the frequency of the applied electric field. Although some variations of ion density in front of the powered electrode were simulated in a low-frequency (1.9 MHz) discharge ignited in a light gas (He) [9], in conventional CCP discharge, the assumption of constant ion flow is usually valid [10]. Equations (2) and (3) can be used in the form

$$\frac{dU(t)}{dt} = \frac{I_d}{2\pi l_p} \frac{1}{\epsilon_0} \ln \frac{s}{r_p}, \quad (6)$$

where  $l_p$  is the probe length. The electric schema of the whole system is sketched in figure 2(a).

The system of equations (1)–(5) was solved numerically and the unknown value of the ion current ( $I_i$ ) and the initial value of the sheath voltage ( $U(0)$ ) were fitted so that the calculated plasma potential was periodic and the mean value

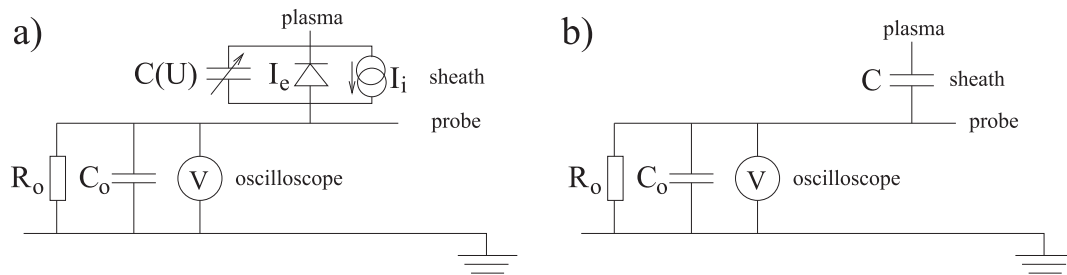


**Figure 2.** Electric scheme of the uncompensated probe circuit. (a) The system solved in the presented work. (b) An approximation of the sheath around the probe by a capacitor, which is tested in section 6.1.

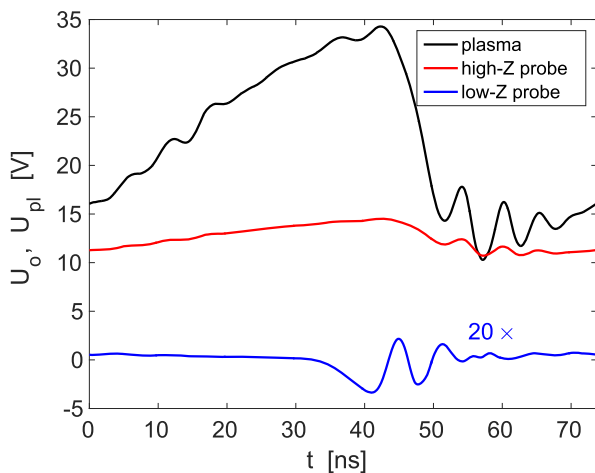


**Figure 3.** Waveforms of plasma (black), high-impedance probe (red) and low-impedance probe (blue) potentials measured in a capacitively coupled discharge in argon at 6 Pa. The low-impedance probe potential was  $20 \times$  increased.

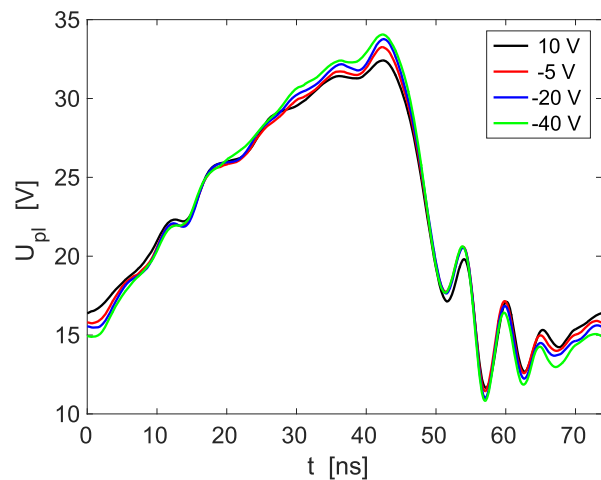


**Figure 4.** Comparison of plasma potential waveforms calculated from probe measurements realized at various values of the probe DC voltage. Measured in argon at 6 Pa.

of the calculated plasma potential agreed with the mean value measured by the RF compensated Langmuir probe.

One example of the measured high-impedance uncompensated probe voltage waveform and the calculated plasma potential waveform is shown in figure 3, which demonstrates a significant difference between the probe and the plasma potential waveforms. Consequently, it is necessary to model the voltage of the sheath around the probe when the plasma potential waveform is measured. Figure 3 further depicts a waveform measured by the low-impedance uncompensated probe. Comparison of the high- and low-impedance probe method will be discussed in section 6.2.

#### 4. Test of the method

In order to test the method, the probe was artificially biased to various DC potentials from  $-40$  V to  $+10$  V and plasma potential waveforms were measured at various DC probe potentials. The DC biasing was realized via a series of coils in order to eliminate any significant distortion of RF signals caused by the DC biasing. Since plasma potential should not be affected by the probe bias, the obtained plasma potential waveforms should not differ. Nevertheless, the change of the

DC bias from  $10$  V to  $-40$  V led to a change of the sheath voltage ( $U$ ) by ca 300%. Therefore, the sheath model (1)–(5) is used in several significantly different conditions, including a situation with negative DC bias where the model has a very strong effect on the shape of the obtained plasma potential waveform. As a result, an inaccuracy of the model should lead to a discrepancy between the obtained plasma potential waveforms and, therefore, the comparison of waveforms obtained from measurements with various probe DC bias can be used as a test of the reliability of the method.

Figures 4 and 5 show examples of the described test realized in a capacitively coupled discharge ignited in argon at pressure 6 Pa and 16.5 Pa, respectively. Although the sheath voltage was changed by hundreds of percent during the test, the resulting plasma potential waveforms differ at most by several percent, which indicates a satisfactory reliability of the presented method.

The behaviour of the probe was also tested for probe DC potential values that were higher than  $10$  V. At high positive bias values the sheath around the probe was collapsing (i.e.  $U \leq 0$ ) for a non-negligible part of the discharge period. This is a situation that cannot be described reliably by the model (1)–(5) and a more accurate model should be used in such cases.

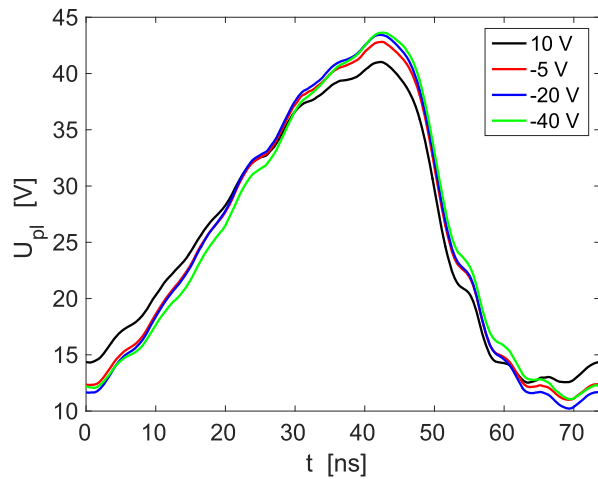


**Figure 5.** Comparison of plasma potential waveforms calculated from probe measurements realized at various values of the probe DC voltage. Measured in argon at 16.5 Pa.

A second short test of the method was realized by the addition of a 4 pF capacitor between the probe and the ground. Plasma potential waveforms acquired by means of the probe with an increased load again did not differ significantly from waveforms acquired by a non-loaded probe.

### 5. Sensitivity to input parameters

Since the presented method of plasma potential waveform measurement requires knowledge of electron concentration, electron temperature and the mean (DC) value of the plasma potential, the sensitivity of the method to these three parameters was examined. The dominant component of the current flowing to the probe is the displacement current. When the probe is negatively biased, the electron current can be neglected and equation (6) in the form

$$\frac{dU}{dt} = \frac{I - \langle I \rangle}{2\pi l_p} \frac{1}{\varepsilon_0} \ln \frac{s}{r_p}, \quad (7)$$

can be used instead of equations (3)–(5). Since equation (7) does not depend on electron temperature, the proposed method is independent of the value of electron temperature at sufficiently low probe biasing.

When the probe is floating (it is not biased), the electron current is not negligible and both the values of electron concentration and temperature are required as input parameters. For a floating probe, the sensitivity of the method to the values of these input parameters is demonstrated in figures 6 and 7. These figures display five different plasma potential waveforms that were calculated from the same measurement realized by a floating probe in an argon discharge at the pressure of 6 Pa. The displayed waveforms differ in the value of electron concentration or temperature that was used during the evaluation of the measurement. These figures demonstrate that even when the input parameter (electron concentration or electron temperature) was twice

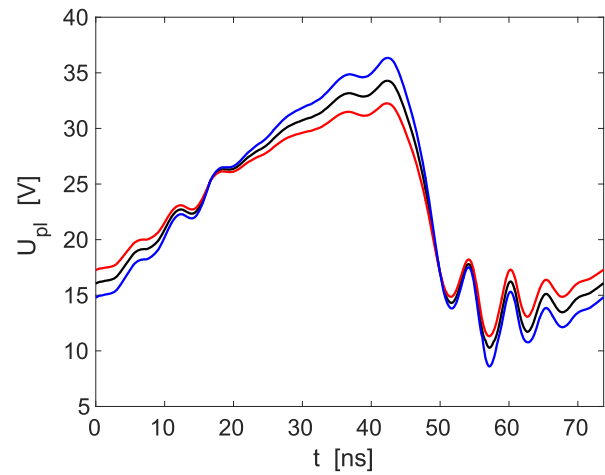


**Figure 6.** Comparison of plasma potential waveforms calculated for correct (black line), doubled (red) and half (blue) value of electron concentration. Calculated from voltage waveforms measured by a floating probe.

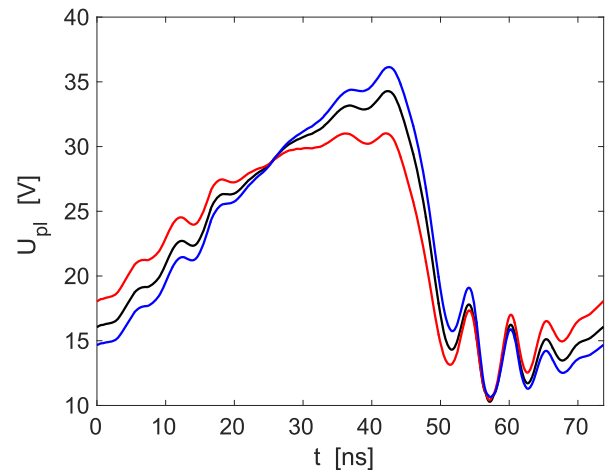


**Figure 7.** Comparison of plasma potential waveforms calculated for correct (black line), doubled (red) and half (blue) value of electron temperature. Calculated from voltage waveforms measured by a floating probe.

overvalued or undervalued, the obtained plasma potential waveforms were distorted by less than 10% of the peak-to-peak value of the obtained waveform.

Thanks to the fact that the dominant current component is the displacement current and the presented method is not very sensitive to the values of electron concentration and temperature, the method is relatively robust; it will not be affected strongly by eventual effects like a decrease of electron concentration due to the presence of the probe and probe holder, collisions of charged particles in the sheath around the probe, reflection or emission of electrons from the probe surface or temporal variations of the ion current.

Since the electron current flowing to the probe is usually much weaker than the displacement current, even when the

**Table 1.** Comparison of the mean plasma potential values estimated by means of the uncompensated probe and measured by the Langmuir probe. Measured in a capacitively coupled discharge in argon.

Pressure [Pa]	Estimation of $\langle U_{pl} \rangle$ [V]	Measurement of $\langle U_{pl} \rangle$ [V]
16.5	25.25	25.58
6	22.47	22.53
3.3	24.62	20.52

probe is floating, it is probably not possible to use the uncompensated probe for precise measurement of electron concentration and temperature unless the probe is biased to higher values of DC voltage. The evaluation of measurement with higher probe bias would require a more accurate model of the sheath around the probe that would reliably describe even the situation when the probe potential is higher than the plasma potential.

The final required input parameter is the mean value of the plasma potential. Of course, the mean value of the resulting plasma potential waveform follows the value of this input parameter. Nevertheless, the resulting RF components of the plasma potential are relatively insensitive to changes of this input parameter as long as the calculated sheath around the probe is far from the collapse. In our measurements, the peak-to-peak range of the resulting plasma potential waveform was changed only by a few percent when the value of the plasma potential was doubled.

Since ion current to a floating probe must be compensated by electron current, the mean potential of the floating probe usually sets itself to such a value that ensures that the sheath around the probe is close to its collapse at one moment of the discharge period. This supposition can be used for an estimation of the mean value of plasma potential, even without knowledge of electron temperature. In order to test this hypothesis, the following experiment was realized. Waveforms of probe voltage were measured when the probe was floating and when it was biased to  $-40$  V. The measurements realized at the negative bias were evaluated since an evaluation of these measurements does not require knowledge of electron temperature. The value of the mean plasma potential was explored so that the resulting plasma potential waveform touches the floating probe potential waveform in one moment of the period. A comparison of the obtained mean values of plasma potential and values measured by means of a Langmuir probe are shown in table 1. This comparison shows reasonable agreement and demonstrates that the uncompensated probe can be used for the measurement of the mean plasma potential value. A more accurate method for the determination of mean plasma potential by an uncompensated probe will probably require a deeper analysis of measurements realized with various biasing of the uncompensated probe and a more accurate model of the sheath around the probe. Since the sheath model is not very sensitive to the value of electron concentration, the described method can be used for a rough estimation of the plasma

potential waveform with only a rough guess of electron concentration, i.e. even without precise knowledge of any of the three input parameters.

## 6. Comparison with previous methods

In order to compare the described method with previous methods, a series of experiments was performed in a capacitively coupled discharge in various gases (Ar, N<sub>2</sub>, O<sub>2</sub>, H<sub>2</sub>) in the pressure range 2–20 Pa. Measurements by both the high- and low-impedance probe were realized simultaneously and voltage waveforms of both these probes were evaluated by various models of the sheath around the probe. The following two subsections discuss the comparison of the results. Since the combination of the high-impedance probe with the model (1)–(5) described in this work is believed to be the most reliable from all the compared methods, the reliability of the previous methods is discussed by comparison of their results with the result of the method presented in this work.

### 6.1. Comparison with capacitive sheath model

The described method was compared with the previous method shown in [6, 7], where the sheath around the probe was modeled as a capacitor. In this method, the electric circuit drawn in figure 2(b) is solved and each frequency component of the plasma potential ( $u_{pl}$ ) is calculated according to

$$u_{pl} = u_o \left( 1 + \frac{C_o}{C} - \frac{i}{\omega CR_o} \right), \quad (8)$$

where  $u_o$  is the probe voltage measured by the oscilloscope,  $C_o$  and  $R_o$  are the capacity and resistance of the probe to the ground, respectively, and  $C$  is the capacity of the sheath around the probe. In our test, the sheath capacity was calculated as a capacity of a cylindrical capacitor

$$C = \frac{2\pi\epsilon_0 l_p}{\ln \frac{s}{r_p}}, \quad (9)$$

where the value of the sheath radius  $s$  was chosen so that its corresponding sheath voltage value calculated by equation (2) was equal to the true mean value of the sheath voltage  $\langle U_{pl} \rangle - \langle U_o \rangle$ . The mean value of the plasma potential  $\langle U_{pl} \rangle$  was measured by a Langmuir probe.

The plasma potential waveforms obtained by this simplified method were compared with the plasma potential waveforms acquired by the presented method based on the model (1)–(5). The results of the comparison varied from an excellent agreement to a significant difference. Examples of a relatively good agreement and a poor agreement are shown in figures 8 and 9, respectively.

We conducted further tests in order to replace the used value of the sheath capacity (9) by a value that was determined in a different way used in [6]. The probe was loaded by various additional capacitors (i.e. the value of  $C_o$  was increased). For each capacitor added, a probe voltage waveform was measured and such a value of the sheath capacity

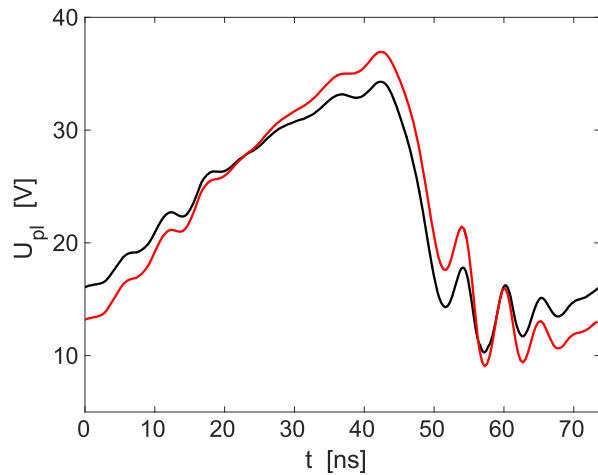


**Figure 8.** Comparison of plasma potential waveforms calculated by the presented model (black) and by the capacitive sheath model (red). Measured in argon at 6 Pa.

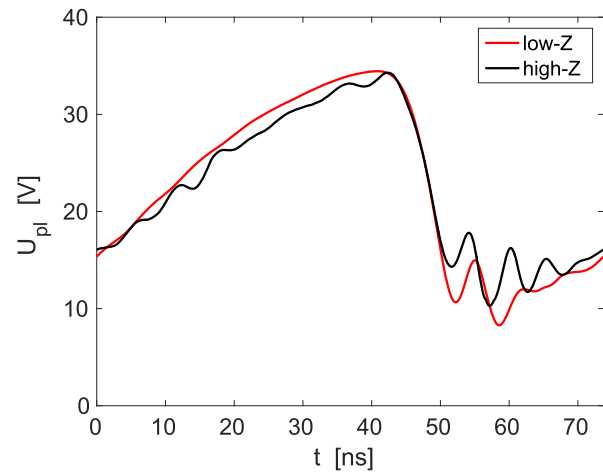


**Figure 10.** Comparison of plasma potential measured by a high- and low-impedance probe in argon at 6 Pa.

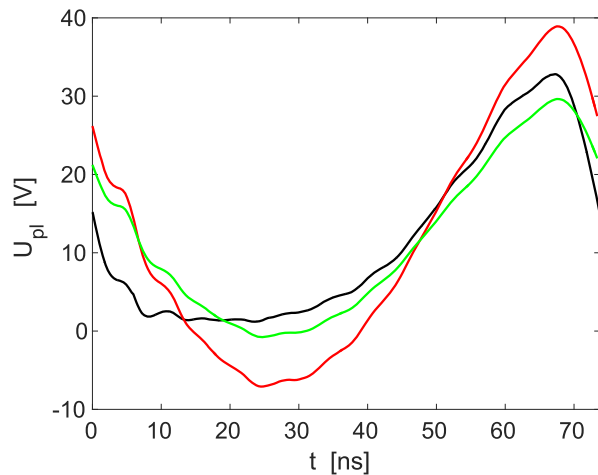


**Figure 9.** Comparison of plasma potential waveforms calculated by the presented model (black), by the capacitive sheath model (red) and by the capacitive sheath model with optimized capacity value (green). Measured in nitrogen at 17 Pa.

was found that minimized differences between the resulting plasma potential waveforms. However, this attempt did not lead to any better agreement with the plasma potential waveforms determined by equations (1)–(5). Finally, a third value of the sheath capacity was tested. In this case, the sheath capacity value was set so that it minimized the resulting difference between the plasma potential waveforms obtained by the capacitive sheath approximation (8) and by the model (1)–(5). An example of the resulting plasma potential waveform is shown by the green line in figure 9.

The described test indicates that the electric behaviour of the sheath around a high-impedance uncompensated probe is, in most cases, close to the behaviour of a capacitor. However, evident violations of this approximation exist, as demonstrated by the difference between the black and the green line in figure 9. Moreover, it can be problematic to determine the

correct value of the sheath capacity, as demonstrated, for example, by the red line in figure 9 that differs significantly from both the green and the black line.

#### 6.2. Comparison with low-impedance probe

Another previous method was based on the model (1)–(5), but a low-impedance uncompensated probe was used instead of the high-impedance probe [8]. In order to test this previous method, measurements with the low-impedance probe were realized simultaneously with the high-impedance probe measurements, and plasma potential waveforms obtained by these two measurements were compared. This comparison was again realized in Ar, N<sub>2</sub>, O<sub>2</sub> and H<sub>2</sub> in the pressure range 2–20 Pa.

The results of the test varied between a reasonable agreement to a serious disagreement. An example of a reasonable agreement is shown in figure 10. This figure manifests the general observation that the low-impedance probe suppresses the higher harmonic frequencies of the plasma potential. Although there was a relatively good agreement between the plasma potential waveforms measured by the high- and the low-impedance probe in a number of experiments, there were experiments with a strong disagreement where the plasma potential amplitude measured by the low-impedance probe was almost twice as high as the amplitude measured by the more reliable high-impedance probe.

### 7. Examples of measured waveforms

The waveforms of plasma potential that were measured by the presented method agreed well with the theoretical models presented in [4, 5, 11, 12]. The plasma potential of the capacitive discharge contained a number of higher harmonic frequencies. Two effects responsible for the generation of higher harmonics are visible in examples of plasma potential waveforms shown in figures 11 and 12 and in figures 4 and 5,

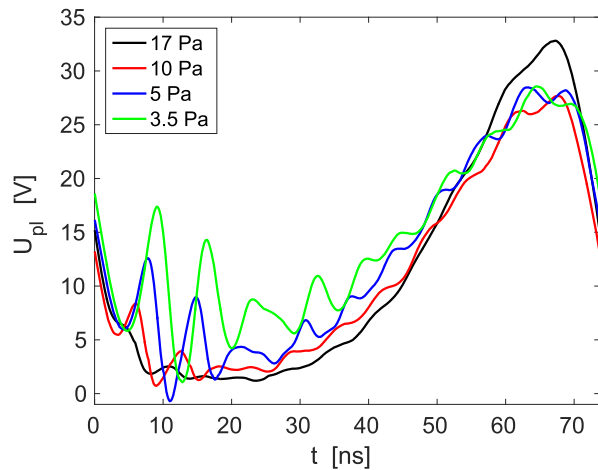


**Figure 11.** Plasma potential waveforms measured in a nitrogen capacitively coupled discharge at various pressures.

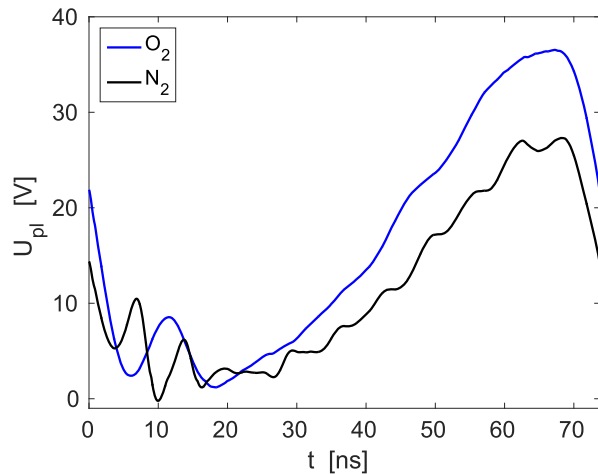


**Figure 12.** Plasma potential waveforms measured in oxygen and nitrogen capacitively coupled discharge at 7 Pa.

as previously shown. Firstly, electric oscillations at the frequency of the series plasma–sheath resonance [13, 14] were ignited, especially at the moment of expansion of the sheath at the powered electrode. Secondly, the base plasma potential waveforms revealed slowly developing minima and sharpened asymmetric maxima as a result of the nonlinear nature of the  $V$ – $A$  characteristics of the sheaths. Figure 11 demonstrates that the self-excited high-frequency oscillations were intensive, especially at low pressure when its damping by electron–neutral collisions was weak. Further, these oscillations were stronger in discharges with a higher concentration of electrons. This observation is demonstrated in figure 12, which compares plasma potential waveforms measured in a nitrogen discharge with electron concentration  $5 \cdot 10^{14} \text{ m}^{-3}$  and in an electronegative oxygen discharge with electron concentration  $3 \cdot 10^{15} \text{ m}^{-3}$ . A specific higher harmonic frequency was further amplified when its frequency was close to the frequency of the series plasma–sheath resonance, which also depends on the electron concentration. The fact that the

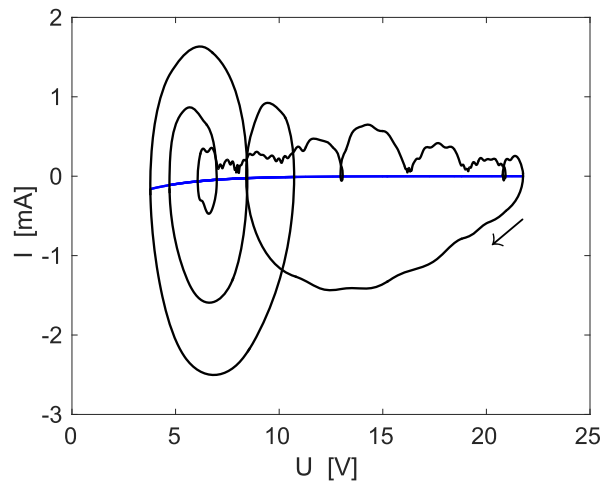


**Figure 13.** Dependence of the total probe current (black) on the sheath voltage for the high-impedance probe biased to 10 V in a capacitively coupled discharge ignited in argon at 6 Pa. The blue curve shows the electron component of the probe current.

amplitude of higher harmonic frequencies depends on electron concentration is important for an explanation of some monitoring techniques that are used in deposition or etching processes. Higher harmonics are used for end-point detection of etching processes [15–17] and for detection of mode transition in reactive magnetron sputtering [17, 18]. Both these monitoring techniques rely on the sensitive reaction of higher harmonic frequencies on electron concentration, whether its behaviour is controlled by surface processes or volume ionization [17, 19].

Figure 13 shows the relation of voltage on the sheath around the high-impedance probe and current flowing through the sheath to the probe. Besides the total probe current, the electron current component is shown in the figure in order to demonstrate that the displacement current is usually the dominant component of electric current flowing to the probe. The ion current is not shown in the figure since it has a constant value that is much lower than the magnitude of the total current. The oscillation of plasma current that was self-excited during the sheath expansion at the powered electrode is the dominant feature of figure 13—these oscillations are responsible for the formation of the spiral part of the curve in the left part of the figure. The oscillation damping caused by the collisions of electrons leads to a decrease of the spiral radius and to the oscillation vanishing after a few rounds of the spiral. Second, a much weaker excitation of plasma oscillations is than visible during the expansion of the sheath at the grounded electrode, i.e. during the increase of the sheath voltage  $U$  in figure 13.

## 8. Conclusion

Measurement by a high-impedance probe (with no RF compensation) was evaluated by means of a simple model of the sheath around the probe in order to acquire reliable

waveforms of the plasma potential. In particular, the temporal development of plasma potential during an RF period of a low-pressure capacitively coupled discharge was measured in this work. This method of plasma potential measurement was tested by means of DC probe biasing, which ensured significant changes of the thickness of the sheath around the probe. Despite the strong variation of the sheath thickness, the resulting plasma potential waveforms were practically identical within several percent of their peak-to-peak voltage, which indicates a good reliability of the presented method. The reliability of the presented method is restricted to measurements when the probe is not biased to high positive voltage values, since the model used is not suitable for situations when the probe potential is higher than the instantaneous plasma potential. For this reason, a generalized sheath model will probably be required when such a probe with no RF compensation will be used for the measurement of electron concentration and temperature. Besides the  $U > 0$  requirement (i.e. the sheath around the probe should not collapse), the described method assumes that the ion current is constant, i.e. that the frequency of the supplied discharge voltage is higher than the ion plasma frequency. Further, equation (5) was derived for low pressure when the mean free path of electrons is higher than the sheath radius. If these conditions are not fulfilled and the electron/ion current is not negligible, equations (4) and (5) should be generalized. Fortunately, the ion and electron current usually create only a small part of the probe current and, therefore, the presented method is not very sensitive to the validity of the last two conditions.

The basic version of the measurement requires knowledge of the mean (DC) value of the plasma potential, electron concentration and electron temperature. However, it was observed that the method is not very sensitive to the values of electron temperature and concentration, and that the uncompensated probe enables an estimation of the mean value of plasma potential. Consequently, for approximate measurements of plasma potential waveforms, the presented method can be used even without knowledge of any of these three input parameters.

The presented method was compared with previous methods of plasma potential waveform measurements that differ from the presented method either by an approximation of the sheath around the probe by a capacitor or by use of a low-impedance probe. The basic shape of plasma potential waveforms measured by means of the previous methods was usually similar to waveforms measured by the presented method. On the other hand, in some experiments a significant

disagreement was found and, therefore, the presented method is recommended for measurements of plasma potential waveforms instead of previous methods.

Finally, the described method was used for plasma potential waveform measurements in a low-pressure capacitively coupled discharge. In agreement with theoretical models, the plasma potential contains a number of higher harmonic frequencies that reached high amplitudes, especially at low pressure, at high electron concentration and when their frequency was close to the frequency of the plasma–sheath resonance.

## Acknowledgments

This research was supported by the project LO1411 (NPU I) funded by the Ministry of Education Youth and Sports of the Czech Republic.

## References

- [1] Hopkins M B 1995 *J. Res. Natl Inst. Stand. Technol.* **100** 415
- [2] Braithwaite N S J, Benjamin N M P and Allen J E 1987 *J. Phys. E: Sci. Instrum.* **20** 1046
- [3] Lieberman M A 1988 *IEEE Trans. Plasma Sci.* **16** 638
- [4] Czarnetzki U, Mussenbrock T and Brinkmann R P 2006 *Phys. Plasmas* **13** 123503
- [5] Dvořák P 2013 *Plasma Sources Sci. Technol.* **22** 045016
- [6] Sobolewski M 1995 *IEEE Trans. Plasma Sci.* **23** 1006
- [7] Yatsuzuka M, Morishita K, Satoh K and Nobuhara S 1985 *Japan. J. Appl. Phys.* **24** 1724
- [8] Dvořák P 2010 *Plasma Sources Sci. Technol.* **19** 025014
- [9] Schulze J, Donkó Z, Luggenhölscher D and Czarnetzki U 2009 *Plasma Sources Sci. Technol.* **18** 034011
- [10] Donkó Z 2011 *Plasma Sources Sci. Technol.* **20** 024011 s 5
- [11] Mussenbrock T and Brinkmann R P 2006 *Appl. Phys. Lett.* **88** 151503
- [12] Klick M 1996 *J. Appl. Phys.* **79** 3445
- [13] Ku V P T, Annaratone B M and Allen J E 1998 *J. Appl. Phys.* **88** 6536
- [14] Yamazawa Y, Nakaya M, Iwata M and Shimizu A 2007 *Japan. J. Appl. Phys.* **46** 7453
- [15] Law V J, Kenyon A J, Thornhill N F, Srigengan V and Batty I 2000 *Vacuum* **57** 351
- [16] Lisovskiy V, Booth J P, Landry K, Douai D, Cassagne V and Yegorenkov V 2008 *Vacuum* **82** 321
- [17] Dvořák P, Vašina P, Buršíková V and Žemlička R 2010 *Plasma Phys. Control. Fusion* **52** 124011
- [18] Dvořák P and Vašina P 2010 *Plasma Sources Sci. Technol.* **19** 055016
- [19] Sobolewski M 2011 *Appl. Phys. Lett.* **99** 201502

# Monitoring of magnetron target poisoning by measurement of higher harmonics of discharge voltages

P Dvořák and P Vašina

Department of Physical Electronics, Masaryk University, Kotlářská 2, Brno 611 37, Czech Republic

E-mail: [pdvorak@physics.muni.cz](mailto:pdvorak@physics.muni.cz)

Received 5 March 2010, in final form 21 July 2010

Published 20 September 2010

Online at [stacks.iop.org/PSST/19/055016](http://stacks.iop.org/PSST/19/055016)

## Abstract

Reactive magnetron sputtering suffers from processing stability problems and the optimal experimental conditions for thin film deposition usually lie very close to an abrupt transition from the metallic to the compound mode. Therefore, a fast feedback method is needed to automatically control either the flow of the reactive gas, or the discharge power to keep the process at the desired operating point. A promising method for this process of monitoring, based on the measurement of amplitudes of higher harmonic frequencies of discharge voltages, is proposed. The measurement of the amplitudes can be performed either by an uncompensated probe in the plasma or on the cable between the RF generator and the sputtered target. The sensitivity of the proposed method is significantly better than measurement of other electrical quantities conventionally used for process control. Physical reasons for the change in amplitudes of higher harmonic frequencies during the mode transition are found. The paper shows that the observed changes in amplitudes of higher harmonics by the transition are not caused either by the pressure change, or by the changes in the composition of the gas in the reactor volume. It is found that the amplitudes of higher harmonics reflect primarily the state of the magnetron target poisoning. The amplitudes thus belong to a group of process parameters representing the target state, which are considered to be the best for reliable process control.

(Some figures in this article are in colour only in the electronic version)

## 1. Introduction

The magnetron sputtering deposition process is an important industrial technique, which is frequently used for the deposition of thin films [1, 2]. A wide range of compound materials can be deposited adding a reactive gas to the deposition chamber. In addition the reactive magnetron sputtering process enables the deposition of various effective insulating materials. However, problems associated with the sputtering of highly insulating materials are widely reported [3–5]. Adding a reactive gas to the deposition process leads simultaneously to the formation of an insulating layer on the areas away from the racetrack areas of the target and at the grounded parts of the reactor [6]. These areas are continuously charged up and an arcing occurs. The arc formation avoids the stable operation of the deposition process and results in

the formation of defects, inhomogeneities and droplets in the growing film [7, 8]. To avoid this undesirable arcing, it is necessary to repetitively neutralize the surface charge built up on the target using either radio frequency or pulsed magnetron sputtering [9, 10].

Another feature of reactive sputtering controlled by the flow of the reactive gas is its hysteresis behaviour. When the reactive gas flow rate is small, most of the reactive gas is incorporated into the deposited material and the amount of reactive gas in the volume is very low. The process runs in the so-called metallic mode. Conditions in the deposition chamber are given mainly by the simultaneous processes of the formation of compound molecules at the target either by chemisorptions [11–13] or by the implantation of the reactive gas [14], cleaning of the target by out-sputtering of compound molecules, growth of the film from sputtered species and

incorporation of the reactive gas at the growing film. At a given sputtering power, the amount of reactive gas which can be gettered by the growing film and at the target is always limited. When a certain flow of the reactive gas is achieved, a part of the reactive gas cannot be gettered any more and its partial pressure increases. The resulting target poisoning and drop in the gettering rate lead to a further increase in the reactive gas concentration in the volume, higher flux of the reactive gas on the target and more intense target poisoning. This in a manner of positive feedback leads to a fast and radical change of conditions in the deposition chamber that is known as a transition from the metallic to the compound mode. After the transition, the target surface is almost fully covered by the compound and the deposition rate drops. In order to retrieve the reverse transition from the compound to the metallic mode it is necessary to substantially decrease the reactive gas flow.

Since films with the desired stoichiometry are deposited under conditions that are very close to or lie within the transition from the metallic to the compound mode, continuous monitoring of the deposition process is highly desirable. Various markers are used to monitor whether the process runs in the narrow range of the optimal experimental condition or whether it is necessary to intervene. The most common and reliable are the following: cathode voltage, intensity of atomic lines and/or intensity of molecular spectral band [15–19]. Recently, another method suitable for radio frequency sputtering has been introduced [20]. The method is based on the measurement of higher harmonic frequencies of the discharge voltages and was shown to be an extremely sensitive method for monitoring the state of reactive magnetron sputtering.

Higher harmonics of discharge voltage and current are produced in capacitive discharges due to the nonlinearity of sheaths [19, 21]. Since the sheaths are in contact with bulk plasma, higher harmonics are strong in particular when their frequencies are close to the series plasma–sheath resonance [22]. Also, the harmonics are strong when they are not damped by collisions between electrons and neutrals. Both conditions are fulfilled at pressures typically below 10 Pa [23] which is a typical range of pressures used for magnetron sputtering. The text above indicates that the behaviour of higher harmonics depends on pressure, electron concentration and collision frequency [21, 22, 24]. Further, it depends on the sheath voltages [19, 25], position in the reactor and the distance between the electrodes [22]. Since higher harmonics are produced in sheaths, they should depend on other parameters that influence sheaths such as discharge asymmetry or mean free path of positive ions, which influences sheath thickness and electrical characteristics. Since the sheaths are in contact with the electrodes, the presence of higher harmonics depends on the whole RF circuit including the matching unit configuration [25, 26] and impedance of the reactor with the plasma [27]. Moreover, the plasma in the magnetron is magnetized which altogether leads to a complex behaviour of higher harmonic frequencies.

Since the behaviour of higher harmonics sensitively depends on many plasma parameters, higher harmonics are used for monitoring and diagnostics purposes. They are used,

e.g., for the end-point detection of etching processes [27], monitoring of dust growth [28] and for the measurement of electron concentration and collisional frequency [24]. It has been shown recently [20] that the amplitude of higher harmonic frequencies changes pronouncedly by the transition from the metallic to the compound mode of the reactive magnetron sputtering deposition process. In this paper, the previous study is extended; the method is studied for two different reactive gases in a broader range of pressures and at various measurement points and the physical reason for the changes in amplitudes of the higher harmonics by the transition is sought.

## 2. Experimental

A diagram of the experimental device is shown in figure 1. The experiment was performed in the industrial sputtering deposition system Alcatel SCM 650. The cylindrical vacuum chamber, 65 cm in diameter and 35 cm in height, is equipped with a set of four well-balanced magnetron heads, two are located on the top and two at the bottom of the deposition chamber. A rotating substrate holder is placed between them. A titanium target of 20 cm diameter and 99.9% purity is mounted on one of the top magnetron heads. RF power is supplied by Advance Energy Cesar 1.2 kW RF power generator, which generates electric field with a frequency of 13.56 MHz. Prior to the measurement, the chamber is evacuated by a turbo molecular pump backed by a rotary pump. The turbo molecular pump is throttled during the experiment to obtain the desired pumping speed. Argon and the reactive gases (nitrogen and oxygen) are dosed using thermal mass flow regulators. Floating potential waveforms are measured by means of a home-made uncompensated probe made from a 15 cm long metallic wire with a diameter of 0.5 mm that is by a coaxial cable connected to an oscilloscope. The uncompensated probe is positioned in parallel between the target and the substrate at a distance of 2 cm from the target. Waveforms of the cathode and of the probe voltages are recorded by a digital LeCroy Waverunner 6100A 1 GHz oscilloscope with an input impedance of 1 M $\Omega$ . Amplitudes of fundamental and higher harmonics were derived from the measured data by Fourier transformation. The amplitudes of the harmonics are compared with other quantities usually used for process monitoring: the cathode bias is derived directly from the waveform of the cathode voltage, the intensity of Ti lines was measured by a Jobin-Yvon Triax 320 grating spectrometer equipped with a CCD camera and the pressure is registered by a precise MKS 1 Torr baratron. Unless written otherwise, the experimental conditions were the following: RF power 1 kW, Ar supply 20 sccm and partial pressure of argon 1 Pa.

## 3. Results and discussion

The hysteresis nature of reactive magnetron sputtering is demonstrated in figure 2 where the emission of a selected Ti line measured at 365 nm is plotted as a function of the nitrogen and oxygen reactive gas supply. The hysteresis region is clearly defined by the different evolution of the

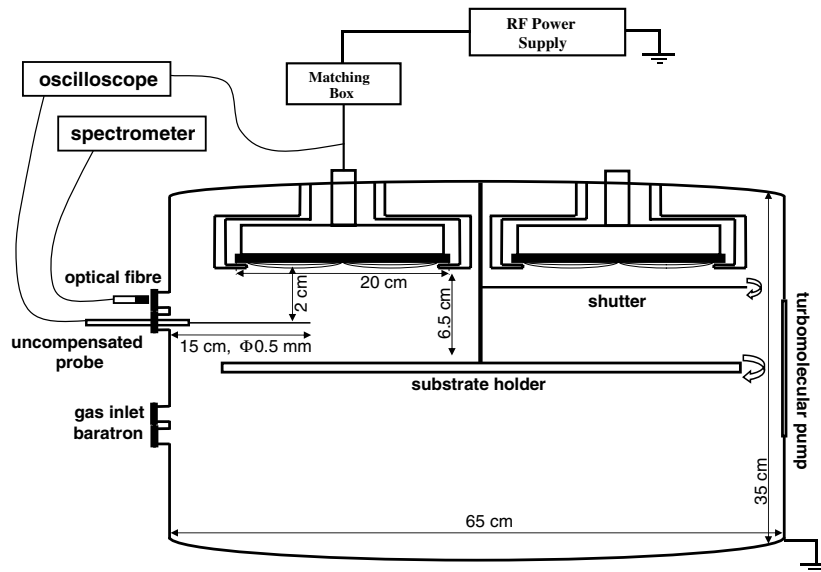


Figure 1. Schematic drawing of the experimental setup.

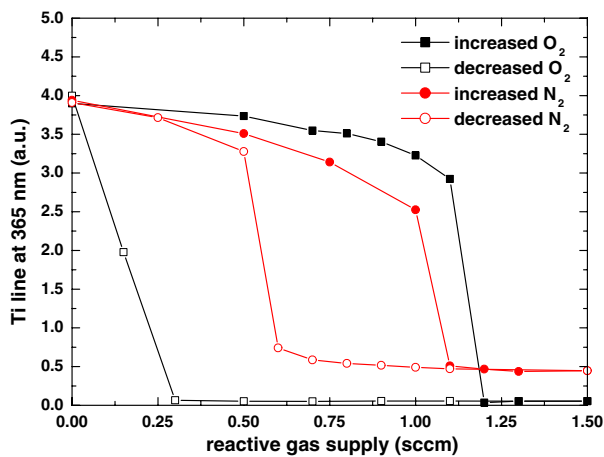


Figure 2. Intensity of Ti line measured at 365 nm as a function of the nitrogen and oxygen reactive gas supply.

curves corresponding increase and decrease in the supply of the reactive gas. On recording the emission corresponding to molecular bands or to atomic lines of nitrogen or oxygen, inverse behaviour is observed. Within the hysteresis loop, there exist, for a certain supply of the reactive gas, two different stable operations of reactive magnetron sputtering. The metallic regime characterized by high intensity of Ti lines, high deposition rate, low reactive gas content in the growing film and in the reactor volume can turn into the compound regime which is characterized by low intensity of Ti lines, low deposition rate and high reactive gas content in the film and in the reactor volume. Films with the right stoichiometry are deposited under conditions that are very close to or lie within the mode transition, i.e. under conditions where the process is extremely sensitive to changes in any of the process parameters mainly to the RF power and the reactive gas supply.

Figure 2 demonstrates that optical emission spectroscopy is a method which provides reliable quantities to control the state of reactive magnetron sputtering and thus, it could be used to control the state of the deposition process. This method, although very powerful, is not however always suitable for controlling a real industrial situation. The real industrial deposition devices are not usually equipped with windows that can be used for the recording of emissions. If a suitable window is available, the film deposition on the window changes its transparency and the method requires either frequent cleaning of the deposits or a measurement performed before each deposition to provide a correction of the measured values to the current transparency of the window.

An alternative parameter that characterizes the state of the reactive sputtering process is cathode voltage. The cathode voltage changes rapidly by the mode transition and as an electrical measurement it does not require any modification of the deposition chamber. Under certain conditions, such as when Si target is sputtered in oxygen, the cathode voltage changes from 700 V for pure Si target to 200 V for a target covered by SiO<sub>2</sub> [3]. However, there is a wide range of sputtered materials where the changes in the cathode voltage are very small or even nonmeasurable. A very good overview of the values of the cathode voltage in metallic and compound modes has recently been provided by Depla *et al* [29]. In the cases where the changes in the cathode voltage are low, another sensitive method enabling the distinction between the regimes of reactive magnetron sputtering is desired, which does not require the presence of windows or other redundant modifications of the deposition chamber.

Recently, a diagnostic method suitable for radio frequency sputtering has been introduced [20], which can be used for the control of the state of the deposition process. The method uses the changes in the nonlinear discharge behaviour that are induced by the transition from the metallic to the compound mode and vice versa. It is based on the measurement

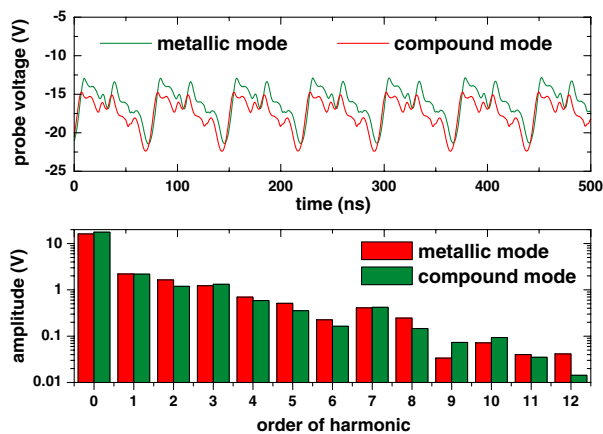


**Figure 3.** Typical voltage waveforms recorded by the uncompensated probe both in the metallic and compound (1.5 sccm  $O_2$ ) modes and the spectral distribution of the higher harmonics in the measured signal.

of amplitudes of higher harmonic frequencies of discharge voltages. These higher harmonics can be measured by means of an uncompensated probe immersed in the plasma [30, 31], or by a grounded electrode [30] or a segment of the reactor wall that collects a part of the discharge current [24]. Another possibility is to perform measurements of voltage or current on the line between the power generator and the powered electrode [27]. In this study, the probe was introduced into the chamber via a standard flange. Alternatively, the sensor for the detection of higher harmonics can be integrated directly into the wall of the deposition chamber. Small diameter of the probe excludes any significant perturbation of plasma [32]. Since sputtering of a floating probe is negligible and eventual insulating films growing on its surface have only small effects on the signal with high frequency, we have not observed any change in probe performance during our experiments. However, all these eventual effects can be excluded by measurements on the electric line to the powered electrode, as described below. Typical voltage waveforms recorded by the uncompensated probe both in the metallic and compound modes (1.5 sccm of  $O_2$ ) are plotted in figure 3. The nonlinear nature of the discharge leads to a rather complicated waveform of the measured signal. The originally sinusoidal signal coming from the generator is transformed by plasma sheaths to a multi-frequency signal with a rich proportion of higher harmonics. In addition, the spectral distribution of the higher harmonics in the measured signal is plotted in figure 3.

The proposed method of monitoring the state of magnetron sputtering is based on the fact that waveforms of the measured voltage differ in the metallic and compound modes. However, these changes in the visual appearance of the waveforms should be represented by a sensitive and reproducible parameter that would be easy to measure. Rich amount of higher harmonics in the waveforms prompts the use of their amplitudes as the desired monitoring parameter. The relation between the voltage waveform measured by the probe and the discharge current or the plasma potential waveform is generally quite complex since the oscilloscope input impedance is not matched

with the probe impedance and the probe is surrounded by a thin nonlinear sheath [31]. However, for monitoring purposes it is not necessary to perform the complete analysis of the measured data. Simple monitoring of the amplitudes of the measured higher harmonic frequencies is entirely sufficient.

The signal from the probe was recorded as a function of the reactive gas supply for both branches of the hysteresis curve. Since the amplitude of harmonics decreases with their frequency (except several exceptions), the evolution of only the first 15 harmonics was studied. Almost all of the studied harmonics measured by the probe show hysteresis behaviour. The amplitude of some harmonics was increased by the transition from the metallic to the compound regime; the amplitude of others was decreased. In figures 4 and 5 the evolution of amplitudes of selected higher harmonics measured by the uncompensated probe is plotted as a function of the nitrogen or oxygen reactive gas supply. Data are plotted for both branches of the hysteresis curve. All plotted dependences clearly show the hysteresis region. The changes in amplitude of all studied harmonics observed by the mode transition do not depend significantly on the type of the reactive gas but do strongly depend on the order of the harmonic. Some of the harmonics change only by several per cent during the transition from the metallic to the compound mode, some by several tens of per cent, or even more. In this study, the amplitude of the ninth harmonic changed by about 130% when the abundance of the oxygen supply caused transition from the metallic to the compound mode. It is almost impossible to predict, for certain experimental configuration, which harmonic is the most sensitive without performing the real experiment. In practice, it should first be determined which harmonic is sensitive enough for the actual experimental geometry. Subsequently, this harmonic can be filtered out from the measured signal, rectified and used to drive a standard feedback system.

The harmonics can be measured not only in the plasma, but also on the coaxial cable between the RF generator and the sputtered electrode. In this position, the amplitudes of higher harmonics are usually relatively small when compared with the fundamental harmonic [19]. However, the difference in values corresponding to the metallic and compound modes is still sufficiently high to provide reliable control of the reactive magnetron sputtering deposition process, as shown in figure 6. The measurements at the coaxial cable are less sensitive than the measurements made by the probe. In this study, the amplitudes of harmonics changed maximally by 20% by the mode transition. On the other hand, the lower sensitivity of measurement on the cable is compensated by a practical advantage: it is not necessary to introduce any probe into the plasma chamber.

In this study the electrical quantity most sensitive to the state of the process is the amplitude of a selected higher harmonic measured by the probe in the plasma. It is followed by the amplitude of a selected higher harmonic measured on the coaxial cable between the RF generator and the sputtered electrode. The less reliable electrical quantity is the cathode self-bias voltage. Similar succession can be expected also for other combinations of sputtered materials and reactive gases. There are only a few cases where the cathode self-bias changed sufficiently by the transition [29]. In every

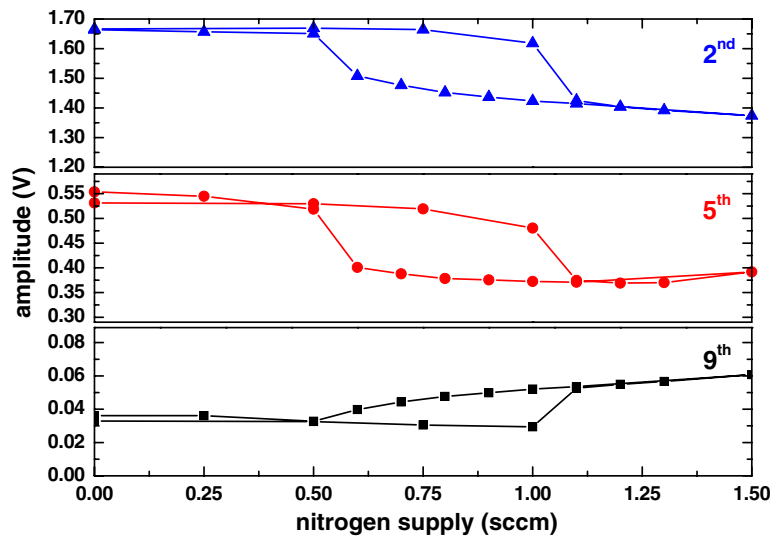


**Figure 4.** Evolution of selected amplitudes of higher harmonics measured by the uncompensated probe as a function of nitrogen reactive gas supply. Typical standard deviation of the measured data is around 1%.

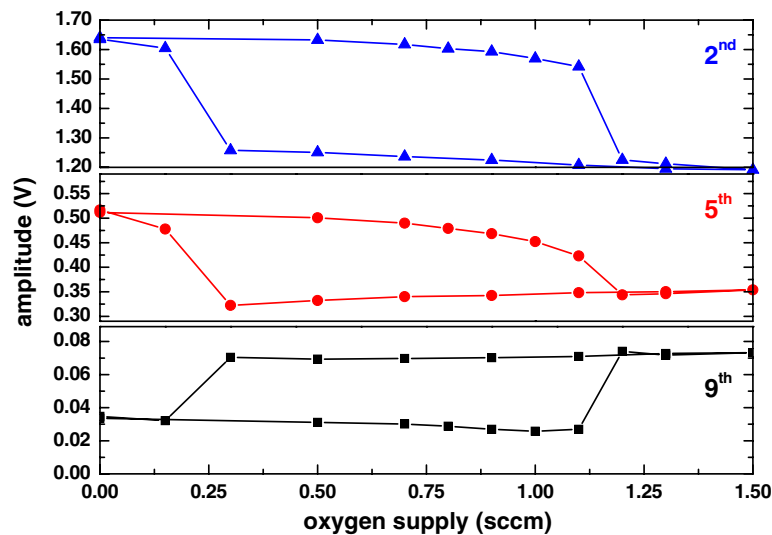


**Figure 5.** Evolution of selected amplitudes of higher harmonics measured by the uncompensated probe as a function of oxygen reactive gas supply. Typical standard deviation of the measured data is around 1%.

other case, the higher harmonics could be the only reliable electrical quantity to control the state of the reactive magnetron sputtering deposition process.

The behaviour of higher harmonic frequencies strongly depends on pressure [23]. Therefore, their response to the transitions between the metallic and the compound mode was studied as a function of pressure. The aim was to test the validity of the proposed method in the whole range of pressure which is typical for reactive magnetron sputtering. The amplitudes of higher harmonics measured by the uncompensated probe were measured in two cases: both in pure argon (metallic mode) and in a mixture of argon with 5 sccm of oxygen or nitrogen (compound mode). As an example of the results, the amplitude of the fifth harmonic is

plotted as a function of actual pressure in figure 7. In the metallic mode, the actual pressure corresponds to the pressure of pure argon whereas in the compound mode the actual pressure is increased by the contribution of the reactive gas. Figure 7 demonstrates that the amplitudes of harmonics are changed significantly by the mode transition in the whole range of studied pressure. The same positive result was obtained for harmonics measured on the coaxial cable between the RF generator and the sputtered electrode.

The amplitudes of harmonics evidently depend on the pressure. The mode transition is accompanied by a small change in pressure as the reactive gas ceases to be incorporated into the growing film and remains in the reactor volume. However, the amplitude variation observed by the mode

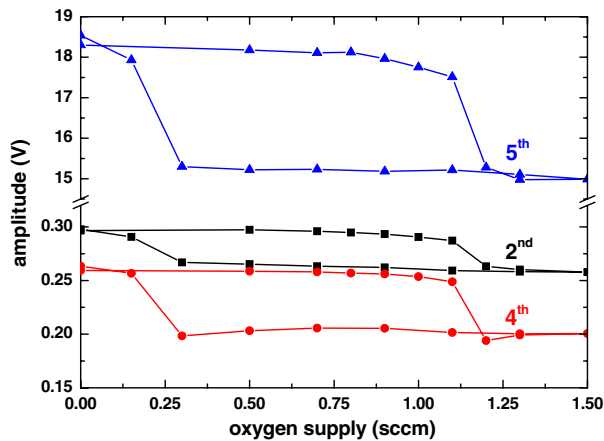


**Figure 6.** Evolution of selected amplitudes of higher harmonics measured on the coaxial cable as a function of oxygen reactive gas supply. Typical standard deviation of the measured data is around 1%.

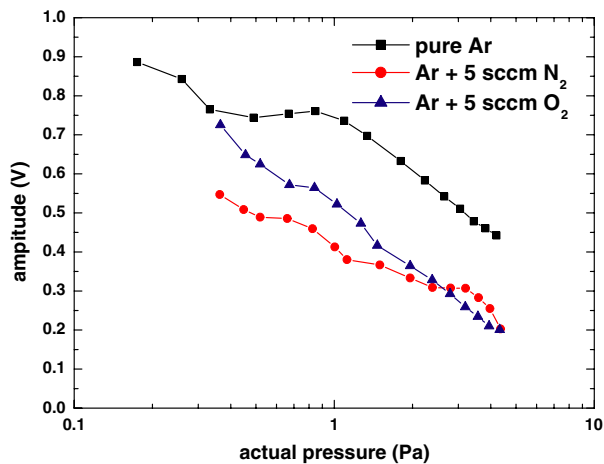


**Figure 7.** Amplitude of the fifth harmonic measured by the uncompensated probe in metallic and compound modes as a function of actual pressure. Typical standard deviation of the measured data is around 1%.

transitions is significantly higher than that corresponding to the pressure change induced by the transition. Thus, it is necessary to examine the influence of other effects on the behaviour of higher harmonics.

The change in higher harmonic amplitudes during the transition from the metallic to the compound mode (and vice versa) could be caused by many physical effects. After excluding the role of the actual pressure on the observed changes by the transition, there remain other effects to investigate. The partial pressure of the reactive gas is increased during the transition leading to changes in gas composition followed by changes in electron density, electron temperature and collision frequency. Moreover, the chemical composition of the surface of the sputtered target changes leading to changes in sputtering yield and Tausend  $\gamma$  coefficient. Thus, the degree of target poisoning may affect the electron concentration and temperature as well.

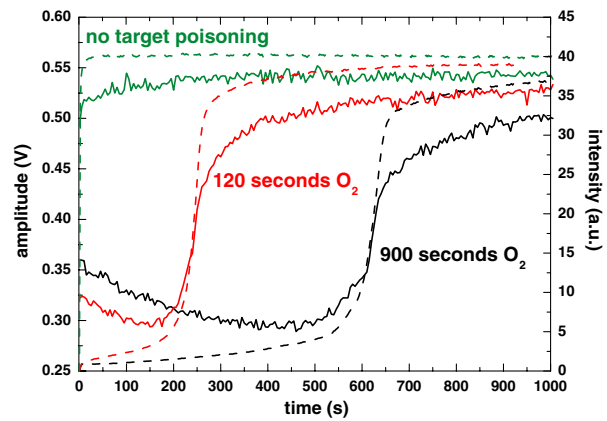


**Figure 8.** Temporal evolution of amplitude of the fifth harmonic measured by the probe (solid line) and intensity of titanium atomic line (dashed) for intentionally fully poisoned target being cleaned in pure argon gas.

In order to distinguish whether the gas or the target composition is responsible for the behaviour of the higher harmonic frequencies by the mode transition the following experiments were performed. First, the target was cleaned by sputtering in argon gas. After that, 10 sccm of oxygen was added to the plasma in order to fully poison the target. The poisoning took either 900 s, 120 s or it was omitted. In the next step, the discharge and the oxygen flow were stopped simultaneously and oxygen gas was fully evacuated from the sputtering chamber. Then, a discharge was ignited in pure argon and temporal behaviour of higher harmonics was studied simultaneously with the evolution of titanium emission line. Sputtering of the oxide layer in pure argon led to target cleaning as it occurs by the transition from the compound to the metallic mode. However, in this case no significant changes in the gas composition took place. The results of these experiments are plotted in figure 8. It was observed that the strongest change in higher harmonic amplitudes occurred simultaneously when the intensity of the titanium line was increased, i.e. at the moment when the oxide layer on the target was being removed. As expected, the cleaning lasted longer for a thicker oxide layer, i.e. for oxide created during a longer time of poisoning. As demonstrated in figure 9, the amplitudes of all studied harmonics changed at the same time.

A comparison of figure 9 with figure 5 shows that the changes in amplitudes of higher harmonic frequencies induced only by the cleaning of the target are almost the same as the changes that occur during the transition from the compound to the metallic mode. The same finding was obtained also for other harmonics. Consequently, the behaviour of higher harmonic frequencies, during transitions between the metallic and the compound mode, is caused only by the changes in target composition and the consequent effects on the discharge and not by the changes related to neutral gas composition. The same finding was obtained when oxygen was replaced by nitrogen. The compound (oxide or nitride) layers have a different coefficient of secondary electron emission from the pure target surface [33]. Consequently, transition to the compound mode leads to a change in electron concentration

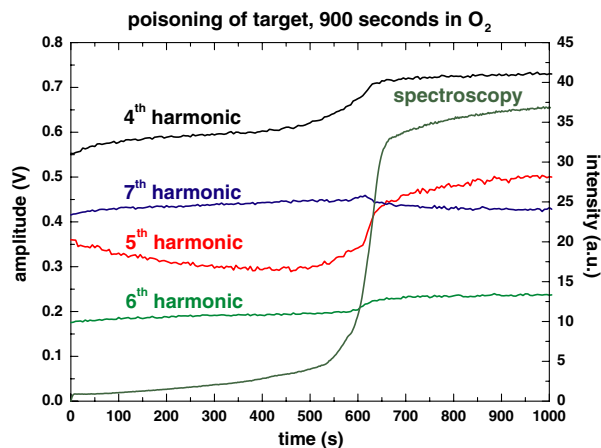


**Figure 9.** Temporal evolution of amplitudes of higher harmonics measured by the probe and intensity of titanium atomic line for intentionally fully poisoned target being cleaned in pure argon gas.

in the plasma accompanied by a shift in the eigenfrequency of plasma oscillations that can explain the change in amplitudes of higher harmonic frequencies. The amplitude of a higher harmonic is usually strong if its frequency is close to the eigenfrequency of the system of plasma, sheaths and reactor [22]. This eigenfrequency is usually several times higher than the fundamental frequency (13.56 MHz) and, therefore, its change should influence the amplitudes of higher harmonic frequencies. The observed results are compatible with the findings of Depla *et al* [29] that small changes, in particular at the target level, have a strong influence on the discharge voltage, because the discharge voltage depends strongly on the ion induced electron emission yield and hence, on the electronic properties of the target. The cited findings were derived for dc sputtering. Similarly, our study concluded that the properties of the target surface and the amplitudes of the higher harmonics of the discharge voltages are strongly correlated.

#### 4. Conclusion

A very sensitive method suitable for monitoring the state of the reactive magnetron sputtering deposition process is proposed. It is based on the measurement of amplitudes of higher harmonic frequencies which are produced due to the nonlinear behaviour of plasma sheaths. The amplitudes of all studied harmonics show hysteresis behaviour caused by transitions between the metallic and the compound mode. The changes in the amplitudes of different harmonics are not identical, the amplitude of some is increased by the transition from the metallic to the compound regime; the amplitude of others is decreased. Typically, the changes in the amplitudes are several tens of percent during the transition from the metallic to the compound mode, the maximal observed change by the transition was 130%. The behaviour of higher harmonics was studied in the whole range of pressures that is usually used for magnetron sputtering. The sputtered material was titanium and two different reactive gases (nitrogen and

oxygen) were used. It was found that the proposed method is useful, sensitive and reproducible in the whole range of studied experimental conditions. Higher harmonics were measured at two different locations: directly in the plasma and at the cable between the power generator and the target. The most sensitive measurements were done by means of a home-made uncompensated probe immersed in the plasma. Harmonics measured on the cable between the RF generator and the sputtered target are less sensitive markers of the mode transition, but their sensitivity is entirely sufficient and better than other electrical quantities conventionally used for process control. The lower sensitivity of measurement is compensated by the fact that there is no need to introduce any probe into the plasma reactor. Physical reasons for the change in amplitudes of higher harmonic frequencies during the mode transition were sought. The influence of pressure and composition of the gas in the reactor volume was excluded. It was found that the properties of the target surface and the amplitudes of the higher harmonics of the discharge voltages are strongly correlated quantities and that the observed changes in the amplitudes by the transition can be fully explained by the changes in the state of the sputtered target.

#### Acknowledgments

This work has been supported by the Czech Ministry of Education, contract MSM0021622411 and by the Czech Science Foundation, contract GA202/08/P038.

#### References

- [1] Rizk A, Youssef S B and Habib S K 1988 *Vacuum* **38** 93
- [2] Vossen J L, Krommenhooes S and Koss A V 1991 *J. Vac. Sci. Technol. A* **9** 600
- [3] Safi I 2000 *Surf. Coat. Technol.* **127** 203
- [4] Tsiogas C D and Avaritsiotis J N 1992 *J. Appl. Phys.* **71** 5173
- [5] McMahon R, Affinito J and Parsons R R 1982 *J. Vac. Sci. Technol.* **20** 376
- [6] Guttler D, Grotzschel R and Moller W 2007 *Appl. Phys. Lett.* **90** 263502
- [7] Rosenberg H M 1984 *The Solid State* (Oxford: Oxford University Press)
- [8] Schiller S, Goedicke K, Reschke J, Kirchhoff V, Schneider S and Milde F 1993 *Surf. Coat. Technol.* **61** 331–7
- [9] Frach P, Heisig U, Gottfried C and Walde H 1993 *Surf. Coat. Technol.* **59** 177–83
- [10] Glocker D A 1993 *J. Vac. Sci. Technol. A* **11** 2989–93
- [11] Berg S, Blom H O, Larsson T and Nender C 1987 *J. Vac. Sci. Technol. A* **5** 202
- [12] Berg S, Larsson T, Blom H O and Nender C 1988 *J. Appl. Phys.* **63** 887
- [13] Berg S and Nyberg T 2005 *Thin Solid Films* **476** 215
- [14] Depla D, Heirwegh S, Mahieu S and De Gryse R 2007 *J. Phys D: Appl. Phys.* **40** 1957
- [15] Schiller H S, Heisig U, Steinfeld K, Strumpf J, Voigt R, Fendler R and Techsner G 1982 *Thin Solid Films* **96** 235
- [16] Touzeau M, Pagnon D and Bretagne J 1999 *Vacuum* **52** 33
- [17] Bretagne J, Boisse Laporte C, Gousset G, Leroy O, Minea T M, Pagnon D, de Poucques L and Touzeau M 2003 *Plasma Sources Sci. Technol.* **12** S33
- [18] Sproul W D, Rudnik P J, Gogol C A and Mueller R A 1989 *Surf. Coat. Technol.* **39–40** 499

- [19] Lieberman M A 1988 *IEEE Trans. Plasma Sci.* **16** 638
- [20] Vašina P and Dvořák P 2009 *Europhys. Lett.* **85** 15002
- [21] Czarnetzki U, Mussenbrock T and Brinkmann R P 2006 *Phys. Plasmas* **13** 123503
- [22] Ku V P T, Annaratone B M and Allen J E 1998 *J. Appl. Phys.* **84** 6536
- [23] Mussenbrock T and Brinkmann R P 2006 *Appl. Phys. Lett.* **88** 151503
- [24] Klick M, Rehak W and Kammeyer M 1997 *Japan. J. Appl. Phys.* **36** 4625
- [25] Dvořák P and Moravec Z 2008 *Chem. Listy* **102** s1356
- [26] Rauf S and Kushner M J 1998 *J. Appl. Phys.* **83** 5087
- [27] Law V J, Kenyon A J, Thornhill N F, Srigengan V and Batty I 2000 *Vacuum* **57** 351
- [28] Boufendi L, Gaudin J, Huet S, Viera G and Dudemaine M 2001 *Appl. Phys. Lett.* **79** 4301
- [29] Depla D, Mahieu S and De Gryse R 2009 *Thin Solid Films* **517** 2825
- [30] Sobolewski M A 1995 *IEEE Trans. Plasma Sci.* **23** 1006
- [31] Dvořák P 2010 *Plasma Sources Sci. Technol.* **19** 025014
- [32] Godyak V A, Piejak R B and Alexandrovich B M 1992 *Plasma Sources Sci. Technol.* **1** 36
- [33] Depla D, Li X Y, Mahieu S and De Gryse R 2008 *J. Phys. D: Appl. Phys.* **41** 202003

## Letter

# Electric field development in $\gamma$ -mode radiofrequency atmospheric pressure glow discharge in helium

Zdeněk Navrátil<sup>1</sup>, Raavo Josepson<sup>1</sup>, Nikola Cvetanović<sup>2</sup>, Bratislav Obradović<sup>3</sup> and Pavel Dvořák<sup>1</sup>

<sup>1</sup> Department of Physical Electronics, Faculty of Science, Masaryk University, Kotlářská 2, 611 37 Brno, Czech Republic

<sup>2</sup> Faculty of Transport and Traffic Engineering, University of Belgrade, Vojvode Stepe 305, 11000 Belgrade, Serbia

<sup>3</sup> Faculty of Physics, University of Belgrade, Studentski trg 12, 11001 Belgrade, Serbia

E-mail: [zdenek@physics.muni.cz](mailto:zdenek@physics.muni.cz) and [raavo.josepson@ttu.ee](mailto:raavo.josepson@ttu.ee)

Received 11 May 2015, revised 27 January 2016

Accepted for publication 4 February 2016

Published 16 March 2016



CrossMark

### Abstract

Time development of electric field strength during radio-frequency sheath formation was measured using Stark polarization spectroscopy in a helium  $\gamma$ -mode radio-frequency (RF, 13.56 MHz) atmospheric pressure glow discharge at high current density ( $3 \text{ A cm}^{-2}$ ). A method of time-correlated single photon counting was applied to record the temporal development of spectral profile of He I 492.2 nm line with a sub-nanosecond temporal resolution. By fitting the measured profile of the line with a combination of pseudo-Voigt profiles for forbidden ( $2^1\text{P}-4^1\text{F}$ ) and allowed ( $2^1\text{P}-4^1\text{D}$ ) helium lines, instantaneous electric fields up to  $32 \text{ kV cm}^{-1}$  were measured in the RF sheath. The measured electric field is in agreement with the spatially averaged value of  $40 \text{ kV cm}^{-1}$  estimated from homogeneous charge density RF sheath model. The observed rectangular waveform of the electric field time development is attributed to increased sheath conductivity by the strong electron avalanches occurring in the  $\gamma$ -mode sheath at high current densities.

Keywords: radiofrequency discharge, atmospheric pressure, electric field, helium

(Some figures may appear in colour only in the online journal)

## 1. Introduction

Radio-frequency atmospheric pressure plasmas have become a useful tool in various plasma processing applications [1]. Using bare metal planar electrodes and a radio-frequency (RF) power source, a non-thermal, so-called radio-frequency atmospheric pressure glow discharge (RF APGD) can be easily obtained in helium, neon and argon [2–5]. When a discharge gap is below several millimetres and the applied RF power is low, the discharge operates in a homogeneous  $\alpha$ -mode. The RF APGD transits into  $\gamma$ -mode at a higher RF

power. Although the discharge is constricted to a smaller electrode area and the neutral gas temperature is increased in the  $\gamma$ -mode, it is an efficient source of charged particles, metastables and reactive species [6, 7].

RF APGD in helium in the planar electrode gap was a subject of numerous studies [4, 8–19]. Since the direct measurement of the electric field in RF APGD is difficult, the electric field was obtained by a numerical modelling or estimated from the measurement of the applied voltage and of the discharge current. The electric field of  $1\text{--}3 \text{ kV cm}^{-1}$  was identified in an  $\alpha$ -mode discharge bulk [4, 18]. The time averaged electric

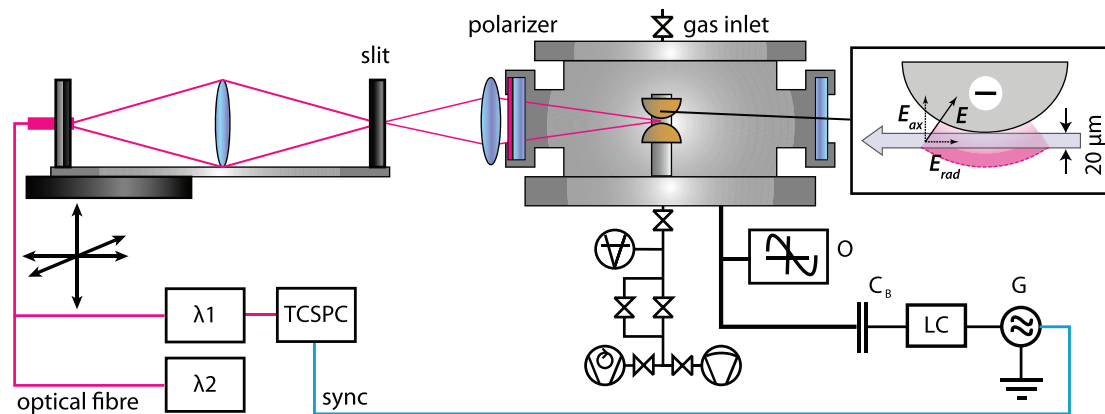


**Figure 1.** Scheme of experimental set-up. G—13.56 MHz generator, O—oscilloscope LeCroy WaveRunner 6100 A,  $\lambda 1$ —monochromator JY HR-640, TCSPC—time correlated single photon counter BH SPC-150,  $\lambda 2$ —Horiba FHR-1000 spectrometer with CCD. The curvatures in the zoomed figure are largely exaggerated.

field, obtained from the modelling, reached  $5 \text{ kV cm}^{-1}$  in  $\alpha$ -mode RF sheath, decreasing linearly from the electrode [6]. The evaluation of the electric field in  $\gamma$ -mode discharge from electrical measurement is even more complicated because of discharge non-uniformity, uncertain electrode coverage and also RF sheath thickness decreasing to about  $100 \mu\text{m}$  and less at high current densities [4, 6]. The time-averaged electric field calculated with a 1D model for a current density of  $106 \text{ mA cm}^{-2}$  reached  $12 \text{ kV cm}^{-1}$  in  $\gamma$ -mode RF sheath, also decreasing linearly from the electrode [6].

Since electron impact excitation occurs inside the sheath of  $\gamma$ -mode discharges [16], the light emission from the  $\gamma$ -mode RF sheath is significant and the electric field in the sheath can be determined from Stark splitting of atomic spectral lines using optical emission spectroscopy. In case of RF electric field (13.56 MHz), the high frequency Stark effect observed in microwave electric fields [21] does not occur and the Stark shift dependence on instantaneous electric field is the same as in the DC field [20]. In this work, we applied a method of Stark polarization spectroscopy of helium 492.2 nm line for the time-resolved measurement of electric field in RF sheath of  $\gamma$ -mode RF APGD. Splitting of hydrogen atomic lines [22] could not be used due to their low intensity in the discharge and their excitation mechanism [23, 24]. Helium 492.2 nm line has already been applied for the electric field measurement in cathode fall of low pressure DC glow discharge and of atmospheric pressure diffuse barrier discharge [25, 26, 28]. Stark broadening of the same line can be used for electron density measurement for values of density higher than  $10^{16} \text{ cm}^{-3}$  [27].

## 2. Experimental setup

The stable  $\gamma$ -mode RF APGD was generated between hemispherical bare metal electrodes inside a steel vacuum chamber (see figure 1). The electrodes were made of brass, 8 mm in diameter and they were cooled by oil-cooling circuit. The chamber was evacuated first down to 5 Pa by a rotary oil pump and then filled with helium (gas purity 5.0) up to atmospheric

pressure. A gas flow of 200 sccm was kept constant during the measurements using a membrane pump. The discharge gap was 2 mm. The harmonic 13.56 MHz signal was generated by a function generator (Agilent 33220A) and amplified with RF power amplifier (Hüttinger TIS 0.5/13560). Electrical parameters were monitored by a digital storage oscilloscope (LeCroy WaveRunner 6100A). The use of hemispherical electrodes decreased the voltage needed for  $\alpha$ - $\gamma$  mode transition. The amplitudes of voltage and current were 240 V and 0.6 A, respectively.

The vacuum chamber was equipped with quartz windows for optical diagnostics. A glass polarizer introduced into the optical path extracted the light polarized in the direction of the interelectrode axis. A spatial resolution of the optical measurements was achieved by projecting the discharge with unit magnification by a quartz lens onto a  $20 \mu\text{m}$  slit, with an optical fibre located beyond it. The slit was located at the position of the maximum intensity of He I 492.2 nm line at the driven electrode. Temporally resolved optical emission spectroscopy was performed by the method of time-correlated single photon counting (TCSPC). The light collected by the optical fibre was first spectrally resolved (Jobin Yvon HR-640, grating  $1200 \text{ gr mm}^{-1}$ , instrumental FWHM 0.075 nm) and then analyzed by a single photon counter (Becker and Hickl SPC-150) with a photomultiplier working in a photon counting mode (PMC-100-4). Arrivals of the individual photons were correlated with the RF signal, taken from the function generator, with a temporal resolution of 0.8 ns. The monochromator scanned slowly over the spectral profile at 492.2 nm with a step of 0.02 nm. Temporally unresolved optical emission spectra were recorded by Horiba FHR-1000 spectrometer (grating  $2400 \text{ gr mm}^{-1}$ , instrumental FWHM 0.005 nm, CCD detector).

## 3. Results and discussions

Temporally unresolved spectral profiles of He I 492.2 nm line measured with the CCD at varied RF power at the driven electrode are displayed in figure 2. The measured profiles consist of uncommonly broad allowed ( $2^1\text{P}-4^1\text{D}$ ) and forbidden

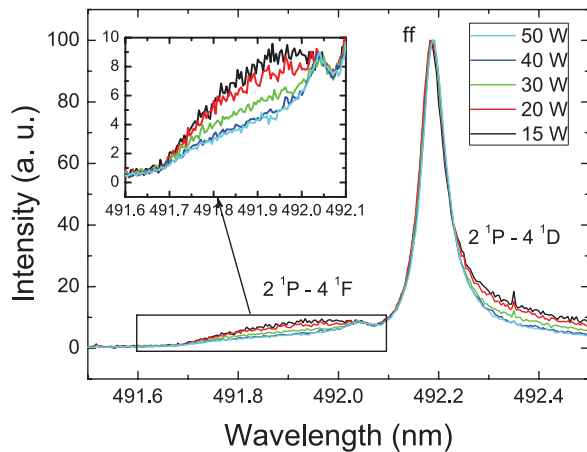


**Figure 2.** Time-unresolved spectral profiles of He I 492.2 nm line in  $\gamma$ -mode discharge measured at the driven electrode for varied RF power. The spectral profiles were normalized according to the maximum. The forbidden component is shown magnified in a smaller plot.

( $2\ ^1P-4\ ^1F$ ) helium line. Time averaging and limited space resolution led to inclusion of components from different sheath regions into the measured profile (see zoomed drawing in figure 1). The field strength distribution in the measured regions is then reflected as the distribution of wavelength shift. Since the forbidden component is emitted only in the high field regions due to the braking of selection rules in the dipole approximation, the result is a broad line. On the other hand, since the allowed line is emitted in all of the sheath regions, the result is a large wing on the red side of the measured profile, instead of a single shifted line. The wing appears as a part of a non-shifted peak of the allowed line at the central wavelength of 492.19 nm, which corresponds to radiation from low field regions (so-called field-free or ff component) [28].

When the RF power is low, a broad peak of the forbidden line is observed shifted at wavelengths 491.7–492.1 nm. The increase of RF power (and current) decreases the sheath thickness [6, 12] and the observed spatial region becomes a region of lower electric field. The broad forbidden line therefore disappears and only a small narrow peak appears instead at 492.04 nm (approximately at zero-field wavelength of the forbidden line). The measured FWHM of the field-free component of 0.06 nm does not vary with increased power, since a negligible impact of Stark broadening is expected under the studied conditions [27]. The most important broadening mechanisms, van der Waals and resonance broadening by helium ground state atoms, broaden the allowed component to FWHM of 0.055 nm, in agreement with the measured value.

The time evolution of spectral profile of He I 492.2 nm line measured with TCSPC at the driven electrode is shown in figure 3(a). Most of the light is emitted within 30 ns during the sheath formation, when the voltage on the driven electrode is the most negative (compare with figure 3(c)). When the voltage on the driven electrode is positive, the light intensity maximum is located at the other (grounded) electrode. The non-zero intensity of ff component ( $\Delta\lambda = 0$  nm) observed in times between the intensity maxima is then mostly due to

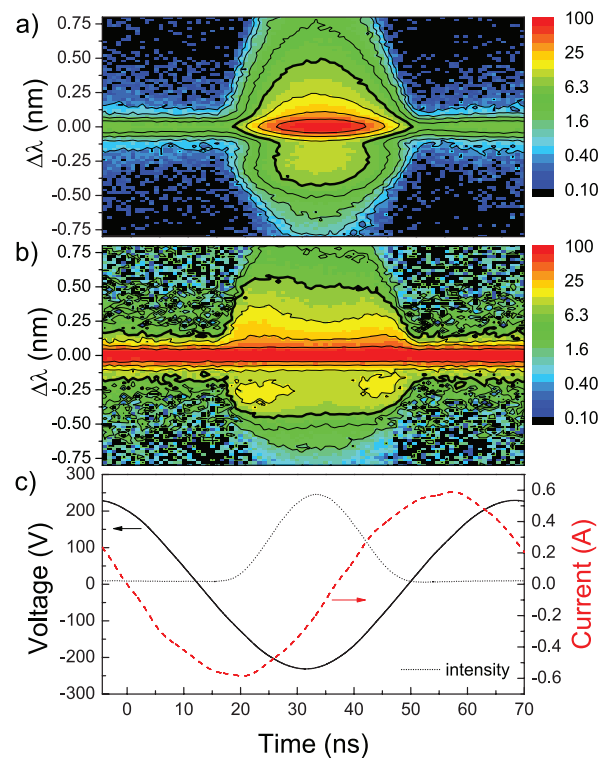


**Figure 3.** Time-resolved spectral profile of He I 492.2 nm line measured with TCSPC during the sheath formation in  $\gamma$ -mode discharge at the driven electrode. (a)—global intensity normalization in the plot, (b)—each spectral profile normalized separately. Thick line denotes an intensity of half maximum of the forbidden component. (c)—time-development of voltage, current and line intensity integrated over the spectral profile. Time 0 ns corresponds to the time of the discharge current inversion.

reflected light originally emitted at the grounded electrode. In the late phase of the emission maximum, the ff component decays exponentially with a decay time of about 3.6 ns, the forbidden and the allowed components decrease even somewhat faster (decay time about 2 ns). The radiative lifetimes of helium  $4\ ^1D$  and  $4\ ^1F$  states are 36 and 67 ns, respectively [29]. However,  $4\ P$ ,  $4\ D$  and  $4\ F$  levels are strongly coupled by excitation transfer induced by collisions with helium ground state atoms [30, 31]. Quenching of  $4\ ^1D$  and  $4\ ^1F$  states by helium atoms [31] results in decay times of 38 and 75 ps, respectively. It may be concluded that the intensity of He I 492.2 nm line always follows the instantaneous discharge development. On the other hand, the time resolution of electric field measurement is not limited by the lifetimes of the excited states, since the delay in photon emission does not influence the photon wavelength dictated by instantaneous Stark shift during the photon emission.

The time evolution of spectral profile of He I 492.2 nm line, but with each spectral profile normalized independently, is shown in figure 3(b). The appearance of the forbidden line during the intensity maximum confirms the existence of a region with a high electric field strength, i.e. of the sheath region. Outside this region the electric field is small and cannot be measured. Two small maxima appear during this forbidden

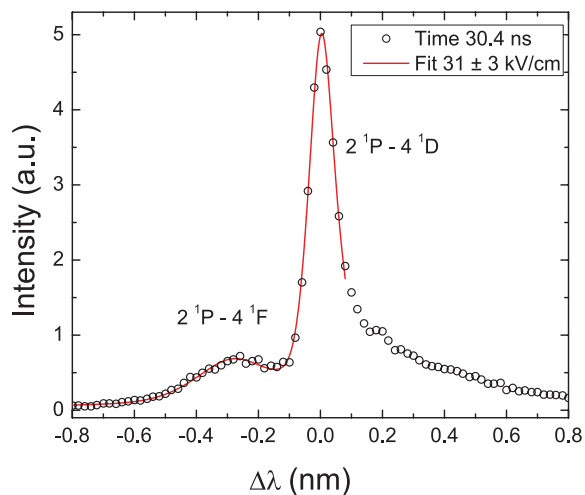


**Figure 4.** Fitted time-resolved He I 492.2 nm spectral profile measured with TCSPC at time 30.4 ns at the driven electrode. Only the forbidden and field-free component were included in the fitting domain.

line development. The line intensity obtained as an integral over the spectral profile is displayed together with the voltage and current waveforms in figure 3(c). The intensity reaches maximum approximately at the time when the electrode is the most negative, as simulated in [16]. A small delay 2.2 ns of the intensity is comparable to the experimental error of signal correlation. The phase shift between the voltage and current is around  $60^\circ$ , but the current is distorted by higher harmonics as predicted in atmospheric pressure RF discharges [32].

An example of time-resolved spectral profiles slotted in figure 3 is shown in figure 4. The time-resolved profiles are broader in contrast to the observations in atmospheric pressure barrier discharges [26]. As explained, this can be due to insufficient spatial resolution and/or presence of non-axial electric field (see zoomed drawing in figure 1). The sheath thickness below  $100 \mu\text{m}$  [6] is comparable with the expected spatial resolution (optical slit width was  $20 \mu\text{m}$ ). The spatial resolution is further reduced due to the use of round electrodes for discharge stabilization, since the curvature of the discharge near the electrodes leads to inclusion of different regions along the optical path into the measured profile.

The measured allowed component was very broad and could not be used for field determination. For this reason a fitting method based on wavelength distance between the forbidden component (emitted only in the high field regions) and the field-free (non-shifted) component was developed. Namely, the fitting function is a superposition of two pseudo-Voigt profiles and the shift of the forbidden component is directly related to the field strength via dependence given in [28]. The intensities of two components and their widths are free fitting parameters while the field strength is directly obtained from the fit. In this case, the shifted allowed line is excluded from the fitting domain (see figure 4).

Whereas the width of the ff component obtained from fitting agrees with value calculated from expected broadening mechanisms and instrumental width ( $\approx 0.1 \text{ nm}$ ), the forbidden

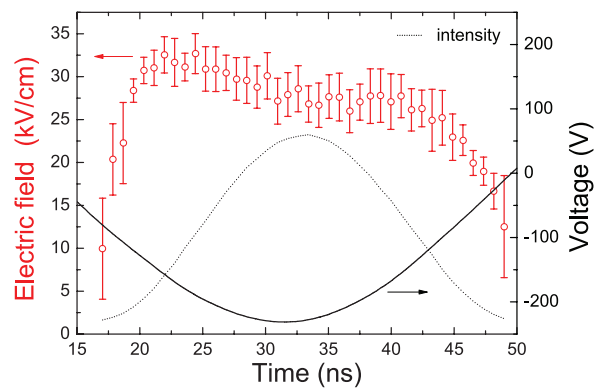


**Figure 5.** Time-development of electric field strength at the driven electrode obtained from the fit of forbidden and field-free component. Solid and the dotted line denote the applied RF voltage development and the development of intensity integrated over the spectral profile, respectively.

component is much wider than expected ( $\approx 0.3 \text{ nm}$ ). Since this suggests, that the forbidden line still contains light emission from regions with various electric fields, the electric field strengths obtained from the fit should be taken only as an average value of the field in the cathode sheath.

The time-development of electric field strength, determined from the fits of the time resolved spectral profiles, together with the development of He I 492.2 nm line intensity and applied RF voltage is shown in figure 5. The electric field time development has almost a rectangular shape reaching  $32 \text{ kV cm}^{-1}$ . The field is slightly higher at the beginning and the end of the sheath formation, which can be seen from the two maxima appearing in the forbidden line time development (see figure 3(b)). As mentioned, large broadening of the forbidden line introduces an uncertainty in the field determination and implies the presence of a wider range of the electric field strengths. Since the field strengths of  $\approx 30 \text{ kV cm}^{-1}$  shown here should be taken as average field values inside the cathode sheath, the maximum field strength at the cathode is expected to be at least twice higher,  $E \gtrsim 60 \text{ kV cm}^{-1}$ . The large width of the forbidden line also did not allow the measurement of the electric field lower than about  $10 \text{ kV cm}^{-1}$ .

A direct comparison of the measured electric field with the results of previous numerical modelling as in [6] is not possible due to a large difference in current density. The time-averaged electric field at the driven electrode, calculated from the presented time-resolved electric field development (figure 5), is  $11.3 \text{ kV cm}^{-1}$ . This value was obtained as the time average of the measured field over the whole voltage period with assumed zero field outside the measured time interval. On the other hand, the electric field of  $6 \text{ kV cm}^{-1}$ , averaged in time and over the sheath, was calculated for the much lower RMS current density of  $106 \text{ mA cm}^{-2}$  [6] compared to the current density  $j_{\text{RMS}} \approx 3 \text{ A cm}^{-2}$  in the presented measurement. These electric field values are at least consistent taking into account the trend of increasing electric field with the increasing current density [6].

The measured development of the electric field can be explained by a simple RF sheath model. The current density  $j$

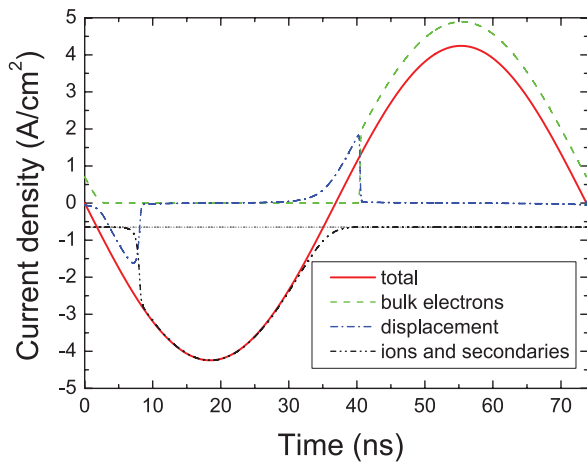


**Figure 6.** Modelled densities of currents flowing from the electrode: total current (red), current of ions and secondary electrons (black), the Bohm flow of ions from bulk plasma is depicted by a grey dotted line, current of electrons from bulk plasma (green), displacement current (blue). Total RMS current density was set  $3 \text{ A cm}^{-2}$  according to the experimental value. Time 0 ns corresponds to the time of the total discharge current inversion.

flowing from the electrode surface can be expressed as a sum of the displacement current density  $\epsilon_0 dE/dt$ , ion current density  $j_i$ , current density of secondary electrons  $\gamma j_i$  and flux of electrons from the bulk plasma. The flux of ions flowing through the plasma-sheath boundary ( $-nv_B$ , where  $v_B = \sqrt{kT_e/m_i}$  is the Bohm velocity,  $T_e$  electron temperature and  $m_i$  ion mass) is in the sheath amplified due to ionization caused by avalanches ignited by secondary electrons. The resulting amplified ion current density at the electrode can be expressed by

$$j_i = \frac{-nev_B}{1 - \gamma \left[ e^{\int_0^s \alpha(x) dx} - 1 \right]}, \quad (1)$$

where  $n$  is the bulk electron density and  $s$  is actual sheath thickness. Townsend ionization coefficient ( $\alpha = Ap e^{-Bp/E}$ ,  $A = 2.1 \text{ m}^{-1} \text{ Pa}^{-1}$ ,  $B = 25.5 \text{ Vm}^{-1} \text{ Pa}^{-1}$ ,  $E$  is the electric field strength), and secondary electron emission coefficient ( $\gamma = 0.01$ ) were taken in the same form as in [12]. Assuming homogeneous ion density in the sheath  $n$  and much shorter ion transport time through the sheath compared to the RF period (which is justified by the small sheath thickness in the  $\gamma$ -mode), the total current density can be written as

$$j(t) = -ne \frac{ds(t)}{dt} - \frac{nev_B(1 + \gamma)}{1 - \gamma \left[ e^{\int_0^{s(t)} \alpha(x,t) dx} - 1 \right]} + \frac{1}{4} ne \sqrt{\frac{8kT_e}{\pi m_e}} e^{-eU_{sh}(t)/(kT_e)}, \quad (2)$$

where  $m_e$  is the electron mass and  $U_{sh} \approx nes^2/(2\epsilon_0)$  is the actual sheath voltage.

The equation (2) was solved numerically for sinusoidal current density  $j$  together with the condition, that sheath voltages at the beginning and at the end of the period must be equal (identical in our case with the condition of zero DC

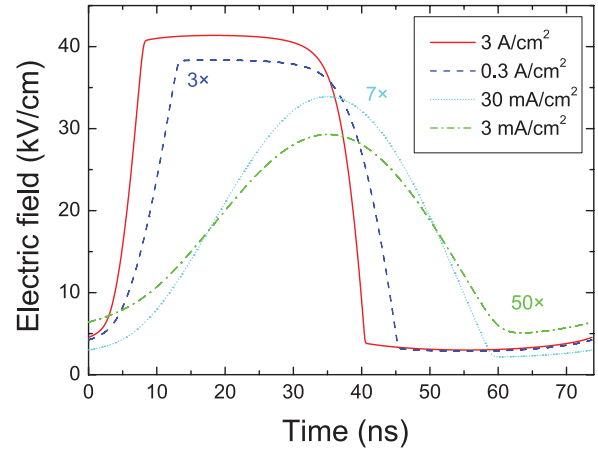


**Figure 7.** Modelled average electric field strengths for constant ratio  $j_{\text{RMS}}/n$  and various total discharge current densities  $j_{\text{RMS}}$ :  $3 \text{ A cm}^{-2}$  (red),  $300 \text{ mA cm}^{-2}$  (blue,  $3 \times$  increased),  $30 \text{ mA cm}^{-2}$  (turquoise,  $7 \times$ ) and  $3 \text{ mA cm}^{-2}$  (green,  $50 \times$ ). The field strength is spatially averaged over the RF sheath, having half the maximum value at the electrode.

current flowing through the sheath). The waveforms of current density components, obtained from the model for the total current density  $j_{\text{RMS}} = 3 \text{ A cm}^{-2}$  taken from the experiment, are shown in figure 6. When the sheath voltage increases sufficiently, the sheath conductivity rises sharply due to the increase of the term  $\gamma \left[ e^{\int_0^s \alpha(x) dx} - 1 \right]$ . As a result, most of the current is taken over by secondary avalanches, whereas the displacement current ( $-ne ds/dt$ ) is stopped, preventing the sheath voltage from further growth. A similar situation occurs in the second half of the period, when the sheath voltage is very small and the sheath conductivity is high due to the electron current, which has to compensate the high ion current from the first half of the RF period.

Several examples of the modelled electric field strength for different current densities, obtained by solution of equation (2) and then spatially averaged over the sheath, are shown in figure 7. The development of the electric field strength for the conditions closest to the presented experiment is depicted by the curve calculated for the highest discharge current density  $j_{\text{RMS}} = 3 \text{ A cm}^{-2}$ ; the used bulk electron density  $n = 10^{13} \text{ cm}^{-3}$  [6] is only a rough estimate. As concluded from figure 6, strong electron avalanches initiated by  $\gamma$  processes in high current  $\gamma$ -mode RF sheath can cause a strong increase of sheath conductivity in most of the discharge period. Consequently, the growth of the sheath thickness is stopped and the sinusoidal waveform of electric field strength is replaced with the rectangular one (see figure 7). The maximum electric field strength of  $80 \text{ kV cm}^{-1}$  at the electrode (twice the average value in homogeneous charge density model) corresponds well to the maximal Stark shift of the forbidden component observed in figures 2 and 3. The calculated maximum sheath thickness of  $45 \mu\text{m}$  obtained for the presented discharge conditions is in agreement with the small sheath thickness expected in the  $\gamma$ -mode discharge [6, 19].

#### 4. Conclusion

In conclusion, time development of electric field strength during radio-frequency sheath formation was measured using Stark polarization spectroscopy in helium  $\gamma$ -mode radio-frequency atmospheric pressure glow discharge. Instantaneous, but spatially averaged electric fields up to  $32\text{ kV cm}^{-1}$  were measured in the  $\gamma$ -mode RF cathode sheath, roughly in agreement with the result of the RF sheath modelling (space averaged  $40\text{ kV cm}^{-1}$ ). The observed rectangular waveform of the electric field was attributed to the strong increase of the sheath conductivity due to electron avalanches initiated by the  $\gamma$  processes at high current densities. Improved spatial resolution of the measurement may reveal a higher maximal electric field strength at the electrode, as expected from the RF sheath modelling.

#### Acknowledgments

The present work was supported by grant GA13-24635S of Czech Science Foundation, project CZ.1.05/2.1.00/03.0086 funded by European Regional Development Fund, project CZ.1.07/2.3.00/30.0009 co-financed from European Social Fund and the state budget of the Czech Republic and project LO1411 (NPU I) funded by Ministry of Education, Youth and Sports of the Czech Republic. The authors also want to express their gratitude to Prof M S Dimitrijević for helpful discussion on Stark effect in high frequency electric field.

#### References

- [1] Laroussi M and Akan T 2007 *Plasma Process. Polym.* **4** 777
- [2] Park J, Henins I, Herrmann H W, Selwyn G S and Hicks R F 2001 *J. Appl. Phys.* **89** 20
- [3] Navrátil Z, Dosoudilová L, Josepson R, Dvořák P and Trunec D 2014 *Plasma Sources Sci. Technol.* **23** 042001
- [4] Laimer J and Störi H 2006 *Plasma Process. Polym.* **3** 573
- [5] Li S-Z, Wu Q, Wang D and Uhm H S 2011 *Phys. Lett. A* **375** 598
- [6] Shi J and Kong M G 2005 *IEEE Trans. Plasma Sci.* **33** 624
- [7] Schröder D, Burhenn S, Kirchheim D and Schulz-von der Gathen V 2013 *J. Phys. D: Appl. Phys.* **46** 464003
- [8] Park J, Henins I, Herrmann H W and Selwyn G S 2001 *J. Appl. Phys.* **89** 15
- [9] Yuan X and Raja L L 2003 *IEEE Trans. Plasma Sci.* **31** 495
- [10] Yang X, Moravej M, Nowling G R, Babayan S E, Panelon J, Chang J P and Hicks R F 2005 *Plasma Sources Sci. Technol.* **14** 314
- [11] Shi J and Kong M G 2005 *J. Appl. Phys.* **97** 023306
- [12] Moon S Y, Rhee J K, Kim D B and Choe W 2006 *Phys. Plasmas* **13** 033502
- [13] Shi J J and Kong M G 2007 *Appl. Phys. Lett.* **90** 111502
- [14] Iza F, Lee J K and Kong M G 2007 *Phys. Rev. Lett.* **99** 2
- [15] Schulz-von der Gathen V, Buck V, Gans T, Knake N, Niemi K, Reuter S, Schaper L and Winter J 2007 *Contrib. Plasma Phys.* **47** 510
- [16] Liu D W, Iza F and Kong M G 2009 *Appl. Phys. Lett.* **95** 031501
- [17] Niemi K, Waskoenig J, Sadeghi N, Gans T and O'Connell D 2011 *Plasma Sources Sci. Technol.* **20** 055005
- [18] Hemke T, Eremin D, Mussenbrock T, Derzsi A, Donkó Z, Dittmann K, Meichsner J and Schulze J 2013 *Plasma Sources Sci. Technol.* **22** 015012
- [19] Kawamura E, Lieberman M A, Lichtenberg A J, Chabert P and Lazzaroni C 2014 *Plasma Sources Sci. Technol.* **23** 035014
- [20] Sobelman I I 1996 *Atomic Spectra and Radiative Transitions* (New York: Springer)
- [21] Hicks W W, Hess R A and Cooper W S 1972 *Phys. Rev. A* **5** 490
- [22] Videnović I R, Konjević N and Kuraica M M 1996 *Spectrochim. Acta B* **51** 1707
- [23] Navrátil Z, Brandenburg R, Trunec D, Brablec A, St'ahel P, Wagner H-E and Kopecký Z 2006 *Plasma Sources Sci. Technol.* **15** 8
- [24] Ivković S S, Obradović B M and Kuraica M M 2012 *J. Phys. D: Appl. Phys.* **45** 275204
- [25] Kuraica M M and Konjević N 1997 *Appl. Phys. Lett.* **70** 1521
- [26] Obradović B M, Ivković S S and Kuraica M M 2008 *Appl. Phys. Lett.* **92** 191501
- [27] Lara N, González M Á and Gigosos M A 2012 *Astron. Astrophys.* **542** A75
- [28] Cvetanović N, Martinović M M, Obradović B M and Kuraica M M 2015 *J. Phys. D: Appl. Phys.* **48** 205201
- [29] Khayrallah G A and Smith S J 1978 *Phys. Rev. A* **18** 559
- [30] Shaw M J and Webster M J 1976 *J. Phys. B: At. Mol. Phys.* **9** 2839
- [31] Catherinot A and Dubreuil B 1981 *Phys. Rev. A* **23** 763
- [32] Dvořák P 2013 *Plasma Sources Sci. Technol.* **22** 045016

# Coplanar surface barrier discharge ignited in water vapor—a selective source of OH radicals proved by (TA)LIF measurement

V Procházka<sup>1</sup>, Z Tučková<sup>1,2</sup>, P Dvořák<sup>1</sup> , D Kováčik<sup>1,2</sup>, P Slavíček<sup>1</sup>, A Zahoranová<sup>2</sup> and J Voráč<sup>1</sup>

<sup>1</sup> Department of Physical Electronics, Faculty of Science, Masaryk University, Kotlářská 2, 611 37 Brno, Czechia

<sup>2</sup> Department of Experimental Physics, Faculty of Mathematics, Physics and Informatics, Comenius University in Bratislava, Mlynská dolina, 842 48 Bratislava, Slovakia

E-mail: [v.proch@mail.muni.cz](mailto:v.proch@mail.muni.cz)

Received 31 August 2017, revised 26 October 2017

Accepted for publication 15 November 2017

Published DD MM 2017



## Abstract

Coplanar dielectric barrier discharge (DBD) was ignited in pure water vapor at atmospheric pressure in order to generate highly oxidizing plasma with one specific type of reactive radicals. In order to prevent water condensation the used plasma reactor was heated to 120 °C. The composition of the radical species in the discharge was studied by methods based on laser-induced fluorescence (LIF) and compared with analogous measurements realized in the same coplanar DBD ignited in air. Fast collisional processes and laser-surface interaction were taken into account during LIF data processing. It was found that coplanar DBD ignited in water vapor produces hydroxyl (OH) radicals with concentration in the order of  $10^{20} \text{ m}^{-3}$ , which is  $10\times$  higher than the value measured in discharge in humid air (40% relative humidity at 21 °C). The concentration of atomic hydrogen radicals in the DBD ignited in water vapor was below the detection limit, which proves that the generation of oxidizing plasma with dominance of one specific type of reactive radicals was achieved. The temporal evolution, spatial distribution, power dependence and rotational temperature of the OH radicals was determined in the DBD ignited in both water vapor and air.

Keywords: laser-induced fluorescence, TALIF, hydroxyl, OH, dielectric barrier discharge, DBD, water vapor

## 1. Introduction

Nowadays, the potential application of atmospheric-pressure plasma generated by various dielectric barrier discharges (DBDs) producing highly reactive species for the surface treatment of different materials is widely investigated. The macroscopically homogeneous nonequilibrium plasma of the coplanar DBD, variability of the used working gases and the high-speed of surface processing are the main advantages in the field of surface treatment [1–3]. The disadvantage of using gaseous mixtures such as ambient air as the working atmosphere is the formation of various types of functional groups on the plasma-treated surface. In order to obtain well-defined surface modifications, treatment with only one specific type of

reactive radicals would be advantageous. The desirable solution could be the surface modification exclusively by the hydroxyl (OH) functional groups generated by the atmospheric-pressure highly oxidizing plasma [4, 5]. Such surfaces with high concentration of OH groups play an important role, e.g. for the immobilization of TiO<sub>2</sub> nanoparticles [6], proteins [7] and other biologically active molecules [8] on chemically inert polymers. For this purpose, we designed and constructed a plasma reactor capable of generating the coplanar DBD in pure water vapor at elevated temperature at atmospheric pressure, since this discharge is expected to produce OH radicals of high concentration. The presented work deals with the diagnostics of reactive species produced in this plasma source.

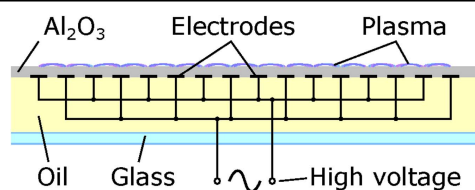


Figure 1. Scheme of coplanar DBD electrode system.

Diagnostics based on laser-induced fluorescence (LIF) [9, 10] is suitable for the detection of reactive radical species in discharges, since it is a sensitive method that enables us to realize spatially and temporally-resolved measurements of absolute concentration of the detected species. The OH radical concentration was measured in various types of atmospheric-pressure discharges, namely in jets [4, 11–14] and in DBD [15, 16]. However, measurement in atmosphere that is rich in water vapor is complicated due to the fast quenching of the excited state, which is further accompanied by vibrational and rotational energy transfer. Moreover, fluorescence measurements in the coplanar DBD are challenging due to the vicinity of the surface of the dielectric plate, since photoemission of the surface charge by laser shot can artificially ignite the discharge event and because fluorescence of the dielectric contributes to the measured signal [17, 18]. The presented work concentrates on LIF measurement of OH radicals in a coplanar DBD ignited in pure water vapor.

## 2. Experimental

### 2.1. Discharge setup

The coplanar DBD is a planar plasma source with a large active plasma area of  $200 \times 80$  mm. Its electrode system consists of 16 pairs of 1.5 mm-wide electrodes with 1 mm gap, see figure 1. The strips were placed on the planar ceramic plate ( $\text{Al}_2\text{O}_3$ –96% purity) with a thickness of 0.6 mm. To heat the ceramics and prevent the undesirable sparking between adjacent electrodes, the insulating oil was in direct contact with the electrode strips.

The atmospheric-pressure plasma in water vapor was generated in the chamber of a unique double-shell heated stainless-steel plasma reactor shown in figure 2. As a source of water vapor, the boiling water in a closed boiling flask was used. Subsequently, this water vapor was introduced into the reactor by a thermally insulated hose. The measurement of LIF spectroscopy in water vapor was carried out after 10–15 min. The indicator of the successful chamber saturation with water vapor was the visual change of the ignited plasma (figure 15), as well as the change in current waveform measured during the whole LIF spectroscopy data acquisition, and the visual control of the gas flow of water vapor through the gas outlet. To prevent the condensation of water vapor on the chamber walls and to heat the atmosphere in the chamber, the components of the plasma reactor were continually heated using five heating elements (Easytherm.sk s.r.o, Slovakia)

with power of 150 W. The atmosphere temperature in the reactor chamber was controlled by a thermoregulator and the temperature of the ceramics was regulated by a separate oil thermostat to more than 120 °C.

During the reactor construction, emphasis was put on the possibility of precisely adjusting the position of four quartz glass windows to allow optical emission spectrometry (OES) and LIF spectroscopic measurements. To prevent the ineligible scattering of laser beam, the two side windows were placed on the ends of the heated stainless-steel tubes at Brewster's angle ( $55.55^\circ$ ). In order to adjust the position of the coplanar DBD electrode system and reduce scattering on the ceramics, the electrode system was placed on an adjustable three-point holder with micrometric screws. All four window enclosures were heated by separate heating elements to prevent the condensation of water vapor.

The coplanar DBD was supplied by an AC high-voltage power source ( $\sim 14$  kHz) VF 700 (LIFETECH, Brno, Czech Republic) and the input power was set in the range 175–350 W, which corresponds to voltages of 16–19 kV (peak-to-peak). To synchronize the high-voltage source with the laser pulses, a variable transformer MA 4804 (from Metrel, Slovenia) and two-channel arbitrary waveform generator RIGOL DB4162 with bandwidth 160 MHz were used.

### 2.2. Diagnostics setup

The scheme of the experiment is shown in the figure 3. A laser system consisting of a 30 Hz Q-switched pumping laser (Quanta-Ray PRO-270-30), a dye laser (Sirah, PRSC-D-24-EG) and a frequency doubling or tripling unit was used to produce short laser pulses (ca 8 ns) with a wavelength around 282 or 205 nm for the excitation of OH radicals or atomic hydrogen radicals, respectively. In case of atomic hydrogen two-photon absorption LIF (TALIF), the laser beam was focused into the central part of the reactor; in the case of OH radical LIF, a rectangular aperture (approx. 2 mm high and 5 mm wide) was used to shape the laser beam only to the area near the dielectric surface. The fluorescence signal was recorded by an intensified CCD camera (PI-MAX 1024RB-25-FG43) with interference filters. The energy of each pulse was detected by a pyroelectric energy sensor (Ophir).

Monochromator FHR-1000 by Jobin-Yvon-Horiba (2400 gr/mm, CCD detector Symphony cooled by a four-stage Peltier cooler, spectral resolution of 0.05 nm, spectral range 200–750 nm) was used for the spectral measurement of spontaneous discharge emission in the range 305–340 nm. The discharge emission in a wider range was detected by an Andor Shamrock 750 spectrometer (1200 gr/mm, CCD detector DU940P-BU2 Andor, spectral resolution 0.04 nm, spectral range 200–1000 nm). The optical fiber was positioned perpendicularly to the plasma layer, so that emission from several microdischarges was acquired. The acquisition time for the recorded spectra was set to 100 s.

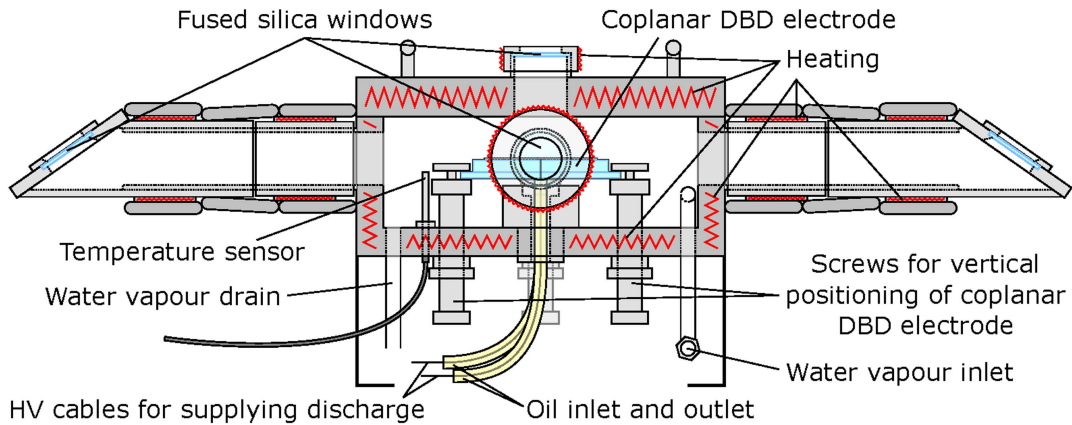


Figure 2. Scheme of the reactor for plasma generation by coplanar DBD in water vapor.

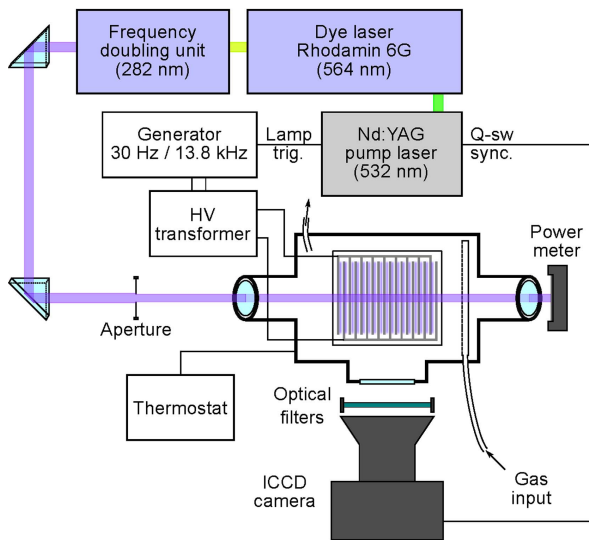


Figure 3. Scheme of LIF setup.

### 3. Diagnostic methods

#### 3.1. OES

Radiation emitted from the discharge during spontaneous transfer between  $A^2\Sigma^+$  and  $X^2\Pi$  was observed using OES. The measured spectrum range 305–334 nm includes four vibrational bands (0–0), (1–1), (2–2) and (3–3) for rotational levels up to 35. Using known line positions and emission coefficients for several transfers from each vibrational and rotational state, it was possible to calculate the relative population of that state even if most of the emission lines overlap. The emission spectra of the coplanar DBD in heated air, hot air with increased concentration of water vapor, and in pure water vapor was measured.

#### 3.2. LIF

**3.2.1. Principle of OH LIF.** In order to spectrally separate the measured fluorescence signal from the scattered laser radiation, the OH radicals were excited from the ground

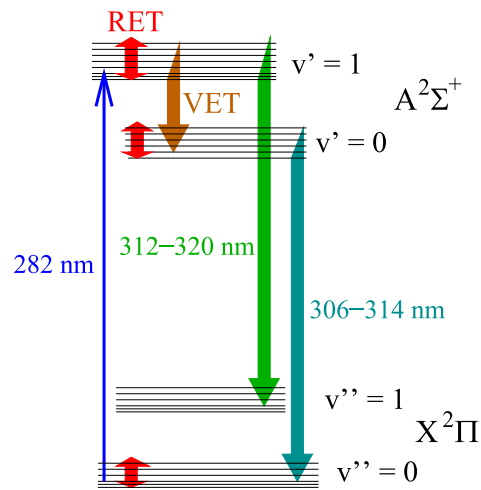


Figure 4. Excitation and fluorescence schema.

vibronic state  $X^2\Pi(v'' = 0)$  to the vibrationally-excited state  $A^2\Sigma^+(v' = 1)$  by laser shots with wavelengths in the range 282–284 nm, see figure 4. Due to the vibrational energy transfer (VET) in the excited state, the vibronic state  $A^2\Sigma^+(v' = 0)$  was also populated due to collisions of excited radicals with neighboring molecules. Consequently, the two vibrational (1–1) and (0–0) bands of fluorescence radiation with approx. wavelength ranges 306–314 and 312–320 nm, respectively, were detected and used for the calculation of OH concentration. The detection of scattered laser radiation was eliminated by means of long-pass and bandpass interference filters.

The intensity of the measured fluorescence signal is given by the sum of the contributions from all rotational lines of the radiation generated by the excited OH radical

$$M_f = \int \int \int \frac{\Omega}{4\pi} \int_0^\infty \left( \sum_{ij} F_{ij}^{(1)} C_{ij}^{(1)} A_{ij}^{(1)} N_i^{(1)} + \sum_{ij} F_{ij}^{(0)} C_{ij}^{(0)} A_{ij}^{(0)} N_i^{(0)} \right) dt dV \quad (1)$$

with the following meaning of the used symbols: lower indexes  $i$  and  $j$  denote particular rotational levels of the excited  $A^2\Sigma^+$  and ground  $X^2\Pi$  electronic states, respectively, upper indexes  $(^1)$  and  $(^0)$  denote the vibronic state  $A^2\Sigma^+(v' = 1)$  and  $A^2\Sigma^+(v' = 0)$ , respectively.  $N_i^{(0)}$  and  $N_i^{(1)}$  are concentrations of OH radicals in a particular rotational level of the  $v' = 0$  and  $v' = 1$  vibronic  $A^2\Sigma^+$  state,  $F_{ij}$  are filter transmittances and  $C_{ij}$  quantum efficiencies of the ICCD camera for the wavelength of the particular  $i \rightarrow j$  rotational line of the relevant vibrational band.  $A_{ij}$  is the radiative transition probability of the particular line and  $\Omega$  is the solid angle at which the fluorescence is collected by the ICCD camera. Only vibrational bands  $1 \rightarrow 1$  and  $0 \rightarrow 0$  are taken into account, since the wavelength of other OH bands lies outside the transmission range of the used filters. The signal is integrated over the whole detection volume and the whole duration of the fluorescence process.

In spite of the fact that only one level is excited by laser excitation directly, tens of rotational levels participate in the fluorescence process due to fast rotational energy transfer (RET) and VET induced by collisions of excited OH radicals with neighboring molecules. In principle, the concentration of all these levels can be calculated by means of a set of ten kinetic equations. However, with the assumption that RET causes fast transition to rotational equilibrium of the particular vibronic  $A^2\Sigma^+$  state, the situation can be simplified and only three effective excited levels can be taken into account: first effective level comprises all rotational levels of the  $A^2\Sigma^+(v' = 0)$  state and we expect that the population of these rotational levels is in equilibrium that is described by rotational temperature  $T$ . The OH distribution to particular rotational sublevels in this effective level will be described by the Boltzmann factor  $f^{(0)}$ . The second effective level is an analogous system of all rotational levels of the  $A^2\Sigma^+(v' = 1)$  state that are in equilibrium, and its concentration and Boltzmann factors will be marked  $N_1$  and  $f^{(1)}$ , respectively. The second effective level also contains the rotational level that is directly excited by laser, but only with concentration described by the Boltzmann factor ( $N_1 f_{\text{excited}}^{(1)}$ ). The third effective level contains all the excess  $A^2\Sigma^+(v' = 1)$  OH radicals that are in the one rotational level that is directly excited by laser and that are over the corresponding equilibrium part of concentration  $N_1$ . Quantities related to this third effective level will be described by the index  $e$ .

The listed assumptions for the linear LIF regime (with no saturation) lead to

$$M_f = N_{X_i} \frac{\kappa B}{c} E_{lf} \tau_e \left[ \sum_j F_{ej} C_{ej} A_{ej} + R\tau_1 \sum_{ij} F_{ij}^{(1)} C_{ij}^{(1)} A_{ij}^{(1)} f_i^{(1)}(T) + V\tau_0 (1 + R\tau_1) F_{ij}^{(0)} C_{ij}^{(0)} A_{ij}^{(0)} f_i^{(0)}(T) \right] \times \int \int_V \int \frac{\Omega}{4\pi} s \, dV, \quad (2)$$

where  $N_{X_i}$  is the concentration of OH radicals in the particular rotational level of the ground vibronic state  $X^2\Pi(v'' = 0)$  from which the excitation occurred.  $B$  is the absorption

coefficient of the particular excitation transition,  $c$  is the speed of light and  $\kappa$  is the overlap term of the absorption and laser line [19],  $E_{lf}$  is the mean energy of laser pulses during the measurement of the fluorescence.  $\tau$  is the life-time of the relevant vibronic state,  $R$  is the RET rate constant of the depopulation of the effective level  $e$  and  $V$  is the  $A^2\Sigma^+(v' = 1) \rightarrow A^2\Sigma^+(v' = 0)$  VET rate constant. When the RET rate is very fast, equation (2) transforms to

$$M_f = N_{X_i} \frac{\kappa B}{c} E_{lf} \tau_1 \left[ \sum_{ij} F_{ij}^{(1)} C_{ij}^{(1)} A_{ij}^{(1)} f_i^{(1)}(T) + V\tau_0 F_{ij}^{(0)} C_{ij}^{(0)} A_{ij}^{(0)} f_i^{(0)}(T) \right] \int \int_V \int \frac{\Omega}{4\pi} s \, dV. \quad (3)$$

In this work, we present the results calculated by equation (2). Approximation used in equation (3) changes the obtained OH concentration value by only 1%–2%, provided that laser excitation to the level with the highest population in a rotational equilibrium is performed. Some aspects of quantities introduced in equation (2) are discussed below.

**3.2.2. Deexcitation rates.** At atmospheric pressure, collisional processes including quenching, VET and RET play a crucial role. Naturally, these processes must be taken into account in the calculation of the life-times and distribution of excited rotational and vibrational levels. The life-times of the vibronic states can be expressed as a reciprocal value of the total depopulation rate constant of the given vibronic states

$$\tau_e = \frac{1}{Q_e + V + A_e + R} \quad (4)$$

$$\tau_1 = \frac{1}{Q_1 + V + A_1} \quad (5)$$

$$\tau_0 = \frac{1}{Q_0 + A_0}, \quad (6)$$

where  $Q$  are the quenching rates and  $A$  are the rates of radiative deexcitation of the relevant states. All the deexcitation rates involved in equations (4)–(6) can be calculated as effective sums of all transitions between particular rotational levels, for example, the total radiation deexcitation of the upper vibronic state can be expressed as an effective sum of all radiative transition rates to rotational levels in all  $X^2\Pi$  vibronic states

$$A_{1,0} = \sum_{ij} A_{ij}^{(1,0)} f_i^{(1,0)}(T) \quad (7)$$

$$A_e = \sum_j A_{ej}^{(1)}. \quad (8)$$

The assumption of rotational equilibrium leads to

$$f_i = \frac{(2J_i + 1) \exp\left(-\frac{E_i}{kT}\right)}{\sum_j (2J_j + 1) \exp\left(-\frac{E_j}{kT}\right)}, \quad (9)$$

where  $E_i$  and  $J_i$  are the energy and quantum number of angular momentum of the  $i$ th rotational level. The sum over  $j$  denotes summation over levels with all rotational quantum

**Table 1.** Used values of OH LIF parameters.

	water vapor	humid air
$T$	460 K	473 K
$A_1$	$8.41 \cdot 10^5 \text{ s}^{-1}$	$8.47 \cdot 10^5 \text{ s}^{-1}$
$A_0$	$1.42 \cdot 10^6 \text{ s}^{-1}$	$1.43 \cdot 10^6 \text{ s}^{-1}$
$Q_1$	$69.3 \cdot 10^{-11} \text{ cm}^3 \text{ s}^{-1}$	$14.1 \cdot 10^{-11} \text{ cm}^3 \text{ s}^{-1}$
$Q_0$	$72 \cdot 10^{-11} \text{ cm}^3 \text{ s}^{-1}$	$5.1 \cdot 10^{-11} \text{ cm}^3 \text{ s}^{-1}$
$V$	$5 \cdot 10^{-11} \text{ cm}^3 \text{ s}^{-1}$	$13,9 \cdot 10^{-11} \text{ cm}^3 \text{ s}^{-1}$
$\tau_1$	$7.30 \cdot 10^{-11} \text{ s}$	$1.94 \cdot 10^{-10} \text{ s}$
$\tau_0$	$7.54 \cdot 10^{-11} \text{ s}$	$1.06 \cdot 10^{-9} \text{ s}$
$\kappa$	$2.47 \cdot 10^{-11} \text{ s}$	$5.36 \cdot 10^{-11} \text{ s}$

numbers and both spin-rotational components [11, 20]. Formally, equation (3) could also be used for a more general description of the LIF signal when Boltzmann factors  $f_i$  are replaced by nonequilibrium concentration factors that take into account the eventual excess of OH radicals in the directly excited level and other nonequilibrium phenomena.

The values of the required rate constants were sought in the literature: values for quenching, VET and RET are described in works [21–31], [24, 27–30] and [30, 32, 33], respectively. The used values and selected parameters of our experimental setup can be found in table 1.

**3.2.3. Spectral profiles.** In order to determine the spectral overlap  $\kappa$ , the spectral shape of the used absorption lines was measured and fitted by the Voigt profile. The measured absorption lines P<sub>1</sub>(1)–P<sub>1</sub>(4) were broader in pure water vapor (FWHM 6.45 pm) than in heated laboratory air of 40% relative humidity (FWHM 3.5 pm). Then, the parameter  $\kappa$  was calculated as

$$\kappa = \int_{\nu} a(\nu) l(\nu) d\nu, \quad (10)$$

where  $a(\nu)$  and  $l(\nu)$  are the spectral profiles of the absorption line and laser line, respectively. These profiles are normalized according to  $\int a d\nu = \int l d\nu = 1$ . The problem of the spectral overlap including its sensitivity to saturation effects was discussed in [19]. In the presented measurements, the energy of the laser pulses was set to a sufficiently low value, so that no saturation was observed.

**3.2.4. Rotational distribution in the ground vibronic state.** In order to determine the rotational temperature of the OH radicals, these radicals were excited successively from different rotational levels and the LIF intensity was measured individually for each particular excitation. Excitation from levels with  $J = 1.5$ – $5.5$  (i.e. levels with rotational quantum number 1–5, spin-orbit component 1, i.e.  $\Omega = 1.5$ ) was used for rotational temperature measurement. At discharge power of 175 W rotational temperature ( $460 \pm 57$ ) K and ( $473 \pm 49$ ) K was measured in water vapor and air, respectively.

The rotational temperature was used to calculate the ratio between the concentration of all OH radicals in the ground vibronic state  $X^2\Pi(v'' = 0)$  and in the one particular

rotational state that was used for excitation during LIF experiments by means of the formula

$$N_X = N_{X_i}/f_{X_i} = N_{X_i} \frac{2 \sum_j (2J_j + 1) \exp\left(-\frac{E_j}{kT}\right)}{(2J_i + 1) \exp\left(-\frac{E_i}{kT}\right)}. \quad (11)$$

The factor 2 is caused by the  $\Lambda$ -doubling [11, 34]. In case of the Q<sub>1</sub>(3) line, the values of the Boltzmann factor  $f_{X_i}$  were 0.0663 and 0.0655 for temperatures 460 and 473 K, respectively.

**3.2.5. Rayleigh calibration.** Since it is difficult to predict the value of the integral  $\int \int_V \int_{\frac{\Omega}{4\pi}} s dV$  that is used in equation (2), its value was calibrated by means of Rayleigh scattering of the laser beam in argon gas at atmospheric pressure. The Rayleigh-scattering signal intensity can be expressed as

$$M_r = \frac{d\sigma_r}{d\Omega} N_r \frac{E_{lr}}{h\nu_r} C_r \int \int_V \int \Omega s dV, \quad (12)$$

where  $d\sigma_r/d\Omega$  is the differential cross-section for Rayleigh scattering,  $N_r$  is the concentration of argon atoms,  $E_{lr}$  is the mean energy of laser pulses during the collection of the scattering signal,  $\nu_r$  is the frequency of laser radiation and  $C_r$  is the quantum efficiency of the ICCD camera for the laser wavelength. The spatial laser beam profile  $s$  is proportional to the area density of laser energy and it is normalized to one when integrated in the plane perpendicular to the laser beam direction, i.e.  $\int_s \int s dS = 1$ . Since the detection of LIF and Rayleigh-scattering signals by ICCD camera enables us to realize spatially-resolved measurements, the volume integral  $\int \int \int \Omega s dV$  that appears in both equations (2) and (12) denotes integration of the fluorescence signal coming from the whole region that is observed by the particular pixel of the ICCD camera. Since all other quantities in equation (12) are known, the Rayleigh-scattering experiment enables us to determine the value of this integral.

**3.2.6. Parasitic signals and temporally-resolved measurements.**

Unfortunately, the signal measured during LIF experiments does not contain only the fluorescence of OH radicals, but it further consists of fluorescence of the dielectric, a part of the scattered laser radiation that was not eliminated by the filters, spontaneous discharge radiation and dark camera signal. Moreover, the artificial discharge ignition occurring when the laser hits the dielectrics causes an excess discharge radiation, which increases the background signal. In order to solve these problems, the laser was synchronized with the discharge and phase-resolved measurements with the laser wavelength tuned to the center of the OH absorption line and the laser wavelength detuned from the line were realized. As discussed in [17], measurements with the detuned laser enable us to determine the parasitic signals (fluorescence of the dielectrics, enhanced discharge emission,

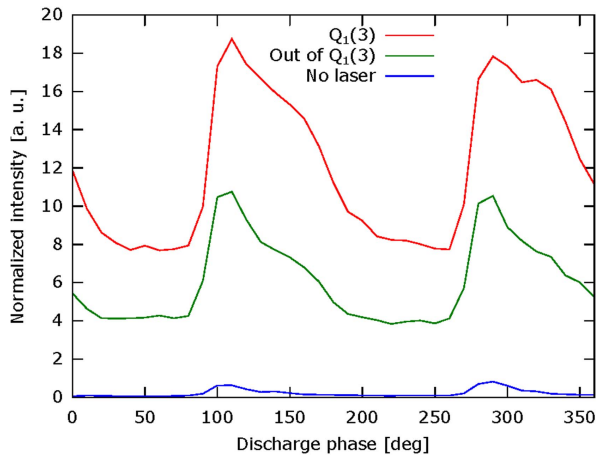


**Figure 5.** Phase-resolved signals measured in a coplanar DBD ignited in water vapor with laser wavelength tuned to the center of the absorption line  $Q_1(3)$ , laser wavelength detuned from the absorption line and with no laser. Measured at delivered discharge power of 175 W.

scattered laser) and to subtract them by means of the formula

$$M_f = M_t - D - (M_d - D) \frac{E_{lf}}{E_{ld}}, \quad (13)$$

where  $M_t$  and  $M_d$  are the signals measured with tuned and detuned laser wavelength, respectively,  $D$  is the signal measured with no laser and  $E_{ld}$  is the energy of laser pulses during the measurements with detuned laser wavelength. The combination of equations (2), (11), (12) and (13) enables us to get the maps of OH concentration.

Temporally-resolved signals measured with laser wavelength tuned to the center of the  $Q_1(3)$  line, with detuned laser wavelength and with no laser are shown in figure 5. The baseline of the green line measured with the detuned laser can be attributed to the scattered laser and fluorescence of the dielectric, while the increase of the green line in discharge phases with high electric field was caused mainly by laser-caused enhancement of discharges. Spontaneous discharge emission was significantly smaller (blue line in the figure 5). All three measurements were realized with the same set of filters in front of the ICCD camera. The signal  $M_f$  obtained from measurements shown in figure 5 by equation (13) is shown in figure 6 together with its fit by an expected behavior, as will be explained in section 4.3. In order to eliminate any artificial discharge ignition by laser radiation, the measurements presented in section 4.3 were realized in the discharge phase when the electric field was small and it was not possible to ignite the discharge.

Phase-resolved measurements presented in figures 5 and 6 can be presented with spatial resolution. Such graphs are shown in figures 7 and 8 for coplanar DBD ignited in pure water vapor and in humid air, respectively. Since signals shown in these figures were measured via the interference filters, these figures do not represent the distribution of all

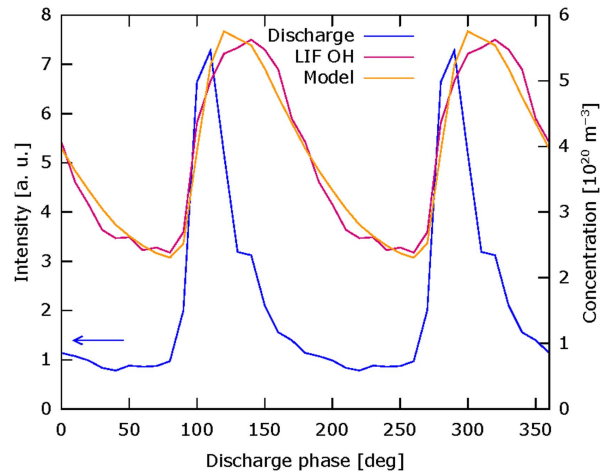


**Figure 6.** The OH LIF signal ( $M_f$ ) obtained by equation (13) (purple). The signal is compared with spontaneous discharge radiation (blue, increased) and a convolution of the spontaneous discharge radiation with exponential decay (orange). Related OH concentration is shown on the right axis.

visible / UV discharge emission. Both in water vapor and in air, the spatial distribution of spontaneous discharge emission observed with no filter was similar to the spatial LIF distribution measured with laser wavelength tuned to the center of the excitation line. Figures 7 and 8 demonstrate the inhomogeneous distribution of both the discharge radiation and distribution of radicals and emphasize the need to realize spatially-resolved measurements. In our case, it was easy to fulfill this demand thanks to the ICCD camera that was used for the detection of signals. Further discussion of figures 7 and 8 is presented in section 4.3.

Finally, it was verified that the LIF signal intensity was a linear function of the laser pulse energy. This confirms that saturation of the fluorescence process did not occur. Furthermore, this shows that the OH concentration is not artificially increased by laser photodissociation of molecules (e.g.  $H_2O_2$ ) in plasma, since OH generation by laser would lead to a convex shape of the LIF signal dependence on laser pulse energy. This conclusion is supported by the fact that the OH signal disappeared immediately when discharge was switched off, which would not happen if the signal was caused by photodissociation of stable molecules generated in plasma (such as  $H_2O_2$ ).

**3.2.7. TALIF of atomic H radicals.** The measurement of reactive species in the coplanar DBD was supplemented by the detection of atomic hydrogen radicals by means of TALIF [35, 36]. In these measurements, the laser beam was focused to a vicinity of the surface of the dielectric plate and a laser wavelength of 205 nm was used for the two-photon excitation of free hydrogen atoms from their ground state  $1s^2S_{1/2}$  to the state  $3d^2D_{3/2,5/2}$ . Fluorescence radiation with a wavelength of 656.3 nm ( $H_\alpha$  line) was detected. The method of H TALIF

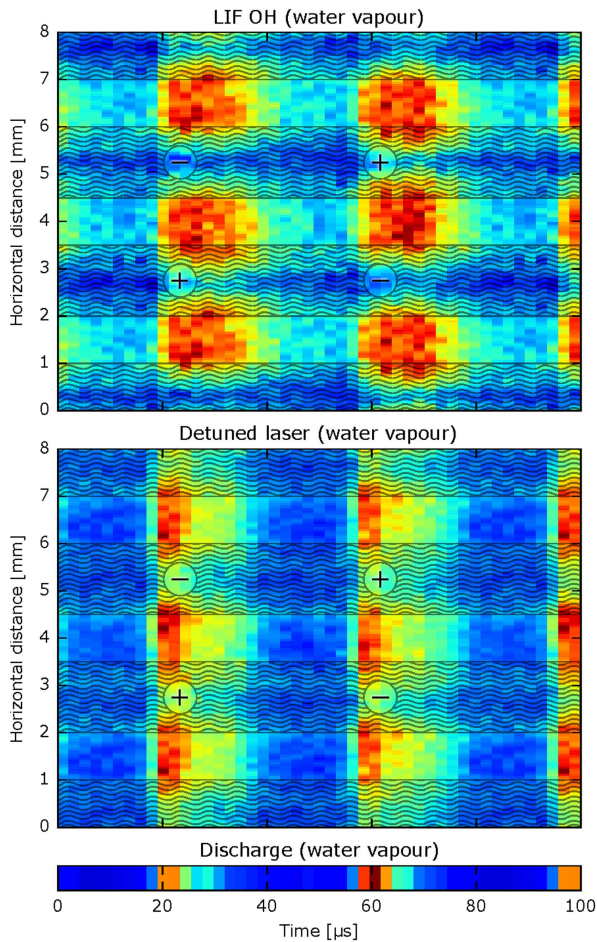


**Figure 7.** Spatially- and temporally-resolved measurements of OH fluorescence and signal measured with laser wavelength detuned from the OH absorption line realized in a coplanar DBD in water vapor. The bottom line presents temporally-resolved spontaneous discharge radiation. The wavy strips represent the position of the electrodes that are hidden behind the dielectric.

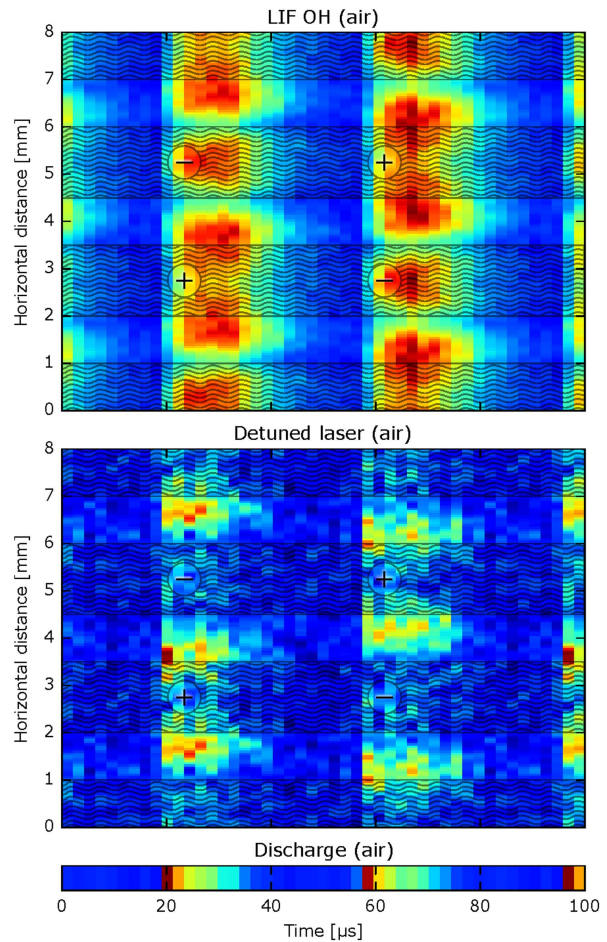


**Figure 8.** Spatially- and temporally-resolved measurements of OH fluorescence and signal measured with laser wavelength detuned from the OH absorption line realized in a coplanar DBD in air. The bottom line presents temporally-resolved spontaneous discharge radiation. The symbols (+) and (−) denote which electrode is the instantaneous anode and cathode, respectively.

measurements in DBDs ignited at atmospheric pressure was in detail analyzed in works [37, 38].

## 4. Results

### 4.1. OES

First, information related to the composition of reactive species in the discharge can be obtained by OES. Whereas  $N_2$  emission dominates to the discharge ignited in hot air, the spectrum emitted from pure water vapor was formed practically only from OH radiation. No nitrogen impurity or oxygen radiation was detected. Besides OH radiation, only a very weak  $H_\alpha$  line was observed, as shown in figure 9. This is the first indication that the production of OH radicals in the coplanar DBD ignited in water vapor highly exceeds the production of H atoms. However, emission spectra give only

information about the excited state, and direct proof of the composition of radicals in the plasma should be given by means of (TA)LIF, as will be shown in the sections 4.2 and 4.3.

It should be noted that the OH spectrum spreads from 306 nm to wavelengths over 330 nm, which shows high vibrational and rotational excitation of OH radicals in the  $A^2\Sigma^+$  state. The OH emission spectrum can be fitted in order to get relative concentrations of individual rovibronic levels of the OH  $A^2\Sigma^+$  state. These relative concentrations are shown in the form of the Boltzmann plot, i.e. the logarithm of relative concentration divided by degeneracy of the corresponding level as a function of level energy, as shown in figure 10. High rovibronic excitation is shown in this graph up to the energy 6.5 eV (related to the ground rovibronic level of the  $X^2\Pi$  state), which is the dissociation energy of the OH radical in the  $A^2\Sigma^+$  state. The plotted dependencies for all observed vibrational bands strongly deviate from straight lines, demonstrating that rotational

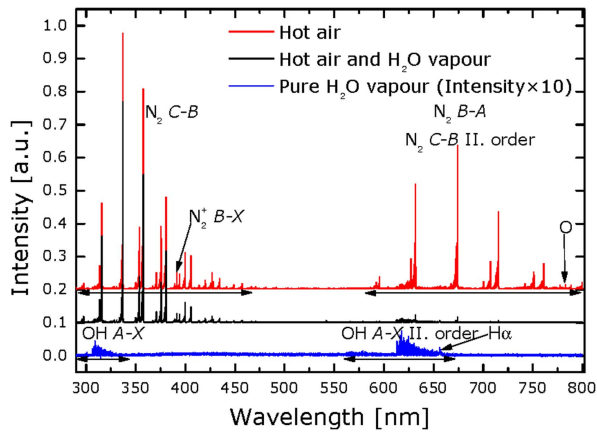


**Figure 9.** Spontaneous emission spectra of the coplanar DBD ignited in air, air mixed with water vapor and in pure water vapor.

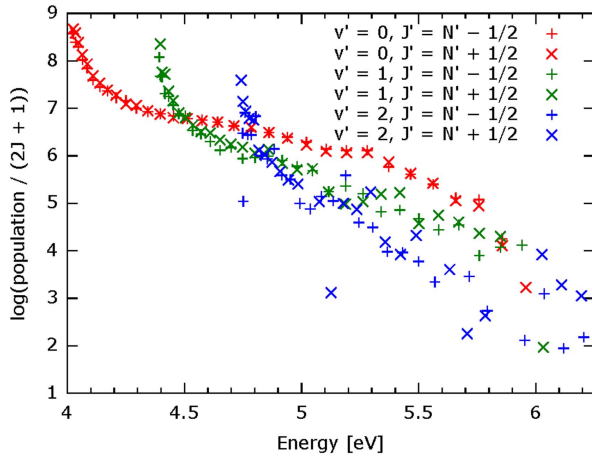


**Figure 10.** Boltzmann plot of rovibronic level populations of the excited OH  $A^2\Sigma^+$  state in the coplanar DBD ignited in pure water vapor.

populations in the excited OH state are far from thermal equilibrium. This is the result of OH  $A^2\Sigma^+$  generation in highly rotationally- and vibrationally-excited levels and a short OH  $A^2\Sigma^+$  life-time caused by fast collisional quenching that does not enable us to reach the rotational and vibrational equilibrium [39, 40].

#### 4.2. TALIF of atomic hydrogen

Since electron dissociation of the water molecule produces not only highly oxidizing OH radicals but highly reducing atomic hydrogen radicals, we tried to detect atomic hydrogen radicals by means of TALIF. Whereas H atoms were easily detected when the discharge was ignited in air, their concentration was well below our detection limit ( $10^{18}$ – $10^{19}$   $\text{m}^{-3}$ ) in the discharge ignited in water vapor. This fact can be explained by the fast reaction  $\text{H} + \text{H}_2\text{O} \rightleftharpoons \text{H}_2 + \text{OH}$  [41], which in the environment with high excess of  $\text{H}_2\text{O}$  molecules quickly converts H atoms to OH.

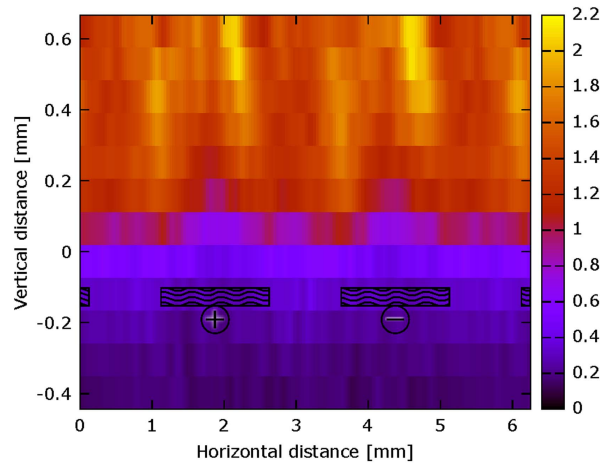


**Figure 11.** Signal of water droplets. The DBD was ignited in water vapor at 175 W. Zero on the vertical axis indicates the surface of the dielectric plate.

#### 4.3. Fluorescence measurement of OH radicals

First, we concentrate on the ICCD signal that was measured when the interior of the reactor was irradiated by laser with wavelength that was detuned from the absorption line of OH radicals. Since the laser was synchronized with the feeding voltage, it was possible to observe this signal in such a phase of feeding voltage, when the electric field in the gas was low and there was actually no discharge. This signal, shown in figure 11, reaches maximum in the gas phase, not at the surface of the ceramics as it would occur if this signal was caused by fluorescence of the ceramics. Since the observed signal was presented with higher intensity when the discharge was switched off (and when gas was not heated by the discharge) but it totally disappeared when water vapor was exchanged by air, it was attributed to laser radiation scattered on the water droplets (although optical filter transmissivity for scattered laser radiation was five orders of magnitude lower than transmissivity for fluorescence signal). The concentration of water droplets was low in the area close to the planar electrode, where the gas was heated by both the discharge and hot ceramic surface. In addition to this vertical inhomogeneity, the distribution of droplets reveals a more complex structure with horizontal periodicity that coincides with the periodicity of the electrode strips. This demonstrates that the droplet distribution was influenced by the discharge.

When detuned laser was synchronized to the feeding voltage phase with high electric field, it caused an increase of discharge radiation during the time of ICCD measurement and increased the signal-to-noise ratio for the measurement of discharge emission. The discharge structure measured in this way (after subtracting the signal of water droplets) is shown in figure 12. Unlike the situation in nitrogen or air, in water vapor the discharge emission reaches its maximum above the interelectrode area. Here, it creates a bow-like structure with thickness around 0.3 mm, which is in agreement with previous coplanar DBD studies [42, 43].

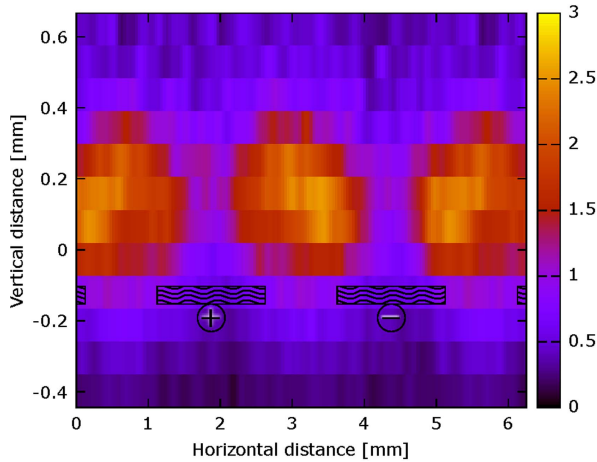


**Figure 12.** Spatial structure of the discharge emission. The DBD was ignited in water vapor at 175 W. Discharge ignition was synchronized with ICCD measurement by a laser shot.

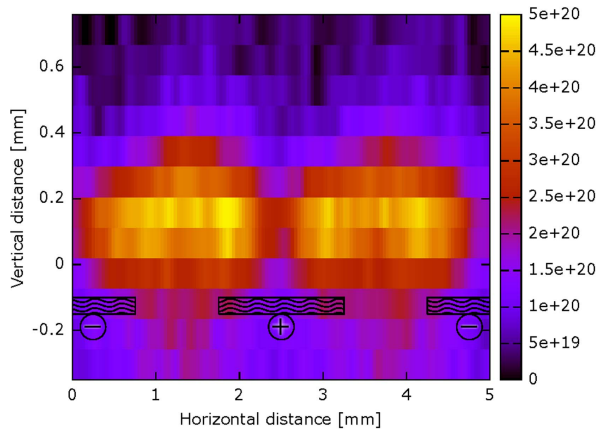


**Figure 13.** OH concentration in the coplanar DBD ignited in water vapor. Power delivered to the discharge was 300 W.

When the laser wavelength was tuned to the center of the OH absorption line, the OH fluorescence was observed and used for the calculation of OH concentration by the procedure described in section 3.2. The obtained concentration maps for coplanar DBD ignited in water vapor and in air are shown in figures 13 and 14, respectively. The OH concentration in water vapor reached more than  $5 \cdot 10^{20} \text{ m}^{-3}$ , which was approximately  $10\times$  higher than the OH concentration measured in the discharge ignited in air at the same delivered power. The concentration shown in figures 13 and 14 were measured in the phase  $190^\circ\text{--}200^\circ$  of the supplied voltage (see figure 6), i.e. in the phase with relatively low OH concentration. The peak OH concentration at the end of the active discharge phase was approx.  $2\times$  higher than the values shown in figures 13 and 14. The OH concentration was measured in the range of the delivered power from 175–350 W, in which a stable discharge could be generated. Both in air and in water vapor, the OH concentration was directly proportional to the delivered power.

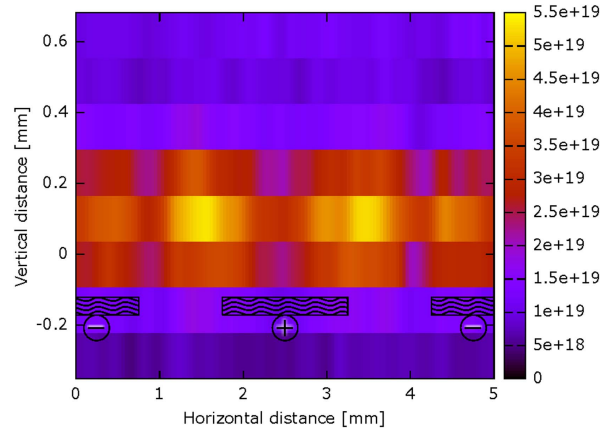


**Figure 14.** OH concentration in the coplanar DBD ignited in air. Power delivered to the discharge was 300 W.

This concentration increase was probably caused by an increase of microdischarge density, which was observed even by the naked eye when the delivered power was increased.

As shown in figures 5–8, the OH concentration was not constant in time, but increased during the active discharge phase and then decreased quickly. With the assumption that OH radicals are created mainly during the active discharge and that their generation rate is directly proportional to the intensity of spontaneous discharge emission, the temporal evolution of OH concentration can be modeled as the convolution of the temporal evolution of discharge emission intensity with an exponential concentration decay. The real decay dependence can be more complex [44], but for the OH life-time estimation the assumption of exponential decay is sufficient. As shown in figure 6, the used convolution follows well the measured OH concentration and can be, therefore, used for determination of the life-time of OH radicals. In both water vapor and air, the OH life-time was approximately  $10 \mu\text{s}$ .

Figures 7, 8, 13 and 14 demonstrate that the spatial distribution of OH radicals was not homogeneous. Regions with high OH concentration reproduced the shape of the visible discharge (see figure 15): in water vapor, the OH-rich region follows the bow-like structure of the visible discharge that bridges the interelectrode area. The position of these bridges was not completely symmetrical, but slightly shifted to the instantaneous anode. In air, the main maxima were observed close to the anode edges, and another maximum was placed at the center of the instantaneous cathode. This location of main maxima correlates well with the spatially- and temporally-resolved measurements realized in a coplanar DBD ignited in air [43], where the intensity of the second positive  $\text{N}_2$  system also reached its maximum in the region close to the anode edge. The described spatial distribution of OH radicals was not changed markedly by a change of the delivered power.

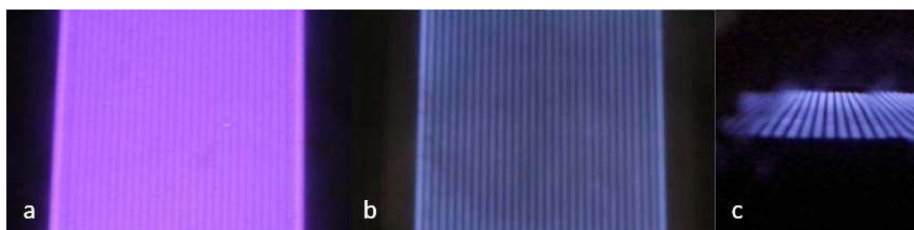


Figure 15. Photo of coplanar DBD (a—in humid air, b—in water vapor, c—in water vapor through the front window).

## 5. Conclusion

It was shown by means of OES and (TA)LIF that the coplanar DBD ignited in water vapor at atmospheric pressure generates plasma with high dominance of OH radicals. Concentration of other radical species was negligible. It means that this discharge can be used for well-defined surface treatment by one specific type of reactive radicals. A significant increase of OH concentration was achieved by the use of pure water vapor as the working gas: the concentration of OH radicals in the discharge ignited in water vapor was in the order of  $10^{20} \text{ m}^{-3}$ , which was an order of magnitude higher than the value measured in the discharge ignited in air. The OH concentration was directly proportional to the electric power delivered to the discharge. As a result, the coplanar DBD ignited in water vapor at atmospheric pressure presents a promising plasma source for the specific oxidation of solid surfaces.

The OH concentration was neither constant in time nor uniform in space. The life-time of OH radicals in both water vapor and air was approx.  $10 \mu\text{s}$ . The spatial OH distribution was well correlated with the distribution of visible light emitted by the discharge: in the case of water vapor discharge, OH radicals were concentrated above the interelectrode space and electrode edges, in the bow-like-shaped discharge path. In case of air discharge, OH radicals were located mainly at the anode edges and cathode center. Finally, the LIF of OH radicals was used for the measurement of the rotational temperature inside the active discharge, which reached the value  $200 \text{ }^\circ\text{C}$ .

Finally, it was demonstrated that fluorescence methods can be used in surface discharges ignited in water vapor in spite of complications caused by fast quenching and the interaction of laser with the solid and liquid surfaces. Quenching, RET and VET need to be taken into account during the processing of LIF data. Furthermore, parasitic signals that can be measured when plasma is irradiated by laser with wavelength that is detuned from absorption lines of the presented species should be subtracted.

## Acknowledgments

This research has been supported by the Czech Science Foundation under contract nos. 17-04329S and 16-09721Y, by the projects CZ.1.05/2.1.00/03.0086 funded by the European Regional Development Fund and LO1411 (NPU I) and

7AMB14SK204 funded by the Ministry of Education, Youth and Sports of Czech Republic.

## ORCID iDs

P Dvořák  <https://orcid.org/0000-0003-0282-0267>

## References

- [1] Černák M, Černáková L, Hudec I, Kováčik D and Zahoranová A 2009 *Eur. Phys. J. Appl. Phys.* **47** 22806
- [2] Černák M, Kováčik D, Ráhel J, Stáhel P, Zahoranová A, Kubincová J, Tóth A and Černáková L 2011 *Plasma Phys. Control. Fusion* **53** 124031
- [3] Kelar J, Čech J and Slavíček P 2015 *Acta Polytech.* **55** 109
- [4] Lu X, Naidis G V, Laroussi M, Reuter S, Graves D B and Ostrikov K 2016 *Phys. Rep.* **630** 1
- [5] Oehr C, Muller M, Elkin B, Hegemann D and Vohrer U 1999 *Surf. Coatings Technol.* **116** 25
- [6] Madaeni S S, Zinadini S and Vatanpour V 2011 *J. Membr. Sci.* **380** 155–62
- [7] Zuwei M, Changyou G, Jian J and Jiacong S 2002 *Eur. Polym. J.* **38** 2279–84
- [8] Siow K S, Britcher L, Kumar S and Griesser H J 2006 *Plasma Process. Polym.* **3** 392–418
- [9] Amorim J, Baravian G and Jolly J 2000 *J. Phys. D: Appl. Phys.* **33** R51
- [10] Niemi K, Schulz-von der Gathen V and Döbele H F 2005 *Plasma Sources Sci. Technol.* **14** 375
- [11] Voráč J, Obrusník A, Procházka V, Dvořák P and Talába M 2014 *Plasma Sources Sci. Technol.* **23** 25011–2
- [12] Verreycken T, Mensink R, van der Horst R, Sadeghi N and Bruggeman P J 2013 *Plasma Sources Sci. Technol.* **22** 055014
- [13] Li L, Nikiforov A, Xiong Q, Britun N, Snyders R, Lu X and Leys C 2013 *Phys. Plasmas* **20** 093502
- [14] Yonemori S and Ono R 2014 *J. Phys. D: Appl. Phys.* **47** 125401
- [15] Dilecce G and De Benedictis S 2011 *Plasma Phys. Control. Fusion* **53** 124006
- [16] Teramoto Y, Kim H H, Ogata A and Negishi N 2014 *J. Appl. Phys.* **115** 133302
- [17] Voráč J, Dvořák P, Procházka V, Morávek T and Ráhel J 2015 *Eur. Phys. J. Appl. Phys.* **71** 20812
- [18] Ambrico P F, Ambrico M, Šimek M, Colaianni A, Dilecce G and De Benedictis S 2009 *Appl. Phys. Lett.* **94** 231501
- [19] Voráč J, Dvořák P, Procházka V, Ehlbeck J and Reuter S 2013 *Plasma Sources Sci. Technol.* **22** 025016
- [20] Herzberg G and Spinks J W T 1950 *Molecular Spectra and Molecular Structure: Diatomic Molecules* vol 1 (van Nostrand)

Q2

Q3

- [21] Dilecce G, Ambrico P F, Simek M and Benedictis S D 2012 *Chem. Phys.* **398** 142–7
- [22] Copeland R A and Crosley D R 1984 *Chem. Phys. Lett.* **7** 295–300
- [23] Copeland R A, Dyer M J and Crosley D R 1985 *J. Chem. Phys.* **82** 4022–32
- [24] Copeland R A, Wise M L and Crosley D R 1988 *J. Chem. Phys.* **92** 5710
- [25] Wysong I J, Jeffries J B and Crosley D R 1990 *J. Chem. Phys.* **92** 5218–22
- [26] Bailey A E, Heard D E, Henderson D A and Paul P H 1999 *Chem. Phys. Lett.* **302** 132–8
- [27] Williams L R and Crosley D R 1996 *J. Chem. Phys.* **104** 6507
- [28] Hartlieb A T, Markus D, Kreutner W and Kohse-Höinghaus K 1997 *Appl. Phys. B* **65** 81–91
- [29] Rahmann U, Kreutner W and Kohse-Höinghaus K 1999 *Appl. Phys. B* **69** 61–70
- [30] Burris J, Butler J, McGee T and Heaps W 1988 *Chem. Phys.* **124** 251–8
- [31] Burris J, Butler J, McGee T and Heaps W 1991 *Chem. Phys.* **151** 233–8
- [32] Jörg A, Meier U, Kienle R and Kohse-Höinghaus K 1992 *Appl. Phys. B* **55** 305
- [33] Kienle R, Jörg A and Kohse-Höinghaus K 1993 *Appl. Phys. B* **56** 249–58
- [34] Dilecce G, Martini L M, Tosi P, Scotoni P and De Benedictis S 2015 *Plasma Sources Sci. Technol.* **24** 034007
- [35] Boogaarts M, Mazouffre S, Brinkman G, van der Heijden H, Vankan P, van der Mullen J and Schram D 2002 *Rev. Sci. Instrum.* **73** 73
- [36] Niemi K, von der Gathen V S and Döbele H 2001 *J. Phys. D: Appl. Phys.* **34** 2330
- [37] Mrkvičková M, Ráhel J, Dvořák P, Trunc D and Morávek T 2016 *Plasma Sources Sci. Technol.* **25** 055015
- [38] Dvořák P, Talába M, Obrusník A, Kratzer J and Dědina J 2017 *Plasma Sources Sci. Technol.* **26** 085002
- [39] Voráč J, Synek P, Procházka V and Hoder T 2017 *Plasma Sources Sci. Technol.* **50** 294002
- [40] Bruggeman P J, Iza F, Guns P, Lauwers D, Kong M C, Gonzalvo Y A, Leys C and Schram D C 2010 *Plasma Sources Sci. Technol.* **19** 015016
- [41] Jenkins D R and Sugden T M 1971 *Flame Emission and Atomic Absorption Spectrometry, Volume 1-Theory* (New York: Marcell Dekker) 151–87 ch Radicals and molecules in flame gases
- [42] Šimor M, Ráhel J, Vojtek P and Černák M 2002 *Appl. Phys. Lett.* **81** 2716
- [43] Hoder T, Šíra M, Kozlov K V and Wagner H E 2008 *J. Phys. D: Appl. Phys.* **41** 035212
- [44] Pei X, Wu S, Xian Y, Lu X and Pan Y 2014 *IEEE Trans. Plasma Sci.* **42** 1206

# Concentration of atomic hydrogen in a dielectric barrier discharge measured by two-photon absorption fluorescence

P Dvořák<sup>1</sup>, M Talába<sup>1</sup>, A Obrusník<sup>1</sup>, J Kratzer<sup>2</sup> and J Dědina<sup>2</sup>

<sup>1</sup> Department of Physical Electronics, Faculty of Science, Masaryk University, Kotlářská 2, Brno 611 37, Czech Republic

<sup>2</sup> Institute of Analytical Chemistry of the CAS, v. v. i., Veveří 97, 602 00 Brno, Czech Republic

E-mail: [pdvorak@physics.muni.cz](mailto:pdvorak@physics.muni.cz)

Received 9 January 2017, revised 23 May 2017

Accepted for publication 5 June 2017

Published 14 July 2017



CrossMark

## Abstract

Two-photon absorption laser-induced fluorescence (TALIF) was utilized for measuring the concentration of atomic hydrogen in a volume dielectric barrier discharge (DBD) ignited in mixtures of Ar, H<sub>2</sub> and O<sub>2</sub> at atmospheric pressure. The method was calibrated by TALIF of krypton diluted in argon at atmospheric pressure, proving that three-body collisions had a negligible effect on quenching of excited krypton atoms. The diagnostic study was complemented with a 3D numerical model of the gas flow and a zero-dimensional model of the chemistry in order to better understand the reaction kinetics and identify the key pathways leading to the production and destruction of atomic hydrogen. It was determined that the density of atomic hydrogen in Ar–H<sub>2</sub> mixtures was in the order of 10<sup>21</sup> m<sup>-3</sup> and decreased when oxygen was added into the gas mixture. Spatially resolved measurements and simulations revealed a sharply bordered region with low atomic hydrogen concentration when oxygen was added to the gas mixture. At substoichiometric oxygen/hydrogen ratios, this H-poor region is confined to an area close to the gas inlet and it is shown that the size of this region is not only influenced by the chemistry but also by the gas flow patterns. Experimentally, it was observed that a decrease in H<sub>2</sub> concentration in the feeding Ar–H<sub>2</sub> mixture led to an increase in H production in the DBD.

Supplementary material for this article is available [online](#)

Keywords: laser-induced fluorescence, TALIF, atomic hydrogen, H, dielectric barrier discharges

## 1. Introduction

Atomic hydrogen is one of the most common reactive species produced in plasma. It plays an important role in plasma chemistry and numerous plasma applications since it is a strong reducing and etching agent. Atomic hydrogen is produced by dissociating common species, such as molecular hydrogen, water, hydrocarbons and others, by a number of reaction channels [1, 2]. In hydrogen plasma, these reactions include dissociation of the hydrogen molecule by electron impact, the fast ionic reaction  $H_2^+ + H_2 \rightarrow H_3^+ + H$  and (dissociative) recombination of hydrogen ions ( $H_3^+$ ,  $H_2^+$ ,  $H^+$ ) with electrons or negative ions ( $H^-$ ). The charge recombination can take place both in the gas phase and on solid

surfaces [3]. Further production mechanisms of hydrogen atoms include dissociation by metastable species, stepwise vibrational excitation of molecules leading to dissociation or dissociative attachment of slow electrons by vibrationally excited molecules  $H_2(v) + e \rightarrow H + H^-$ . A wide spectrum of analogical production channels of atomic hydrogen can be found in discharges ignited in other hydrogen-containing gases or for example at a vicinity of humid surfaces. The main sinks for free hydrogen atoms are the (three-body) recombination in the gas phase and the diffusion to reactor walls with consequent surface recombination. In reactive gases, hydrogen can be preferentially consumed in reactions with other neutrals, e.g.  $H + O_2 \rightarrow OH + O$ ,  $CH_4 + H \rightarrow CH_3 + H_2$ ,  $H + H_2O \leftrightarrow H_2 + OH$  [4].

The concentration of atomic hydrogen is typically measured by spectroscopic methods. At low pressure, comparison of relative intensities of atomic and molecular spectral lines [5], titration [6] or actinometry can be used. In specific cases a catalytic probe [7] can be used, which is however non-selective. Absorption measurements are not restricted to low-pressure discharges but they do not provide spatially resolved data directly and they require wavelengths in the vacuum UV range, which make them challenging. The disadvantage of the resonance-enhanced multiphoton ionization [8] is a complicated quantitative calibration. Consequently, two-photon absorption laser-induced fluorescence (TALIF) is currently the most suitable method of measuring atomic hydrogen concentration in a wide range of discharges [9, 10].

When measuring the density of atomic hydrogen using TALIF, absorption of intense focused laser light with a wavelength of 205 nm is typically employed. The laser excites hydrogen atoms via two-photon absorption from the ground state to the  $n = 3$  state and the subsequent  $H\alpha$  fluorescence radiation at 656.3 nm is detected [9, 10]. Since collisional quenching is an important deexcitation mechanism, decreasing the quantum efficiency of the fluorescence, it is necessary to know the quenching rate constants for excited hydrogen atoms. These quenching rate constants for H ( $n = 3$ ) were published in [10, 11]. The TALIF of hydrogen atoms is usually calibrated by measuring TALIF of krypton at known pressure. The cross-section ratio for two-photon excitation of krypton and hydrogen was published in [9, 10] and the ratio of Einstein coefficients for the fluorescence emission in [12]. The TALIF method has been further used for measuring atomic hydrogen concentration in flames [13] and in low-pressure discharges [14–16], where the problem of collisional quenching is reduced. In the following text, we present the first TALIF measurement of atomic hydrogen concentration in an electric discharge ignited at atmospheric pressure, specifically a dielectric barrier discharge (DBD) atomizer.

DBDs have recently been proven [17–20] as a promising alternative to externally heated quartz tube atomizers (QTA) which are typically applied for hydride atomization in the technique of hydride generation (HG) for atomic absorption spectrometry (AAS) detection [21]. HG-AAS allows one to determine the elements forming volatile hydrides, e.g. arsenic, selenium or bismuth at ng/ml concentration levels. According to the present knowledge of hydride atomization processes [22], hydrogen atoms play an essential role there. The atomization mechanism of hydrides in DBD atomizers is a subject of investigation [23]. Optimum atomization of Bi, Se and As hydrides [18–20] in a DBD atomizer was reached at 14–17 W of DBD power in Ar discharge (60–125 sccm of Ar). It must be highlighted that ca 15 sccm of  $H_2$  is always present in the discharge gas since hydrogen is a side product of hydride generation. Traces of oxygen originating from gas impurities and dissolved in solutions of chemicals are present in the gaseous phase transported to the DBD atomizer. Extra addition of oxygen to the discharge gas (3–7 ml/min of  $O_2$ ) was found to result in trapping of analyte hydride on the inner surface of the DBD instead of its atomization [18, 20]. The

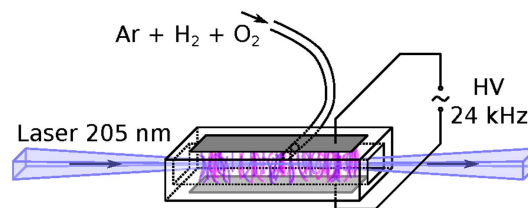


Figure 1. Scheme of the atomizer.

trapped analyte can be subsequently released and atomized in Ar- $H_2$  discharge as soon as the oxygen flow is switched off. This preconcentration can improve the detection limit of HG-DBD-AAS by an order of magnitude down to 0.1 ng/ml as demonstrated for arsenic [20].

The present work aims to determine the atomic hydrogen distribution in the DBD atomizer because of the above mentioned assumed essential role of hydrogen atoms in hydride atomization. No hydrides were introduced into the atomizer for the sake of simplicity but mixtures of Ar with  $H_2$  and  $O_2$  in concentrations and flow rates typically used for hydride atomization and preconcentration in DBD atomizers [18–20] were employed. Since the DBD was ignited at atmospheric pressure, the presented work is also relevant for a much wider range of atmospheric pressure low-temperature plasma applications.

To interpret the results as well as to identify the key reaction pathways involving atomic hydrogen, we have devised a numerical model of the gas flow dynamics as well as relevant chemical reactions. Since the plasma operates in a mixture of argon, hydrogen and oxygen, the reaction scheme was derived from previously published schemes for hydrogen/oxygen flames [4] by including electron-impact dissociation channels. Additionally, the model provides insight into the gas dynamics phenomena in the device.

## 2. Experimental

### 2.1. Discharge setup

The hydrogen atoms were detected in a volume dielectric barrier discharge ignited in the DBD atomizer, which is shown in figure 1 and described in greater detail in [18]. It is a T-shaped vessel with a rectangular-shaped optical arm in which plasma is sustained (inner dimensions of the plasma channel 7 mm  $\times$  3 mm and length of 75 mm). Two copper electrodes (50 mm long; 12 mm wide; 0.15 mm thick) were placed on the horizontal outer sides of the optical arm and they were supplied with sinusoidal voltage with a frequency of 24 kHz. The electric power delivered to the DBD atomizer was 25 W. A quartz tube (20 mm long, 2 mm inner diameter, 4 mm outer diameter) was welded to the center of the optical arm and served as an inlet to supply the gas mixture (Ar,  $O_2$ ,  $H_2$ ) into the optical arm. Argon, hydrogen and oxygen were used as working gases, krypton diluted in argon (from 1:50–1:400) was used for calibration measurements. In the presented experiments, the argon flow rate was varied

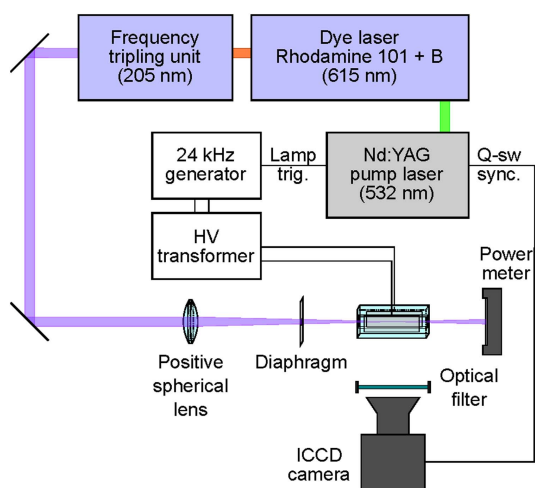


Figure 2. Scheme of the experimental setup.

between 40 sccm and 220 sccm (if not explicitly stated otherwise the value 147 sccm was used), the hydrogen flow rate was varied between 5 sccm and 30 sccm and the oxygen flow rate was varied between 0 sccm and 10 sccm.

## 2.2. Diagnostics setup

The scheme of the experiment is shown in figure 2. A three-component laser system consisting of a Q-switched pumping laser (Quanta-Ray PRO-270-30), a dye laser (Sirah, PRSC-D-24-EG) and a frequency tripling unit was used to produce short laser pulses with a wavelength of 205 or 204 nm for the two-photon excitation of atomic hydrogen or krypton, respectively. The spectral width and duration of laser pulses were ca  $0.06 \text{ cm}^{-1}$  and 8 ns, respectively. The laser beam positioned along the axis of the optical arm was focused onto the center of the optical arm. The fluorescence signal was recorded by an intensified CCD camera (PI-MAX 1024RB-25-FG43) with an interference filter. The spatial resolution of the camera was 0.1 mm in the set of H TALIF experiments. In order to increase the signal-to-noise ratio, typically 500 accumulations of the signal on the CCD chip were used. The energy of each pulse was detected by the pyroelectric energy sensor (Ophir PE9). The energy of laser pulses was varied between 10 and 300  $\mu\text{J}$  in the case of TALIF of H. In most of the measurements it was kept near to the bottom border of this energy range in order to minimize parasitic effects like depletion of the ground state, photoionization of the excited state or stimulated emission from the excited state. For measurements of Kr TALIF, which were used for calibration purposes, the laser-pulse energies were by an order of magnitude smaller than in the H TALIF measurements, since krypton is more sensitive to the listed parasitic effects. The estimated maximum irradiance in the focal plane of the focusing lens during the H TALIF experiments was in the order of  $10^{12} \text{ J/m}^2\text{s}$ .

Laser induced fluorescence (LIF) of OH radicals was further used for preliminary measurements of gas

temperature. In this experiment, OH radicals were successively excited from various rotational levels of the ground vibronic state via the series of at least the first six  $P_1$  absorption lines in the wavelength range of 281–286 nm. The obtained rotational distribution of the ground vibronic state corresponded to a temperature of 550 K.

## 3. Description of model

The experimental characterization of the atomizer is complemented by a numerical model. The model consists of two parts—(i) the gas dynamics part describing the flow pattern of the Ar/H<sub>2</sub>/O<sub>2</sub> mixture in close-to-real 3D geometry as well as admixing of air from the ambient atmosphere, and (ii) a 0D chemistry model which describes the reaction kinetics of active species in the atomizer. Since the gas dynamics model provides the gas velocity, the residence time in the 0D chemistry model is converted to position along the axis of the atomizer.

These two models are practically decoupled—the 0D chemistry model solves the balance equations for different species as a function of the residence time in the plasma,  $t$ , while the gas dynamics model only provides the residence time scale so that the residence time  $t$  can be converted to position within the atomizer  $x$ . The model is, therefore, not capable of capturing the effects of cross-streamline diffusion (differential diffusion). Despite that, the model shows reasonable agreement with the experiment and the cross-streamline diffusion only plays a role in the region close to the gas inlet, as discussed in the results section 4.

### 3.1. Gas dynamics model

The gas dynamics model is, in terms of the underlying physics, very similar to the gas dynamics models which have previously been validated on different experimental setups and published [24, 25]. The model solves the incompressible Navier–Stokes equation without turbulence (the Reynolds number for the typical flow rate of 147 sccm is approx. 700) self-consistently with three diffusion equations (for H<sub>2</sub>, O<sub>2</sub> and ambient air). The Navier–Stokes equations are solved for the whole mixture, so the density and viscosity in the momentum Navier–Stokes equation depend on the local gas composition. The viscosities of individual components (Ar, H<sub>2</sub>, O<sub>2</sub>, air) were obtained from [26] and the mixture viscosity in each point is calculated using Wilke's mixture rules [27]. The diffusion equations in the gas dynamics model are solved in the Fick form. The diffusion coefficients were calculated from binary Chapman–Enskog coefficients (refer to chapter 5 in [28]) using mixture rules and therefore, they also depend on the local gas composition.

The 3D computational geometry of the gas dynamics model is shown in figure 3 and the equations are constrained by several boundary conditions, depending on the boundary. At the gas inlet, the velocity is prescribed to have a parabolic profile so that it is zero at the walls of the inlet and the average flow speed is  $u_{\text{avg}} = (Q_{\text{Ar}} + Q_{\text{H}_2} + Q_{\text{O}_2})/S_{\text{in}}$ , with

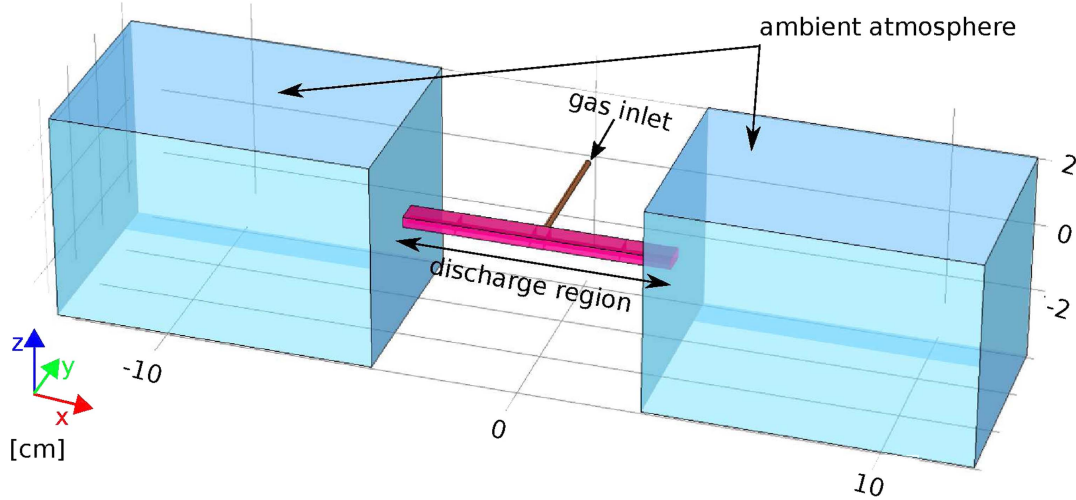


Figure 3. The computational geometry for the gas dynamics and mixing model.

Table 1. Electron-impact reactions added to the Gerasimov reaction scheme [4].

No.	Reaction	Reference
Re01	$e + \text{H}_2 \rightarrow e + \text{H}_2(b^3\Sigma) \rightarrow e + 2\text{H}$	[29]
Re02	$e + \text{O}_2 \rightarrow e + \text{O}_2^* \rightarrow e + 2\text{O}$ where $^* = \{A^3\Sigma_u^+, C^3\Delta_u, c^1\Sigma_u^-\}$	[29]

$S_{\text{inl}}$  being the inlet surface area. Additionally, the mole fractions of each species is prescribed at the gas inlet setting  $x_i = Q_i / \sum_j Q_j$ . At the walls of the gas inlet pipe and the discharge region (purple and orange boundaries in figure 3), the no-slip boundary condition is imposed, setting the velocity at the wall to zero. Finally, in the far-field (blue boundaries), the Dirichlet boundary condition for pressure  $p = 1$  atm is imposed along with a boundary condition for the mole fractions, setting  $x_{\text{air}} = 1$  and mole fractions of other components to zero. The blue regions in figure 3 correspond to the volume outside of the atomizer, where the working gases mix with ambient air upon escaping from the atomizer.

### 3.2. Chemistry model

The chemistry in the Ar/H<sub>2</sub>/O<sub>2</sub> atomizer is studied using a 0D model. The reaction scheme is based on work of Gerasimov and Shatalov [4] which describes the kinetic mechanism of hydrogen/oxygen combustion with special attention paid to the low gas temperature region,  $T < 1000$  K, in which the DBD atomizer also operates. The complete reaction scheme used, including the rate coefficients, is available as a supplementary material to this contribution. Since the gas temperature in the plasma atomizer is approximately 550 K (this value was measured by LIF of OH radicals), the rate of the reaction which normally initializes the combustion kinetics,  $\text{H}_2 + \text{O}_2 \rightarrow 2\text{OH}$  is very low [4] and the active species are preferentially produced by electron-impact dissociation of oxygen and hydrogen. For this reason, the

reaction scheme by Gerasimov was complemented by adding two averaged electron-impact dissociation channels listed in table 1. The necessary reaction cross sections were obtained from the IST-Lisbon database [29] and the reaction rates were calculated using BOLSIG+ [30]. The electron density  $n_e$  and temperature  $T_e$  in the chemistry model are held constant throughout the whole discharge region. Despite this relatively strong assumption, the model is capable to capture the reaction kinetics in the DBD atomizer and provide insight into the key reaction pathways. It should also be mentioned that the plasma is in fact filamentary but since the gas travels only the distance of  $50 \mu\text{m}$  during one voltage cycle, it is reasonable to describe the plasma as quasi-homogeneous with  $n_e$  and  $T_e$  being the ‘effective’ electron density and temperature.

At electron temperatures around 1–2 eV, typical for comparable plasma sources [31], molecular hydrogen is dissociated primarily via excitation of molecular hydrogen to the  $b^3\Sigma$  state with the energy of 8.9 eV [32] (denoted Re01 further on). Other dissociation channels, such as ionization of H<sub>2</sub> and subsequent dissociative recombination (15.4 eV) or dissociative excitation  $e + \text{H}_2 \rightarrow e + \text{H} + \text{H}(n > 1)$  (15 eV) were not included because the BOLSIG+ calculation showed that their rates are at least two orders of magnitude lower than the rate of Re01. The same applies to metastable-induced dissociation, because the rate of argon metastable production gets comparable to Re01 only at the electron temperature of 4 eV.

As concerns dissociation of molecular oxygen, again only the most prominent dissociation channels were considered (Re02), with intermediate excited species with the energy around 6 eV. The cumulative cross section for the electron-impact ionization of oxygen is also available in [29].

The particle balance in the chemistry model is solved with respect to  $t$ —the residence time in plasma. The residence time is then converted to the distance traveled by integrating the gas velocity from the gas dynamics model along a particular streamline. This allows to obtain one-dimensional profiles of the species’ number densities along the axis of the

atomizer, at the assumption that cross-streamline diffusion is neglected. The initial value of all active species' number densities (i.e. except for Ar, H<sub>2</sub> and O<sub>2</sub> that are determined from the equation of state) are set to 10<sup>9</sup> m<sup>-3</sup>, which is effectively zero.

As concerns the numerics and implementation, both the gas dynamics and the chemistry model are implemented in COMSOL Multiphysics simulation platform. The gas dynamics equations are discretized using the Finite element method on a tetrahedral grid with 50000 elements and solved using the PARDISO direct solver available in COMSOL. The transient chemistry model is solved using the Generalized-alpha integration. The details of the discretization procedure and the numerical solvers can be found in the documentation to COMSOL Multiphysics 5.0 and references therein [33].

## 4. Experimental results

### 4.1. Collisional quenching of excited krypton

For the calculation of the concentration of atomic hydrogen, it is necessary to know the lifetime of excited species. Due to short lifetimes, it was not possible to measure these values directly. Therefore, the lifetimes of hydrogen and krypton atoms in excited states were calculated using quenching rate coefficients [10], which can only be used in the case when binary collisions play a key role in the quenching of excited states and the triple collisions and collisions of higher orders can be neglected. In order to minimize any systematic error of the calibration procedure, the krypton calibration was performed directly in the atomizer investigated without any vacuum chamber being used. However, this method required calibration measurement at the atmospheric pressure. Consequently, the role of quenching by triple collisions had to be determined.

The role of higher order collisions on quenching of excited krypton states can be examined by means of the fact that the fluorescence signal ( $S$ ) is proportional to the partial pressure of the fluorescent gas ( $p$ ) and the lifetime of excited states ( $\tau$ )

$$S \propto p \cdot \tau. \quad (1)$$

The lifetime can be expressed

$$\frac{1}{\tau} = \frac{1}{\tau_r} + k_{q1} \cdot p + k_{q2} \cdot p^2 + \dots \quad (2)$$

where  $\tau_r$  is the natural radiative lifetime,  $k_{q1}$  and  $k_{q2}$  are quenching coefficients characterizing the binary and triple collisions, respectively [34, 35]. It follows from the equations (1) and (2)

$$\frac{p}{S} \propto \frac{1}{\tau_r} + k_{q1} \cdot p + k_{q2} \cdot p^2 + \dots \quad (3)$$

Consequently, the role of triple (and eventual higher order) collisions can be determined from the polynomial dependence (3) if the fluorescence signal is measured for various gas pressures at constant gas composition.

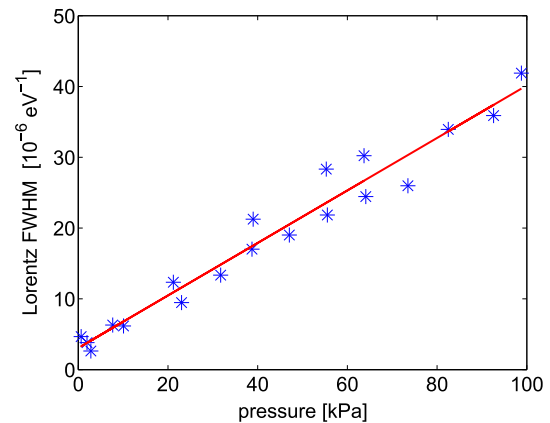


**Figure 4.** Dependence of the Lorentz width of the two-photon absorption krypton line profile on pressure of the Ar:Kr mixture.

Such measurements were realized inside a vacuum silica tube, which was pumped by a rotary pump. A mixture of argon and krypton with the constant ratio 30:1 was supplied to the silica tube and its pressure was varied in the range 10<sup>-2</sup>–10<sup>5</sup> Pa. The TALIF of krypton was measured in the gas without any discharge ignition. First, the spectral profile of the krypton absorption line was measured for various pressures and fitted by the Voigt profile. During the fit calculation, the Doppler broadening coefficient was assumed to be identical for all pressures since all these experiments were realized at room temperature, whereas the Lorentz broadening coefficient  $\gamma$  was expected to depend on the gas pressure. Figure 4 shows a linear dependence of the Lorentz broadening coefficient on the pressure. The ratio of gas pressure and spectrally integrated TALIF intensity ( $p/S$ ) also linearly depended on pressure indicating that quenching of excited krypton atoms by triple collisions plays a negligible role.

To confirm this finding, the following experiment was performed. After evacuating the silica tube, the pumping was stopped and the tube was continuously filled with the Ar:Kr mixture up to the atmospheric pressure. During the pressure increase, the TALIF of krypton was measured with laser wavelength tuned to the center of the absorption line. The measured fluorescence signal was then multiplied by the pressure-dependent ratio between the spectrally integrated TALIF signal intensity and the TALIF signal in the line center. This ratio was known from the fit of Voigt profiles described in the paragraph above. Since the described measurement procedure was fast, it enabled to obtain a high number of measured data and minimize the measurement time in order to suppress effects of eventual laser instability. Figure 5 depicts three examples of the obtained  $E^2 p/S$  polynomials. In order to correct the temporal variations of laser pulse energy, the signal  $S$  was divided by the square of laser pulse energy ( $E$ ). All the measurements again show satisfactory linear dependence and confirm the key role of binary collisions and negligible role of collisions of higher orders on quenching of excited krypton atoms in krypton mixtures with a dominance of argon even at atmospheric pressure.

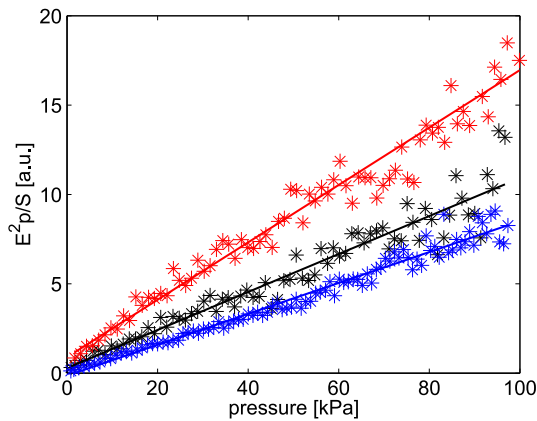


**Figure 5.**  $E^2 p/S$  ratio as a function of the pressure of the Ar:Kr mixture. Various slopes of these dependencies were caused by various experimental settings (e.g. the shape of the laser profile) for the three shown measurements.

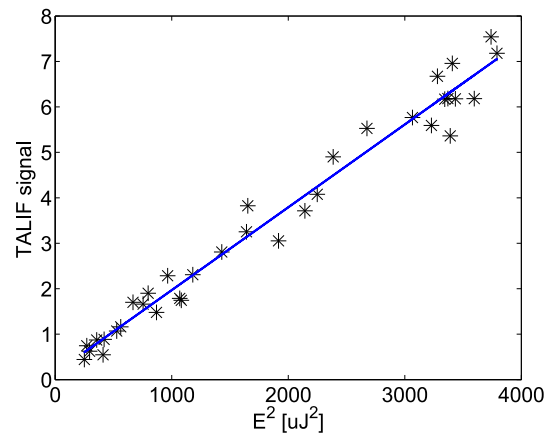


**Figure 6.** Dependence of atomic hydrogen fluorescence signal on square of energy of laser pulses.

#### 4.2. Parameters of hydrogen fluorescence

Before the signal measured by the ICCD camera was used for calculation of atomic hydrogen concentration, several procedures were implemented in order to check and minimize parasitic effects on the measurement. First, the signal with laser switched off was measured and subtracted from the measured data in order to subtract the dark signal of camera, spontaneous plasma radiation and potential ambient light. It was verified that the dark signal measured with laser switched off was identical to the signal measured with laser switched on but with laser wavelength detuned from the absorption line of hydrogen atoms. This test was necessary to prove that there is no additional signal originating from fluorescence of silica walls and that there is no significant influence of the discharge by the laser radiation [36, 37]. In order to completely exclude the risk of discharge ignition by laser radiation, the laser and ICCD camera were synchronized with the discharge and in most of measurements, the laser shots were set to such a part of the period of the supplied voltage when the electric field was small and it was not possible to ignite the discharge artificially by the laser radiation, as described in [36].

Figure 6 shows the dependence of TALIF intensity on the square of energy of laser pulses. The straight line demonstrates that there was no saturation of the fluorescence process. When the discharge was switched off, the TALIF signal disappeared, which demonstrates that there is no significant photodissociation of hydrogen molecules by laser radiation and confirms that there is no significant parasitic fluorescence of atomizer walls. An example of the spectral profile of the absorption line of atomic hydrogen is shown in figure 7. In most of measurements, the fluorescence was measured only with laser wavelength tuned to the center of the absorption line and the complete (spectrally integrated) fluorescence intensity was determined by means of the known fit of the Voigt profile to the measured profile of the absorption line. Since the lifetime of excited hydrogen atoms was too small and it was not possible to measure it directly,

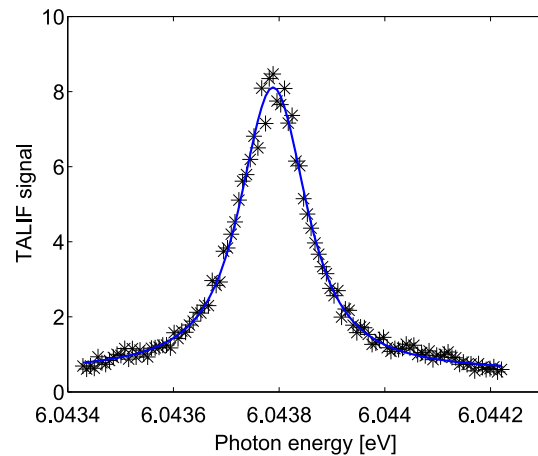


**Figure 7.** Spectral profile of two-photon absorption line of atomic hydrogen.

the quenching rate of excited atomic hydrogen was calculated by means of quenching rate constants published in [10]. Since the TALIF method used was calibrated by measuring TALIF of krypton, the following formula was used for calculation of atomic hydrogen concentration:

$$N_H = N_{Kr} \frac{S_H}{S_{Kr}} \left( \frac{E_{Kr}}{E_H} \right)^2 \left( \frac{\nu_H}{\nu_{Kr}} \right)^2 \frac{\sigma_{Kr}^{TA}}{\sigma_H^{TA}} \frac{A_{Kr} \tau_{Kr}}{A_H \tau_H} \frac{T_{Kr} C_{Kr}}{T_H C_H}, \quad (4)$$

where  $N$  denotes concentration,  $S$  measured TALIF signal that was spectrally integrated over the whole absorption line profile,  $\nu$  laser radiation frequency,  $E$  energy of laser pulses,  $\sigma^{TA}$  cross section for two-photon absorption,  $A$  Einstein coefficient of spontaneous radiation,  $\tau$  lifetime of excited states,  $T$  transmission of an interference filter and  $C$  sensitivity of the ICCD camera. The indexes  $H$  and  $Kr$  differentiate if the quantity is related to atomic hydrogen or krypton, respectively. The ratio  $\sigma_{Kr}^{TA}/\sigma_H^{TA} = 0.62$  was taken from [10], the ratio  $A_{Kr}/A_H = 0.614$  from [12]. The photoionisation rate of excited hydrogen atoms and depletion rate of the ground state of hydrogen atoms estimated by means of cross sections

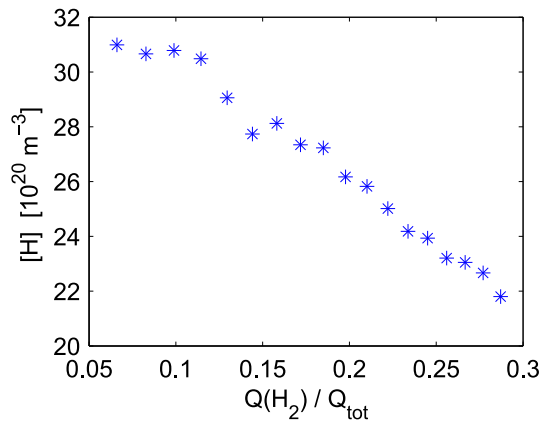


**Figure 8.** Atomic hydrogen concentration as a function of gas composition in a mixture of Ar (147 sccm) and H<sub>2</sub> (10–60 sccm).

published in [38] were significantly smaller than other depopulation mechanisms of the excited state and than the repopulation of the ground state, respectively, which supports the use of the equation (4).

#### 4.3. Hydrogen atom concentration in Ar–H<sub>2</sub> (–O<sub>2</sub>) mixtures

In the first set of measurements, the discharge in the Ar–H<sub>2</sub> mixture was studied. The discharge event occurs several times within the period of the supplied voltage (42 μs), in our discharge setting and delivered power we observed three discharge events in each half of the period by time-resolved discharge imaging. Each discharge event represents a source of radical species that is followed by a slow loss of radicals, which could lead to temporal variations of atomic hydrogen concentration. Therefore, the detection system was synchronized with the discharge power supply and temporal evolution of atomic hydrogen concentration during a period of supplied voltage was measured. It was observed that the atomic hydrogen concentration was within few percents stable during the whole voltage period. This is in an agreement with the lifetime (ca 2 ms) of hydrogen atoms in the Ar–H<sub>2</sub> mixture calculated by means of the model presented in section 3. In the following experiments, the TALIF measurements were realized in such a part of the period of the supplied voltage, when the electric field was small and it was not possible to ignite a discharge event artificially by the laser pulse [36].

The dependence of atomic hydrogen concentration on the flow rates of argon and hydrogen was studied. As discussed later, in these gas mixtures with no oxygen, the atomic hydrogen radicals were distributed almost uniformly along the axis of the optical arm. Providing the constant ratio of hydrogen and argon flow rates, no influence of the total gas flow rate in the range between 100 sccm and 250 sccm on atomic hydrogen concentration was observed. However, the concentration of hydrogen atoms varied with the composition of the gas, i.e. with the ratio of hydrogen and argon flow rates, as illustrated in figure 8. The concentration of atomic hydrogen decreased by tens of percents with increasing

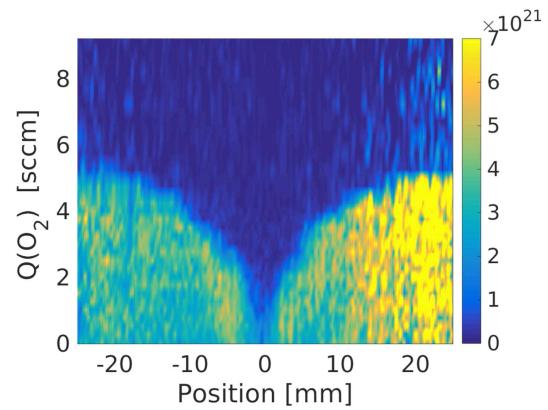


**Figure 9.** Spatial dependence of atomic hydrogen concentration [ $\text{m}^{-3}$ ] for various oxygen flow rates. Flow rate of hydrogen was 10.3 sccm, flow rate of argon was 147 sccm.

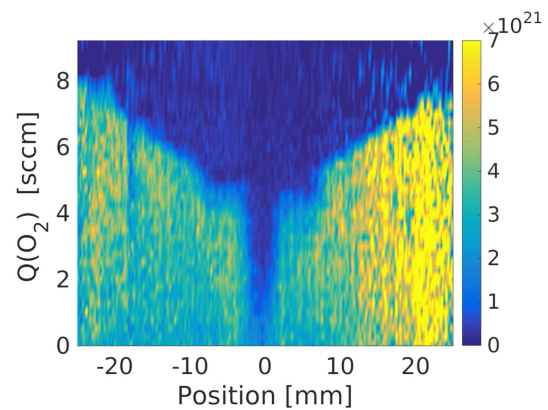


**Figure 10.** Spatial dependence of atomic hydrogen concentration [ $\text{m}^{-3}$ ] for various oxygen flow rates. Flow rate of hydrogen was 22 sccm, flow rate of argon was 147 sccm.

hydrogen concentration from 10% to 30%. The same trend was found when quenching rate constants from [11] (including extreme values from their confidence intervals) were used in evaluation of measured data instead of rate constants presented in [10]. Consequently, the decrease cannot be attributed to an uncertainty in calculated quenching rates and lifetimes of the excited hydrogen state.

The presented value of atomic hydrogen concentration of  $3 \cdot 10^{21} \text{ m}^{-3}$  in the volume DBD can be compared with that in a surface coplanar DBD measured in parallel by the same method, which was found to be higher by an order of magnitude [39], probably as a result of discharge confinement to the thin surface layer.

The spatial distribution of atomic hydrogen concentration is illustrated in figures 9 and 10. Distribution measured with Ar/H<sub>2</sub> mixture with no addition of oxygen are depicted at the bottom row of these figures. With the exception of the very center of the optical arm of the DBD atomizer, the concentration of hydrogen atoms is basically homogeneous. On the right side of the optical arm, the laser was no longer focused sufficiently, which resulted in a worse signal-to-noise

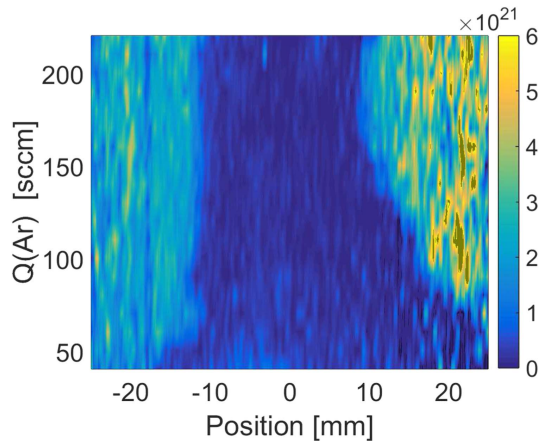


**Figure 11.** Spatial dependence of atomic hydrogen concentration [ $\text{m}^{-3}$ ] as a function of argon flow rate. Constant flow rate of hydrogen and oxygen was 22 and 5.7 sccm, respectively.

ratio at positions above 15 mm in figure 9 and 10 and also in figure 11 below. Therefore, a measurement with laser focused to the area at the electrode edge (25 mm from the atomizer center) was performed and it was verified that the atomic hydrogen concentration is homogeneous through the whole discharge up to the electrode edge. It should be pointed out that in the very center of the optical arm, at the gas inlet, there is a very narrow region with a low H atom concentration (figures 9 and 10), which is probably caused by a small air impurity. In order to exclude any effect of this narrow region on results presented in figure 8, the concentration values shown in this figure were calculated from intensity of hydrogen TALIF that was produced in the region between  $-17$  mm and  $-2$  mm.

When oxygen is added to the Ar–H<sub>2</sub> mixture, the chemical composition of the gas is no more uniform, as discussed below. Hydrogen and oxygen is consumed and water vapor is produced. Since water molecule is an effective quencher, the lifetime of excited H atoms is spatially-dependent and should be calculated for each position in the discharge according to

$$\frac{1}{\tau} = \frac{1}{\tau_0} + q_{\text{Ar}}n_{\text{Ar}} + q_{\text{H}_2}n_{\text{H}_2} + q_{\text{O}_2}n_{\text{O}_2} + q_{\text{H}_2\text{O}}n_{\text{H}_2\text{O}}, \quad (5)$$

where  $\tau_0$  is the radiative lifetime,  $q_{\text{Ar}}$ ,  $q_{\text{H}_2}$ ,  $q_{\text{O}_2}$  and  $q_{\text{H}_2\text{O}}$  are the quenching rate constants and  $n_{\text{Ar}}$ ,  $n_{\text{H}_2}$ ,  $n_{\text{O}_2}$  and  $n_{\text{H}_2\text{O}}$  are the local concentrations of Ar, H<sub>2</sub>, O<sub>2</sub> and H<sub>2</sub>O, respectively. The local concentrations for each input composition of the gas were taken from the simulation.

The effect of oxygen on the spatial distribution of atomic hydrogen concentration for two different hydrogen flow rates is demonstrated in figures 9 and 10. The addition of small flow rates of oxygen, up to around 20% of the hydrogen flow rate, only slightly reduces the H atom concentration in the very narrow region at the center of the optical arm. When increasing the oxygen inlet, the H atom deficient central region is gradually extended to cover the whole observed region from position  $-25$  mm to position 25 mm for an

oxygen flow rate close to half of the hydrogen flow rate, i.e. the stoichiometric ratio with respect to water. A further increase in the oxygen flow rate then does not change the situation visibly.

Figure 11 illustrates how the flow rate of argon influences the sharply bordered region with low atomic hydrogen concentration in the discharge center. Hydrogen and oxygen flow rates were kept constant whereas the argon flow rate was varied. The observed narrowing of the low-H-concentration region with the addition of argon is discussed in section 6. (In this figure, the lifetime of excited H atoms was calculated only from the chemical composition of the gas at the input. The simulation cannot follow the asymmetric shape of the H-poor region that was observed at low gas flow rates and that could be caused by an asymmetric gas flow through the atomizer. Therefore, the simulated gas composition cannot be used for the calculation of the H\* lifetime in this measurement. As a result, the H concentration in the H-rich region is underestimated by approx. 30%.)

Finally, the uncertainty of the obtained concentration values was estimated. The experimental standard deviation of data obtained in one experiment was only a few percent, which indicates the high reliability of measured trends. The uncertainty of the absolute values of the atomic hydrogen concentration is significantly higher. The experimental standard deviation of concentration values measured on different days and calibrated by different measurements of krypton TALIF was ca 20%. Moreover, there are differences between the data in the literature used in the evaluation of the atomic hydrogen concentration. For example, the ratio of two-photon excitation cross sections for krypton and hydrogen ( $\sigma_{\text{Kr}}^{\text{TA}}/\sigma_{\text{H}}^{\text{TA}}$ ) differs by ca 10% in [10] and [9] and the quenching rate coefficients differ by ca 2% to 20% in [10] and [11]. All these factors together lead to the uncertainty of absolute atomic hydrogen concentration below 40%.

## 5. Results of the model

The gas dynamics model reveals that a laminar vortex is formed close to the gas inlet, where the gas enters the discharge region (see figure 12(a)). This vortex is formed due to the rapid change in the inertia of the gas flow hitting the wall opposite to the orifice. However, from approx.  $|x| > 8$  mm, the flow stabilizes and forms a nearly ideal Poiseuille flow. As concerns the gas mixing, figure 12(b) confirms that the amount of air that gets mixed into the atomizer from ambient atmosphere is negligible as its mole fraction reaches values comparable to the air impurity in argon gas (100 ppm) only at the very edges,  $|x| > 30$  mm, of the atomizer.

To comprehend the spatial profiles of atomic hydrogen that were observed in the TALIF measurements, i.e. the fact that atomic hydrogen onset changes with the amount of oxygen added, the gas dynamics model has to be used together with the chemistry model. In all cases, the effective electron density and temperature in the chemistry model were assumed to take the values of  $n_e = 10^{19} \text{ m}^{-3}$  and  $T_e = 1.2 \text{ eV}$ . These values are reasonable for a mostly argon

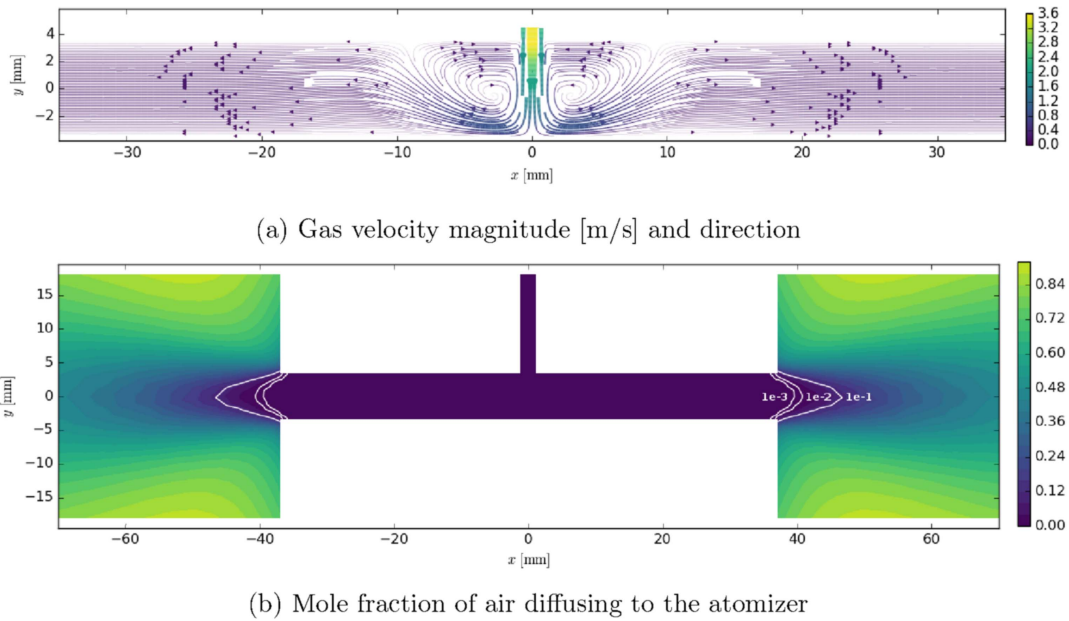


**Figure 12.** 2D transverse cut through the atomizer showing the gas velocity (a) and mole fraction of air (b) in the atomizer at  $Q_{\text{Ar}} = 147$  sccm,  $Q_{\text{H}_2} = 10.3$  sccm and  $Q_{\text{O}_2} = 5$  sccm.

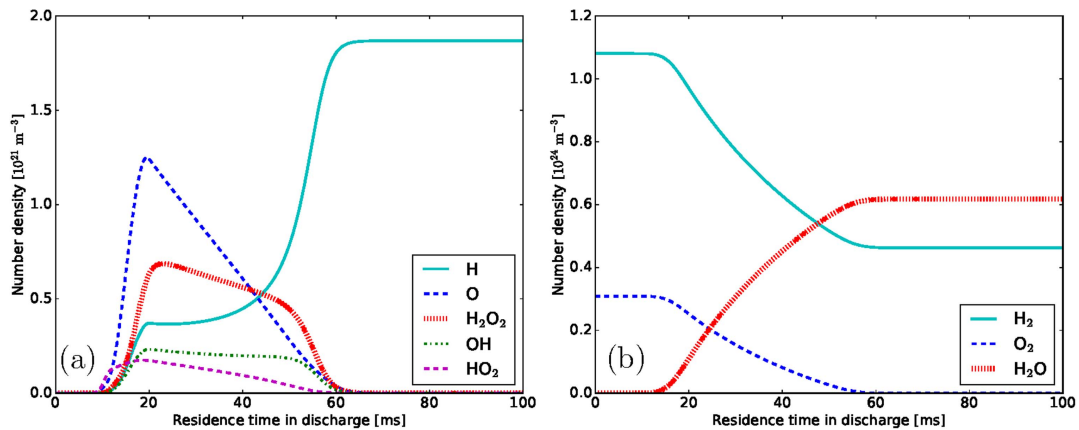


**Figure 13.** Number densities of the key active species (a) and ground-state species (b) for  $Q_{\text{H}_2} = 10.3$  sccm,  $Q_{\text{O}_2} = 3$  sccm and  $Q_{\text{Ar}} = 147$  sccm.

DBD operating at the atmospheric pressure [31, 40] and they were chosen so that the maximum number densities of H reach values consistent with the measurements (approx.  $3 \cdot 10^{21} \text{ m}^{-3}$ ). Furthermore, the electron density and temperature in the chemistry simulation were ramped up across the time span of 5 ms to achieve better computational stability and also to account for the fact that even in the experiment, the plasma onset is never an ideal step function. The necessity of the 5 ms ramp function in the plasma parameters follows from the model approximation of spatially and temporally uniform electron density and temperature. The actual plasma, however, consists of transient filaments which uniformly fill the discharge chamber volume. The approximation of spatially uniform ‘effective’ plasma parameters, therefore, makes sense only after the gas flow intersected a sufficient number of

filaments but does not hold close to the gas inlet. The length of the ramp function, 5 ms, was found empirically and corresponds approx. to 160 discharge periods.

Figure 13 shows the number densities of the atomic hydrogen, atomic oxygen, hydroxyl radical, hydroperoxyl and hydrogen peroxide as a function of the residence time in the discharge. It is observed that atomic oxygen appears slightly earlier than atomic hydrogen because less energy is required for its dissociation (6.0 eV versus 8.9 eV). The presence of oxygen hinders the production of atomic hydrogen because as long as either molecular or atomic oxygen is present, atomic hydrogen is lost in a series of fast reactions, most importantly to  $\text{HO}_2$  via the reaction  $\text{H} + \text{O}_2 + \text{M} \rightarrow \text{HO}_2 + \text{M}$  (RG32–RG35 of the supplement). The second most important H loss process involving oxygen is three-body formation of the

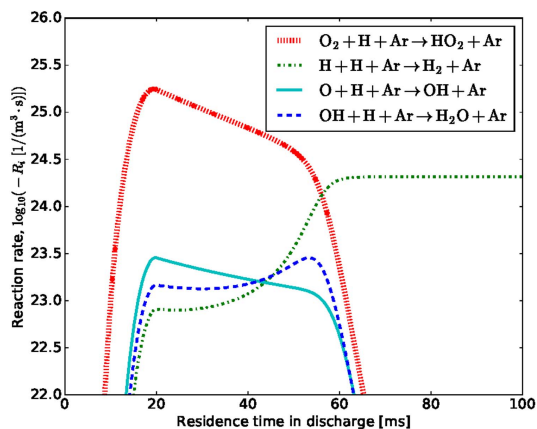


**Figure 14.** Rates of the most important reactions leading to atomic hydrogen loss calculated for gas composition identical with figure 13. The rate coefficients of three-body reactions depend slightly on the third body (Ar, H<sub>2</sub> or O<sub>2</sub>), so we plot reactions involving argon, the most important third body.

hydroxyl radical  $O + H + M \rightarrow OH + M$  (RG21–RG23). However, once most of the oxygen is converted to water and the number density of atomic hydrogen exceeds the value of approx.  $10^{21} \text{ m}^{-3}$ , the three-body re-association of atomic hydrogen becomes the most important loss channel which counterbalances the electron-impact dissociation and results in the flat hydrogen density profile that was also observed in the experiment. The rates of the four most important reactions leading to the loss of atomic hydrogen are plotted in figure 14. It should be added that in the absence of oxygen, the flat maximum of the hydrogen number density appears almost immediately and the rise time is given only by the 5 ms ramp function in the electron density and temperature.

In the region where atomic oxygen dominates over atomic hydrogen, the hydroperoxyl radical HO<sub>2</sub> produced by reactions (RG32–RG35) is an intermediate species which is quickly converted to OH upon colliding with either O or H or to hydrogen peroxide in the reaction  $HO_2 + HO_2 \rightarrow H_2O_2 + O_2$ . Hydrogen peroxide itself is very stable but as the concentration of atomic hydrogen becomes higher, H<sub>2</sub>O<sub>2</sub> is converted to water and hydroxyl radical by the reaction  $H_2O_2 + H \rightarrow H_2O + OH$  (RG52). The hydroxyl radical also eventually forms water due to the lack of oxygen, e.g. via the three-body reaction  $OH + H + M \rightarrow H_2O + M$  (RG28–RG31) which would be only of minor importance in oxygen-rich environments.

To validate the chemistry model, the number densities of hydrogen along the discharge region were compared to the TALIF measurements presented above. Figure 15 shows results of simulations which were run for the same gas compositions that were used in figures 9 and 10, i.e. either 10.3 or 22 sccm of hydrogen with varying oxygen flow rate. The residence time, the independent variable in the 0D model, was converted to the  $x$ -coordinate by integrating the velocity along a selected streamline from the gas inlet to the edge of the atomizer.

When a small amount of oxygen is added to the gas mixture, hydrogen atoms at the inlet of gases are rapidly consumed by reactions with oxygen mainly to HO<sub>2</sub>, OH and H<sub>2</sub>O as detailed in figures 13 and 14. With increasing oxygen input the H atom deficient section in the center extends—atomic hydrogen appears only after all oxygen has formed stable products (mostly water) and does not further interact with the atomic hydrogen. In other words, all the molecular oxygen was converted to water outside the H atom deficient section. With increasing oxygen flow rate, the onset of H moves towards the edges of the atomizer and the number density of H drops by an order of magnitude once the H<sub>2</sub>/O<sub>2</sub> approaches the stoichiometric ratio (the oxygen flow rate reaches half of hydrogen flow rate). Further increase of oxygen flow rate leads to an excess of oxygen in any position in the atomizer. Consequently, at this moment the region with small atomic hydrogen concentration spreads over the whole discharge volume. It should be mentioned that, for a given oxygen input below the stoichiometric ratio, the H concentration in the optical arm sections outside the H atom deficient section is constant along the optical arm position.

The simulated data (figure 15) showing a gradual shift of the onset position of atomic hydrogen with increasing oxygen flow rates, provide a reasonably good agreement with the experiments shown in figures 9 and 10 with the exception of the more ‘funnel-like’ shape observed for lower O<sub>2</sub> flow rates, especially in experiments realized with a high H<sub>2</sub> flow rate. This is, most likely, a consequence of the approximations that had to be taken when using the 0D model, see the discussion below.

## 6. Discussion

The observed decrease in atomic hydrogen concentration with increasing hydrogen concentration in the Ar + H<sub>2</sub> mixture (figure 8) can be explained by discharge changes induced by the change in gas composition. The addition of molecular hydrogen is expected to create a sink of electron energy that is transmitted for example to vibrational excitation of hydrogen molecules, to cause quenching of argon metastables and to attach free electrons to negative hydrogen ions [41]. The combination of these effects can lead to a decrease in the dissociation rate and a decrease in the atomic hydrogen concentration. This observation is in agreement with analogous observations realized in the atmospheric pressure plasma jets that were reviewed in [42]. The addition of O<sub>2</sub> to the He–O<sub>2</sub> mixture led to a decrease in the atomic oxygen concentration for the O<sub>2</sub> amount above 0.6% and the addition of N<sub>2</sub> to the He–N<sub>2</sub> mixture led to a decrease in the atomic nitrogen concentration for the N<sub>2</sub> amount above 0.25%.

This conclusion is confirmed by narrowing of the H-poor region with the addition of argon to the Ar + H<sub>2</sub> + O<sub>2</sub> mixture, which is shown in figure 11. The dilution of H<sub>2</sub> and O<sub>2</sub> by Ar should promote the expansion of the H-poor region, since the dilution of reactive gases leads to a drop in reaction rates and a consequent increase in the time needed for the consumption of reactive oxygen species. In addition, the

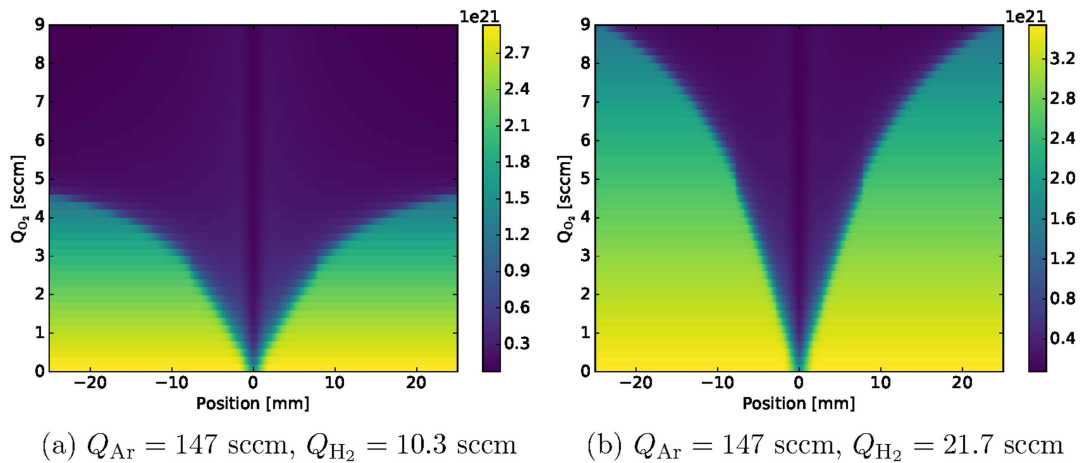


**Figure 15.** Number density of atomic hydrogen as obtained from the numerical model. These figures can be compared to figures 9 and 10, where analogical experimental data are shown. The values of electron density and temperature were set to  $n_e = 10^{19} \text{ m}^{-3}$ ,  $T_e = 1.2 \text{ eV}$ .

increase in the gas velocity caused by the increase in the Ar flow rate should promote the expansion of the H-poor region as well, since the gas mixture can reach more distant regions during the time needed for oxygen consumption. However, the opposite narrowing trend was observed, which supports the hypothesis that an increase in the argon percentage in the gas mixture increases the efficiency of the discharge leading to an increase in the dissociation rate induced by fast electrons and metastables and a consequent increase in the rate of chemical reactions.

The fact that the concentration of atomic hydrogen decreases with the increased fraction of molecular hydrogen in Ar gas (figure 8) is in accord with the observation that signal in DBD-HG-AAS in pure hydrogen as discharge gas is ca 50% lower compared to Ar discharge with ca 15%  $\text{H}_2$  content (side product of hydride generation) [18–20]. Assuming a temperature of 550 K in the plasma, the highest atomic hydrogen concentration (between 6% and 12% hydrogen in the gas, see figure 8) leads to the dissociation degree of hydrogen molecule of 0.002–0.004.

Similar to the experiment, the simplified chemistry simulation predicts a section of low H atom concentration in the atomizer optical arm center (see figure 15). The size of this H-poor region increases gradually with the amount of oxygen in the simulation while it follows a distinct funnel shape in the experiment (figures 9 and 10). The likely explanation lies in the gas recirculation pattern formed close to the gas inlet (see figure 12(a)). Since atomic hydrogen is quickly scavenged by oxygen, it can appear in high concentrations only after all oxygen has been converted to  $\text{H}_2\text{O}$ . Consequently, if the admixture of  $\text{O}_2$  is low enough and a high concentration of atomic hydrogen is reached anywhere between  $|x| = 0$  and  $|x| < 9 \text{ mm}$ , it can be advectively transported back towards the gas inlet by the recirculating flow. The model cannot account for this effect due to the fact that it neglects cross-streamline diffusion (as discussed in section 3). When the  $\text{O}_2$  admixture exceeds a certain value, atomic hydrogen is formed too far downstream (further than

the size of the recirculation pattern, approx.  $|x| > 9 \text{ mm}$ ), it cannot be transported back by the flow and the model and experiment shows similar sizes of the H-poor region. This explanation is consistent with the fact that the slope of the ‘funnel’ in figures 9 and 10 changes close to  $|x| = 9 \text{ mm}$ .

The mechanism of hydride trapping in oxygen-rich (with respect to hydrogen) atmosphere described in the Introduction in section 1 and discussed in detail in references [21, 22] can be explained by the TALIF measurements under given conditions (figures 9 and 10) in which a clear zone free of hydrogen atoms appears in the central part of the DBD atomizer. The width of this zone depends on oxygen amount added reaching a width from few millimeters to 40 mm for oxygen flow rates of 3–7 sccm. Analyte hydride is supposed to be trapped exactly in this zone in the absence of free H atoms since atomization of analyte would occur outside this zone in the presence of H atoms. As soon as the flow of oxygen is switched off, the hydrogen atoms fill again the whole volume of the DBD atomizer homogeneously as discussed above and depicted in the bottom rows in figures 9 and 10. Preconcentrated analyte is released and atomized under these conditions as proven in previous works [18, 20].

## 7. Conclusion

TALIF measurement and simulation of atomic hydrogen concentration were performed in a dielectric barrier discharge ignited at atmospheric pressure in a mixture of argon, hydrogen and oxygen. Since TALIF of krypton was used for the calibration of the fluorescence method, quenching of excited krypton atoms at atmospheric pressure was studied, which is an important parameter for quantitative treatment of measured data. It was shown that triple (and higher order) collisional processes do not play a significant role in  $\text{Kr}^*$  quenching in an argon environment. This finding is important for the realization of TALIF calibration in Ar + Kr flow at atmospheric pressure. This simple calibration method does

not require implementation of any vacuum vessel and, therefore, eliminates the risk of a systematic error caused by changes in the optical path of laser.

The concentration of atomic hydrogen was in the order of  $10^{21} \text{ m}^{-3}$  in the Ar–H<sub>2</sub> mixture, and the maximum dissociation degree of hydrogen was ca 0.3%. The highest production of free hydrogen atoms was observed in the Ar–H<sub>2</sub> mixtures with a relatively low amount of hydrogen indicating that the addition of hydrogen decreases the dissociation ability of the DBD. When oxygen was added to the gas mixture, the atomic hydrogen concentration decreased rapidly, primarily due to the reaction  $\text{O}_2 + \text{H} + \text{Ar} \rightarrow \text{HO}_2 + \text{Ar}$ . When only a sub-stoichiometric amount of oxygen was added to the gas mixture, oxygen was consumed during typically tens of milliseconds by chemical reactions. At the point where oxygen was consumed, the atomic hydrogen concentration increased quickly. As a result, a sharply bordered region with low atomic hydrogen concentration was created at the inlet of gases. The width of this region was an increasing function of oxygen supply until the stoichiometric ratio of H<sub>2</sub>:O<sub>2</sub> = 2:1 was reached and the region spread to the whole discharge volume. At low oxygen supply the width of the region with low atomic hydrogen concentration was noticeably affected by a vortex flow that was formed at the inlet of the gases.

Both the TALIF measurements of atomic hydrogen as well as theoretical simulations of gas flows and chemical reactions in the gaseous phase performed in this work have been proven to be a valuable tool to gain insights into atomization of elements forming volatile hydrides in DBD atomizers. The results obtained in this work may consequently lead to further improvements in HG-DBD-AAS applications to analytical chemistry issues. Good correlation between the results of HG-DBD-AAS optimization studies on the one hand and TALIF measurements and computational simulations on the other have been reached.

## Acknowledgments

This research has been supported by the Czech Science Foundation under contracts GA13-24635S, 17-04329S and P206/14-23532S, by the projects CZ.1.05/2.1.00/03.0086 funded by European Regional Development Fund and LO1411 (NPU I) funded by the Ministry of Education, Youth and Sports of Czech Republic and by Institute of Analytical Chemistry of the CAS, v. v. i., Institutional Research Plan no. RVO: 68081715. Adam Obrusník is a Brno PhD Talent scholarship holder—funded by the Brno City municipality.

## References

- [1] Otorbaev D, van de Sanden M and Schram D 1995 *Plasma Sources Sci. Technol.* **4** 293
- [2] Salabas A, Marques L, Jolly J, Gousset G and Alves L L 2004 *J. Appl. Phys.* **95** 4605
- [3] Babkina T, Gans T and Czarnetzki U 2005 *Europhys. Lett.* **72** 235
- [4] Gerasimov G Y and Shatalov O P 2013 *J. Eng. Phys. Thermophys.* **86** 929–36
- [5] Lavrov B, Pipa A and Röpcke J 2006 *Plasma Sources Sci. Technol.* **15** 135
- [6] Niemi K, Mosbach T and Döbele H 2003 *Chem. Phys. Lett.* **367** 549
- [7] Mozetic M, Drobnič M, Pregelj A and Zupan K 1996 *Vacuum* **47** 943
- [8] Redman S, Chung C, Rosser K and Ashfold M 1999 *Phys. Chem. Chem. Phys.* **1** 1415
- [9] Boogaarts M, Mazouffre S, Brinkman G, van der Heijden H, Vankan P, van der Mullen J and Schram D 2002 *Rev. Sci. Instrum.* **73** 73
- [10] Niemi K, von der Gathen V S and Döbele H 2001 *J. Phys. D: Appl. Phys.* **34** 2330
- [11] Bittner J, Kohse-Höinghaus K, Meier U and Just T 1988 *Chem. Phys. Lett.* **143** 571
- [12] Jolly J and Booth J 2005 *J. Appl. Phys.* **97** 103305
- [13] Meier U, Kohse-Höinghaus K and Just T 1986 *Chem. Phys. Lett.* **126** 567
- [14] Chérigier L, Czarnetzki U, Luggenhölscher D and von der Gathen V S 1999 *J. Appl. Phys.* **85** 696
- [15] Lamara T, Hugon R and Bougdira J 2006 *Plasma Sources Sci. Technol.* **15** 526
- [16] de Pouques L, Bougdira J, Hugon R, Henrion G and Alnot P 2001 *J. Phys. D: Appl. Phys.* **34** 896
- [17] Zhu Z, Zhang S, Lv Y and Zhang\* X 2006 *Anal. Chem.* **78** 865–72
- [18] Kratzer J, Boušek J, Sturgeon R E, Mester Z and Dědina J 2014 *Anal. Chem.* **86** 9620–5
- [19] Duben O, Boušek J, Dědina J and Kratzer J 2015 *Spectrochim. Acta B* **111** 57–63
- [20] Novák P, Dědina J and Kratzer J 2016 *Anal. Chem.* **88** 6064–70
- [21] Dědina J and Tsalev D L 1995 *Hydride Generation Atomic Absorption Spectrometry* (Chichester: Wiley)
- [22] Dědina J 2007 *Spectrochim. Acta B* **62** 846–72
- [23] Kratzer J, Zelina O, Svoboda M, Aturgeon R E, Mester Z and Dědina J 2016 *Anal. Chem.* **88** 1804–11
- [24] Voráč J, Obrusník A, Procházka V, Dvořák P and Talába M 2014 *Plasma Sources Sci. Technol.* **23** 25011–2
- [25] Synek P, Obrusník A, Zajickova L, Hübner S and Nijdam S 2015 *Plasma Sources Sci. Technol.* **24** 025030
- [26] Lemmon E W, McLinden M O and Friend D G 2009 Thermophysical properties of fluid systems *NIST Chemistry WebBook, NIST Standard Reference Database Number 69* <http://webbook.nist.gov/chemistry/fluid/JQ8>
- [27] Alkandry H, Boyd I and Martin A 2013 (*American Institute of Aeronautics and Astronautics*) *ch Comparison of Models for Mixture Transport Properties for Numerical Simulations of Ablative Heat-Shields Aerospace Sciences Meetings 0* (<https://doi.org/10.2514/6.2013-303>)
- [28] Cussler E L 2009 *Diffusion: Mass Transfer in Fluid Systems* vol. 2 3rd edn. (Cambridge: Cambridge University Press)
- [29] Ist-lisbon database <http://ixcat.net> retrieved: 2015-09-15
- [30] Hagelaar G J M and Pitchford L C 2005 *Plasma Sources Sci. Technol.* **14** 722–33
- [31] Subedi D P, Tyata R B, Shrestha R and Wong C S 2014 *AIP Conf. Proc.* **1588** 103–8
- [32] Trevisan C and Tennyson J 2002 *Plasma Phys. Control. Fusion* **44** 2217–30
- [33] Comsol multiphysics software <http://comsol.com> version 5.0
- [34] van Gessel A F H, van Grootel S C and Bruggeman P J 2013 *Plasma Sources Sci. Technol.* **22** 055010
- [35] Dvořák P, Mrkvičková M, Kratzer J, Dědina J and Procházka V 2017 *Plasma Sources Sci. Technol.* **26** 065020
- [36] Voráč J, Dvořák P, Procházka V, Morávek T and Ráhel J 2015 *Eur. Phys. J. Appl. Phys.* **71** 20812

- [37] Ambrico P F, Ambrico M, Šimek M, Colaianni A, Dilecce G and De Benedictis S 2009 *Appl. Phys. Lett.* **94** 231501
- [38] Amorim J, Baravian G, Touzeau M and Jolly J 1994 *J. Appl. Phys.* **76** 1487–93
- [39] Mrkvičková M, Ráheľ J, Dvořák P, Trunec D and Morávek T 2016 *Plasma Sources Sci. Technol.* **25** 055015
- [40] Massines F, Rabeji A, Decomps P, Gadri R B, Segur P and Mayoux C 1998 *J. Appl. Phys.* **83** 2950
- [41] Amemiya H and Sakamoto Y 1987 *Japan. J. Appl. Phys.* **26** 1170
- [42] Lu X, Naidis G V, Laroussi M, Reuter S, Graves D B and Ostrikov K 2016 *Phys. Rep.* **630** 1–84

# Spatially resolved measurement of hydroxyl radical (OH) concentration in an argon RF plasma jet by planar laser-induced fluorescence

J Voráč<sup>1</sup>, A Obrusník<sup>1,2</sup>, V Procházka<sup>1</sup>, P Dvořák<sup>1</sup> and M Talába<sup>1</sup>

<sup>1</sup> Department of Physical Electronics, Faculty of Science, Masaryk University, Kotlářská 2, Brno 611 37, Czech Republic

<sup>2</sup> Plasma Technologies at CEITEC, Masaryk University, Kotlářská 2, Brno 611 37, Czech Republic

E-mail: vorac@mail.muni.cz

Received 29 July 2013, revised 27 January 2014

Accepted for publication 30 January 2014

Published 20 March 2014

## Abstract

A spatially resolved two-dimensional quantitative measurement of OH concentration in an effluent of a radio-frequency-driven atmospheric pressure plasma jet ignited in argon is presented. The measurement is supported by a gas dynamics model which gives detailed information about the spatially resolved gas composition and temperature. The volume in which the OH radicals were found and partially also the total amount of OH radicals increase with the argon flow rate, up to a value for which the flow becomes turbulent. In the turbulent regime, both the emission from the jet and the OH concentration are confined to a smaller volume. The maximum concentration of about  $5.4 \times 10^{21} \text{ m}^{-3}$  is reached at the tip of the visible discharge at the flow rate of 0.6 slm and high driving powers. An increase in hydroxyl concentration due to admixing of humid ambient air to the argon flow was observed.

Keywords: planar laser induced fluorescence, hydroxyl radical, OH, spatially resolved, atmospheric pressure, radio-frequency plasma jet, gas dynamics simulation

(Some figures may appear in colour only in the online journal)

## 1. Introduction

Atmospheric pressure discharges are the focus of intense scientific research, largely owing to their great potential for real-life applications. The presence of reactive radicals is one of the key components to the compound effect of the plasma. However, their concentration under various conditions of the discharges in the open atmosphere is rather difficult to obtain. Laser-induced fluorescence (LIF) is one of the few methods capable of such measurements, with the advantage of being suitable to obtain two-dimensional images with very good spatial resolution.

The works focusing on LIF of OH are numerous. It is a well-established method for visualizing various aspects of a combustion process, e.g. [1–4] and many others. In an optically thick environment, a combination of LIF and absorption measurement can be used to obtain quantitative

results [5, 6]. However, atmospheric pressure plasmas are often optically thin and reasonable absorption measurement is possible only upon multiple passing of the laser through the discharge, as in the cavity ring-down spectroscopy method.

Several works have used a planar LIF setup to display spatially resolved fluorescence in a discharge but have used a single photomultiplier for calibrated measurement to increase the signal-to-noise (S/N) ratio [7, 8]. Extending the usual LIF scheme to higher energies of exciting laser pulses, i.e. the region of weak saturation as in [9, 10], allows us to increase the S/N ratio while preserving the advantages of a planar LIF setup.

The measurements are supported by a gas dynamics model. There have been several works dealing with this problem for thermal argon plasma jets [11–13]. Although some of the models are in principle quite similar to the model presented in this work, the related simulations focus

only on thermal plasma jets characterized by temperature and velocity very different from our discharge. Moreover, the model presented in this work uses a somewhat different, and presumably more accurate, method of calculating the thermodynamic properties of the mixture. The model is validated against the experiment and provides a tool for predicting the gas composition in the jet when only the flow rate and inlet temperature are known. Apart from argon jet simulations, there have been several works focusing on numerical simulations of helium jets emerging into ambient air [14–16].

In this paper, we present an application of the procedure introduced in our previous publication [10] to spatially resolved two-dimensional images of the fluorescence in order to obtain a cross-section of the OH concentration in the effluent of the plasma pencil.

## 2. Experimental setup

### 2.1. Plasma pencil

The plasma pencil is a monoelectrode RF plasma jet ignited in argon flowing through a silica capillary [17, 18]. The electrode is placed at the outer surface of the silica capillary and is driven by RF voltage with frequency 13.56 MHz. The argon flows through the capillary (with the inner diameter of 2 mm) to ambient air. The discharge is ignited in a region with relatively pure argon, both inside the capillary and in the effluent, where the plasma can be used, e.g., for surface treatment. In the presented experiments, the argon flow rate was varied between 0.25 and 4 slm, and RF power was varied between 65 and 100 W.

Argon was supplied to the plasma pencil through stainless steel and polyethylene tubing. However, the last part of the tubing was made from silicone because of its resistance to high temperatures. Its high permeability for gases can be used for supplying water vapour to argon. Therefore, 60 cm of the silicone tube (with 1 mm wall thickness) were immersed into distilled water. The resulting humidity of argon was measured by a capacitive aluminum oxide moisture sensor (Panametrics, MMS 35) with the calibration range from  $0.4 \mu\text{g l}^{-1}$  (frost point  $-80^\circ\text{C}$ ). During the experiments, the humidity of argon flowing to the jet was in the range  $120\text{--}760 \mu\text{g l}^{-1}$  (frost point  $-38.1$  to  $-19.9^\circ\text{C}$ ), see table 1. The relative humidity of ambient air was 46% at the temperature of  $25^\circ\text{C}$ , which corresponds to the absolute humidity  $11 \text{ mg l}^{-1}$ .

### 2.2. Optical setup

The scheme of the experiment is shown in figure 1. A frequency-doubled pulsed Nd:YAG laser (Quanta-Ray PRO-270-30) was used to pump a dye laser (Sirah PRSC-D-24-EG). The dye laser radiation was further frequency-doubled to the wavelength of absorption, around 306.5 nm. The  $R_1(2)$ ,  $R_1(4)$  and  $R_1(7)$  lines<sup>3</sup> of the  $A^2\Sigma^+(v' = 0) \leftarrow X^2\Pi(v'' = 0)$  transition were used for excitation. Whenever lower temperatures were expected (low driving power or

<sup>3</sup> Hund's case (b) notation is used in this paper.

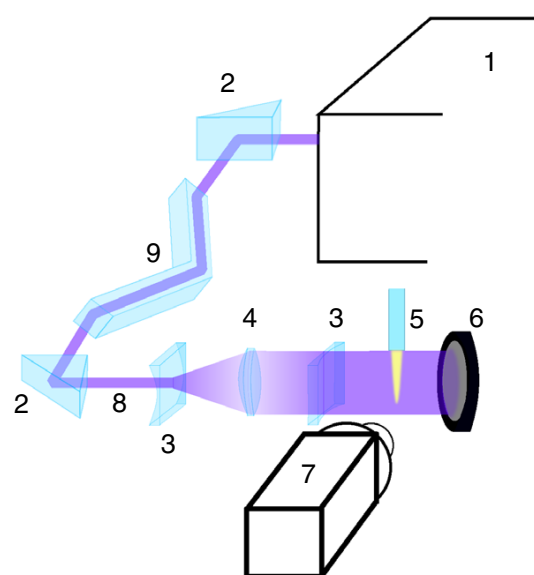


**Figure 1.** Experimental setup: 1—dye laser with frequency doubling unit, 2—right-angle prism, 3—cylindrical negative lens, 4—spherical positive lens, 5—plasma pencil, 6—laser power meter, 7—ICCD detector, 8—laser beam, 9—Fresnel rhomb (turns polarization).

high argon flow rates), the  $R_1(5)$  or  $R_1(6)$  line was used in addition to increase the accuracy. The laser power was varied between 20 and  $200 \mu\text{J}$  for the gain parameter measurement, see section 3.1. The manufacturer's documentation states the spectral width of the output laser line to be approximately 0.4 pm. The output beam polarization is horizontal, which is disadvantageous for the Rayleigh-scattering measurement used for calibration (see section 3.5). Therefore, a Fresnel rhomb was used to turn the laser polarization to vertical. The laser was expanded to a sheet using a telescope—a horizontally oriented negative cylindrical lens for vertical expansion, a spherical positive lens for vertical collimation and horizontal shrinking and a vertically oriented cylindrical negative lens for horizontal collimation. The resulting sheet was oriented vertically, along the axis of the plasma pencil capillary. The thickness of the sheet was significantly lower than the inner diameter of the capillary. The height of the sheet is limited by the mounting of the lenses (25.4 mm). The intensity also gradually decreases upwards and downwards from the centre. Spatially and temporally integrated energy of each laser pulse was measured by a pyroelectric head and logged to a computer file.

The fluorescence was measured by an ICCD camera (PI-MAX 1024RB-25-FG43, 16-bit grey-scale resolution) with an objective lens. The spatial resolution was around  $100 \mu\text{m}$  per pixel. The fluorescence signal was much stronger than the spontaneous emission. Therefore, no wavelength filter was used and the spontaneous emission was subtracted as background. To avoid recording of the scattered laser light, the acquisition gate was set to start after the end of the laser pulse.

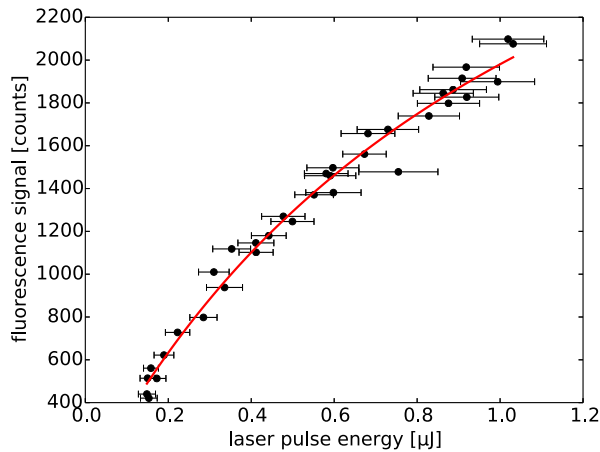


**Figure 2.** An example of fitting equation (1) for RF driving power of 80 W and argon flow rate of 0.6 slm for a single pixel at the position  $x = 0.0$  mm,  $y = 1.7$  mm. The fluorescence signal ( $R_1(2)$  excitation) is shown after the background subtraction. The laser energy is shown per the particular pixel row, i.e. after the correction described in section 3.5. The fitted parameter is  $\alpha_F = (3720 \pm 140)$  counts  $\mu\text{J}^{-1.4}$ .

### 3. Measurement

#### 3.1. Weak saturation

If the laser power is kept sufficiently low, the fluorescence versus laser power dependence can be expressed as

$$M_F = \frac{\alpha_F(x, y) E_{LF}(y)}{1 + \beta(x, y) E_{LF}(y)}, \quad (1)$$

where  $M_F$  is the measured fluorescence signal,  $\beta$  is a parameter introduced because of the saturation effects,  $E_{LF}(y)$  is the measured laser pulse energy per pixel row (see section 3.5) and  $\alpha_F E_{LF}$  is the theoretical unsaturated signal [9]. During the measurement series of 35 images, the laser pulse energy was varied in a step-wise manner and recorded together with the fluorescence signal. An image of the spontaneous emission of the discharge with identical detector settings and discharge conditions was subtracted as background. Equation (1) was fitted to the measured dependence. An example is shown in figure 2. The images were taken with 350 ns gate width and 100 on-CCD accumulations. For the argon flow rate of 4.0 slm, the gate was set to 700 ns due to the extremely long lifetime of the excited OH (up to 180 ns).

This measurement was carried out for excitations through all absorption lines.

#### 3.2. Rotational equilibrium

In [10] we justified the assumption that in both the excited and the ground electronic states, the rotational thermal equilibrium is reached rapidly and maintained during the whole fluorescence process. The emission coefficient can be then expressed as a weighted average of the emission coefficients

<sup>4</sup> All the errors reported in this paper are the standard deviations (68% confidence interval).

for particular rotational lines with the weight given by the appropriate Boltzmann fraction for the particular upper states:

$$A(v'=0) = \sum_{v''} \sum_{(N', J')} \sum_{(N'', J'')} \frac{(2J' + 1) e^{-E_{N'}/(kT)} A_{v'', (N', J'), (N'', J'')}}{\sum_{J'} (2J' + 1) e^{-E_{N'}/(kT)}}, \quad (2)$$

where single primed values are related to the upper state of the transition whereas the double primed values are related to the lower one. The rovibronic states are labelled by the quantum numbers  $N$  and  $J$  to specify both the rotational state and the respective spin doublet component,  $k$  is Boltzmann's constant,  $T$  is the rotational temperature and the rotational energy  $E_N$  is calculated from the rotational number according to [19].

Very similar reasoning is applied to the lower state. For example, when  $R_1(4)$  line was used for excitation, the measured concentration is that of the OH in the state with  $N'' = 4$ ,  $J = 9/2$ , parity  $e$ . To obtain the total concentration of OH in the ground vibronic state, we must divide the result by the appropriate Boltzmann fraction

$$\frac{1}{f_B(T, N'', J'')} = \frac{\sum_{(N'', J'')} 2(2J'' + 1) e^{-E_{N''}/(kT)}}{(2 \times 9/2 + 1) e^{-E_4/(kT)}}, \quad (3)$$

where the factor of 2 in the numerator comes from the assumption that the  $\Lambda$ -doublet components of the  $^2\Pi$  state are degenerate. It is not in the numerator, since the  $R_1(4)$  transition is allowed only from the  $e$ -parity component by the parity selection rule and the absorption coefficients in LIFBASE 2.1.1, used in this work, take the  $\Lambda$ -doubling into account. Similar arguments apply to all used absorption lines.

The calculated mean emission coefficient and Boltzmann fraction for the range of temperatures relevant for this publication are shown in figure 3.

#### 3.3. Rotational temperature measurement

The rotational temperature of the OH radicals may be extracted by comparing the fluorescence signal induced by exciting from different rotational states of the ground vibronic state. Under the assumption that rotational thermal equilibrium in the excited vibronic state is reached rapidly, the fluorescence signal is expected not to depend on the exact rotational state populated by the laser excitation. The strength of the fluorescence signal is given by the Einstein coefficient for absorption and the population of the lower state of the transition which, in thermal equilibrium, is governed by the Boltzmann distribution, see (3).

The dependence of the fluorescence signal on the laser power, as described in section 3.1, was measured for different rotational lines. For every pixel of each measurement, the gain parameter  $\alpha_F(x, y, N'', J'')$  was determined. Then, for each pixel, a Boltzmann plot was constructed, with the rotational energies of the lower states of the particular transitions on the  $x$ -axis and the following logarithm on the  $y$ -axis:

$$\ln \left( \frac{\alpha_F(x, y, N'', J'')}{(2J'' + 1) B(N', J', N'', J'')} \right), \quad (4)$$

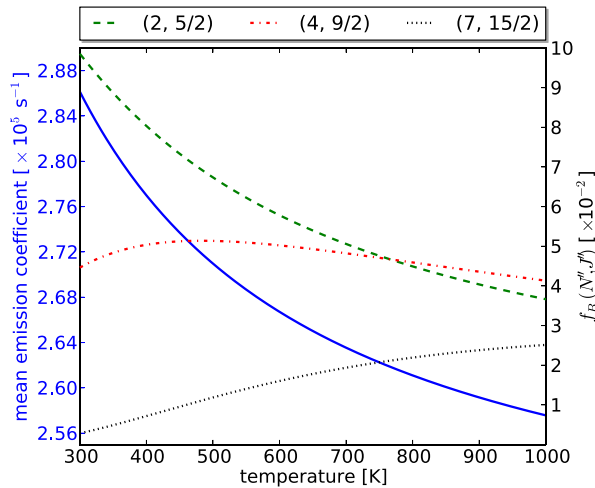


**Figure 3.** Mean emission coefficient (blue, solid) and Boltzmann fractions of the states, labelled in the legend by their quantum numbers ( $N''$ ,  $J''$ ), calculated according to equations (2) and (3) versus the rotational temperature in the range relevant for the presented experiment.

where  $B(N', J', N'', J'')$  is the Einstein coefficient for absorption between states ( $N''$ ,  $J''$ ) and ( $N'$ ,  $J'$ ). The slope of the linear regression line of the Boltzmann plot equals  $-1/(kT)$ . This can be done for every pixel with sufficiently strong signal, resulting in a map of rotational temperature of the OH radicals.

In the preparation phase of the experiment, this procedure was performed for seven different rotational lines— $R_1(2-7)$  and  $R_2(6)$ . An example of the linear regression line is shown in figure 4. As can be seen, the linear regression fits well. This further supports the expectation, implicitly assumed when using formula (3) that the rotational thermal equilibrium is reached in the ground vibronic state. The Boltzmann plot suggests that a fairly reliable measurement could be achieved with as few as three rotational transitions. This was indeed the standard number of  $\alpha_F(x, y, N'', J'')$  measurements in the presented experiment. The lines  $R_1(2)$ ,  $R_1(4)$  and  $R_1(7)$  were selected, because the rotational states with  $N'' > 7$  are usually populated quite weakly at the temperatures found in the plasma pencil. For high argon flow rates or lower driving power, the signal from the  $R_1(7)$  line was quite weak and also excitation through the  $R_1(6)$  or  $R_1(5)$  lines was used to increase the reliability of the measurement. The resulting temperature maps are shown in figure 5.

### 3.4. Temporally resolved fluorescence measurement

The assumption of rotational thermal equilibrium implies that the depopulation of the upper vibronic state after the end of the laser pulse can be described by a single exponential with lifetime  $\tau$ . Spatially resolved  $\tau$  measurement is based on the assumption that the plasma does not change over the time of the measurement. A series of fluorescence images was taken with the gate width of 5 ns. The gate delay with respect to the laser pulse was increased in exponentially increasing steps.

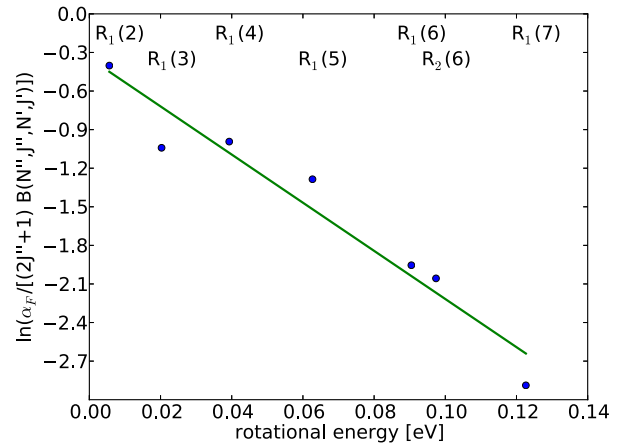


**Figure 4.** An example of the regression line fitted to the measured fluorescence signal for different rotational transitions. The transitions used to access the particular rotational states are indicated on the top of the plot. The discharge driving power was 80 W, the argon flow rate was 0.6 slm. A pixel at the discharge axis  $x = 0$ ,  $y = 1.7$  mm is presented. The rotational temperature from the fit is  $T = (620 \pm 9)$  K.

Each image was recorded with 500 on-CCD accumulations. A single exponential was then fitted to the measured data for each pixel, see figure 6. The product  $\tau \times A_{(v'=0)}$  defines the quantum efficiency of the fluorescence.

Since the measurement described in section 3.1 starts after the end of the laser pulse, a correction must be introduced to take into account the portion of fluorescence that took place before the start of the measurement. A convolution of a single exponential decay with the measured lifetime  $\tau$  and of the laser pulse is calculated to reconstruct the full temporal profile of the fluorescence and determine the portion of fluorescence lost. The laser temporal profile for the sake of this reconstruction was measured by a fast photodiode and its temporal shape is assumed to be independent of spatial coordinates.

### 3.5. Calibration by Rayleigh scattering

The detection sensitivity is calibrated by Rayleigh scattering on laboratory air. The cross section for the scattering into the direction of the detector,  $4\pi (d\sigma_{RS}/d\Omega)$ , obtained from [20, 21] is  $7.12 \times 10^{-30} \text{ m}^2$ . The fraction  $p_{\text{air}}/kT_{\text{air}}$  expresses the concentration of air particles in terms of pressure and temperature in the laboratory and Boltzmann's constant.

The expansion of the laser to the sheet is not homogeneous and a correction must therefore be introduced. In the region of interest, the laser power distribution in the vertical direction ( $y$ ) did not depend on the position in the direction of the laser propagation ( $x$ ). The vertical laser power distribution  $E_{\text{LRS}}(y)$  is then calculated from the Rayleigh scattering measurement  $M_{\text{RS}}(x, y)$  as

$$E_{\text{LRS}}(y) = \frac{\sum_x M_{\text{RS}}(x, y)}{\sum_y \sum_x M_{\text{RS}}(x, y)} \times E_{\text{meas, RS}} \quad (5)$$

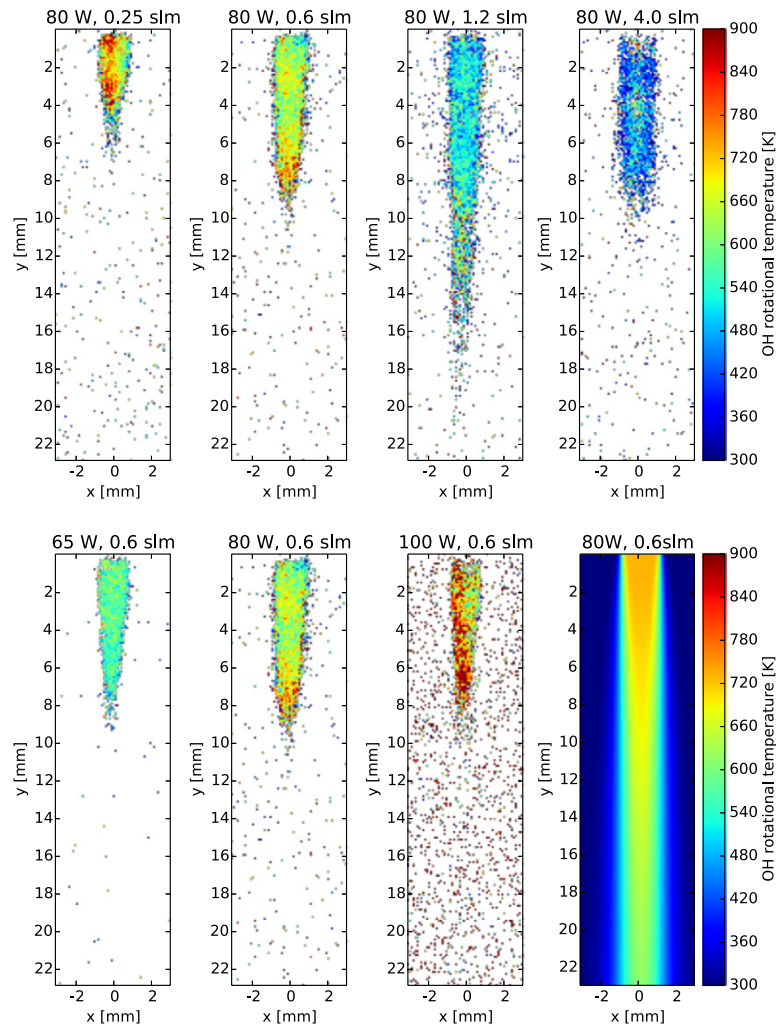


**Figure 5.** The measured temperature maps for various discharge conditions. A sample of the temperature from the model for 80 W, 0.6 slm is shown at the bottom right.

with  $x$  and  $y$  being the coordinates of individual pixels and  $E_{\text{meas, RS}}$  is the spatially integrated laser pulse energy measured by the pyroelectric head. Since we assumed that the vertical distribution did not change in time, the same profile was used for fluorescence measurement:

$$E_{\text{LF}}(y) = \frac{\sum_x M_{\text{RS}}(x, y)}{\sum_y \sum_x M_{\text{RS}}(x, y)} \times E_{\text{meas, F}}, \quad (6)$$

where  $E_{\text{meas, F}}$  is the spatially integrated laser pulse energy measured by the pyroelectric head during the fluorescence measurement.

The purpose of the calibration is to find the gain of the Rayleigh scattering  $M_{\text{RS}}(x, y)/E_{\text{LRS}}(y)$  of each pixel for given laser sheet geometry and wavelength and for the particular scattering medium. In accordance with prior tests of the detector, the gain map appears to be homogeneous and the gain of 99% of the pixels was in the interval (2.304; 2.315) counts per  $\mu\text{J}$  of the laser pulse energy.

### 3.6. Calculating the OH concentration

Putting the parameters from the preceding sections together, the following formula for OH concentration can be derived (see [10] for a more detailed treatment)

$$n_{\text{OH}}(x, y) = \frac{\alpha_{\text{F}}(x, y, N'', J'')}{\tau(x, y) A_{(v'=0)}(T_{\text{OH}}(x, y))} \frac{E_{\text{LRS}}(y)}{M_{\text{RS}}(x, y)} \frac{p_{\text{air}}}{k T_{\text{air}}} \times \frac{4\pi (d\sigma_{\text{RS}}/d\Omega)}{\kappa \sigma_{\text{abs}}(N', J', N'', J'')} \frac{1}{f_{\text{B}}(T_{\text{OH}}(x, y), N'', J'')}. \quad (7)$$

In the equation above,  $\kappa = (8.2 \pm 2.5) \times 10^{-11}$  s is the overlap term of the absorption line and the laser line<sup>5</sup>,  $\sigma_{\text{abs}}$  is the cross section for absorption that can be obtained from the tabulated Einstein coefficients  $B_{\text{abs}}$  as  $\sigma_{\text{abs}} = h\nu B_{\text{abs}}/c$ , where  $h\nu$  is

<sup>5</sup> The overlap term was determined for three different absorption lines at different positions in the discharge. No obvious correlation between the value of  $\kappa$  and other conditions was observed. The reported value is the arithmetic average and the error is the standard deviation of the different results.

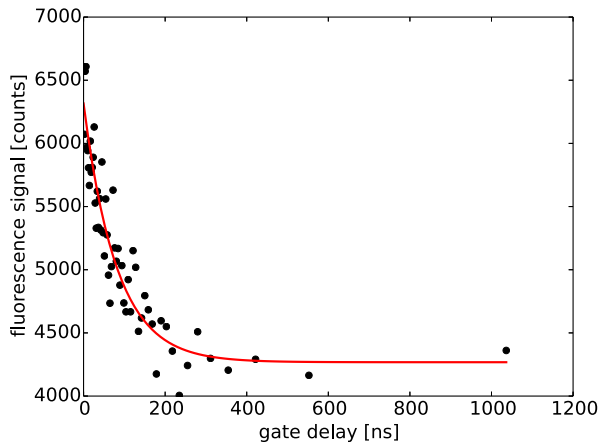


**Figure 6.** An example of the single exponential fit to the measured decay of the fluorescence signal for RF driving power of 80 W and argon flow rate of 0.6 slm at the position  $x = 0.0$  mm,  $y = 1.7$  mm. The fitted lifetime is  $\tau = (81 \pm 10)$  ns.

the energy of the transition and  $c$  is the speed of light. All spectroscopic constants are taken from LIFBASE 2.1.1 [22].

### 3.7. Gas mixing estimation

The effective lifetime  $\tau$  of the excited OH is given by the inverse sum of the Einstein coefficient for emission  $A_{(v'=0)}$  and the rates of quenching by various collisional partners  $\sum Q_i$ . The rates  $Q_i$  can be expressed as a product of the concentration of the particular species  $n_i$  and its quenching coefficient  $q_i$ :

$$\frac{1}{\tau} = A_{(v'=0)}(T) + \sum n_i(T) q_i(T), \quad (8)$$

where, for fixed pressure, every term is temperature dependent. The measured maps of temperature  $T$  and lifetime  $\tau$  can be used to estimate the fraction of ambient air admixed into argon in the effluent.

The estimate is based on comparing the measured lifetime  $\tau_{\text{meas}}(x, y)$  of the excited OH with the theoretical predicted lifetime in the effluent gas  $\tau_{\text{Ar}}$  or in ambient air  $\tau_{\text{air}}$ . The effluent gas is assumed to be only argon with a small admixture of water. The amount of water is taken from the inlet gas humidity measurement summarized in table 1. The ambient air is assumed to consist of  $\text{N}_2$  (77.8%),  $\text{O}_2$  (20.9%) and  $\text{H}_2\text{O}$  (1.3%), which corresponds to the measured relative humidity of 46% mentioned in section 2.1. Other constituents, such as OH, are neglected. All constituents of the two environments are assumed to mix equally rapidly.

The predicted lifetimes  $\tau_{\text{Ar}}$  and  $\tau_{\text{air}}$  are obtained from LASKIN simulations [23]. The fluorescence process after the excitation through the  $\text{R}_1(4)$  line was simulated and the temporal profile of the total fluorescence was fitted with a single exponential decay to obtain the respective theoretical lifetime. Since the rates of collision-induced energy transfer in LASKIN are temperature dependent, the simulations for the respective gas mixture were performed for temperatures between 300 and 1000 K in steps of 25 K. The molar fraction

of the ambient air admixed into the effluent gas is then calculated as

$$\frac{n_{\text{air}}}{n_{\text{Ar}} + n_{\text{air}}} = \frac{1/\tau_{\text{meas}}(x, y) - 1/\tau_{\text{Ar}}(T(x, y))}{1/\tau_{\text{air}}(T(x, y)) - 1/\tau_{\text{Ar}}(T(x, y))}, \quad (9)$$

where  $T(x, y)$  is the temperature from the simulated set closest to the value from the respective temperature map for the particular discharge conditions. The resulting maps of the molar fraction of ambient air admixed into the effluent are shown in figure 7. Points with large relative error (>25%) of the temperature or the measured lifetime are omitted.

## 4. Gas dynamics simulations

The measurements presented in this work are complemented by a gas dynamics model. The main motivation for the model is to obtain a tool that would allow us to predict the gas composition for various flow rates when the gas temperature near the inlet is known. Furthermore, the results obtained from the model strongly support the hypothesis that the contraction of the jet at higher flow rates is caused by turbulent admixing of air. The model describes the gas flow of hot argon and its mixing with room temperature air. As mentioned above, the temperature at the inlet is the only experimental input, although the gas mixing is relatively insensitive to temperature changes.

The model was developed using the COMSOL Multiphysics [24] platform. It solves the stationary Navier–Stokes equations for laminar and turbulent flows of an inhomogeneous argon–air gas mixture self-consistently with the diffusion equation for argon–air mixing and the heat equation for the mixture. Even though the Reynolds number near the inlet is of the order  $10^1$ – $10^3$  for flow rates between 0.1 and 5 slm, practice shows that the flow is laminar at least up to 2.0 slm and turbulence certainly develops above 3.0 slm. The fluid model is, of course, not capable of describing the transition between laminar and turbulent flows but can provide reliable results for both fully laminar and fully turbulent flow regimes.

As far as turbulence is concerned, the Reynolds-averaged Navier–Stokes (RANS) equation is solved, which accounts for the turbulence through additional turbulent viscosity. To obtain the turbulent viscosity, the RANS equation is solved together with the standard two-equation  $k$ – $\varepsilon$  model [25]. The turbulent mixing is accounted for through additional diffusivity given by

$$D_T = \frac{\nu_T}{Sc_T} \quad (10)$$

with  $\nu_T$  being the turbulent kinematic viscosity and  $Sc_T$  the turbulent Schmidt number, set to 0.7 [26].

The boundary conditions (BCs) imposed for the Navier–Stokes equations are the non-slip BC for velocity at the walls of the glass tube (with wall functions when turbulence is taken into account) and a Dirichlet BC for pressure at boundaries far away from the nozzle outlet,  $p = 1$  atm.

As far as diffusion is concerned, we have used a Fick-like expression for the flux with the diffusion coefficient calculated from binary diffusion coefficients using the rule of mixtures

$$D_i = \frac{1 - \omega_i}{\sum_{j \neq i} (x_j / \mathcal{D}_{ij})}. \quad (11)$$

**Table 1.** Summary of discharge conditions and main results.  $P_{\text{RF}}$  is the driving RF power,  $Q_{\text{Ar}}$  is the argon feed gas flow rate, the humidity is that of the argon gas on the inlet. The temperature  $T$  is the rotational temperature from the measurements shown in figure 5 and is averaged over the region with strong fluorescence signal. The maximal OH concentration  $[\text{OH}]_{\text{max}}$  is averaged over several pixels in the region with maximum concentration values. The method for estimating the total amount of OH radicals is described in section 5.

$P_{\text{RF}}$ (W)	$Q_{\text{Ar}}$ (slm)	Humidity ( $\mu\text{g l}^{-1}$ )	$T$ (K)	$[\text{OH}]_{\text{max}}$ ( $\text{m}^{-3}$ )	OH amount estimate
65	0.6	450	560	$5.4 \times 10^{21}$	$4.6 \times 10^{13}$
80	0.25	760	640	$3.8 \times 10^{21}$	$2.2 \times 10^{13}$
80	0.6	450	640	$5.4 \times 10^{21}$	$8.4 \times 10^{13}$
80	1.2	300	520	$4.4 \times 10^{21}$	$9.2 \times 10^{13}$
80	4.0	120	440	$2.2 \times 10^{21}$	$3.8 \times 10^{13}$
100	0.6	450	730	$4.8 \times 10^{21}$	$8.4 \times 10^{13}$

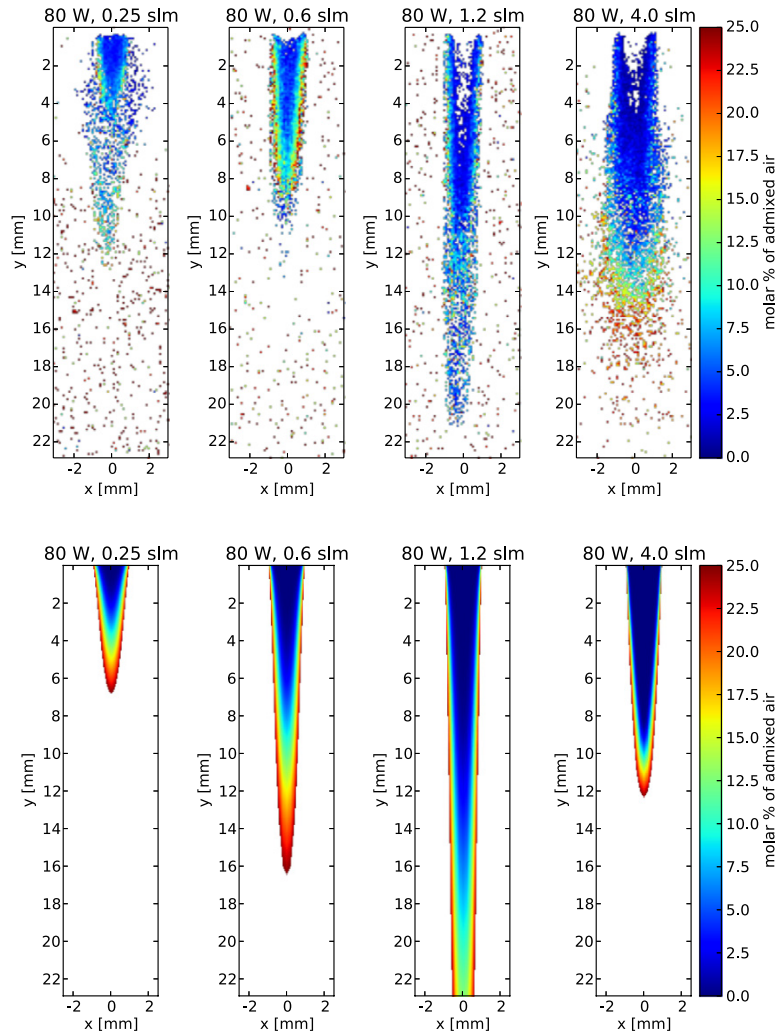


**Figure 7.** Estimate of the molar fraction of admixed ambient air into the effluent gas for different argon flow rates at the driving power of 80 W. The measurements are shown above, the results from the model below.

where the binary diffusion coefficient  $\mathcal{D}_{ij}$  is calculated from the Chapman–Enskog theory [27]:

$$\mathcal{D}_{ij} = \frac{1.86 \times 10^{-3} \times T^{3/2} \sqrt{M_i^{-1} + M_j^{-1}}}{p \sigma_{ij}^2 \Omega} \quad (\text{cm}^2 \text{s}^{-1}). \quad (12)$$

In the equation above, the temperature  $T$  is in kelvin,  $M_i$  are the components' molar masses in a.m.u.,  $\sigma_{ij}$  is a parameter

characteristic of the gas pair and  $\Omega$  is a collision integral depending on the temperature to Lennard-Jones potential ratio. Both  $\sigma_{ij}$  and  $\Omega$  are tabulated in [27]. A Dirichlet BC for the mass fraction,  $\omega_{\text{Ar}} = 1$ , is imposed at the nozzle outlet.

As far as the heat equation is concerned, we use the Dirichlet BC for temperature at the inlet,  $T_{\text{inl}}$ , taken from experimental measurement of the rotational spectra. By doing so, we implicitly assume that the neutral gas heating occurs

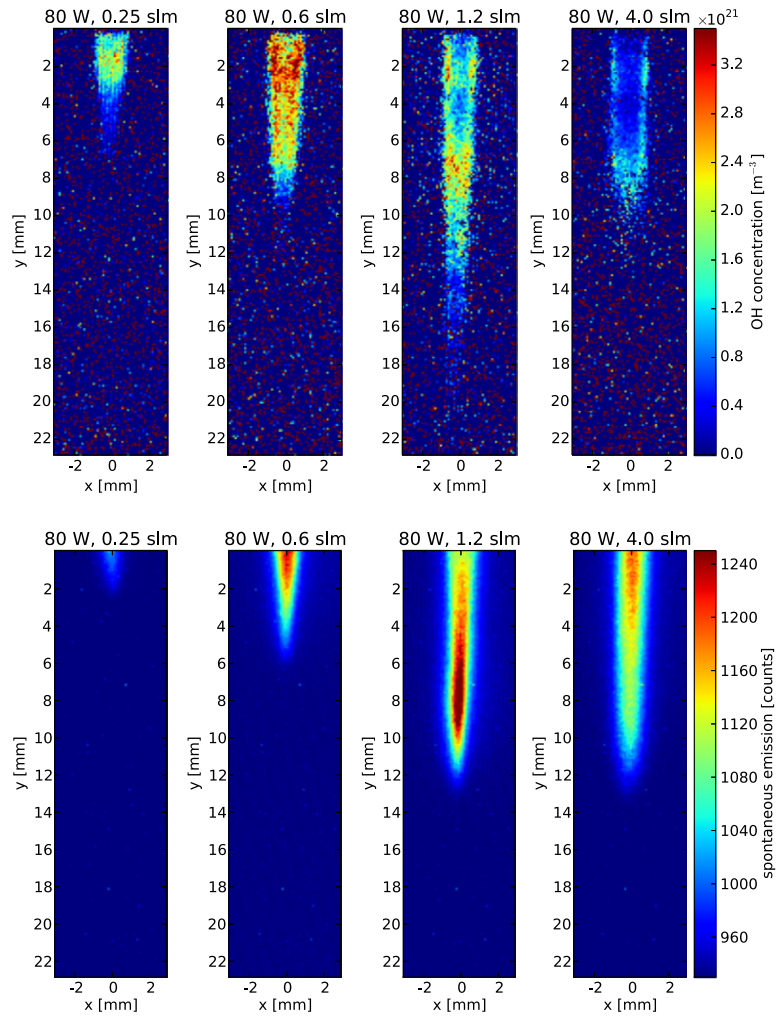


**Figure 8.** Spatially resolved OH concentration (top) and spontaneous emission of the discharge (bottom) for various argon flow rates at the driving power of 80 W.

primarily inside the glass tube and not in the jet itself. At other boundaries, the homogeneous Neumann BC is imposed.

The thermal conductivity in the heat equation and the viscosity in the Navier–Stokes equations are not only functions of temperature but also of the local gas composition, which introduces additional strong coupling between all the equations. For this reason, a good initial estimate is necessary for the self-consistent solution to converge. The initial estimate was obtained by solving the equations uncoupled and taking the results as the initial condition.

The thermal conductivity  $\lambda_{\text{mix}}$  and viscosity  $\mu_{\text{mix}}$  of the mixture were calculated from the components' thermal conductivities and viscosities using the equations derived for viscosity in [28].

$$\mu_{\text{mix}} = \sum_i \frac{\mu_i}{1 + (1/x_i) \sum_{j \neq i} x_j \Phi_{ij}} \quad (13)$$

and an analogous equation for thermal conductivity [29]. In equation (13), both the indices  $i$  and  $j$  run over all species and

$\Phi_{ij}$  is a semi-empirical weighting parameter depending on the components' molar masses and viscosities [28].

The validity of the model was tested by a direct comparison with the experiment. In particular, the molar fraction of ambient air admixed into the flowing argon was chosen as the testing variable. Experimentally, this was determined from the lifetime of OH radicals in the  $A^2\Sigma$  state, similarly to [30], see section 3.7. The agreement between the experiment and the model is shown in figure 7.

## 5. Results

The OH concentration was measured for six different discharge conditions. Both the argon flow rate and the driving RF power were varied. The results are presented in figures 8 and 9. The maximal concentration of about  $5.4 \times 10^{21} \text{ m}^{-3}$  was reached at the flow rate of 0.6 slm and high RF powers.

By comparing the images of the visible discharge in figures 8 and 9 with results in figure 7 we can see that the active discharge is very sensitive to impurities. Except at the

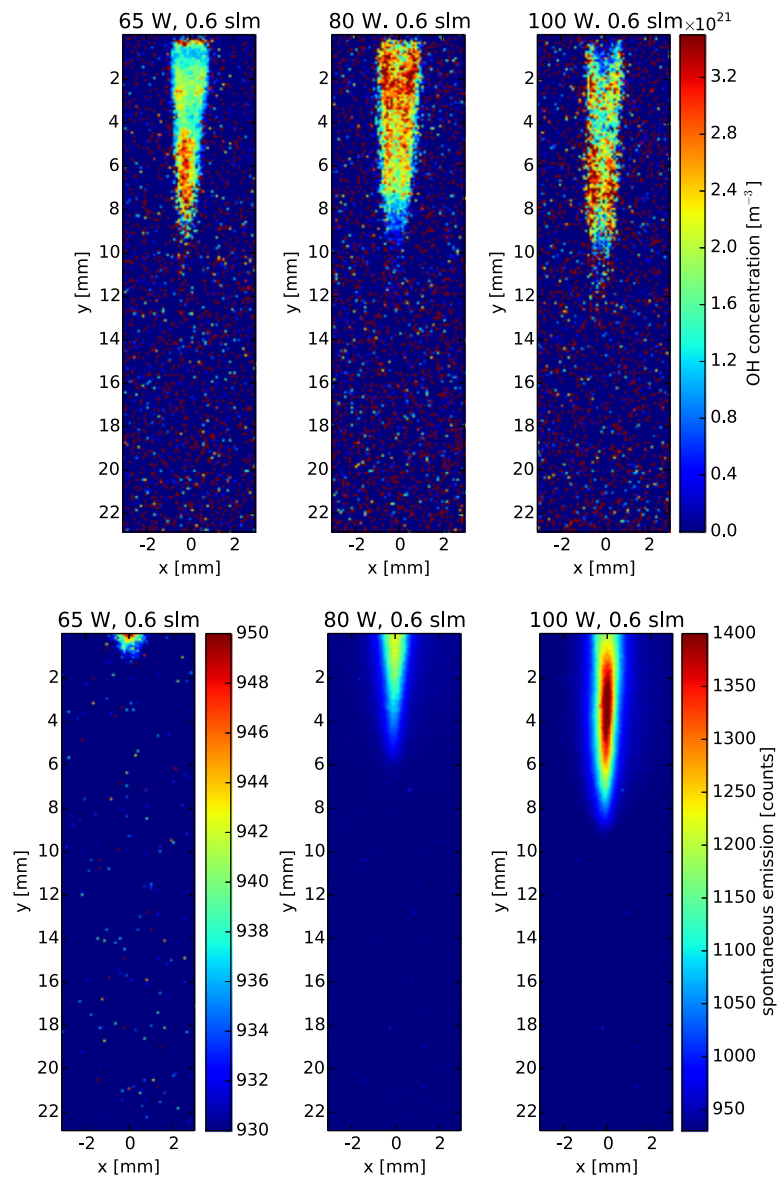


**Figure 9.** Spatially resolved OH concentration (top) and spontaneous emission of the discharge (bottom) for various driving powers at the argon flow rate of 0.6 slm.

power of 100 W and the argon flow rates greater than 1.2 slm, the tip of the visible discharge is in the region with less than 3% of admixed air. The elongation of the active discharge into the region with higher air molar fraction with increasing argon flow rate is probably due to higher velocity of the energetic particles.

Under most of the experimental conditions, the region with the highest OH concentration was found close to the tip of the visible discharge. This is in agreement with the hypothesis proposed in [10] that the electric field strength and thus the mean electron energy is expected to be highest at the tip of the visible discharge, where the electron density quickly drops. Consequently, the rate of OH production from  $\text{H}_2\text{O}$  molecules by electron impact is expected to reach its maximum at the discharge tip. This is similar to the situation

in streamers, where the highest dissociation is known to occur at the streamer head [31]. In addition, there are two other mechanisms that help us to place the hydroxyl concentration maximum to the discharge tip. Firstly, the hydroxyl radical is produced not only at the discharge tip but also inside the whole discharge. Since the hydroxyl lifetime in pure argon is long, hydroxyl concentration should rise from the interior of the capillary towards the discharge tip due to its accumulation. Secondly, the ambient air humidity is much higher than the humidity of argon, see section 2.1. Therefore, the highest concentration of water molecules inside the active discharge must be placed at its tip due to higher amount of admixed air. This fact further increases the dissociation rate of  $\text{H}_2\text{O}$  molecules at the discharge tip. The increase in hydroxyl concentration caused by air admixing is visible also at side

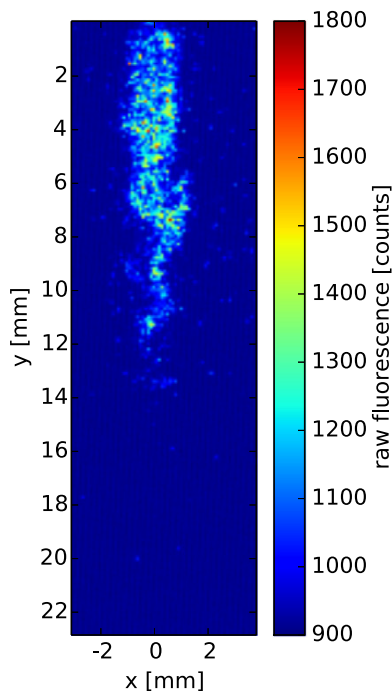


**Figure 10.** Single-shot image of OH raw fluorescence and the (weak) background spontaneous emission in the turbulent regime (80 W, 4.0 slm). No corrections are applied to this image.

edges of the discharge. Most of the hydroxyl concentration maps shown in figures 8 and 9 reveal local concentration maxima at the sides of the discharge, especially close to the capillary where the humidity at the discharge axis is the lowest. The small shift of maximum hydroxyl concentration under the position of the visible discharge tip at argon flow rate 0.6 slm and RF powers 65 and 80 W indicates that, together with  $\text{H}_2\text{O}$  dissociation by electron impact, the dissociation by reaction with argon metastables [32] plays a role.

Different situation with maximum hydroxyl concentration in the region of the visible discharge was found only at 80 W, 1.2 slm. These conditions are atypical due to a low power density (the discharge was elongated without any increase in delivered RF power). In addition, changes of plasma chemistry due to the high air concentration at the tip of the visible discharge are expected to play a significant role, see e.g. [33].

Increasing the argon flow rate to approximately 3 slm led to an elongation of the active discharge. However, a further increase in argon flow was accompanied by shortening of the discharge and quiet rustling caused by transition of the flow to the turbulent regime. The turbulent character of the flow was clearly visible on single-shot images of hydroxyl LIF, see figure 10. The turbulences led to an increase in gas mixing shown in figure 7 and an increase in the discharge width. The measured rotational temperature in the turbulent regime is significantly lower compared with the other cases. In addition to the cooling by stronger gas flow, this is partially owed to the fact that many pixels were outside the active discharge during some of the individual laser shots due to the turbulence instabilities, see figure 10.

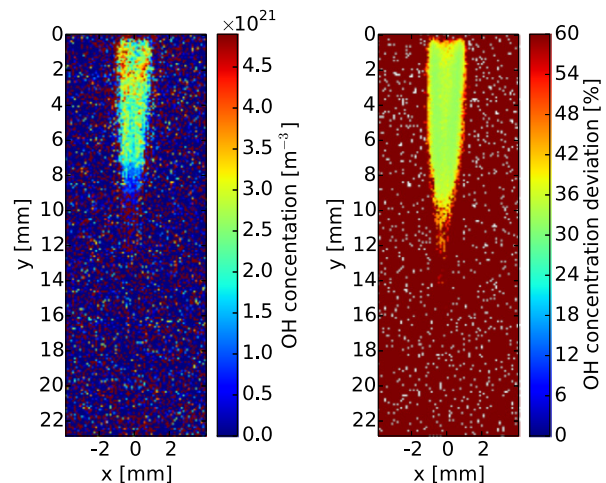


**Figure 11.** A typical relative standard deviation of the OH concentration from the error propagation formula applied to the standard deviation of the parameters in formula (7). The shown example was obtained for driving power of 80 W and argon flow rate of 0.6 slm.

The relative uncertainty of the results is roughly indirectly proportional to the fluorescence intensity. The application of the standard error propagation formula to the uncertainty of the fit parameters yields a value around 35% in the region with maximal OH concentration as can be seen in figure 11. The main contribution to the uncertainty was from the uncertainty of the overlap parameter  $\kappa$ . The concentration maps obtained by exciting through different absorption lines were in very good agreement with each other because of the linearity of the Boltzmann plots, as mentioned in section 3.3.

A rough estimate of the total amount of OH radicals in the effluent was made. It is based on the assumption that the laser plane is very thin compared with the effluent and passing right through the axis of rotational symmetry. The OH concentration was integrated over the region with less than 50% relative uncertainty. Since the relative uncertainty was well anti-correlated with the found OH concentration, this can be considered a reasonable criterion for the region with OH presence. The results are shown in table 1. The amount of OH radicals is greater when the visible discharge is longer but the radicals are spread over a larger volume.

Maps of rotational temperature measured by LIF of hydroxyl radicals show the expected increase in gas temperature with increasing RF power. In addition, the gas temperature decreases with the increase in argon flow rate, see figure 5. In most of the measurements the temperature maps reveal maximum gas heating at the discharge tip, which is consistent with the previous assumption of maximum electron temperature in this point. The rotational temperature measurement gave reliable data only in regions with sufficiently high concentration of hydroxyl radicals. Therefore, it can be trusted only inside and close to the active discharge. Outside this region, the temperature can be studied from gas dynamic simulations.

The numerical model was successfully validated against the experimental measurements (see figure 7). The model well



Masaryk University. The plots in this paper were produced with the help of the Matplotlib library [34].

## References

- [1] Allen M, McManus K, Sonnenfroh D and Paul P 1995 *Appl. Opt.* **34** 6287–300
- [2] Singla G, Scoufflaire P, Rolon C and Candel S 2006 *Combust. Flame* **144** 151–69
- [3] Cessou A and Stepowski D 1996 *Combust. Sci. Technol.* **118** 361–81
- [4] Kaminski C, Hult J and Aldén M 1999 *Appl. Phys. B: Lasers Opt.* **68** 757–60
- [5] Heinze J, Meier U, Behrendt T, Willert C, Geigle K P, Lammel O and Lückerrath R 2011 *Z. Phys. Chem.* **225** 1315–41
- [6] Versluis M, Georgiev N, Martinsson L, Aldén M and Kröll S 1997 *Appl. Phys. B: Lasers Opt.* **65** 411–7
- [7] Ono R and Oda T 2001 *IEEE Trans. Industry Appl.* **37** 709–14
- [8] Matsuda Y, Muta M and Fujiyama H 1999 *Thin Solid Films* **345** 167–71
- [9] Nemschokmichal S, Bernhardt F, Krames B and Meichsner J 2011 *J. Phys. D: Appl. Phys.* **44** 205201
- [10] Voráč J, Dvořák P, Procházka V, Ehlbeck J and Reuter S 2013 *Plasma Sources Sci. Technol.* **22** 025016
- [11] Cheng K and Chen X 2004 *Int. J. Heat Mass Transfer* **47** 5139–48
- [12] Shao X-J, Zhang G-J, Li Y-X, Zhang Z-H and Zhan J-Y 2011 *High Voltage Eng.* **37** 1775–80
- [13] Wang H-X, Chen X and Pan W 2007 *Plasma Chem. Plasma Process.* **27** 141–62
- [14] Breden D, Miki K and Raja L L 2011 *Appl. Phys. Lett.* **99** 111501
- [15] Naidis G V 2012 *J. Appl. Phys.* **112** 103304
- [16] Sakiyama Y, Graves D B, Jarrige J and Laroussi M 2010 *Appl. Phys. Lett.* **96** 041501
- [17] Janča J, Klíma M, Slaviček P and Zajíčková L 1999 *Surf. Coat. Technol.* **116** 547–51
- [18] Slaviček P, Brablec A, Kapička V, Klíma M and Šíra M 2005 *Acta Phys. Slovaca* **55** 573–6
- [19] Dieke G H and Crosswhite H M 1962 *J. Quant. Spectrosc. Radiat. Transfer* **2** 97–199
- [20] Miles R B, Lempert W R and Forkey J N 2001 *Meas. Sci. Technol.* **12** R33
- [21] Bucholtz A 1995 *Appl. Opt.* **34** 2765–73
- [22] Luque J and Crosley D 1999 *SRI International Report MP 99*
- [23] Bülter A, Lenhard U, Rahmann U, Kohse-Höinghaus K and Brockhinke A 2004 Laskin: Efficient simulation of spectra affected by energy transfer *Proc. LACEA 2004 (Laser Applications to Chemical and Environmental Analysis) (Annapolis)*
- [24] COMSOL, Inc 2013 COMSOL Multiphysics software 4.3a
- [25] Georgiadis N, Yoder D and Engblom W 2006 *AIAA J.* **44** 3107–14
- [26] Yimer I, Campbell I and Jiang L Y 2002 *Can. Aeronaut. Space J.* **48** 195–200
- [27] Cussler I L 2009 *Diffusion: Mass Transfer in Fluid Systems* 3rd edn (Cambridge: Cambridge University Press)
- [28] Wilke C R 1950 *J. Chem. Phys.* **18** 517
- [29] Bird R B, Stewart W E and Lightfoot E R 2002 *Transport Phenomena* 2nd edn (New York: Wiley)
- [30] Yonemori S, Nakagawa Y, Ono R and Oda T 2012 *J. Phys. D: Appl. Phys.* **45** 225202
- [31] Naidis G 2012 *Plasma Sources Sci. Technol.* **21** 042001
- [32] Xiong Q, Nikiforov A Y, Li L, Vanraes P, Britun N, Snyders R, Lu X P and Leys C 2012 *Eur. Phys. J. D* **66** 1–8
- [33] Komuro A, Ono R and Oda T 2013 *J. Phys. D: Appl. Phys.* **46** 175206
- [34] Hunter J D 2007 *Comput. Sci. Eng.* **9** 90–5

# Dependence of laser-induced fluorescence on exciting-laser power: partial saturation and laser – plasma interaction<sup>\*</sup>

Jan Voráč, Pavel Dvořák<sup>a</sup>, Vojtěch Procházka, Tomas Morávek, and Jozef Ráhel

Masaryk University, Faculty of Science, 61137 Brno, Czech Republic

Received: 15 January 2015 / Received in final form: 20 May 2015 / Accepted: 1 July 2015  
Published online: 31 July 2015 – © EDP Sciences 2015

**Abstract.** In recent publications on laser-induced fluorescence (LIF), the measurements are usually constricted to the region of weak exciting-laser power – the so called linear LIF. In this work, a practical formula describing the dependence of partially saturated fluorescence on the exciting-laser power is derived, together with practical implementation suggestions and comments on its limitations. In the conclusion, the practical formula

$$F(E_L) = \frac{\alpha E_L}{1 + \beta E_L}$$

is proposed with the limitation for validity  $\beta E_L \leq 0.4$ , where  $\alpha E_L$  is the hypothetical linear fluorescence without saturation effects, and a more general formula is derived, which is valid for higher values of  $\beta E_L$  as well. Extending the range of exciting laser power to the region of partial saturation enhances the signal-to-noise ratio. Such measurements in a surface dielectric barrier discharge further reveal discharge disruption by photoelectrons emitted from the dielectric surface. Methods of control and solution of this problem are discussed.

## 1 Introduction

Recent publications on selected particle concentration measurements by laser-induced fluorescence are usually constricted to the so-called linear regime, where the laser intensity is kept very low to avoid saturation effects [11, 15]. In this regime the strength of fluorescent signal is proportional to the intensity of the exciting laser. This fairly simplifies the evaluation of the measurements at the cost of weaker signal-to-noise ratio, compared to higher laser intensities.

An alternative approach – so called saturated LIF – was developed for the opposite limit. The laser power is intentionally so strong that the stimulated emission becomes the dominant process for depopulating the laser-excited state. For such cases, equilibrium may be reached and the theoretical analysis is often based on the assumption that, during the laser pulse, the populations of the levels of interest do not change with time. This technique is expected to be insensitive to quenching of the laser-excited state. An excellent review of this technique can be found in reference [5]. It is, however, very difficult to

achieve full saturation over the whole time and probed volume.

An extension of the linear LIF to the region of laser energies where the stimulated emission and the depletion of the ground state by the laser are no longer negligible may help to achieve better signal-to-noise ratio compared to the strictly linear case without the necessity to reach and maintain the full saturation. In references [7, 12–14] the response of the LIF signal to the changing laser-pulse energy  $E_L$  (spatially and temporally integrated intensity) was analysed, looking for the hypothetical fluorescence intensity in the absence of the saturation effects. For this purpose, an intuitive relation

$$F(E_L) = \frac{\alpha E_L}{1 + \beta E_L}, \quad (1)$$

was fitted to the measured dependence. The value  $\alpha E_L$  was assumed to express the hypothetical unsaturated fluorescence and the parameter  $\beta$ , without further insight, was said to describe the degree of saturation. It was observed, however, that the relation (1) holds only for weak saturation, say for  $\beta E_L < 0.4$ . If points with greater  $E_L$  were included in the fit, the results were significantly distorted, suggesting that formula (1) is correct only to the first few orders. The motivation for this work is to support formula (1) theoretically and offer a more general relation between the fluorescence signal and laser intensity.

<sup>a</sup> e-mail: pdvorak@physics.muni.cz

<sup>\*</sup> Contribution to the topical issue “The 14th International Symposium on High Pressure Low Temperature Plasma Chemistry (HAKONE XIV)”, edited by Nicolas Gherardi, Ronny Brandenburg and Lars Stollenwerk

## 2 Four-level model and numerical solutions

A four-level model, similar to that by Lucht and Laurendeau [6], by Dunn and Masri [4] or by Verreycken et al. [11], was implemented and used to test the theory derived in Section 3. Since there are some minor differences from the cited sources, we shall describe the model in detail.

The model is particularly suitable for a diatomic molecule excited from ground vibronic state to excited electronic state with  $v' = 0$ , i.e., for moderate temperatures (say  $< 1000$  K), there is no vibrational energy transfer that should be accounted for. However, as was shown by Verreycken et al. in reference [10], it can describe also more complicated cases with sufficient precision.

There are two laser-coupled rovibronic levels, here labelled with 0 and 1 and two bath levels (2, 3), see Figure 1. Before the laser pulse, the relative population of the 0 level will be equal to the rotational Boltzmann fraction,  $\frac{n_0}{n_0+n_3} = f_{B0}$ . As level 0 gets depleted by the laser excitation (with rate coefficient  $B_{01} I$ ), it is repopulated from the bath level 3 by rotational energy transfer (RET) ( $Q_{RET0}$ ) that strives to keep the system in rotational thermal equilibrium<sup>1</sup>. Similarly, as the molecules undergo the laser excitation to level 1, they are rapidly rotationally thermalised with rate  $Q_{RET1}$  until only the Boltzmann fraction  $f_{B1}$  (with respect to rotational levels) occupy the level 1 and the rest of excited molecules is in the level 2. The (directly or indirectly) excited molecules in the states 1 and 2 then undergo spontaneous transitions to the lower levels, either radiative ( $A_{10}, A_{13}, A_{20}, A_{23}$ ) or non-radiative caused by super-elastic collisions ( $Q_{10}, Q_{13}, Q_{20}, Q_{23}$ ). Level 1 can be also depopulated by stimulated emission with the rate  $B_{10} I$ . This can be written as a set of rate equations

$$\begin{aligned} \frac{dn_0}{dt} = & (-B_{01} I - (1 - f_{B0})Q_{RET0}) n_0 \\ & + (B_{10} I + A_{10} + Q_{10}) n_1 \\ & + (Q_{20} + A_{20}) n_2 + (f_{B0} Q_{RET0}) n_3, \end{aligned}$$

$$\begin{aligned} \frac{dn_1}{dt} = & B_{01} I n_0 + (-B_{10} I - A_{10} - Q_{10} \\ & - A_{13} - Q_{13} - (1 - f_{B1})Q_{RET1}) n_1 \\ & + f_{B1} Q_{RET1} n_2, \end{aligned}$$

$$\begin{aligned} \frac{dn_2}{dt} = & (1 - f_{B1}) Q_{RET1} n_1 + (-f_{B1} Q_{RET1} \\ & - A_{20} - Q_{20} - A_{23} - Q_{23}) n_2, \end{aligned}$$

$$\begin{aligned} \frac{dn_3}{dt} = & (1 - f_{B0}) Q_{RET0} n_0 + (A_{13} + Q_{13}) n_1 \\ & + (A_{23} + Q_{23}) n_2 - f_{B0} Q_{RET0} n_3. \end{aligned}$$

<sup>1</sup> The RET rate for particular system may be modeled by LASKIN software [2].

The broadband fluorescence is defined as:

$$F_{4t} = (A_{10} + A_{13}) \int_0^\infty n_1 dt + (A_{20} + A_{23}) \int_0^\infty n_2 dt. \quad (2)$$

This set of equations appears to be analytically soluble, however, we have not been able to simplify the solution into a practical formula for fluorescence as a function of the laser intensity. Nevertheless, if the RET rates can be considered infinitely fast, the model can be simplified to a 2-level model. This simplification appears to be valid for atmospheric pressure plasma jets in rare gases [10, 12].

## 3 Two-level model and analytic solution

If the RET is infinitely fast, the relations  $\frac{n_0}{n_0+n_3} = f_{B0}$  and  $\frac{n_1}{n_1+n_2} = f_{B1}$  are valid during the whole process and it is no longer necessary to treat the levels separately. If we define the following rate coefficients:

$$A \equiv f_{B1} (A_{10} + A_{13}) + (1 - f_{B1}) (A_{20} + A_{23}), \quad (3)$$

$$Q \equiv f_{B1} (Q_{10} + Q_{13}) + (1 - f_{B1}) (Q_{20} + Q_{23}), \quad (4)$$

$$B_{\text{abs}} \equiv B_{01} f_{B0}, \quad (5)$$

$$B_{\text{stim}} \equiv B_{10} f_{B1}, \quad (6)$$

and the unified levels as:

$$n_{0+3} \equiv n_0 + n_3, \quad (7)$$

$$n_{1+2} \equiv n_1 + n_2, \quad (8)$$

a simple two-level system set of equations may be written:

$$\dot{n}_{0+3} = -B_{\text{abs}} I n_{0+3} + (B_{\text{stim}} I + 1/\tau) n_{1+2}, \quad (9)$$

$$\dot{n}_{1+2} = +B_{\text{abs}} I n_{0+3} - (B_{\text{stim}} I + 1/\tau) n_{1+2}, \quad (10)$$

where  $\tau = 1/(A + Q)$  is the fluorescence lifetime. We subtract equation (10) multiplied by a scaling factor  $\frac{g_0 f_{B1}}{g_1 f_{B0}}$  from equation (9), recalling the relation of Einstein coefficients  $B_{01}/B_{10} = g_1/g_0$  from the principle of detailed balancing, where  $g_0$  and  $g_1$  are the degeneracies of the level 0 and 1, respectively. Defining

$$\delta \equiv n_{0+3} - \frac{g_0 f_{B1}}{g_1 f_{B0}} n_{1+2}, \quad (11)$$

$$N \equiv n_{0+3} + n_{1+2} = \text{const.}, \quad (12)$$

$$B \equiv B_{\text{stim}} + B_{\text{abs}} = \left(1 + \frac{g_0 f_{B1}}{g_1 f_{B0}}\right) B_{\text{abs}}, \quad (13)$$

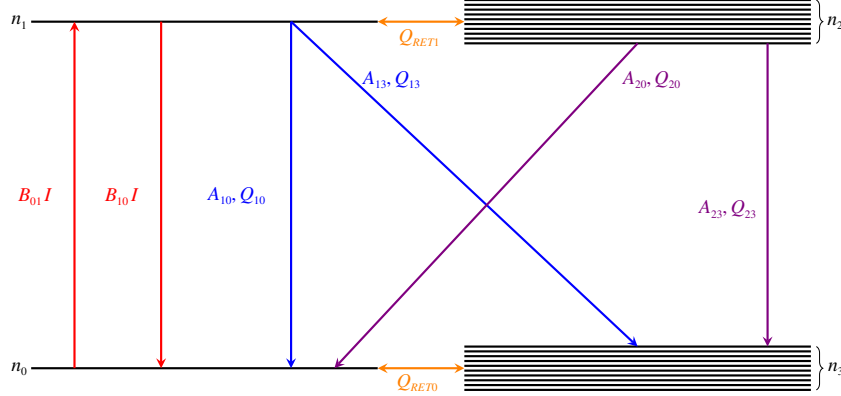


**Fig. 1.** Scheme of the 4-level model used for numerical modeling.

we may write a single rate equation:

$$\dot{\delta} = -(BI + 1/\tau)\delta + N/\tau. \quad (14)$$

This equation has a general solution, for general laser-pulse shape  $I(t)$ .

$$\delta(t) = \frac{N}{\tau} e^{-\int_{-\infty}^t (BI(\vartheta)+1/\tau) d\vartheta} \times \left[ \int_{-\infty}^t e^{\int_{-\infty}^{\vartheta} (BI(s)+1/\tau) ds} d\vartheta + \tau \right], \quad (15)$$

$\delta$  is indeed an important parameter. The total broadband fluorescence in this case is defined as:

$$F = A \int_{-\infty}^{\infty} n_{1+2} dt. \quad (16)$$

Integrating both sides of the equation (10) reveals the relation between  $\delta$  and the total fluorescence. The left-hand side yields:

$$n_{1+2}(\infty) - n_{1+2}(-\infty) = 0. \quad (17)$$

Here we assume, that the population of the laser-excited state returns to its initial value, provided we wait long enough after the laser pulse. Integrating the right-hand side, putting it equal to zero and using the definition (16) yields the relation between the laser intensity and fluorescence

$$F = A\tau B_{\text{abs}} \int_{-\infty}^{\infty} \delta(t) I(t) dt. \quad (18)$$

It is difficult to separate the integration over the laser pulse in relation (15) and get general result. However, the solution for a rectangular laser pulse of height  $I$  and

duration  $T$  (with the laser-pulse energy  $E_L = IT$ ) is relatively simple

$$F_{\text{rect}} = A\tau N B_{\text{abs}} I \times \left[ \frac{T/\tau (BI + 1/\tau)}{(BI + 1/\tau)^2} + \frac{BI(1 - e^{-(BI+1/\tau)T})}{(BI + 1/\tau)^2} \right]. \quad (19)$$

The exponential can be expanded into a Maclaurin series. The first-order approximation of this formula is the widely used linear case

$$F_{\text{1st}}(E_L) = A\tau N B_{\text{abs}} E_L. \quad (20)$$

The second order expansion gives a quadratic dependence peaking at  $BE_L = 1$

$$F_{\text{2nd}}(E_L) = A\tau N B_{\text{abs}} E_L \left( 1 - \frac{1}{2} BE_L \right). \quad (21)$$

This is equal to the first-order expansion of

$$F_{\text{apparent}}(E_L) = A\tau N B_{\text{abs}} \frac{E_L}{1 + \frac{1}{2} BE_L}, \quad (22)$$

which is the intuitive relation (1) used in the previous publications [7, 12–14]. This suggests that this simple formula with two parameters can give satisfactory results whenever the exponential  $e^{-(BI+1/\tau)T}$  may be approximated by the Maclaurin expansion up to the second order. It was observed in practice, that the apparent value of the saturation parameter  $\beta$  depends also on the rates of spontaneous processes, proving the equation (22) partially wrong. However, as will be shown in Section 5, fitting equation (1) to measured data may still yield the parameter  $\alpha$  with sufficient precision.

Using the full expansion of the exponential, the relation (19) may be rearranged to a more comprehensive form

$$F(E_L) = A\tau N B_{\text{abs}} \left( E_L - \frac{BE_L^2}{BE_L + T/\tau} \times \left[ \frac{e^{-(BE_L+T/\tau)} - 1}{BE_L + T/\tau} + 1 \right] \right). \quad (23)$$

The first term in the parenthesis represents the linear case as in equation (20), whereas the other two terms can be interpreted as a correction for both the depletion of the ground state and the depopulation of the upper state caused by stimulated emission. In the limit of high laser power, assuming that no further non-linear effects become important, this dependence approaches a constant value of

$$F(E_L \rightarrow \infty) = A\tau \frac{B_{\text{abs}}}{B_{\text{abs}} + B_{\text{stim}}} N (1 + T/\tau). \quad (24)$$

Note that unlike in the paper by Lucht and Laurendeau [6] or other publications on saturated LIF,  $F$  represents the time-integrated fluorescence.

For least-squares fitting, this equation will be used in the form:

$$F(E_L) = \alpha \left( E_L - \frac{p_1 E_L^2}{p_1 E_L + p_2} \left[ \frac{e^{-(p_1 E_L + p_2)} - 1}{p_1 E_L + p_2} + 1 \right] \right), \quad (25)$$

where  $\alpha$ ,  $p_1$  and  $p_2$  are parameters.

#### 4 Least squares fitting in practice

In the evaluation of real measurements, we are confronted with limited range of data that are also distorted by noise. Furthermore, if a planar LIF measurement is evaluated, it is desirable to perform the least square fitting with maximal time efficiency and as robust as possible. This favours the two-parameter equation (1), also because it can be easily linearised:

$$\frac{1}{F(E_L)} = \frac{1}{\alpha E_L} + \frac{\beta}{\alpha}. \quad (26)$$

In the practical implementation, the values of measured signal that, due to fluctuations, fall to or below zero, should be excluded from the fit. Fitting a linear function is indeed very robust, fast and requires no initial estimate of the parameters.

The equation (25) on the other hand, is in practice rather impractical due to its complexity and also because the three parameters of the fit are strongly correlated for a limited range of data.

In direct comparison<sup>2</sup> on fluorescence of OH radicals measured in a microwave atmospheric-pressure plasma jet, the linearised procedure was almost 30 times faster. The result from the linearised fits is shown in Figure 2. The OH radicals were excited through R<sub>1</sub>(4) line of the A<sup>2</sup>Σ(v' = 0) ← X<sup>2</sup>Π(v'' = 0) transition at ca. 306.5 nm. The fluorescence was detected after the laser pulse and no wavelength filtering was used. For further experimental details see Section 7 or [13].

The relative count of evidently outlying values ( $\alpha_{\text{app}} < 0$  and  $\alpha_{\text{app}} > 1.5 \times 10^{10}$ ) was ca. 19% for the linearised two-parameter function and ca. 31% for the three-parameter function.

<sup>2</sup> lmdr function of FORTRAN minpack library with scipy frontend was used for the iterative least-squares fitting.

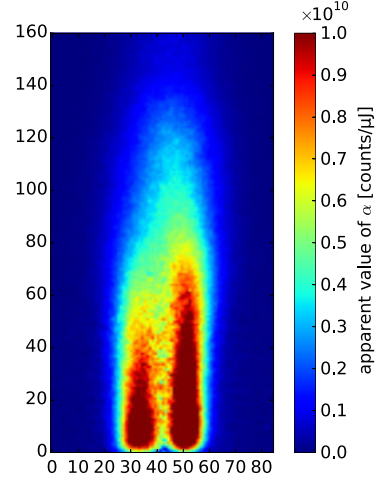


Fig. 2. Results of 2-parameter linearised fit of dependence of fluorescence signal on the exciting laser pulse energy for a microwave atmospheric pressure plasma jet. The  $x$  and  $y$  axes are labelled in pixels.

#### 5 Comparison of two- and three-parameter functions

In this section we would like to show practical limitations for the usage of the two-parameter function (1). To do so, we have employed the 4-level model described in Section 2 with parameters as summarised in Table 1. The choice of the parameters should roughly correspond to the excitation of OH radical on the R<sub>1</sub>(4) line of the A<sup>2</sup>Σ(v' = 0) ← X<sup>2</sup>Π(v'' = 0) transition and typical temperatures and collision partners' concentrations in an atmospheric-pressure plasma jet ignited in a flow of a rare gas.

The temporal shape of the laser was simulated by the function

$$I(t) = a t^b e^{-ct}, \quad (27)$$

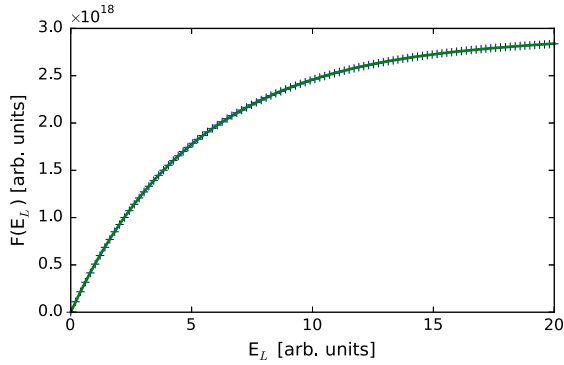
$$E_L = \int_0^{\infty} I(t) dt, \quad (28)$$

with the parameters  $b = 12.6$  and  $c = 2.44 \text{ ns}^{-1}$  that well represents the temporal shape of our pulsed laser. The time-integrated fluorescence was calculated from the 4-level model for a range of laser-power values  $E_L$  and a least squares fit of equations (1) or (25) was performed, see Figure 3.

To compare the performance on limited ranges of data, four loops of least squares fits were performed, each including  $E_L$  up to a different value: 5, 10, 15 and 20 (the units are arbitrary; see Fig. 3 for the relation between  $E_L$  and the degree of saturation). The results are shown in Figure 4. The iterating variable in each of the loops was the lower limit of the  $E_L$  range. As the results for 3-parameter fit (Eq. (25)) did not depend on the upper

**Table 1.** Coefficients used in the 4-level simulation (see Sect. 2).

Dimensionless	Rate ( $\text{s}^{-1}$ )	Rate/ $(E_L)$ ( $\text{ns}^{-1}$ )/ $(E_L)$	Initial population
$g_0 = 2(2 \times 4 + 1)$	$A_{13} = 5 \times 10^{-4}$	$B_{10} = 2$	$n_0 = 8 \times 10^{18}$
$g_1 = 2 \times 5 + 1$	$A_{23} = 5 \times 10^{-4}$	$B_{01} = \frac{g_1}{g_0} B_{10}$	$n_1 = 0$
$f_{B0} = 8 \times 10^{-2}$	$Q_{13} = 10^{-2}$		$n_2 = 0$
$f_{B1} = 5 \times 10^{-2}$	$Q_{23} = 10^{-2}$		$n_4 = 10^{20}$
	$A_{10} = A_{13}/5$		
	$A_{20} = A_{23}/5$		
	$Q_{10} = Q_{13} f_{B0}$		
	$Q_{20} = Q_{23} f_{B0}$		
	$Q_{\text{RET}0} = 10^3$		
	$Q_{\text{RET}1} = 10^3$		

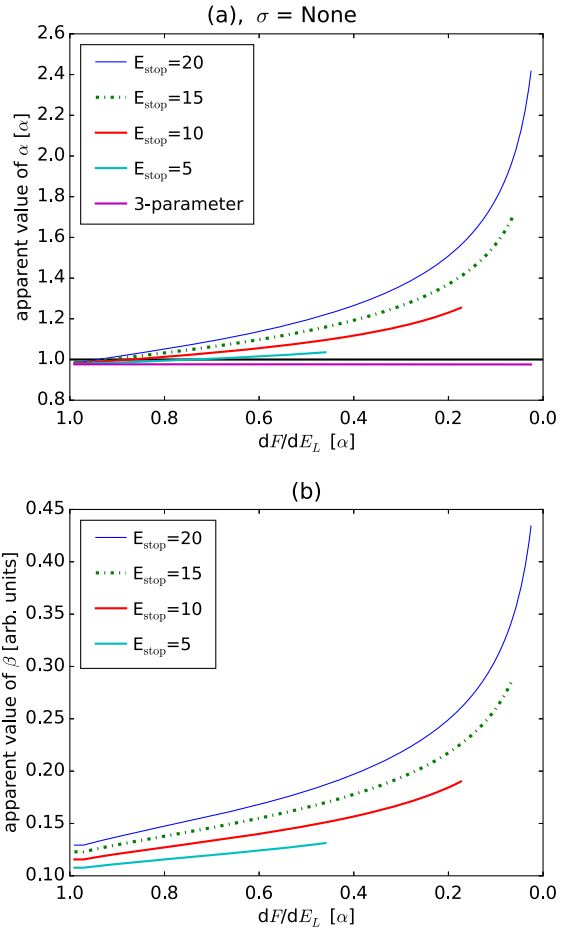

**Fig. 3.** Modelled time-integrated fluorescence  $F$  for a range of laser-power values  $E_L$  (blue crosses) and a least squares fit of equation (25) (green line). Fit of equation (1) is not shown, since it would be indistinguishable from the green line.

limit, only the broadest range (up to  $E_L = 20$ ) is shown. The plotted results of 2-parameter fits (Eq. (1)) can be interpreted as follows: the line indicates the upper limit of the range included in a fit, whereas the  $x$ -position of a point on a line represents the lower limit of the range. The  $y$ -position is then the value of  $\alpha_{\text{app}}$  resulting from the particular fit. To give as general information as possible, the axes are given in the units of  $\alpha$ . In the case of the  $y$ -axis this means that the correct value is unity and the value of  $\alpha_{\text{app}}$  in these units gives directly the answer of how wrong the fit result is.

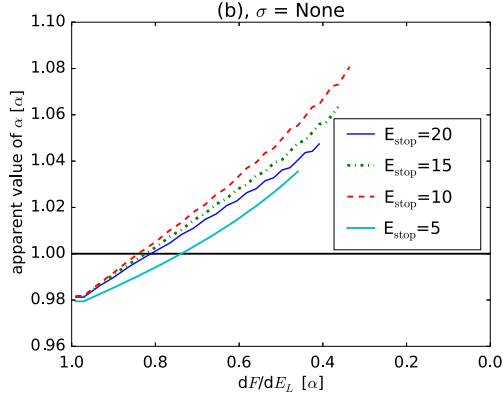
The  $x$ -axis is given in the units of derivative of  $F(E_L)$  with respect to  $E_L$ , again in the units of  $\alpha$ . In these units, 1.0 means perfectly linear growth with no signs of saturation effects, whereas 0 is in the limit of infinite laser power, where  $F$  no longer depends on  $E_L$ .

Figure 4 suggests that the equation (1) is reliable up to  $dF/dE_L \approx 0.5\alpha$ , where the deviation from the right value is less than 20%. This corresponds to the values  $\beta E_L$  of ca. 0.4. The 2-parameter approximation is thus quite reliable if the values of  $E_L$  included in the fit are limited to  $\beta E_L \leq 0.4$ .

Unfortunately, the true degree of saturation is not known initially. As can be seen in Figure 4, the parameters  $\alpha$  and  $\beta$  are strongly correlated. It is also demonstrated


**Fig. 4.** (a) Performance of the least squares fit of equation (25) (labelled by “3-parameter”) and equation (1) in various ranges of  $E_L$ . The correct result should always be 1.0, indicated by a black line, (b) the apparent values of the saturation parameter  $\beta$ .

that when dealing with dataset remarkably influenced by saturation, the results of fitting the whole range  $\alpha_1$  and  $\beta_1$  tend to be overestimated. Therefore, a two-step fitting procedure is suggested. In the first step, the full range of



**Fig. 5.** Apparent values of  $\alpha$  parameter from the two-step linearised fit, cropping the measured values to  $E_L \beta_1 < 1$ .

data is fitted with the linearised two-parameter function, resulting in – potentially overestimated – values of  $\alpha_1$ ,  $\beta_1$ . In the second step, the range is limited to values of energy  $\beta_1 E_L < M$ . It seems natural to use  $M = 0.4$ , based on the preceding discussion. This was, however, found to be too strict, as the value  $\beta_1$  is likely to be exaggerated. In practice, we have used the value of  $M = 1$ , see Figure 5. It can be seen, that even for significantly saturated data, this two-step procedure introduces error below 10%.

## 6 Effect of unknown laser profile

In the preceding section, we have implicitly assumed that the exciting laser power is known accurately. In the real-life measurements, however, we often measure spatially and temporally averaged value of  $E_L$  and  $F$ . To approach the problem in a more statistically correct way, let us introduce a profile of the laser power  $p(E_L - E_0)$ , with mean laser power  $E_0$ . If we assume that the shape of the profile function does not change significantly with  $E_0$ , the averaged value of fluorescence  $\bar{F}$  can be calculated as:

$$\bar{F}(E_0) = \int_{-\infty}^{\infty} F(E_L) p(E_L - E_0) dE_L. \quad (29)$$

To evaluate the effect of profile function of finite width, let us consider  $p(E_L - E_0)$  given by a Gaussian function. Its width can be better understood by directly comparing its  $\sigma$  parameter (given in units of  $E_L$ ) with the  $x$ -axis of Figure 3. In the measurement presented in Figure 2, the typical value of  $\sigma$ , recalculated to the units of Figure 3, would be  $\sigma = 1$ . This uncertainty in measurement of  $E_L$  was introduced by temporal averaging over 100 laser pulses, but uncertainty in the spatial profile of the laser would have introduced an indistinguishable effect. We present also an extreme case of  $\sigma = 5$ , which would be normally considered as a bad experimental setup. The results are shown in Figure 6. These results were obtained analogically to the results in the preceding chapter. The main difference is, that prior to the least-squares

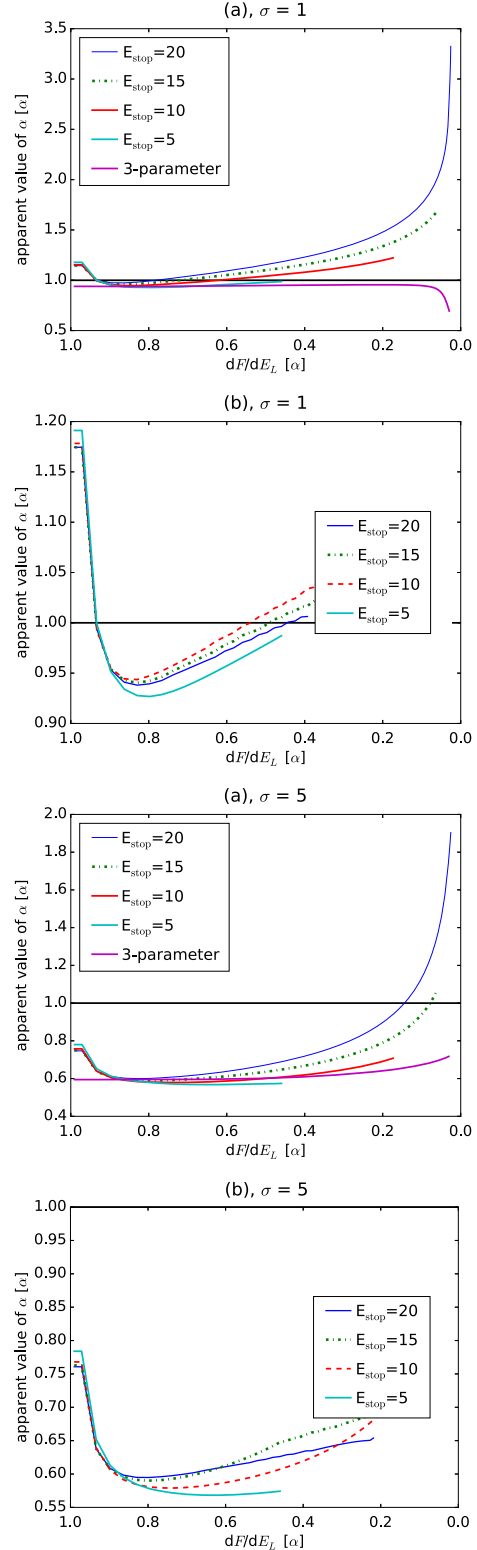


**Fig. 6.** Apparent values of  $\alpha$  after a first least-squares fit (a) and the two-step least square fit (b) for laser power distribution with  $\sigma = 1$  and  $\sigma = 5$ .

fit, the values of  $F$  were convoluted with the Gaussian function, according to equation (29). As can be seen, the two-step fitting procedure gives reliable results for most considered ranges of data if the uncertainty of the laser profile is considerably smaller than the laser power leading to significant saturation (in this case  $\sigma = 1 \ll 20$ , see Fig. 3). If this is not the case (e.g.,  $\sigma = 5$ ), the averaging leads to flattening of the fitted curve and the apparent value of  $\alpha$  tends to be underestimated, here by ca. 40%.

The two-step fitting procedure, limiting the range of data by the condition to  $\beta E_L < 1$  appears to be quite robust even for data affected by reasonable averaging.

## 7 Laser interaction with plasma

The previous sections have discussed the effect of saturation on the dependence of fluorescence signal on energy of laser pulses. However, this dependence can be influenced also by other phenomena, as will be demonstrated in this section on the basis of experimental results. The issue was studied by means of fluorescence measurement of hydroxyl (OH) radicals in a diffuse coplanar surface dielectric barrier discharge (DCSBD), since LIF in surface discharges is very liable to the unwanted effects that will be discussed in this section and that can be revealed by measurement of the relation between fluorescence intensity and energy of laser pulses. DCSBD is a plasma source which enables generation of large-area visually uniform thin layers of high power-density plasmas at atmospheric-pressure and ambient temperatures in practical working gases as air, nitrogen and hydrogen without the use of expensive helium or argon [3, 8]. Both cathode and anode are placed side by side inside a dielectric (ceramics) and the discharge is generated in ca 0.3 mm thin layer at the surface of the ceramics, see Figure 7. In such a thin plasma layer it is not possible to prevent all laser photons from hitting the surface of the dielectric, which influences the fluorescence measurement, as will be shown later. The presented measurements were performed in DCSBD ignited in air by electric field with frequency 16 kHz.

The OH radicals were excited by laser radiation via absorption line  $Q_1(2)$  (wavelength 282 nm) to the  $A^2\Sigma^+$  ( $v' = 1$ ) state. The laser set-up consisted of pumping Nd:YAG laser (Spectra-Physics, Quanta-Ray PRO-270-30), dye laser (Sirah, Precision Scan) and a doubling crystal unit. Fluorescence radiation of the vibronic bands 0-0 and 1-1 was separated from other wavelengths by interference filters and detected by an ICCD camera (Princeton instruments, PI-MAX 1024RB-25-FG-43). The laser was send parallel to the dielectric surface in order to minimize the laser interaction with the surface. The fluorescence radiating in the direction perpendicular to the laser was measured, as sketched in the Figure 7.

The laser was synchronized with the discharge, which enabled to perform measurements of the dependence of the fluorescence signal on mean energy of laser pulses for various phases ( $0^\circ$ ,  $60^\circ$  and  $120^\circ$ ) of the discharge. The measured dependencies were fitted by the

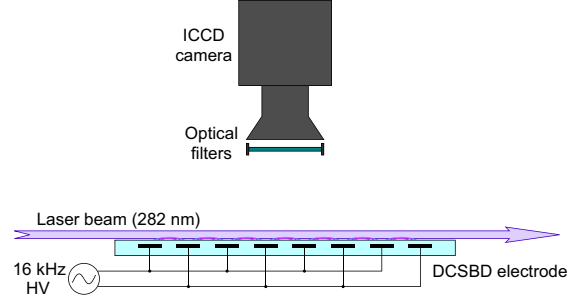


Fig. 7. Schema of the LIF measurement in the diffuse coplanar surface dielectric barrier discharge.

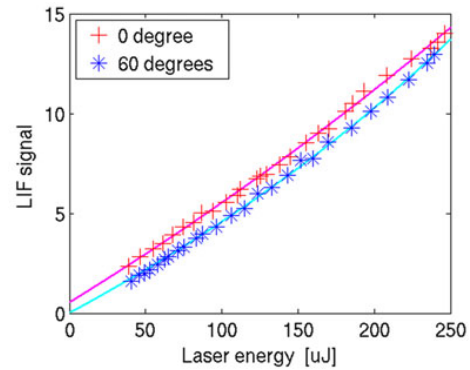


Fig. 8. Dependence of measured fluorescence signal on mean energy of laser pulses. The laser was synchronized with the discharge and measurement in two phases of the discharge period ( $0^\circ$  and  $60^\circ$ ) are shown.

equation (1). Whereas for discharge phases  $60^\circ$  and  $120^\circ$  the curve (1) agreed well with measured data, it was necessary to add a positive vertical shift  $F_0$  to this equation:

$$F(E_L) = \frac{\alpha E_L}{1 + \beta E_L} + F_0, \quad (30)$$

in order to fit data measured for the discharge phase  $0^\circ$ , as shown in the Figure 8.

In order to explain the shift  $F_0$  that appears only for some discharge phases (i.e., only in some parts of discharge period), several dependencies of discharge radiation intensity on discharge phase were realized. During the first measurement the laser was switched off and only the spontaneous discharge radiation was measured. This dependence is shown by the black line in the Figure 9 and shows only small increases in the phase areas  $150^\circ$ – $200^\circ$  and  $-40^\circ$ – $20^\circ$ . In these two parts of discharge period, the electric field is strong enough to ignite discharges and increase the spontaneous plasma emission.

After that, laser radiation was switched on with wavelength tuned to the center of the absorption OH line in order to measure the fluorescence of OH radicals. The measured signal is shown by blue line in the Figure 9 and reveals two distinct maxima around discharge phases  $-20^\circ$  and  $160^\circ$ . We know from the

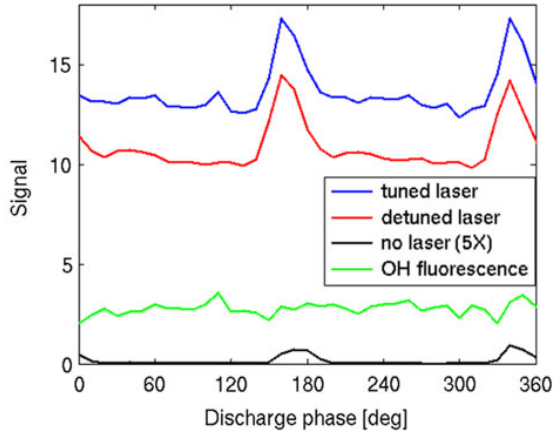


**Fig. 9.** Dependencies of discharge radiation on discharge phase. Black line was measured without laser radiation, blue line with laser tuned to the absorption line of OH radicals and red line with laser wavelength detuned from the absorption line. The green line is the difference between the blue and the red line. The signal depicted by the black line was  $5\times$  increased.

previous paragraph that in these two parts of period active discharges are ignited and it may seem from this measurement, that concentration of OH radicals is strongly increased by the active discharge.

Nevertheless, prior to make such a conclusion the following test was performed: the laser wavelength was detuned from the absorption line of OH radicals and the dependence of measured signal on discharge phase was recorded again. The result, shown by the red curve in the Figure 9, is significantly higher than the signal measured with laser switched off. In such parts of discharge period, when active discharge can not be ignited, the signal measured with detuned laser is practically constant and can be attributed to the fluorescence of the ceramics. Since the active surface discharge is thin, it is not possible to eliminate an impact of a part of laser radiation on the surface of the dielectric and the resulting fluorescence signal of the dielectric must be subtracted from the blue line in the Figure 9.

Surprisingly, we can see again two distinct maxima of measured signal (red curve) around the discharge phases  $-20^\circ$  and  $160^\circ$ . This increase can be attributed neither to an increase of dielectric fluorescence, since fluorescence of the ceramics can not be changed by the discharge significantly, nor to conventional laser induced fluorescence of OH radicals, since laser wavelength was detuned from absorption line of OH radicals and OH radicals were not able to absorb laser radiation. However, when laser hits the surface of the dielectric, it can ignite the discharge [1] if electric field between electrodes is strong enough. Therefore, in the time of high electric field (discharge phases around  $-20^\circ$  and  $160^\circ$ ), laser can increase intensity of discharge in the time of measurement, which leads to an increase of the spontaneous radiation of hydroxyl radicals. As a result, the measured value of radiation intensity measured

by the camera is increased by a signal that has nothing to do with conventional fluorescence. The presented explanation is in agreement with the electric observation that in some parts of discharge period laser can create a peak of electric current flowing through the discharge.

The real fluorescence signal can be obtained as the difference between the two measurements with laser wavelength tuned to and detuned from the absorption line of OH radicals (blue and red lines in Fig. 9). This difference is depicted in the Figure 9 by the green line and does not show any significant variation during the discharge period ( $62.5 \mu s$ ) demonstrating long life-time of OH radicals. It should be noted that measured species concentration might be overestimated in such parts of discharge period, when the electric field is strong, since the artificial increase of discharge current can lead to an increase of concentration of measured species. This problem is absent in the rest of the discharge period, when electric field is weak and the discharge can not be disturbed by impact of laser photons. The strong difference between the behaviour of the originally measured signal (red line) and the real laser induced fluorescence of OH radicals (green line) illustrates, that influence of laser on plasma must be carefully taken into account in surface discharges.

Since relatively low laser energy is sufficient to artificially ignite discharges, this phenomenon can explain the shift of the saturation curve by the value  $F_0$ . However, the Figure 8 reveals one more unexpected feature: The measured curves are convex, not concave, i.e., the fitted constant  $\beta$ , which describes the saturation, is negative. The negative value of  $\beta$  was found for all phases of discharge period. Consequently, it is not an effect of discharges ignited by laser. The observed fluorescence growth that is faster than linear is a sign of artificial increase of hydroxyl concentration by photodissociation. Laser photons have energy high enough to dissociate e.g., ozone molecules produced in the discharge and oxygen atoms created by the ozone photodissociation can react with water vapour to OH radicals [9]. This laser induced increase of OH concentration produces a quadratic term in the dependence of fluorescence signal on laser energy and, consequently, leads to negative fitted value of  $\beta$ . This result emphasizes the fact that for proper treatment of laser induced plasma fluorescence it is necessary to realize measurements of fluorescence signal on laser energy in order to find the region of linear fluorescence. If it is not possible to keep the laser energy in the linear region due to low signal-to-noise ratio, suitable equation (1, eventually 25, 30 or a polynomial of second order) should be fitted to measured data in order to evaluate the linear coefficient in the chosen equation.

## 8 Conclusion

The intuitive relation (1) used in previous publications was subjected to investigation. By solving a coupled set of rate equations describing a closed two-level system, it was found to be correct up to second order of Maclaurin

expansion of the derived result. Comparing the performance of least squares fitting of relation (1) and more rigorous relation (25) to the results of a 4-level model of fluorescence revealed a practical suggestion to use relation (1) for the range of laser pulse energies  $E_L$  limited by  $\beta E_L \leq 0.4$ .

It was shown that measurements of laser induced plasma fluorescence can be invasive, especially if laser radiation can hit a solid surface and increase the discharge intensity or if laser intensity is high enough to influence plasma chemistry by photodissociation. In surface dielectric barrier discharges the measurement can be further complicated by fluorescence of the dielectric and laser scattering on dielectric surface. These problems can be reduced if the contact of laser with the surface is minimized and if the laser energy is kept low. To reveal and solve these problems, it is helpful to synchronize laser with the discharge and to measure the dependence of fluorescence intensity on mean energy of laser pulses. Further, it is recommended to compare phase-resolved measurements of fluorescence signal for laser radiation that is tuned to and detuned from the absorption line of measured species. Afterwards, such a part of discharge period can be chosen for further measurements, when the electric field is weak and discharge can not be artificially ignited by laser radiation.

This research has been supported by the project CZ.1.05/2.1.00/03.0086 funded by European Regional Development Fund and project LO1411 (NPU I) funded by Ministry of Education, Youth and Sports of Czech Republic, by Czech Science Foundation under contract GA13-24635S and by Ministry of Education, Youth and Sports of Czech Republic under contract 7AMB14SK204.

## References

1. P.F. Ambrico, M. Ambrico, M. Simek, A. Colaianni, G. Dilecce, S. De Benedictis, *Appl. Phys. Lett.* **94**, 231501 (2009)
2. A. Bülter, U. Lenhard, U. Rahmann, K. Kohse-Höinghaus, A. Brockhinke, LASKIN: Efficient simulation of spectra affected by energy transfer, in *Proceedings of LACEA 2004* (Laser Applications to Chemical and Environmental Analysis, Annapolis, 2004)
3. M. Cernak, L. Cernakova, I. Hudec, D. Kovacik, A. Zahoranova, *Eur. Phys. J. Appl. Phys.* **47**, 22806 (2009)
4. M.J. Dunn, A.R. Masri, *Appl. Phys. B* **101**, 445 (2010)
5. K. Kohse-Höinghaus, *Progr. Energy Combust. Sci.* **20**, 203 (1994)
6. R.P. Lucht, N.M. Laurendeau, *Appl. Opt.* **18**, 856 (1979)
7. S. Nemschokmichal, F. Bernhardt, B. Krames, J. Meichsner, *J. Phys. D: Appl. Phys.* **44**, 205201 (2011)
8. M. Simor, J. Rahel', P. Vojtek, M. Cernak, A. Brablec, *Appl. Phys. Lett.* **81**, 2716 (2002)
9. Y. Teramoto, H.H. Kim, A. Ogata, N. Negishi, *J. Appl. Phys.* **115**, 133302 (2014)
10. T. Verreycken, R.M. van der Horst, N. Sadeghi, P.J. Bruggeman, *J. Phys. D: Appl. Phys.* **46**, 464004 (2013)
11. T. Verreycken, R. Mensink, R. van der Horst, N. Sadeghi, P.J. Bruggeman, *Plasma Source. Sci. Technol.* **22**, 055014 (2013)
12. J. Voráč, P. Dvořák, V. Procházka, J. Ehlbeck, S. Reuter, *Plasma Source. Sci. Technol.* **22**, 025016 (2013)
13. J. Voráč, J. Hnilica, V. Kudrle, P. Dvořák, *Open Chemistry* **13**, 193 (2015)
14. J. Voráč, A. Obrušník, V. Procházka, P. Dvořák, M. Talába, *Plasma Source. Sci. Technol.* **23**, 025011 (2014)
15. S. Yonemori, Y. Nakagawa, R. Ono, T. Oda, *J. Phys. D: Appl. Phys.* **45**, 225202 (2012)

# Fluorescence (TALIF) measurement of atomic hydrogen concentration in a coplanar surface dielectric barrier discharge

M Mrkvičková, J Ráhel, P Dvořák, D Trunec and T Morávek

Department of Physical Electronics, Faculty of Science, Masaryk University, Kotlářská 2, Brno 611 37, Czech Republic

E-mail: [martinamrkvickova@gmail.com](mailto:martinamrkvickova@gmail.com)

Received 15 January 2016, revised 27 May 2016

Accepted for publication 22 June 2016

Published 25 August 2016



CrossMark

## Abstract

Spatially and temporally resolved measurements of atomic hydrogen concentration above the dielectric of coplanar barrier discharge are presented for atmospheric pressure in 2.2% H<sub>2</sub>/Ar. The measurements were carried out in the afterglow phase by means of two-photon absorption laser-induced fluorescence (TALIF). The difficulties of employing the TALIF technique in close proximity to the dielectric surface wall were successfully addressed by taking measurements on a suitable convexly curved dielectric barrier, and by proper mathematical treatment of parasitic signals from laser–surface interactions. It was found that the maximum atomic hydrogen concentration is situated closest to the dielectric wall from which it gradually decays. The maximum absolute concentration was more than 10<sup>22</sup> m<sup>-3</sup>. In the afterglow phase, the concentration of atomic hydrogen above the dielectric surface stays constant for a considerable time (10 μs–1 ms), with longer times for areas situated farther from the dielectric surface. The existence of such a temporal plateau was explained by the presented 1D model: the recombination losses of atomic hydrogen farther from the dielectric surface are compensated by the diffusion of atomic hydrogen from regions close to the dielectric surface. The fact that a temporal plateau exists even closest to the dielectric surface suggests that the dielectric surface acts as a source of atomic hydrogen in the afterglow phase.

Keywords: laser-induced fluorescence, TALIF, atomic hydrogen, H, dielectric barrier discharge, surface discharge

(Some figures may appear in colour only in the online journal)

## 1. Introduction

Atomic hydrogen is a highly reactive species that plays an important role in the plasma treatment of solid surfaces and plasma chemistry. As a strong reducing and etching agent, atomic hydrogen is used in numerous low-pressure plasma applications, e.g. plasma etching [1], the passivation of defects in silicon industry [2], the removal of weakly bonded compounds during the deposition of hard and resistant thin films [3] etc. Recently, some promising results for the surface hydrogenation of diamond nanoparticles with atmospheric-pressure

hydrogen plasma were accomplished in our laboratories [4], using coplanar dielectric barrier discharge (DBD). However, any wider use of atmospheric-pressure hydrogen plasma treatment raises serious safety concerns on account of high hydrogen flammability when hydrogen is mixed even with a small percentage of oxygen or air [5]. A simple, yet effective approach to mitigate these concerns is to dilute hydrogen with an inert gas, typically argon, to widen its flammability envelope [6]. The drawback of this approach is lower atomic hydrogen generation due to the reduced concentration of H<sub>2</sub>. Fortunately, the presence of Ar atoms introduces several novel

reaction channels for H atom creation, which may to some extent compensate for the effect of H<sub>2</sub> dilution. Two main atomic hydrogen production channels (i.e. electron impact dissociation:  $e + H_2 \rightarrow H + H$ , and ion–electron dissociative recombination  $H_3^+ + e^- \rightarrow H_2 + H$ ) are extended by dissociation by metastables (i.e.  $Ar^* + H_2 \rightarrow Ar + 2H$ ), and by  $ArH^+$  ion–electron dissociative recombination (i.e.  $ArH^+ + e^- \rightarrow Ar + H$ ) [7]. Furthermore, in a confined discharge space of DBD, argon heterogeneous reactions on the dielectric walls ought to be considered as well. This includes the surface dissociative recombination of  $ArH^+$  ions and various Ar-mediated Eley–Rideal mechanism reactions with adsorbed atomic and molecular hydrogen [8]. It should be noted here that the actual contribution of heterogeneous reactions is generally only estimated, and most numerical models do not take into account e.g. material-specific interactions [7]. Such deficiency is quite bewildering when we realize that the most common motivation for generating atomic hydrogen is to use it just for heterogeneous reactions on solid surfaces.

In the presented work we report on our experimental assessment of the ground-state atomic hydrogen concentration above the surface of coplanar DBD, operated at atmospheric pressure in a mixture of argon and hydrogen. Knowledge of the spatio-temporal evolution of atomic hydrogen provides an important insight into the ongoing chemical processes. The electric field distribution of coplanar DBD allows discharge microfilaments to propagate only in the thin (a few tenths of a mm) layer along the dielectric surface, which results in a strong spatial gradient of created species. Owing to this, the experimental technique of choice must offer a high degree of spatial resolution. In this respect, a suitable method is two-photon absorption laser-induced fluorescence (TALIF), which has become a powerful tool for the detection of reactive species in plasma [9–14]. When TALIF is used for the detection of free hydrogen atoms, these atoms are usually excited by the simultaneous absorption of two laser photons with wavelength of 205.08 nm from the ground state to the state  $n = 3$  [15, 16]. This leads to the generation of fluorescent  $H\alpha$  radiation with an intensity proportional to the atomic hydrogen concentration. The necessity of absorbing two-photons makes the emission of the  $H\alpha$  line highly localized only to areas in the laser beam center, which allows the acquisition of detailed H atom concentration maps.

The difficulty in employing TALIF measurement for probing a few tenths of a millimeter above the surface of coplanar DBD lies in our inability to completely prevent any contact of the laser beam with the dielectric. This leads not only to the detection of a redundant signal originating in the fluorescence of the dielectric material, but also to a laser-induced discharge breakdown [18]. Therefore, care must be taken to make the TALIF method non-invasive. The issue of artificial breakdown can be solved by synchronizing laser excitation with the DBD voltage cycle, so the laser shots are taken at the lowest internal field, insufficient to initiate artificial breakdown [19, 20]. Another approach presented in this work is to take measurements in a repetitive afterglow regime, created by a modulated power feed pattern. Besides

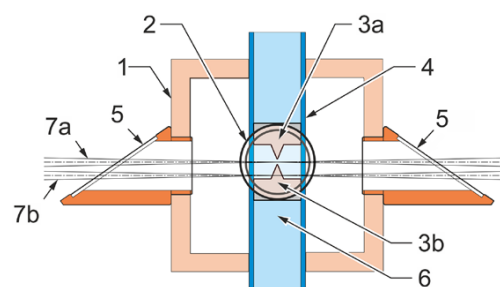


**Figure 1.** The dielectric barrier discharge reactor. 1—chamber, 2—quartz window for fluorescence observation, 3a—upper electrode, 3b—bottom electrode, 4—quartz tube, 5—quartz windows tilted to the Brewster angle, 6—insulation oil, 7—laser beam in position for the first (7a) and the second (7b) set of measurements.

simplified chemical kinetics of the afterglow phase, it has allowed us to monitor the development of atomic hydrogen over a longer time range, thus enabling a better validation of our numerical model. The issue of solid material fluorescence has been successfully addressed by adopting a suitable geometry of the DBD surface, which minimizes laser beam surface impingement. As we will report in this work, the geometry adaptation enabled us to monitor the afterglow H-atom evolution of a single, spatially stabilized coplanar DBD microfilament.

## 2. Experiment

### 2.1. Discharge configuration

The schematic of the investigated surface coplanar dielectric barrier discharge is shown in figure 1. A spatially stabilized single discharge microfilament was ignited on the outer surface of a cylindrical quartz tube (HSQ 300, Heraeus) by a pair of brass triangular electrodes, situated in the tube interior and oriented in parallel to the tube central axis. The tube has an inner diameter of 25 mm and a wall thickness of 1 mm. A relatively small radius of curvature of the quartz tube was adopted intentionally, to effectively divert the dielectric surface from the line of the laser beam, and thus to minimize the parasitic material fluorescence of out-of-focus laser beams impinging on the surface. A quartz dielectric barrier was used for three main reasons: (1) its high thermal shock resistance; (2) its low UV absorption leading to the low intensity of the fluorescence of the dielectric; (3) its smooth surface which minimizes laser radiation scattering to the detector. The latter allowed focusing the laser beam into the closest part of the dielectric surface.

To provide necessary HV electrode insulation and active cooling of the discharge site, insulation oil (Dow Corning 561 silicone transformer liquid) was circulated through the quartz tube. The distance between the electrode tips was set to 4 mm. The tube was housed inside a closed plastic chamber to allow working gas control. In the presented experiment, a mixture of 450 sccm of argon and 10 sccm of hydrogen was continuously flown through the reactor; the whole experiment was carried out at atmospheric pressure.

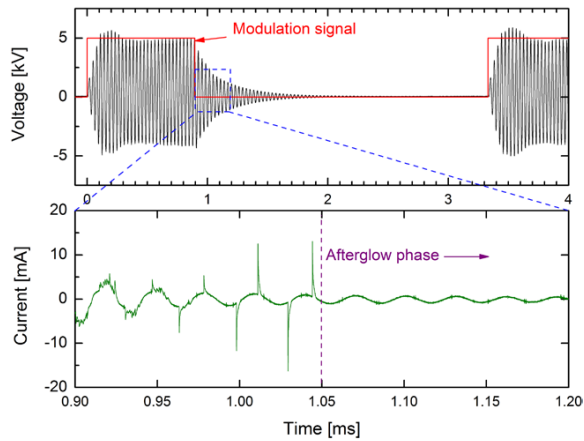


**Figure 2.** Voltage and current waveforms of the modulated coplanar surface DBD.

In-house-built HV power supply was used to power the electrodes by a 33.33 kHz HV driving voltage, modulated by a 300 Hz modulation signal with a duty cycle of 30%. Specifically, a train of 30 discharge cycles with a single-cycle period of 30  $\mu$ s was followed by an off-time (an afterglow phase) and the whole process was repeated at a 300 Hz repetition rate (figure 2). Upon entering the off-time of the modulation signal, the amplitude of the applied voltage oscillations started to decrease. To our benefit, the gradual decrease of the applied voltage resulted in an improved temporal stability of the microdischarge, as can be seen on the discharge current waveform in figure 2. Modulation of the HV power supply was done by the external arbitrary waveform generator (Rigol DG4162) operating in the repetitive N cycle burst mode. This waveform generator was simultaneously used for generating the laser shot synchronization signal. Digital oscilloscope DSO-S204A (Keysight) was used to monitor the discharge current, the applied voltage and the time position of the laser shot. An HV probe P6015A (Tektronix) and current monitor Model 2877 (Pearson) were used.

## 2.2. Diagnostics setup

A laser beam for TALIF measurement was generated by a three-component laser system, shown in figure 3. Pumping Nd:YAG laser (Spectra-Physics, Quanta-Ray PRO-270-30) produced radiation with a wavelength of 1064 nm, doubled to 532 nm utilizing a KDP crystal. The 532 nm radiation was used for pumping a dye laser (Sirah, PrecisionScan PRSC-D-24-EG) with rhodamine 101/B generating a wavelength of 615 nm, tripled to 205 nm in a frequency conversion unit. The output laser beam was focused by a spherical lens with a focal length of 35 cm and passed through the discharge reactor in the vicinity of the dielectric. Two sets of positions of the laser radiation were used for the measurement: for the first set, the vertical position of the focused laser radiation was located in the middle of the gap between the electrodes and the perpendicular distance of the laser beam from the surface of the dielectric was varied. The vertical position of the laser

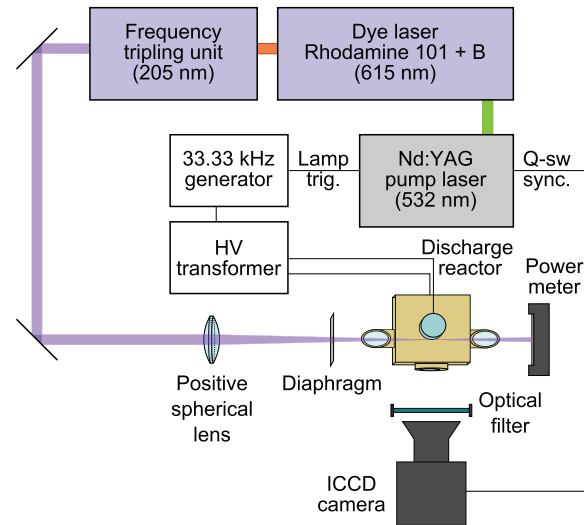


**Figure 3.** Experimental setup.

radiation in the second set of measurements was located in front of the bottom electrode; see figure 1. The areas used for the collection of fluorescence radiation in the two sets of measurements are depicted in figure 4. At the measurement point the radius of the laser beam was below 20  $\mu$ m, which defined our spatial resolution of the measurement in the direction perpendicular to the dielectric surface. For improving the shape of the beam and for limiting its contact with the dielectric, an iris diaphragm was used. In order to minimize the reflections of the laser beam, the reactor windows were oriented at the Brewster angle. In order to perform time-resolved measurement, the pumping laser was synchronized with an HV power supply.

The fluorescence radiation was detected by an ICCD camera (Princeton Instruments, PI-MAX 1024RB-2-FG-43), which was synchronized with the pumping laser. To separate the measured signal from the plasma emission and laser scattering, an interference filter for the  $H\alpha$  line 656.3 nm was used.

## 3. TALIF method

### 3.1. Measurement procedure

The TALIF of hydrogen atoms is based on the excitation of the atoms from their ground state  $1s\ ^2S_{1/2}$  to the state  $3d\ ^2D_{3/2, 5/2}$  via the simultaneous absorption of two photons of laser radiation with a wavelength of 205.08 nm [15, 16]. Two-photon absorption enables one to overcome problems with the generation and manipulation of VUV radiation that would arise if standard single-photon laser-induced fluorescence (LIF) was used. The consequent radiative deexcitation of excited hydrogen atoms to  $2p\ ^2P_{1/2, 3/2}$  state produces fluorescence at 656.3 nm ( $H\alpha$ ), which is detected and its intensity is used for the calculation of the concentration of the hydrogen atoms in the ground state. The method can be calibrated by the TALIF measurement of krypton with known concentration.

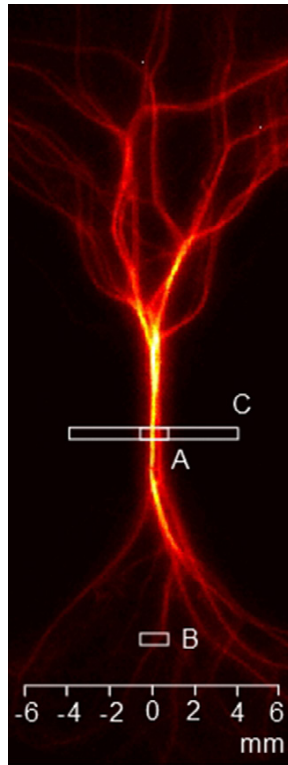


**Figure 4.** Discharge image with marked measurement positions. Rectangles A and B represent the measurement areas for the first and second measurement sets, respectively. Rectangle C represents the area used for spatially resolved measurements in the tangential direction, which are shown in figures 9 and 10.

The measured signal was spectrally, spatially and temporally integrated. For each laser pulse, the ICCD camera was exposed for 50 ns. This exposure time safely covered the whole laser pulse and the fluorescence decay time. After measuring the shape of the absorption line of hydrogen at given conditions, the other part of the experiment could be performed quickly with a laser tuned only to the center of the absorption line and the results were subsequently recalculated to spectral integrals. The measured signal was typically accumulated during 500 laser pulses and averaged over ten frames.

### 3.2. Saturation

Laser pulses with energies in the range of 50–60  $\mu\text{J}$  were used for the TALIF of hydrogen atoms and energies of 10–20  $\mu\text{J}$  were used for the TALIF of krypton that was used for the calibration of the method. In these energy ranges, saturation effects emerged, which were demonstrated by the fact that the log–log dependencies of the fluorescence signal on the energy of the laser pulses had slopes of approximately 1.7 and 1.3 for the TALIF of hydrogen and krypton, respectively. This slope would reach a value of 2 in an unsaturated case. It was not possible to decrease the laser energy enough to avoid saturation either for the hydrogen atoms or for krypton, due to the poor signal-to-noise ratio for low laser energies. Therefore, the saturation effects were taken into account, using the formula

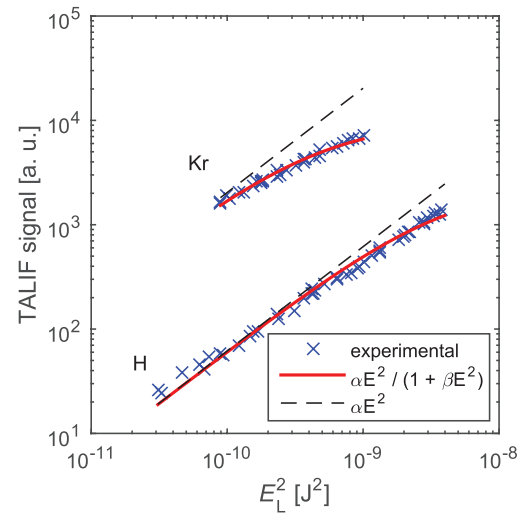


**Figure 5.** Fluorescence signal as a function of the energy of the laser pulses. The measurement data are fitted by equation (1). The dashed line shows the theoretical signal devoid of saturation effects.

$$F = \frac{\alpha E_L^2}{1 + \beta E_L^2}, \quad (1)$$

in analogy to the formula  $F = \alpha E_L / (1 + \beta E_L)$  that was derived for single-photon LIF [19].  $F$  is the measured fluorescence signal,  $E_L^2$  is the mean value of the squared laser-pulse energies,  $\alpha E_L^2$  would be the hypothetical unsaturated signal and the coefficient  $\beta$  describes the saturation effects. When the coefficient  $\beta$  is found, the measured fluorescence signal can be multiplied by  $(1 + \beta E_L^2)$ , which serves as the correction of saturation effects. The measured dependence of the fluorescence signal on the energy of the laser pulses is shown in figure 5, both for atomic hydrogen and for krypton. The formula (1) was fitted to these dependencies and the obtained coefficients  $\beta$  were thereafter used for the correction of saturation in equation (2). Typical values of the correction are shown together with typical values of the laser-pulse energies in table 1.

Finally, the effect of hydrogen atom production by the dissociation of hydrogen molecules in an intense laser beam was examined. Since there was no TALIF signal of atomic hydrogen when the discharge was not running, it was verified that this parasitic production of hydrogen atoms had no significant effect on the presented measurements.

### 3.3. Laser–surface interaction

Although the dielectric was made of quartz with a weak absorption of the used UV radiation and the interference filter in the camera was utilized, some amount of scattered laser light or the fluorescence of quartz was still detected when the laser beam touched the dielectric. This parasitic signal depended linearly on the energy of the laser pulse. Therefore, the following procedure was performed to separate the hydrogen fluorescence signal from other redundant signals. Besides a

**Table 1.** Parameters used for the evaluation of TALIF measurements.

Parameter	H	Kr
$\lambda$	205.08 nm	204.13 nm
$q_{\text{Ar}}$	$3.93 \times 10^{-16} \text{ m}^3 \text{ s}^{-1}$ [16]	$1.29 \times 10^{-16} \text{ m}^3 \text{ s}^{-1}$ [16]
$q_{\text{H}_2}$	$20.4 \times 10^{-16} \text{ m}^3 \text{ s}^{-1}$ [16]	
$q_{\text{Kr}}$		$1.46 \times 10^{-16} \text{ m}^3 \text{ s}^{-1}$ [16]
$\tau_{\text{rad}}$	17.6 ns [16]	34.1 ns [16]
$E_{\text{L}}$	50–60 $\mu\text{J}$	10–20 $\mu\text{J}$
$1 + \beta E_{\text{L}}^2$	1.6–1.9	1.2–1.8
$T$	80%	82%
$C$	5.2%	1.8%
$\sigma_{\text{Kr}}^{\text{TA}} / \sigma_{\text{H}}^{\text{TA}}$		0.62 [16]
$A_{\text{Kr}} / A_{\text{H}}$		0.614 [21]

Note:  $\lambda$  is the laser wavelength,  $q_{\text{Ar}}$ ,  $q_{\text{H}_2}$  and  $q_{\text{Kr}}$  are the rate coefficients for the quenching of excited species at room temperature by binary collisions with Ar, H<sub>2</sub> and Kr, respectively,  $\tau_{\text{rad}}$  is the radiative lifetime of excited species and  $E_{\text{L}}$  is the typical range of the energy of the laser pulses. The remaining quantities are described in section 3.

common dark frame measured without the presence of any laser radiation, each measurement was repeated with the laser detuned some 20 pm from the center of the hydrogen absorption line, i.e. at a wavelength that cannot excite hydrogen atoms but generates practically the same intensity of the fluorescence of the dielectric. The laser-pulse energy of both measurements was kept at similar levels. The pure fluorescence signal of hydrogen  $S$  was calculated as

$$S = \left[ S_{\text{meas}} - S_{\text{dark}} - (S_{\text{detuned}} - S_{\text{dark}}) \cdot \frac{E_{\text{L,meas}}}{E_{\text{L,detuned}}} \right] \cdot (1 + \beta E_{\text{L,meas}}^2), \quad (2)$$

where  $S_{\text{meas}}$  is the signal measured with the laser wavelength tuned to the center of the absorption line;  $E_{\text{L,meas}}$  is the mean value of the laser-pulse energies during this main measurement;  $S_{\text{detuned}}$  is the signal measured with the laser detuned some 20 pm from the center of the absorption line;  $E_{\text{L,detuned}}$  is the mean value of the energies of the detuned laser pulses;  $S_{\text{dark}}$  is the dark signal measured without any laser radiation; and expression  $(1 + \beta E_{\text{L,meas}}^2)$  compensates for the saturation effects. The subtracted parasitic signal  $(S_{\text{detuned}} - S_{\text{dark}})$  was well below 20% of the signal  $(S_{\text{meas}} - S_{\text{dark}})$ .

### 3.4. Absolute concentration values

To determine the absolute densities of the hydrogen atoms, calibration measurement of the TALIF of krypton was performed. A mixture of Ar + 3% Kr was injected into the reactor. The krypton atoms were excited from the ground state  $4p^6 \ ^1S_0$  to the  $5p^5 [3/2]_2$  state by the two-photon absorption of 204.13 nm laser radiation. Subsequent fluorescence radiation was observed on wavelength 826.3 nm during the deexcitation to  $5s^1 [1/2]_1$  state. The absolute concentrations of hydrogen atoms  $N_{\text{H}}$  were calculated by the formula [16]

$$N_{\text{H}} = N_{\text{Kr}} \frac{S_{\text{H}} E_{\text{L,Kr}}^2 \left( \frac{\nu_{\text{H}}}{\nu_{\text{Kr}}} \right)^2 \frac{\sigma_{\text{Kr}}^{\text{TA}}}{\sigma_{\text{H}}^{\text{TA}}} \frac{A_{\text{Kr}} \tau_{\text{Kr}}}{A_{\text{H}} \tau_{\text{H}}} \frac{T_{\text{Kr}}}{T_{\text{H}}} \frac{C_{\text{Kr}}}{C_{\text{H}}}, \quad (3)$$

where  $S$  represents the temporally, spatially and spectrally integrated fluorescence signals with the correction of saturation effects;  $E_{\text{L}}^2$  is the mean value of the squared laser-pulse energies;  $\nu$  is the frequency of the laser photons;  $\sigma^{\text{TA}}$  is the cross section for two-photon absorption;  $A$  is the Einstein coefficient of spontaneous emission from the excited state;  $\tau$  is the lifetime of the excited state (fluorescence decay time);  $T$  is the transmission of the interference filter; and  $C$  is the quantum efficiency of the ICCD camera for the wavelength of the fluorescence. Indices ‘H’ and ‘Kr’ differentiate between quantities related to atomic hydrogen and krypton, respectively. The ratio of the two-photon absorption cross sections for atomic hydrogen and krypton was published in [15, 16].

Since the lifetime of excited hydrogen and krypton atoms was approximately 0.1 ns and 0.3 ns, respectively, it was not possible to determine the lifetimes experimentally. Therefore, they were calculated by means of known quenching coefficients that were taken from [16, 17]. The values of the quenching rate coefficients are summarized in table 1 together with other quantities used for the evaluation of the TALIF measurements in this work. The effect of quenching by three-body collisions was neglected, which is in agreement with the findings described in [22]. However, the temperature dependence of the quenching rates should be taken into account. The values of quenching rate constants depend on the mean speed of the colliding particles and the concentration of collisional partners is a function of the gas temperature as well. The mutual effect of these two factors predicts that the quenching rate is proportional to  $T_{\text{g}}^{-0.5}$ , where  $T_{\text{g}}$  is the gas temperature. According to spectral measurements of the rotational temperature, the value 500 K was used as the gas temperature in the coplanar discharge, whereas the Ar–Kr mixture used for the calibration measurements was assumed to have room temperature. The eventual cooling of the gas in the afterglow phase of the DBD was not analyzed. Consequently, it is possible that the lifetime of the excited hydrogen ( $\tau_{\text{H}}$ ) decreased slightly with time due to the gas cooling in the afterglow phase. Therefore, the real concentration of hydrogen atoms in the late phases of the afterglow or in areas with lower gas temperature might have been a little higher than the values presented in this work. As a result, it is possible that the real duration of the plateau shown in section 4 was in reality slightly longer than is presented in the forthcoming section. Nevertheless, even in the case of complete gas cooling to room temperature during the first 2 ms of the afterglow, the error of the calculated concentration values would be less than 30%.

## 4. Results and discussion

### 4.1. Atomic hydrogen concentration

The concentration of atomic hydrogen in various positions is shown in figures 6 and 7. Immediately after the end of the discharge pulse, the concentration values varied in the range of  $10^{21}$ – $2 \cdot 10^{22} \text{ m}^{-3}$ . The highest values were found in the vicinity of the dielectric surface, where the hydrogen dissociation degree defined as  $[\text{H}]/([\text{H}] + 2[\text{H}_2])$  reached approx. 3%.

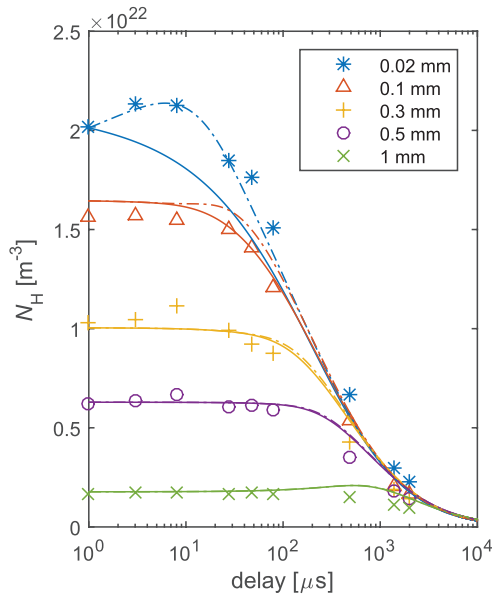


**Figure 6.** Temporal evolution of atomic hydrogen concentration in the afterglow for the first set of positions (between electrodes) for various distances from the dielectric surface. The lines represent the results of the diffusion—recombination model with (dash-and-dot) or without (solid lines) the source term on the surface.

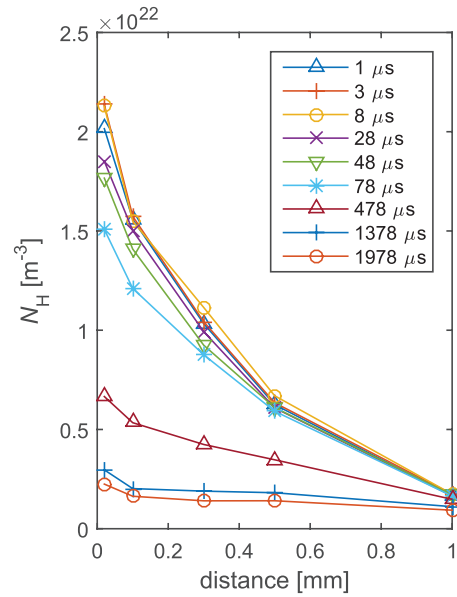


**Figure 8.** Spatial distribution of atomic hydrogen in the plane of symmetry of the reactor; the position shows the distance from the dielectric surface (in front of the inter-electrode gap). Shown for various delay times after the end of the discharge pulse.

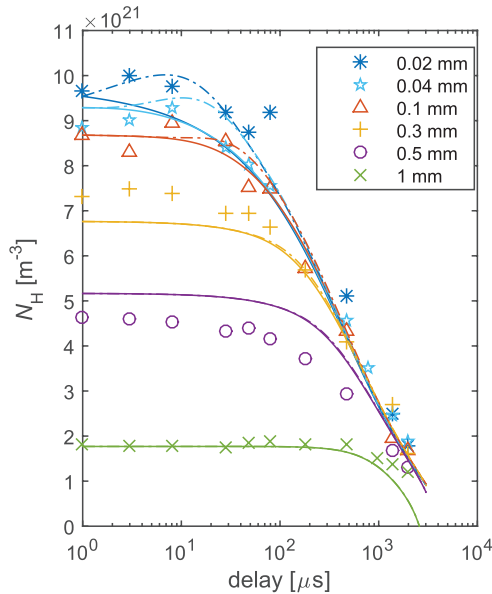


**Figure 7.** Temporal evolution of atomic hydrogen concentration in the afterglow for the second set of positions (at the electrode) for various distances from the dielectric surface. The lines represent the results of the diffusion—recombination model with (dash-and-dot) or without (solid lines) the source term on the surface.

This concentration value can be compared with the atomic hydrogen concentration found in other plasma sources. In an atmospheric pressure volume DBD, concentration over  $10^{21} \text{ m}^{-3}$  was measured by the TALIF method [22]. In low-pressure capacitively coupled discharges the atomic hydrogen

concentration was found to be in the order of  $10^{20} \text{ m}^{-3}$  by means of TALIF [21, 23] and in the range of orders from  $10^{20}$  to  $10^{22} \text{ m}^{-3}$  by means of a method based on the comparison of atomic and molecular line intensities [24]. The same method was used in hydrogen capillary DC-arc discharge and in MW discharge. In both these discharge types, the atomic hydrogen concentration was found to be in the order of  $10^{20} \text{ m}^{-3}$  [24]. Finally, in the expansion region of an Ar–H<sub>2</sub> arc the concentration over  $10^{20} \text{ m}^{-3}$  was determined by the TALIF method [15]. It follows from this comparison that the concentration of atomic hydrogen in the surface coplanar DBD is relatively high, which can be most probably attributed to a high power density in its thin active discharge layer.

As described above, the concentration of free hydrogen atoms was measured in two sets of positions. The first set of measurements was located on the horizontal plane of symmetry of the discharge, i.e. between electrodes. The measurements were repeated for various distances of the focused laser beam from the surface of the dielectric. The atomic hydrogen concentration was averaged over approx. 1 mm of the laser beam path. This measurement area is depicted in figure 4 by rectangle A. The temporal evolution of atomic hydrogen after the end of the discharge pulse in this set of positions is shown in figure 6 for various distances from the surface of the dielectric. It can be seen that after the end of the discharge pulse, atomic hydrogen concentration remained constant for 10–1000  $\mu\text{s}$  and only after this extended time did it start to fall. The duration of the concentration plateau depended on the distance from the surface of the dielectric: it terminated after tens of microseconds in the closest vicinity of the surface but it lasted for approximately 1 ms in the distance of 1 mm from the surface. Figure 7 depicts an analogous set of

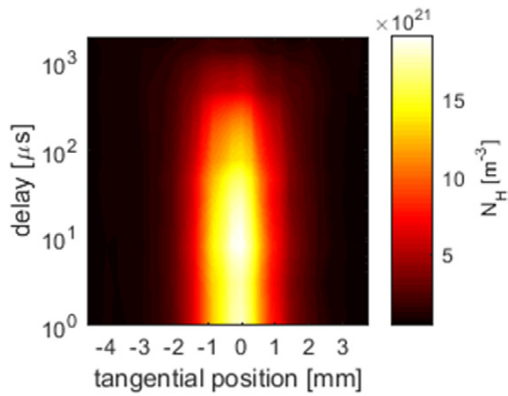


**Figure 9.** Spatio-temporal development of atomic hydrogen concentration in the distance 0.1 mm from the dielectric surface.

measurements realized in front of the bottom electrode (rectangle B in figure 4). The temporal and spatial development of atomic hydrogen at the electrode is similar to the situation in front of the gap, but the concentration values are smaller in front of the electrode, for the filaments are not pinned to a stationary position here as they were at the inter-electrode gap. Atomic hydrogen concentration again decreases when distance from the surface is increased and the temporal evolution again reveals a plateau with slightly longer duration than that in front of the inter-electrode gap. Our explanation for the existence of the plateau will be presented in section 4.2.

The data in figures 6 and 7 can be inverted in order to show the spatial distribution of the atomic hydrogen concentration. The atomic hydrogen spatial distribution in front of the inter-electrode gap is shown in figure 8; the situation in front of the bottom electrode is not shown since it is very similar to the situation in front of the gap. Shortly after the end of the discharge pulse, the spatial profile of atomic hydrogen concentration reveals a nearly exponential decrease with a fall to one half of the maximal concentration at the 0.3 mm distance from the dielectric surface. This finding is in agreement with the optical measurement of the thickness of the active surface coplanar DBD layer reported in [25]. When the time spent in the afterglow phase was increased, atomic hydrogen concentration decreased and its profile was flattened by the diffusion flow and recombination losses in agreement with our model described in section 4.2.

Since the ICCD camera directly measured the image of the fluorescence, we could quite straightforwardly analyze the atomic hydrogen distribution along the laser beam, i.e. in the tangential direction to the discharge axis, as depicted by rectangle C in figure 4. A typical example of the atomic hydrogen concentration spatio-temporal map is shown in figure 9, where spatio-temporal development in the distance 0.1 mm from the dielectric surface is depicted. The shape of the spatio-temporal dependencies in other measurement lines in front of the inter-electrode gap was similar, but the maximum concentration decreased with the distance from the dielectric surface increased. Figure 9 demonstrates that a plateau is also presented alongside the discharge axis with practically the same duration. The width of the atomic hydrogen-rich region can

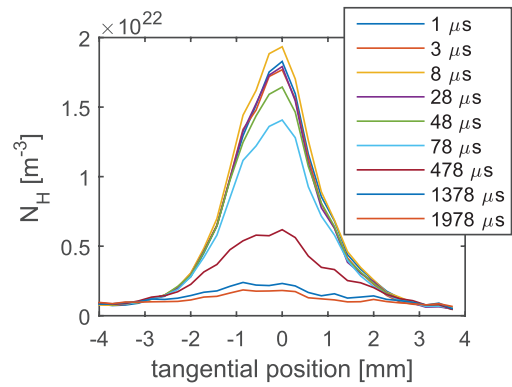


**Figure 10.** The spatial distribution of atomic hydrogen concentration in the direction of the laser beam in the distance 0.1 mm from the dielectric surface for various delay times from the end of the discharge pulse.

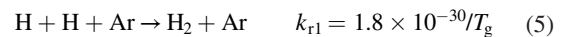
also be seen in figure 10, which shows cuts of figure 9 for decay times of 1  $\mu\text{s}$  to approx. 2 ms. The FWHM rises from an initial 2 mm to approx. 3.5 mm for a delay time of 2 ms. A different situation was found in front of the electrode, where the spatial profile of atomic hydrogen was flat due to the random position of the discharge filaments. This flat concentration profile and the resulting weak diffusion parallel to the surface can explain the fact that the plateau persisted slightly longer in front of the electrode than in front of the inter-electrode gap.

#### 4.2. Model of atomic hydrogen diffusion and recombination

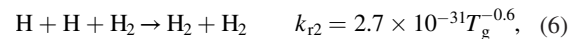
The development of H atom concentration  $n(x, t)$  in front of the dielectric surface was described by the following one-dimensional (1D) equation:

$$\frac{\partial n(x, t)}{\partial t} = D \frac{\partial n(x, t)}{\partial x} - k_r [n(x, t)]^2, \quad (4)$$

where  $x$  is the distance above the dielectric,  $D$  is the diffusion coefficient for hydrogen atoms in argon and  $k_r$  is the recombination coefficient.  $k_r$  is the sum of recombination coefficients  $k_{r1}n_{\text{Ar}}$  and  $k_{r2}n_{\text{H}_2}$  for two possible recombination channels



and



where the recombination coefficient units are  $\text{cm}^6 \text{ molecule}^{-2} \text{ s}^{-1}$  and  $T_g$  is the gas temperature. The temperature of H atoms produced by electron impact dissociation was determined as follows. The dissociation of molecular hydrogen by low-energy electrons occurs mainly via a dissociative excitation process through the lowest repulsive  $b^3\Sigma_u^+$  state. The H(1s) atoms produced in this process have kinetic energy which is estimated to be  $\sim 2\text{--}3 \text{ eV}$  [26]. These hot H atoms are cooled in collisions with Ar atoms. On average 85 collisions are needed to cool the hot H atoms to thermal energies. Using the collision frequency calculated with the cross section from [27] it was estimated that at our experimental conditions the

hot H atoms are cooled down to the gas temperature within 8 ns. So it was considered in the model that the recombining and diffusing H atoms have a temperature equal to the gas temperature. The gas temperature used in the model was  $T_g = 300$  K, since most of the area investigated by the model lay outside the active discharge, where the gas temperature was close to the room temperature. It was also found that the results of the model with higher gas temperature (up to 500 K) are not significantly different from the results calculated with  $T_g = 300$  K. The values of the recombination coefficients were taken from [28]. The value of the diffusion coefficient  $D = 1.4 \text{ cm}^2 \text{ s}^{-1}$  was taken from [29]. Equation (4) was solved numerically by the methods of lines for  $x$  from 0 to  $x_{\text{max}} = 1.2$  cm. The boundary conditions were

$$n(x_{\text{max}}, t) = 0 \quad (7)$$

and

$$-D \frac{\partial n}{\partial x} = -\gamma \frac{1}{4} v_{\text{th}} n + Q(t) \quad \text{at } x = 0, \quad (8)$$

where  $v_{\text{th}}$  is the mean thermal velocity of the H atoms;  $\gamma$  is the surface recombination probability for the H atoms and  $Q(t)$  is the source term, which describes a possible source of H atoms from the dielectric surface. The value of  $\gamma$  at the temperature of 300 K was set to  $10^{-4}$  in the model [30]. The experimental data on H atom concentration at  $t = 1 \mu\text{s}$  were fitted by an exponential function. Afterwards the H atom concentrations calculated using this exponential function were taken as the initial values for the solution of equation (4).

The atomic hydrogen concentration calculated by the model without any surface source of H atoms is shown as solid lines in figures 6 and 7. With the exception of the points located closest to the surface of the dielectrics, the model agrees well with the temporal behaviour found by our TALIF measurements. The model predicts the existence of a concentration plateau followed by the fall of atomic hydrogen concentration. Both the duration of the plateau and the rate of concentration fall calculated by the model are in reasonable agreement with the experiment. For some points above the bottom electrode (positions 0.3 mm and 0.5 mm in figure 7) the calculated concentration values are shifted with respect to the measured data. This originates from the fact that the measured spatial concentration profile did not fit perfectly to the exponential fall function, used as the initial condition for the model.

According to the model the existence of the plateau in the temporal development of atomic hydrogen concentration can be explained as a mutual effect of recombination and diffusion. The recombination losses of hydrogen atoms in regions farther from the dielectric surface are for some time compensated by the diffusion of atomic hydrogen from regions close to the dielectric, where the concentration values are relatively high. The model does not predict the existence of a plateau at the closest vicinity to the surface since there is no diffusion supply of atomic hydrogen to this region. Nevertheless, our measurement revealed that a plateau is present even in the closest vicinity of the dielectric surface. This discrepancy between the model outputs and measurements indicates that the dielectric surface acts in the afterglow as a source of free

hydrogen atoms that were either adsorbed on the surface or directly created on the surface e.g. by surface ion recombination. To prove this hypothesis the model was extended by a source of atomic hydrogen released from the dielectric surface. The flux  $Q$  of H atoms from the surface was described by the following function:

$$Q(t) = A \exp(-kt). \quad (9)$$

The constants  $A$  and  $k$  in this function were chosen so as to achieve good agreement between the measurement and calculation data. The atomic hydrogen concentration calculated by the model with this atomic hydrogen flux is shown as dash-and-dot lines in figures 6 and 7. Good agreement of concentrations was obtained in front of the bottom electrode for  $A = 1 \times 10^{18} \text{ cm}^{-2} \text{ s}^{-1}$  and  $k = 1 \times 10^5 \text{ s}^{-1}$ ; see figure 7. The flux term increased the hydrogen concentration for the three nearest distances from the dielectric surface at a time delay of around  $10 \mu\text{s}$ , which gave significantly better agreement with the measurement data. The concentration of atomic hydrogen at positions more distant from the dielectric surface was not affected. In front of the inter-electrode gap, good agreement of the calculated concentration values with the experimental ones was obtained for  $A = 2.7 \times 10^{18} \text{ cm}^{-2} \text{ s}^{-1}$  and  $k = 1 \times 10^5 \text{ s}^{-1}$ ; see figure 6. In this case there was higher flux of atomic hydrogen from the surface, which could be related to the higher H atom concentration in this region. It is clear that in both cases introduction of the flux term improved the numerical fit to our experimental data in the close vicinity of the dielectric surface.

If the H atom flux from the surface is due to desorption, then it follows from equation (9) that the first-order desorption rate coefficient  $k_{\text{desor}}$  is equal to  $k = 1 \times 10^5 \text{ s}^{-1}$ . This rate coefficient can be shown to have an Arrhenius form

$$k_{\text{desor}} = k_0 \exp\left(\frac{-E_{\text{desor}}}{k_B T}\right), \quad (10)$$

where  $E_{\text{desor}}$  is the depth of the potential well and for chemisorption  $k_0 \sim 10^{13} - 10^{15} \text{ s}^{-1}$  [31]. If  $k_0$  is set to  $10^{14} \text{ s}^{-1}$ , then the value  $E_{\text{desor}} = 0.5 \text{ eV}$  is obtained. Also the constant  $A$  is equal to  $n_{S0} k_{\text{desor}}$ , where  $n_{S0}$  is the initial surface concentration of adsorbed H atoms. For the position in front of the bottom electrode and inter-electrode gap the values of  $n_{S0}$  are  $1 \times 10^{13} \text{ cm}^{-2}$  and  $2.7 \times 10^{13} \text{ cm}^{-2}$ , respectively. Since no other studies dealing with H atom desorption from a quartz surface were found, the obtained values of  $n_{S0}$  and  $E_{\text{desor}}$  were compared with values published in studies of the desorption of other atoms: Marinov *et al* [32] estimated the initial surface concentration of N atoms on a Pyrex surface to be  $3 \times 10^{13} \text{ cm}^{-2}$ , and Guaitella *et al* [33] estimated the initial surface concentration of O atoms on a Pyrex surface to be  $2 \times 10^{14} \text{ cm}^{-2}$ . Marinov *et al* [34] also studied the kinetics of adsorption, desorption and recombination of nitrogen atoms on a silica surface and they concluded that weakly bonding active sites exist on the surface with the binding energy smaller than 1 eV. To conclude, the obtained values of  $n_{S0}$  and  $E_{\text{desor}}$  for H atom desorption from quartz surfaces are consistent with the abovementioned references.

## 5. Conclusion

The difficulties of employing TALIF for the measurement of atomic hydrogen in the vicinity of the dielectric surface of coplanar DBD can be solved by a suitable choice of dielectric material with a smooth surface and low intrinsic fluorescence; by the proposed treatment of redundant signals; by taking measurements during the afterglow phase, so no artificial laser breakdown could be ignited; and by employing coplanar DBD with a convexly curved surface.

The spatio-temporal profile of atomic hydrogen concentration shows that free hydrogen atoms are localized mainly in the 0.3 mm thin layer above the dielectric surface. This corresponds well to the thickness of the active discharge measured by discharge imaging. The area with the highest concentration of atomic hydrogen is situated in the closest vicinity of the dielectric surface and its value is above  $10^{22} \text{ m}^{-3}$ . The lateral diffusion of atomic hydrogen from the axis of localized filaments is approx. 1 mm. The atomic hydrogen concentration measured in the coplanar surface DBD is significantly higher than the values reported for volume DBD.

The temporal evolution of atomic hydrogen concentration shows that the atomic hydrogen concentration stays constant for a certain time after the end of the laser pulse. This concentration plateau lasts from tens of microseconds for positions close to the solid surface, to approximately 1 ms for positions located 1 mm above the surface. Our 1D numerical model explains the formation of the plateau by the combination of the recombination and diffusion of hydrogen atoms. The recombination losses of atomic hydrogen in regions farther away from the dielectric are compensated by the diffusion flow from H-atom-rich regions that are located closer to the dielectric. The fact that the plateau remains for a relatively long time even at the closest vicinity of the dielectric surface indicates that the dielectric surface itself acts for tens of microseconds as a source of atomic hydrogen. The spatio-temporal development of atomic hydrogen is very similar in both investigated regions, i.e. in the center of the inter-electrode gap and above the HV electrode.

## Acknowledgments

This research has been supported by the Czech Science Foundation under contract GA13-24635S, by the project CZ.1.05/2.1.00/03.0086 funded by the European Regional Development Fund, and by projects LO1411 (NPU I) and 7AMB14SK204 funded by the Ministry of Education, Youth and Sports of the Czech Republic.

## References

- [1] Chang R P H, Chang C C and Darack S 1982 *J. Vac. Sci. Technol.* **20** 45
- [2] Pearton S J, Corbett J W and Shi T S 1987 *Appl. Phys. A* **43** 153
- [3] Korner N, Beck E, Dommann A, Onda N and Ramm J 1995 *Surf. Coat. Technol.* **76–7** 731
- [4] Kromka A, Čech J, Kozak H, Artemenko A, Ižák T, Čermák J, Rezek B and Černák M 2015 *Phys. Status Solidi b* **252** 2602
- [5] Schröder V, Emonts B, Janßen H and Schulze H-P 2004 *Chem. Eng. Technol.* **27** 847
- [6] Shebeko Yu N, Tsarichenko S G, Trunev A V, Korolchenko A Ya and Kaplin A Yu 1994 *Combust. Explosion Shock Waves* **30** 183
- [7] Bogaerts A and Gijbels R 2002 *Spectrochim. Acta B* **57** 1071
- [8] Jiménez-Redondo M, Cueto M, Doménech J L, Tanarro I and Herrero V J 2014 *RSC Adv.* **4** 62030
- [9] Amorim J, Baravian G and Jolly J 2000 *J. Phys. D: Appl. Phys.* **33** R51
- [10] Niemi K, Schulz-von der Gathen V and Döbele H F 2005 *Plasma Sources Sci. Technol.* **14** 375
- [11] Döbele H F, Mosbach T, Niemi K and Schulz-von der Gathen V 2005 *Plasma Sources Sci. Technol.* **14** S31
- [12] van Gessel A F H, van Grootel S C and Bruggeman P J 2013 *Plasma Sources Sci. Technol.* **22** 055010
- [13] Bruggeman P and Brandenburg R 2013 *J. Phys. D: Appl. Phys.* **46** 464001
- [14] Ono R 2016 *J. Phys. D: Appl. Phys.* **49** 083001
- [15] Boogaarts M G H, Mazouffre S, Brinkman G J, van der Heijden H W P, Vankan P, van der Mullen J A M, Schram D C and Döbele H F 2002 *Rev. Sci. Instrum.* **73** 73
- [16] Niemi K, Schulz-von der Gathen V and Döbele H F 2001 *J. Phys. D: Appl. Phys.* **34** 2330
- [17] Bittner J, Kohse-Höinghaus K, Meier U and Just T 1988 *Chem. Phys. Lett.* **143** 571
- [18] Ambrico P F, Ambrico M, Šimek M, Colaianni A, Dilecce G and De Benedictis S 2009 *Appl. Phys. Lett.* **94** 231501
- [19] Voráč J, Dvořák P, Procházka V, Morávek T and Ráhel J 2015 *Eur. Phys. J. Appl. Phys.* **71** 20812
- [20] Es-Sebbar E T, Sarra-Bournet Ch, Naudé N, Massines F and Gherardi N 2009 *J. Appl. Phys.* **106** 073302
- [21] Jolly J and Booth J P 2005 *J. Appl. Phys.* **97** 103305
- [22] Dvořák P, Talába M, Obrušnik A, Kratzer J and Dědina J 2016 in preparation
- [23] Chérigier L, Czarnetzki U, Luggenhölscher D and Schulz-von der Gathen V 1999 *J. Appl. Phys.* **85** 696
- [24] Lavrov B P, Lang N, Pipa A V and Röpcke J 2006 *Plasma Sources Sci. Technol.* **15** 147
- [25] Šimor M, Ráhel J, Vojtek P, Černák M and Brablec A 2002 *Appl. Phys. Lett.* **81** 2716
- [26] Tawara H, Itikawa Y, Nishimura H and Yoshino M 1990 *J. Phys. Chem. Ref. Data* **19** 617
- [27] Phelps A V 1992 *J. Phys. Chem. Ref. Data* **21** 883
- [28] Baulch D L et al 1994 *J. Phys. Chem. Ref. Data* **23** 847
- [29] Blyth G, Clifford A A, Gray P and Waddicor J I 1987 *J. Chem. Soc. Faraday Trans. I* **83** 751
- [30] Kim Y C and Boudart M 1991 *Langmuir* **7** 2999
- [31] Zangwill A 1988 *Physics at Surfaces* (Cambridge: Cambridge University Press)
- [32] Marinov D, Guaitella O, Rousseau A and Ionikh Y 2010 *J. Phys. D: Appl. Phys.* **43** 115203
- [33] Guaitella O, Hübner M, Welzel S, Marinov D, Röpcke J and Rousseau A 2010 *Plasma Sources Sci. Technol.* **19** 045026
- [34] Marinov D, Guaitella O, de los Arcos T, von Keudell A and Rousseau A 2014 *J. Phys. D: Appl. Phys.* **47** 475204

# Fluorescence measurement of atomic oxygen concentration in a dielectric barrier discharge

P Dvořák<sup>1</sup>, M Mrkvičková<sup>1</sup>, A Obrusník<sup>1</sup>, J Kratzer<sup>2</sup>, J Dědina<sup>2</sup> and V Procházka<sup>1</sup>

<sup>1</sup> Department of Physical Electronics, Faculty of Science, Masaryk University, Kotlářská 2, Brno 611 37, Czechia

<sup>2</sup> Institute of Analytical Chemistry of the CAS, v. v. i., Veveří 97, 602 00 Brno, Czechia

E-mail: [pdvorak@physics.muni.cz](mailto:pdvorak@physics.muni.cz)

Received 27 November 2015, revised 31 March 2017

Accepted for publication 3 May 2017

Published 6 June 2017



CrossMark

## Abstract

Concentration of atomic oxygen was measured in a volume dielectric barrier discharge (DBD) ignited in mixtures of Ar + O<sub>2</sub>(+ H<sub>2</sub>) at atmospheric pressure. Two-photon absorption laser induced fluorescence (TALIF) of atomic oxygen was used and this method was calibrated by TALIF of Xe in a mixture of argon and a trace of xenon. The calibration was performed at atmospheric pressure and it was shown that quenching by three-body collisions has negligible effect on the life time of excited Xe atoms. The concentration of atomic oxygen in the DBD was around 10<sup>21</sup> m<sup>-3</sup> and it was stable during the whole discharge period. The concentration did not depend much on the electric power delivered to the discharge provided that the power was sufficiently high so that the visible discharge filled the whole reactor volume. Both the addition of hydrogen or replacing of argon by helium led to a significant decrease of atomic oxygen concentration. The TALIF measurements of O concentration levels in the DBD plasma performed in this work are made use of e.g. in the field analytical chemistry. The results contribute to understanding the processes of analyte hydride preconcentration and subsequent atomization in the field of trace element analysis where DBD plasma atomizers are employed.

Keywords: laser induced fluorescence, TALIF, atomic oxygen, O, dielectric barrier discharge, plasma

## 1. Introduction

Dielectric barrier discharges (DBD) present a practical way for generation of low-temperature non-thermal plasma at atmospheric pressure. Complex processes occurring in these plasmas include reactions of electrons, metastables and radical species. In spite of the fact that radicals belong to the most reactive species in plasma and that they are of key importance for the most of practical plasma applications, their concentration in plasma sources is usually unknown. Quantitative spectroscopic measurements of concentration of radicals are complicated, namely at atmospheric pressure, due to fast collisional quenching of excited states of measured species.

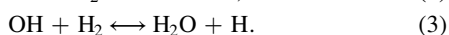
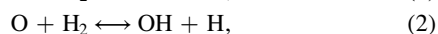
This work focuses on measurement of concentration of monoatomic oxygen radicals by laser-induced fluorescence

(LIF). In order to avoid problems with generation and manipulation of VUV laser radiation, two-photon absorption of laser radiation (TALIF) with wavelength 225.6 nm was used, as was described in [1, 2]. The TALIF method had been used for oxygen radical measurement at atmospheric pressure e.g. in RF [3–5] and MW [2] plasma jets, ns-pulsed discharges [6] and flames [7]. A cross section for two-photon absorption by atomic oxygen was published in [8, 9]. Since TALIF of xenon is usually used for calibration, the ratio of cross sections for TALIF of O and Xe, which was measured in [1], is of higher practical importance for fluorescent measurement of atomic oxygen concentration. Especially at atmospheric pressure, the quenching rate must be known for quantitative evaluation of TALIF measurements. Quenching rate constants for binary collisions of excited atomic oxygen

and xenon with common gases were published in [1, 10, 11] and [2], respectively. Unfortunately, three-body collisions may play a role at atmospheric pressure and their influence on deexcitation of excited atomic oxygen and xenon by other gases is mostly unknown with the exception of xenon quenching by helium atoms [2].

An appealing application of DBD is its use as a hydride atomizer in the technique of hydride generation (HG) with subsequent atomic absorption spectrometry (AAS) detection [12]. HG-AAS is a well established approach to determine virtually all elements forming volatile hydrides, namely arsenic, antimony, bismuth, germanium, lead, selenium, tellurium and tin [13]. The analyte species are reduced, typically by a chemical reaction in acidic media with sodium tetrahydroborate, to a corresponding gaseous hydride. Generated hydride, together with hydrogen evolved as a reaction side product and usually also with some amount of oxygen, is subsequently transported by a flow of inert gas (usually Ar or He) to an atomizer to be converted to analyte free atoms which are detected by AAS. Quartz tubes (QTA) heated to 900°C are predominantly used as atomizers. According to the present knowledge, hydride atomization in QTA proceeds via interaction with free radicals such as H, OH and O [13].

It has convincingly been shown that hydrides cannot be atomized in QTA in the absence of hydrogen [13, 20]. Moreover, even in hydrogen presence, a certain oxygen content in the atomizer is required for achieving optimum sensitivity [20]. This indicates that hydride atomization in QTA proceeds via interaction with radicals produced there by reactions between hydrogen and of oxygen [13]:



The radical concentrations there are thus many orders of magnitude above their equilibrium values [21].

Recently, DBD atomizers have been reported as a useful alternative to QTA [14–17]. Atomization mechanism in DBD atomizers remains unknown, however, free radicals formed in the DBD plasma [12] should be expected to play an analogous role as in QTA [18]. Absolute concentrations and spatial distribution of H radicals in a volume DBD under experimental conditions typical for HG-AAS have been investigated [19]. Concentration of atomic hydrogen was in the order of  $10^{21} \text{ m}^{-3}$  in the Ar–H<sub>2</sub> mixture and the maximum dissociation degree of hydrogen was ca 0.3%.

In principle, there could be, in contrast to QTA, a substantial concentration of free radicals in DBD atomizers even in the absence of hydrogen introduced to the atomizer due to the plasma environment. Absolute concentrations of O radicals in a volume DBD are studied in this work in order to get deeper insights into the atomization of hydride forming elements. This study follows our previous work focused on the investigation of H radicals in the same volume DBD [19]. It must be highlighted that the main source of H<sub>2</sub> in HG-AAS is hydrogen evolved in the hydride generator as a side product during chemical conversion of analyte to a corresponding hydride. The typical sources of O<sub>2</sub> in the system are: (1)

impurities in the carrier/discharge gas (Ar, He), (2) oxygen dissolved in solutions of chemicals and subsequently stripped out during HG and (3) diffusion of air into the DBD atomizers from ambient atmosphere. Additionally, water vapor present in the ambient atmosphere may be a source of both O and H radicals as well. In general, HG-AAS systems with on-line atomization, i.e. with direct introduction of analyte hydride generated into the atomizer, produces around 10–20 sccm of H<sub>2</sub>. Thus, H<sub>2</sub> is in a great excess over O<sub>2</sub>.

However, there are advanced HG-AAS approaches in which preconcentration of analyte hydride generated is employed prior its atomization in order to further decrease the detection limit. Analyte hydride is preconcentrated either in a special device upstream from the atomizer or directly in the atomizer (*in situ*). The role of O<sub>2</sub> and O radicals seems to be crucial in the preconcentration methods, since O<sub>2</sub> to H<sub>2</sub> concentration ratios in the atomizer are much higher than with the on-line atomization approaches. One of the preconcentration approaches includes the collection of analyte hydride in a cryogenic trap cooled by liquid nitrogen [22], which is placed between the hydride generator and atomizer, and the subsequent release of the preconcentrated analyte to the atomizer by heat. Since hydrogen is not captured by the trap, the O<sub>2</sub>/H<sub>2</sub> ratio in the carrier gas is significantly increased.

*In situ* preconcentration of analyte hydrides in a DBD plasma discharge has been described recently [15, 17]. Briefly, the addition of several sccm of O<sub>2</sub> to the Ar plasma results in a retention of analyte hydride in the optical arm of the DBD atomizer. Analyte release and atomization is reached as soon as oxygen flow is stopped. The trapping and volatilization processes are controlled only by presence and absence of oxygen in the discharge gas, respectively.

The aim of the present work was to determine atomic oxygen concentrations in the DBD atomizer under typical operating conditions in HG-AAS, both in the presence (on-line atomization approach) and absence of hydrogen (preconcentration approach). No analyte hydrides were introduced to the atomizer for the sake of simplicity.

However, DBD ignited in Ar + O<sub>2</sub> mixtures are used in a much wider spectrum of plasma applications and, therefore, the topic of the presented work is of importance for a broader range of problems. Atmospheric-pressure plasma jets ignited in mixtures of a rare gas with oxygen are used for surface treatment including the field of plasma medicine [23]. There are two basic types of atmospheric-pressure plasma jets. The first type of jet is ignited by RF (or MW) electric field. Atomic oxygen concentration in this type of helium plasma jet was measured e.g. in [2, 3, 24]. The second plasma jet type is a DBD discharge ignited by frequencies in the kHz range. Values and behavior of atomic oxygen concentration in the DBD are unknown. Moreover, the cited works [2, 3, 24] were realized in He jets, whereas the presented work concentrates on O measurement in an Ar DBD. Concentration of atomic radicals in He and Ar discharges may differ significantly since reaction of common molecular gases with helium metastables leads mainly to ionization, whereas reaction with argon metastables leads to dissociation [23]. The comparison of O

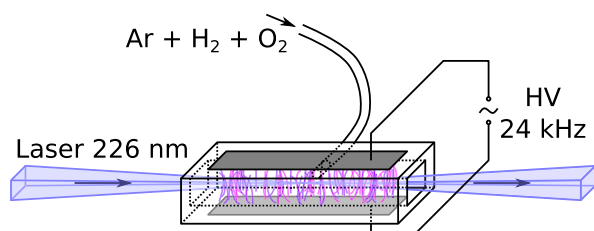


Figure 1. The dielectric barrier discharge atomizer.

concentration in an Ar and He DBD is, therefore, also mentioned in the presented work. In addition, the knowledge of atomic oxygen concentration in DBD discharges is important for understanding the processes in ozone generation, since the main  $O_3$  production channel is the reaction  $O_2 + O + M \rightarrow O_3 + M$  and O atoms also contribute to the ozone destruction by the reaction  $O_3 + O + M \rightarrow 2O_2 + M$  [25].

## 2. Experimental and computational techniques

### 2.1. Discharge configuration

The DBD atomizer setup is described in detail elsewhere [15]. The atomizer (see figure 1) is T-shaped with the rectangular optical arm in which plasma is sustained (inner dimensions of the plasma channel  $7\text{ mm} \times 3\text{ mm}$  and length of  $75\text{ mm}$ ) being located in the axis of the laser beam. A quartz tube ( $20\text{ mm}$  long,  $2\text{ mm}$  inner diameter,  $4\text{ mm}$  outer diameter) was sealed to the center of the optical arm and served as an inlet arm to supply mixture of gases (Ar,  $O_2$ ,  $H_2$ ) into the optical arm. Two copper electrodes ( $50\text{ mm}$  long;  $12\text{ mm}$  wide;  $0.15\text{ mm}$  thick) were placed on the horizontal outer sides of the optical arm and were supplied with sinusoidal voltage with frequency  $24\text{ kHz}$ . If not explicitly stated otherwise, the electric power delivered to the DBD system was  $25\text{ W}$  and the flow rate of argon was  $140\text{ sccm}$ . Oxygen and hydrogen, respectively, were introduced at flow rates of  $0\text{--}10\text{ sccm}$  and of  $0\text{--}20\text{ sccm}$ . In some experiments, argon was replaced by helium. Gas flow rates were controlled by mass flow controllers (Omega Engineering, USA).

### 2.2. Laser setup

Radiation for excitation of atomic oxygen was produced by laser setup consisting of pumping Nd:YAG laser (Spectra-Physics, Quanta-Ray PRO-270-30), dye laser (Sirah, Precision Scan) and a unit for mixing the output radiation from the dye laser ( $620\text{ nm}$ ) with third harmonics of the Nd:YAG ( $355\text{ nm}$ ) in order to produce the radiation with wavelength  $225.6\text{ nm}$ , see figure 2. This UV radiation was focused to the discharge center. The laser beam enters and leaves the DBD atomizer through its open ends. Diaphragms were used to minimize the contact of scattered laser light with the atomizer walls in order to prevent photodetachment of electrons from dielectric walls [26, 27] and fluorescence of walls. The fluorescence radiation was separated from other plasma emission by an interference filter and collected by the ICCD camera (Princeton Instruments, PI-MAX 1024RB-2-FG-43), which was synchronized with the pumping

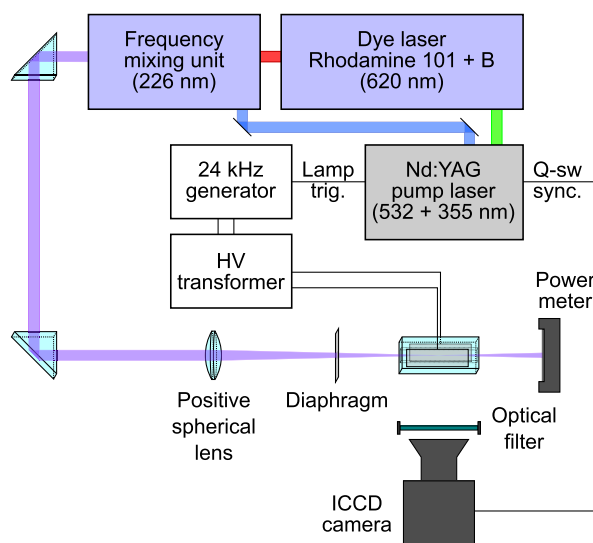


Figure 2. Experimental setup.

laser. Only fluorescence originating from the central part of the atomizer (few millimeters around the center) was used for evaluation, where the laser radiation was focused and the fluorescence signal was high. To realize measurements in defined phases of the discharge period, the pumping Nd:YAG laser was synchronized with the discharge.

### 2.3. Model of plasma kinetics

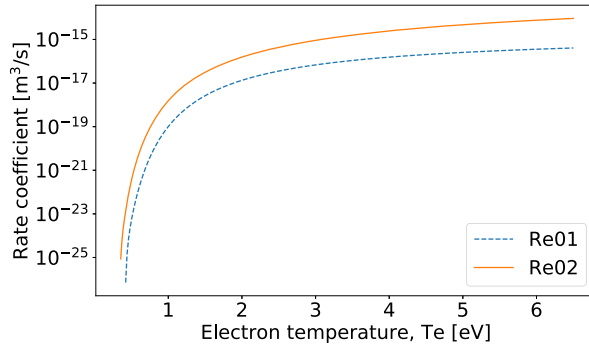
To obtain better insight into the processes in the plasma atomizer, the experimental data were complemented with a 0D model of the plasma kinetics. The reaction scheme is derived from the work of Gerasimov and Shatalov [28] which describes the kinetic mechanism of hydrogen/oxygen combustion with special attention paid to the relatively low gas temperature region,  $T < 1000\text{ K}$ . This temperature range is relevant for the atmospheric-pressure DBD since it is estimated from LIF measurements of rotational temperature of OH radicals that the gas temperature is around  $550\text{ K}$ . At such low temperature, the oxygen/hydrogen chemistry can certainly not be initiated by direct thermal dissociation of the molecules because the activation temperature of thermal dissociation reactions is in the  $10^4\text{ K}$  range. Also the catalytic reaction, which initiates the chemistry in low-temperature flames,  $H_2 + O_2 \rightarrow 2OH$  [28], will in fact have a negligible rate at temperatures below  $1000\text{ K}$ , meaning that the reaction chemistry must be initiated by plasma-specific reactions (electron-impact collisions or reactions with metastables).

For this reason, we added two lumped electron-impact dissociation channels into the numerical model, which are listed in table 1. The rate of these additional reactions are a sum of various electron-impact excitations of  $H_2$  and  $O_2$  into states, which lead to dissociation of these molecules. For the calculation of these rates as a function of electron temperature  $T_e$ , we used BOLSIG+ [29] software and the electron-impact cross-sections were taken from IST-Lisbon database [30].

Analysis of the reaction rates shows that, for electron temperatures  $1\text{--}2\text{ eV}$ , typical for comparable plasma sources

**Table 1.** Electron-impact reactions added to the Gerasimov reaction scheme [28].

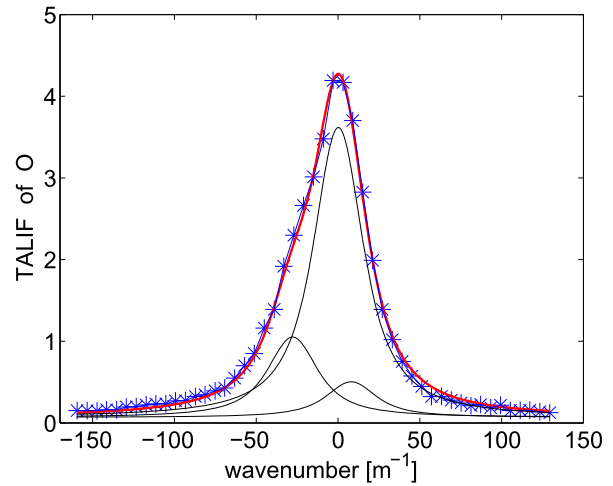
No.	Reaction	References
Re01	$e + \text{H}_2 \rightarrow e + \text{H}_2(b^3\Sigma) \rightarrow e + 2\text{H}$	[30]
Re02	$e + \text{O}_2 \rightarrow e + \text{O}_2^* \rightarrow e + 2\text{O}$ where $*$ = $\{A^3\Sigma_u^+, C^3\Delta_u, c^1\Sigma_u^-\}$	[30]



[31], the most important dissociation channel for  $\text{H}_2$  is its excitation to  $b^3\Sigma$  state with the energy of 8.9 eV [32] followed by the dissociation. Other dissociation channels, such as ionization of  $\text{H}_2$  and subsequent dissociative recombination (15.4 eV) or dissociative excitation  $e + \text{H}_2 \rightarrow e + \text{H} + \text{H}(n > 1)$  have reaction rates several orders of magnitude lower (in the range of  $T_e = 0.5\text{--}2.5$  eV) and can, therefore, be safely excluded. Concerning dissociation of molecular oxygen, again only the most prominent dissociation channels were considered, with intermediate excited species with the energy around 6 eV. The remaining reactions which involve the reactive species produced from  $\text{O}_2$  and  $\text{H}_2$  were taken from [28] and their rates can be found in the referenced publication.

The 0D model of kinetics eventually solves the balance equations for eight species:  $\text{H}_2$ ,  $\text{O}_2$ ,  $\text{H}_2\text{O}$ ,  $\text{H}$ ,  $\text{O}$ ,  $\text{OH}$ ,  $\text{HO}_2$ ,  $\text{H}_2\text{O}_2$ . In DBD plasma atomizers, the plasma is filamentary with the filaments moving stochastically. Considering that even a simulation of a single DBD filament, let alone many of them, is very challenging and from the application perspective, only the production of active species ( $\text{H}$ ,  $\text{O}$ ,  $\text{OH}$ ) is important, we decided to keep the electron density  $n_e$  and temperature  $T_e$  as model parameters. Since the gas in the plasma chamber travels only the distance of approx.  $50 \mu\text{m}$  during one voltage cycle, it is reasonable to describe the plasma as quasi-homogeneous with  $n_e$  and  $T_e$  being the ‘effective’ electron density and temperature. By sensitivity analysis, it was discovered that the model provides atomic oxygen densities within the same range as the experiment if the effective electron density of  $n_e = 10^{18} \text{ m}^{-3}$  and the effective electron temperature of  $T_e = 1.2 \text{ eV}$  are used. Such values are reasonable for this class of plasmas, as discussed above.

To compare the model with the experiment, we averaged the number density of atomic oxygen in the range of  $t \in (0, 30)$  ms, where  $t = 0$  is the time when the electron density is ramped up in the simulation. This time interval for averaging was chosen because in the TALIF experiment, the

**Figure 3.** Spectral profile of the two-photon transition  $2p^4 \ ^3P_2 \rightarrow \ ^3P_{1,2,0}$  fitted by a sum of three Voigt profiles. The relative intensities of the three lines were taken from [8], their relative positions from [37].

signal is collected from a line of a few millimeters close to the gas inlet. If we consider plug flow in the atomizer chamber, the gas travels approximately 2 mm in each direction during the 30 ms time.

### 3. Measurements and results

#### 3.1. Method of TALIF measurement of atomic oxygen concentration

The fluorescence signal used for determination of atomic oxygen concentration represents data integrated temporally (over the whole laser pulse and the following period of fluorescence decay), spatially (over central area of the atomizer) and spectrally (over the whole profile of the absorption line). Oxygen atoms were excited from the ground state  $2p^4 \ ^3P_{2,1,0}$  to the radiative state  $3p \ ^3P_{1,2,0}$ . Since both these states are triplets, there are seven allowed two-photon transitions between these states [1, 8]. In most of the measurements, the transitions only from the lowest  $2p^4 \ ^3P_2$  level were used. Therefore, it was necessary to measure the ratio between numbers of atoms in all three  $2p^4 \ ^3P_{2,1,0}$  levels and in the lowest level  $2p^4 \ ^3P_2$  only. By means of successive excitation from all three  $2p^4 \ ^3P_{2,1,0}$  levels, this ratio was found to be 1.65, which is in reasonable agreement with gas rotational temperature 550 K measured by LIF of hydroxyl ( $\text{OH}$ ) radicals (the rotational temperature was measured by excitation of hydroxyl radicals from various rotational levels of the ground vibronic state and measurement of the following hydroxyl fluorescence intensity, which is proportional to the hydroxyl concentration in the observed rotational level). The three used transitions  $2p^4 \ ^3P_2 \rightarrow 3p \ ^3P_{1,2,0}$  overlap, as can be seen in the figure 3. Since fluorescence signal spectrally integrated over

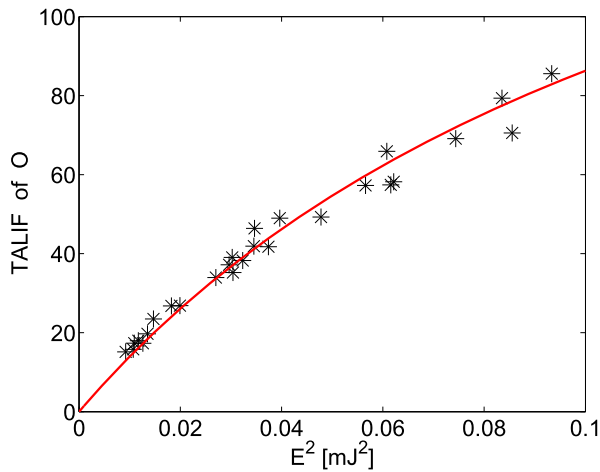


**Figure 4.** Dependence of fluorescence signal on second power of energy of laser pulses together with its fit by equation (4).

the whole absorption line must be used for calculation of atomic oxygen concentration, the ratio between this spectrally integrated fluorescence signal and the fluorescence signal measured with laser wavelength tuned only to the peak of the absorption line was measured prior to other measurements. Afterwards, it was possible to realize only measurements with laser tuned to the peak of the absorption line, which made the measurements substantially faster.

Fluorescence radiation of atomic oxygen transitions  $3p \ ^3P_{1,2,0} \rightarrow 3s \ ^3S$  at 845 nm was detected by the ICCD camera. Before the measured fluorescence signal was used for calculation of atomic oxygen concentration, the presence of defective pixels in the ICCD camera was tested (and the signal of eventual rare defective pixels was corrected) and a signal measured with laser switched off was subtracted in order to subtract the spontaneous discharge radiation and dark signal of the camera. It was checked that signal measured with laser switched on but with laser wavelength detuned from the absorption line of atomic oxygen was identical to the signal measured with laser switched off, which shows that neither fluorescence of walls disrupts the measurements, nor is the discharge influenced by laser pulses [27]. The fluorescence signal was temporally integrated over the whole laser pulse and following tens of nanoseconds and accumulated over typically 100–1000 laser shots.

For laser pulse energies higher than ca 400  $\mu\text{J}$  a fluorescence signal was observed even when the discharge was switched off, demonstrating that at high laser energies, photodissociation of molecular oxygen occurs. The intensity of this parasitic signal was proportional to the third power of laser pulse energy. All presented measurements were realized at lower laser pulse energies (150–300  $\mu\text{J}$ ) when no fluorescence signal was observed for discharge switched off.

Figure 4 shows an example of the dependence of the fluorescence signal on laser pulse energy. For very low laser energies, the TALIF signal is proportional to the second power of laser energy. However, for such low laser energies, the signal to noise ratio is poor. Therefore, fluorescence was

measured for higher laser energies when the signal to noise ratio was enhanced at the cost that parasitic phenomena like depletion of the ground state, photoionization of the excited state or amplified spontaneous emission may occur. In order to quantify the effect of these phenomena, the dependence of fluorescence signal on laser energy was fitted by

$$F = \frac{\alpha E_L^2}{1 + \beta E_L^2}, \quad (4)$$

where  $F$  is the measured signal,  $\alpha E_L^2$  would be the hypothetical signal that would be detected if no parasitic phenomena occurred and the constant  $\beta$  describes the effect of the parasitic phenomena. The equation (4) is an analogy to the formula  $F = \alpha E_L / (1 + \beta E_L)$  that was derived for the case of a single-photon LIF [27], where the coefficient  $\beta$  describes the effects of ground state depletion and stimulated emission. In the case of TALIF, the exact physical meaning of the coefficient  $\beta$  has never been derived. The use of the formula (4) is justified by the fact that it fits well to the measured  $F(E_L)$  dependencies. For evaluation of the measured data, the signal intensity with a correction of saturation effects  $F(1 + \beta E_L^2)$  was used. For laser energy 150  $\mu\text{J}$  and 300  $\mu\text{J}$  the corrections made were 15% and 65%, respectively.

For quantitative treatment of TALIF measurement realized at atmospheric pressure it is necessary to know the quenching rate of excited  $3p \ ^3P$  state of atomic oxygen. In principle, the quenching rate can be obtained from measurement of the fluorescence decay time after the end of the laser pulse. Unfortunately, the fluorescence decay times in the used gas mixtures at atmospheric pressure are short (around 1 ns). As a result, the decay time measurement was encumbered with a high uncertainty. Therefore, quenching rate constants from the literature [1] were used for calculation of the fluorescence decay time. Since the quenching rate of reactant gases ( $\text{O}_2$ ,  $\text{H}_2$ ) differs from quenching rate of the reaction products, quantitative evaluation of TALIF measurements was realized only in the region close to the inlet of gases (up to 2 mm from the atomizer center), where the gases had no time to react and the composition of the gas mixture is known. This hypothesis was verified by the measurement of concentration of atomic hydrogen and simulation of the discharge chemistry in the same DBD atomizer [19]. In order to verify the calculated decay times, the fluorescence decay was measured for several compositions of the gas mixture. Since the fluorescence signal decreases quickly already when the laser pulse is not extinguished totally, the following numerical procedure was used: The temporal profile of the laser pulse was measured by the ICCD camera by detection of Rayleigh scattering of laser photons on ambient air. Since with no saturation the measured fluorescence intensity  $F(t)$  is the convolution of the square of the measured temporal laser profile  $L(t)$  with an exponential decay

$$F(t) = C E_L^2 \int_{-\infty}^t L^2(t') e^{-\frac{t-t'}{\tau}} dt', \quad (5)$$

where  $\tau$  is the fluorescence decay time, integral of  $L$  was normalized to unity and  $C$  is a constant, this convolution was

fitted to the measured temporal profile of fluorescence decay in order to find the fluorescence decay time  $\tau$ . In order to avoid any saturation effects, the equation (5) was fitted only to the tail of the fluorescence pulse. The obtained decay times were in reasonable agreement with their predictions calculated from the decay-rates taken from the literature: the mean difference was 8% and the confidence intervals of the measured and literature-based life-times coincided. This result supports the assumption that neither chemical reactions in the reactor center nor the three-body collisions have significant influence on the life-time of excited oxygen atoms.

Finally, the sensitivity of the setup was calibrated by measurement of TALIF of xenon with known concentration  $N_{\text{Xe}}$ , that was excited by two-photon absorption of 224 nm radiation to the  $6p[3/2]_2$  state [1, 2], and the concentration of atomic oxygen  $N_{\text{O}}$  was calculated by

$$N_{\text{O}} = r_{\text{O}} N_{\text{Xe}} \frac{S_{\text{O}} E_{L,\text{Xe}}^2 \left( \frac{\nu_{\text{O}}}{\nu_{\text{Xe}}} \right)^2}{S_{\text{Xe}} E_{L,\text{O}}^2} \times \frac{\sigma_{\text{Xe}}^{\text{TA}}}{\sigma_{\text{O}}^{\text{TA}}} \frac{A_{\text{Xe}} \tau_{\text{Xe}}}{A_{\text{O}} \tau_{\text{O}}} \frac{T_{\text{Xe}}}{T_{\text{O}}} \frac{C_{\text{Xe}}}{C_{\text{O}}}, \quad (6)$$

where  $r_{\text{O}}$  is the ratio between concentrations of atomic oxygen in all three  $2p^4 \ ^3P_{2,1,0}$  levels and in the lowest  $2p^4 \ ^3P_2$  level,  $S$  are temporally, spatially and spectrally integrated fluorescence signals with the correction of saturation effects,  $E_L^2$  are mean values of square laser-pulse energies,  $\nu$  are frequencies of laser photons,  $\sigma^{\text{TA}}$  are cross sections for two-photon absorption,  $A$  are Einstein coefficients of spontaneous emission from the excited states,  $\tau$  are life-times of excited states (fluorescence decay times),  $T$  are transmissions of interference filters and  $C$  are quantum efficiencies of the ICCD camera for the wavelength of the fluorescence. Indexes ‘O’ and ‘Xe’ differentiate between quantities related to atomic oxygen and to xenon, respectively. The ratio  $\sigma_{\text{Xe}}^{\text{TA}} / \sigma_{\text{O}}^{\text{TA}} = 1.9 \pm 20\%$  was taken from [1] and  $A_{\text{Xe}} / A_{\text{O}} = 0.9001$  was taken from [2].

### 3.2. Three-body collisions of excited xenon

The calibration was performed at atmospheric pressure directly in the atomizer without need of an implementation of a vacuum vessel and a risk of consequent change of optical path. Due to the high price of xenon, a mixture of argon and xenon (100:1) was used. Similarly to the case of oxygen, the decay time of excited xenon is too short to be measured directly. Quenching rates of excited xenon  $6p[3/2]_2$  by two-body collisions with argon or xenon were published in [1, 2, 33]. However, significant role of three-body collisions was reported both in a pure xenon [34] and in a mixture of He + Xe [2]. Therefore, influence of three-body collisions in the used Ar + Xe mixture should be examined.

The lifetime of the excited state satisfies the equation

$$\tau = \frac{1}{\frac{1}{\tau_0} + c_2 p + c_3 p^2}, \quad (7)$$

where  $p$  is the gas pressure and constants  $c_2$  and  $c_3$  determine the impact of two-body and three-body collisions, respectively. As the fluorescence signal  $S$  is directly proportional to

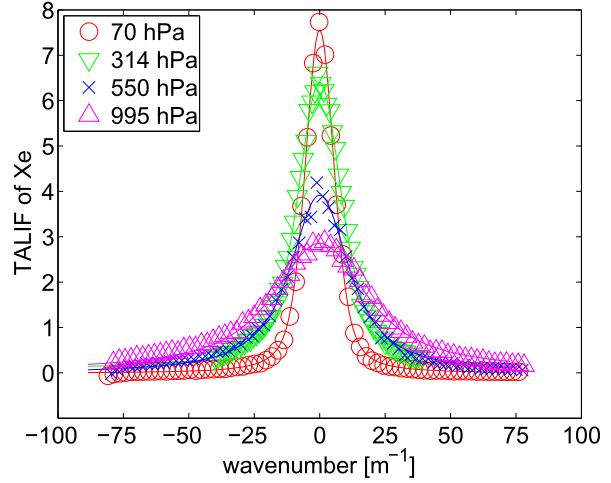


Figure 5. Broadening of the Xe absorption line in mixture of argon and xenon (100:1) for various pressures.

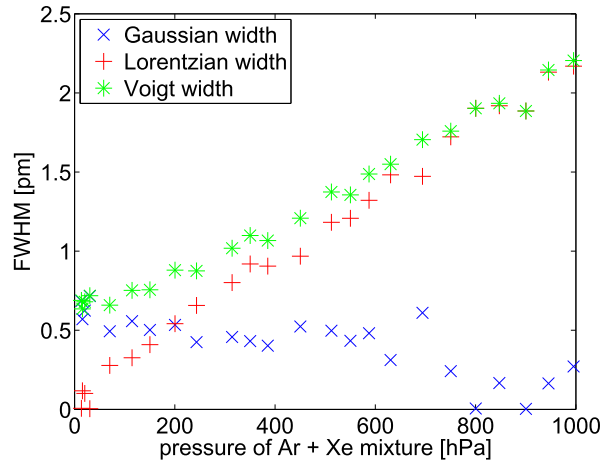


Figure 6. Dependence of FWHM of xenon absorption line on pressure of a mixture of argon and xenon.

the concentration of xenon atoms (i.e. to pressure) and life-time  $\tau$ , we can write

$$\frac{p}{S} \sim \frac{1}{\tau} \sim \frac{1}{\tau_0} + c_2 p + c_3 p^2. \quad (8)$$

The influence of three-body collisions can be examined by comparing of the linear and quadratic part of measured dependence of the ratio  $p/S$  on pressure.

Such an experiment was performed in a vacuum vessel with a mixture of Ar and Xe supplied in the flow-rate ratio 100:1. Since the broadening of absorption lines depends on pressure, the spectral profiles of the absorption line of xenon atoms were measured for the pressure range  $10^3$ – $10^5$  Pa. A sample of four selected measurements is shown in the figure 5. The absorption lines were fitted by Voigt profile and their full widths at half maximum (FWHM) were determined. Dependence of Voigt FWHM and its Gaussian and Lorentzian parts on pressure is presented in the figure 6 and

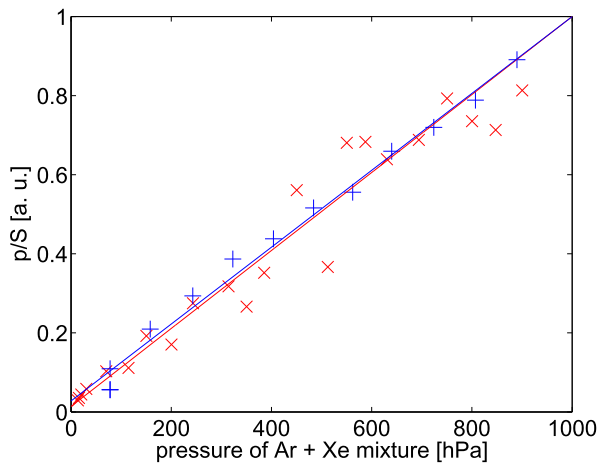


**Figure 7.** Ratio of pressure of a mixture of argon and xenon and spectrally integrated fluorescence intensity depending on the pressure.

demonstrates a linear increase of the Lorentzian width with pressure. In order to compare the measured data with the equation (8), the ratio of pressure and the intensity integrated over the absorption line is plotted as a function of pressure in the figure 7 by red x-signs and reveals a linear dependence.

To validate this result with a faster measurement (in order to minimize e.g. the temporal drift of spatial laser profile), a second experiment was performed: the gas pressure was continuously being increased with Ar–Xe mixture flowing into the chamber and simultaneously the fluorescence intensity in the center of absorption line was measured. By means of known pressure dependence of spectral profiles measured in the previous experiment, the signals were transformed to spectrally integrated intensities. The resulting intensities, in ratio  $p/S$ , are presented in the figure 7 by blue plus signs.

In both experiments, the dependence can be considered as linear, proving a negligible role of three-body collisions in excited xenon quenching. As a result, for evaluation of the excited xenon decay time  $\tau_{Xe}$ , two-body quenching parameters from [2] were used with no need to take the three-body collisions into account.

### 3.3. Atomic oxygen in the DBD

For initial measurements it was convenient to keep the atmosphere in the DBD atomizer as simple as possible. Therefore Ar atmosphere was chosen. To make the measurements of atomic oxygen concentrations meaningful the inlet  $O_2$  concentration must be known. However,  $O_2$  content in the ‘pure’ Ar supplied to the atomizer is unknown mainly because of its diffusion from the ambient atmosphere through tubings and connection elements. Therefore a well defined  $O_2$  flow was introduced to the atomizer not to exceed 0.1 molar fraction.

Since the laser system was synchronized with the AC voltage generator, it was possible to measure the temporal development of atomic oxygen concentration during the discharge period (42  $\mu s$ ). It was observed that whereas the active

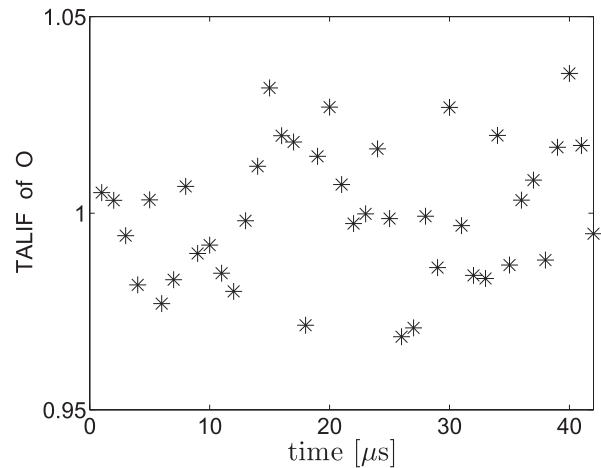


**Figure 8.** Relative TALIF signal of atomic oxygen during a discharge period (42  $\mu s$ ). Measured in a mixture of Ar (140 sccm) and  $O_2$  (1.5 sccm).

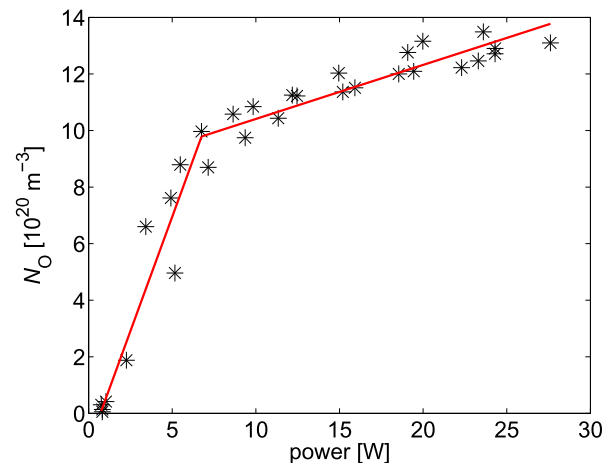


**Figure 9.** Dependence of atomic oxygen concentration on electric power delivered to the DBD system. Measured in mixture of Ar (140 sccm) and  $O_2$  (2 sccm).

discharge is ignited only in two short pulses in each period, the atomic oxygen concentration in the Ar +  $O_2$  mixture does not vary during the period, which is demonstrated in the figure 8. In all the following measurements, the synchronization between the voltage generator and laser was used so that laser shots were set to the part of discharge period when the electric field was low. This setting minimized the background discharge radiation and minimized the risk of discharge disturbance by laser [27]—the laser shots were not able to ignite a discharge pulse when the electric field was low.

Figure 9 shows the dependence of atomic oxygen concentration on electric power delivered to the DBD system. For delivered power below 7 W the filamentary nature of the discharge was clearly visible by naked eyes and the density of filaments increased with increasing power. In this range of powers the atomic oxygen density strongly depended on

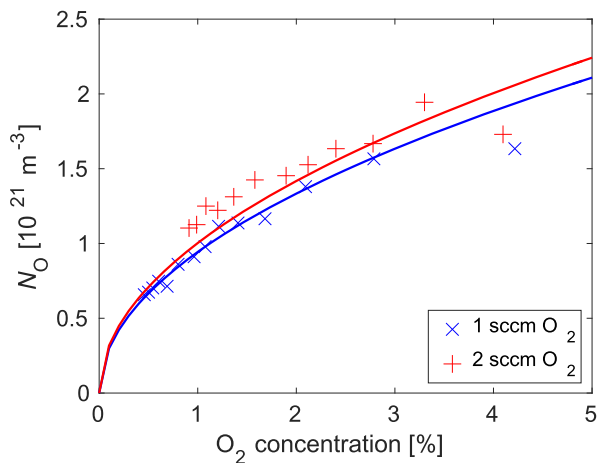


**Figure 10.** Atomic oxygen concentration for various compositions of the Ar + O<sub>2</sub> feed gas mixture. The oxygen flow rate was constant and the argon flow rate was varied. Two sets of measurements with oxygen flow rate 1 sccm (×) and 2 sccm (+) are shown.

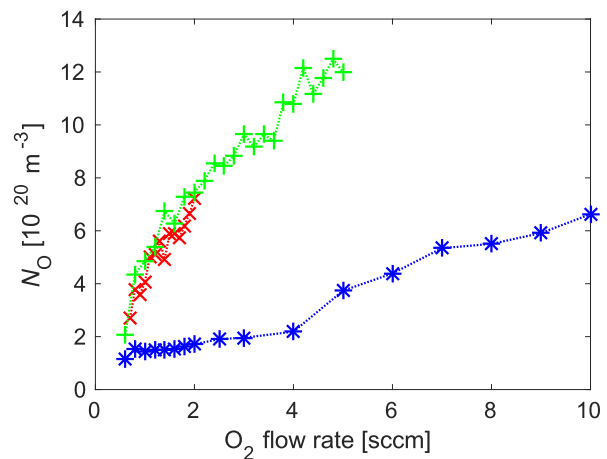
delivered power. In the power range 7–8 W the discharge filled the whole reactor volume and from this point the plasma appeared to be macroscopically homogeneous. Above this point the increase of delivered power caused only relatively small increase of atomic oxygen concentration. It should be highlighted that the optimum performance of an identical DBD atomizer used for analytical applications (hydride atomization) was achieved when the delivered power exceeded 10 W [15, 16]. Depending on the element to be determined (Se, Bi, As, Pb, Sb) the optimum power delivered to the DBD was within the range 14–30 W. The power of 25 W yields oxygen atom concentration  $N_{\text{O}} = 1.3 \times 10^{21} \text{ m}^{-3}$  (figure 9).

Figure 10 shows that oxygen atom concentration follows well the square root of total oxygen concentration in the atomizer. Consequently, it is convenient to estimate the value of the oxygen dissociation constant

$$K_d = \frac{[\text{O}]^2}{[\text{O}_2]},$$

which presents a suitable quantity for expression of the efficiency of the given configuration of DBD plasma to break O<sub>2</sub> molecules. Taking into account the actual temperature of 550 K in the DBD atomizer for the applied electric power of 25 W and concentrations of atomic oxygen and of supplied molecular oxygen shown in figures 9 and 10, the value of the oxygen dissociation constant can be estimated as  $7 \times 10^{18} \text{ m}^{-3}$ .

O atom concentrations shown in figures 9 and 10 could be related to atomic oxygen concentration in other atmospheric pressure plasma sources: in helium RF plasma jets concentration  $10^{21}$ – $10^{22} \text{ m}^{-3}$  was found [3–5]. In helium MW jet and in a nanosecond pulsed discharge in air, respectively, atomic oxygen concentration of  $10^{22} \text{ m}^{-3}$  [2] and  $10^{24} \text{ m}^{-3}$  [6] were determined. The dissociation degrees of over 50% and 7%, respectively, reported in [2, 6] make possible to estimate corresponding oxygen dissociation constants as  $5 \times 10^{21} \text{ m}^{-3}$  and  $7 \times 10^{22} \text{ m}^{-3}$ , i.e. three and four orders of magnitude higher than in the DBD atomizer. The unusually high O concentration in the



**Figure 11.** Atomic oxygen concentration as a function of oxygen flow rate for a mixture of Ar (140 sccm) + O<sub>2</sub> (red and green) and a mixture of Ar (140 sccm), H<sub>2</sub> (15 sccm) and O<sub>2</sub> (blue).

nanosecond pulsed discharge ignited in preheated (1000 K) air was explained by O<sub>2</sub> dissociation due to reactions with nitrogen metastables, that are not present in a significant amount in atomizers. This indicates that MW discharge could be potential atomizers for AAS. Nonmonotone response of O concentration on the amount of oxygen admixed to the He flow was observed in some of RF [24] and MW [2] plasma jets with a decrease of O concentration for O<sub>2</sub> admixtures higher than ca 1%, as a result of discharge extinction caused by high amounts of oxygen. On the contrary, the presented measurement realized in Ar+O<sub>2</sub>(+H<sub>2</sub>) DBD reveals monotone increase of O with O<sub>2</sub> admixture even for 10% of O<sub>2</sub>.

Even though the O atom population formed in the DBD atomizer is much lower than in the above mentioned MW jet or in the nanosecond pulsed discharge it is two to three orders of magnitude higher than analyte concentration in the atomizer under analytical conditions which is in the order of  $10^{18} \text{ m}^{-3}$  [16]. The O atom excess over analyte should be therefore sufficient for a complete hydride atomization.

Behavior of atomic oxygen was significantly changed when hydrogen was added to the Ar + O<sub>2</sub> mixture, thus mimicking the discharge gas composition in real hydride generator system with DBD atomizer and on-line atomization. Addition of hydrogen (1–15 sccm) led to the reduction of atomic oxygen concentration by a factor 5–10. An example of atomic oxygen reduction is shown in the figure 11. The dependence of atomic oxygen concentration on oxygen partial pressure was different in the presence of hydrogen and did not reveal the square root dependence. This indicates that O radicals are removed by reactions with hydrogen containing species as will be discussed by means of the numerical model in the forthcoming text.

Chemical reactions in the Ar–H<sub>2</sub>–O<sub>2</sub> mixture were investigated by means of numerical simulation. The figure 12 demonstrates that the model is capable of reproducing the experimental concentrations of the atomic oxygen radical (compare to figure 11) with the same values of  $n_e$  and  $T_e$  as in

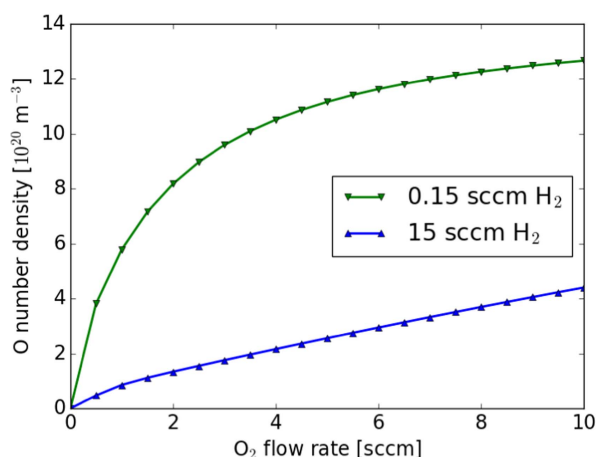


**Figure 12.** Atomic oxygen concentration in the atomizer center as a function of  $O_2$  flow rate. Calculated for Ar flow rate 140 sccm and  $H_2$  flow rates 0.15 and 15 sccm.

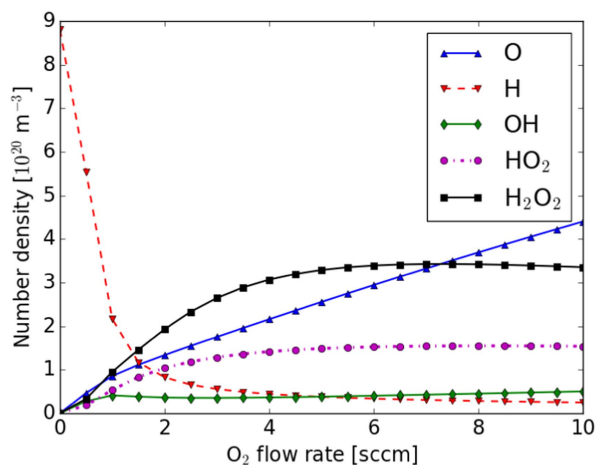


**Figure 13.** Concentration of reactive species in the atomizer center as a function of  $O_2$  flow rate. Calculated for Ar flow rate 140 sccm and  $H_2$  flow rate 15 sccm.

[19]. It should be stated that in the ‘pure’ oxygen case, 0.15 sccm of  $H_2$  impurity had to be included in the calculation (corresponding to 0.1 volume %) in order to reproduce the experimental profile. This can be explained as a consequence of either hydrogen leaking through the flow meter or due to water desorbing from the tubing or reactor walls.

The figure 13 depicts the concentration of main reactive species in the Ar- $H_2$ - $O_2$  mixture for typical conditions used for analyte preconcentration, i.e. for Ar flow rate 140 sccm and  $H_2$  flow rate 15 sccm and variable  $O_2$  content. Besides others, the figure demonstrates that for  $O_2$  flow rate above 1.5 sccm, i.e. even when the  $O_2$  flow is significantly smaller than the stoichiometric flow with respect to water (7.5 sccm), there is an excess of atomic oxygen radicals over atomic hydrogen radicals in the atomizer center, i.e. at the beginning of the reaction zone.

These results from the model can be compared to those observed in real HG-AAS experiments with analyte hydride

preconcentration in the DBD, in which 1.5–6 sccm  $O_2$  is added to the Ar- $H_2$  mixture. The amount of oxygen required for maximum analyte hydride retention, is analyte-dependent. To reach complete signal suppression in the on-line atomization mode, i.e. to achieve complete analyte preconcentration, 1.5 sccm of  $O_2$  has to be admixed in the case of Sb as analyte [35], whereas 3 sccm of  $O_2$  are required for Bi [15] and Se (unpublished data) as analytes and even 6–7 sccm of  $O_2$  has to be added for efficient retention of As hydride [17]. Addition of 7 sccm of  $O_2$  to the Ar plasma was employed in a detailed study of *in situ* trapping of arsenic hydride in the optical arm of the DBD atomizer. Complete analyte release and atomization was reached as soon as oxygen was switched off. Preconcentration efficiency of 100% was observed allowing to decrease the As detection limit to  $0.01 \text{ ng ml}^{-1}$  employing 300 s preconcentration period [17].

Although the exact mechanism of analyte hydride preconcentration in the DBD remains unknown, it must be stated, that the model helps to gain insights into the processes in the plasma. Regardless of the analyte to be preconcentrated, the required  $O_2$  supply rates of 1.5–7 sccm lie in the region, where O concentration in the DBD is higher (see figure 13) than concentrations of both H as well as analyte. Conversion of analyte hydride to another chemical form, most probably elementary metal or analyte oxide, which are deposited at the inner surface of DBD walls, is expected during the first step of preconcentration procedure under conditions when oxygen is added. Figure 13 further demonstrates that switching off the flow of oxygen leads to a strong increase in concentration of H radicals, which are likely to be responsible for volatilization and atomization of analyte deposited in the preceding step of the preconcentration procedure in presence of oxygen. However, the sketched picture of the preconcentration mechanism requires validation and completion and the preconcentration problematic requires further investigation including spatially resolved measurements of reactive species at relevant conditions.

The model further enables study of dominant creation and sink pathways of atomic oxygen radicals. In both studied gas mixtures, the dominant source term of atomic oxygen was  $O_2$  dissociation caused by electron impact. The depletion was controlled by gas-phase reactions, the diffusion to the atomizer walls played a negligible role. In the gas mixture with only a small amount of hydrogen, the dominant O-depleting reaction was the ozone formation  $O + O_2 + M \rightarrow O_3 + M$  followed by the  $O + OH \rightarrow O_2 + H$  reaction, see figure 14. The second reaction illustrates how the residual hydrogen (coming for example from water impurity) influences the resulting concentration of the O radical. A different situation occurred in the hydrogen-rich gas mixture, where the atomic oxygen depletion was controlled mainly by the reaction  $O + HO_2 \rightarrow OH + O_2$  followed by reactions  $O + OH \rightarrow O_2 + H$ ,  $O + H_2 \rightarrow OH + H$  and  $O + O_2 + M \rightarrow O_3 + M$ , see figure 15.

Since DBDs are commonly operated also in helium and helium is more convenient than argon for cryogenic trap hydride collection, the concentration of atomic oxygen radicals in helium atmosphere with  $O_2$  mixtures with these two gases was also determined: the concentration of atomic

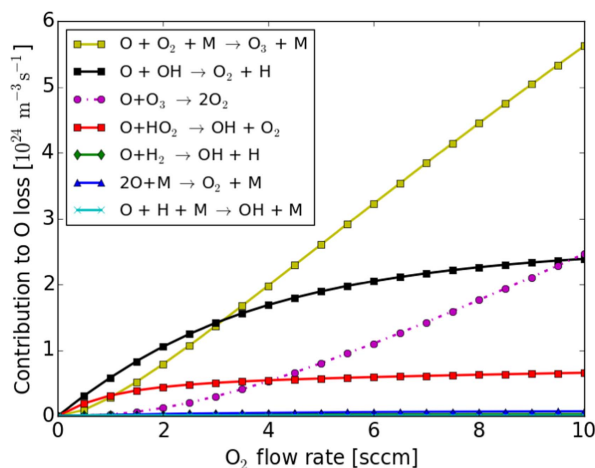


**Figure 14.** Dominant reactions of atomic oxygen in the Ar–O<sub>2</sub> mixture with admixture of 0.15 sccm of H<sub>2</sub>.

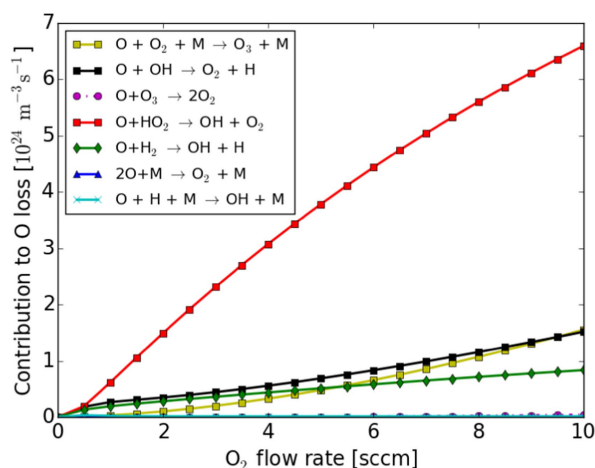


**Figure 15.** Dominant reactions of atomic oxygen in the Ar–O<sub>2</sub> mixture with addition of 15 sccm of H<sub>2</sub>.

oxygen dropped by a factor of 2–9 indicating that He plasma is less efficient for O<sub>2</sub> atomization than Ar plasma. This is in agreement with the assumption that reaction of He metastables leads mainly to ionization of molecular gases whereas reaction of Ar metastables produces atomic radicals [23]. However, different concentration and energy distribution of electrons is expected to play a role as well. The low O concentration in He discharge further corresponds well with the observation that ozone generation is more effective in Ar + O<sub>2</sub> discharge than in He + O<sub>2</sub> discharge [36]. In spite of the fact that the O concentration in the DBD atomizer drops when argon is replaced by helium, the O atom excess over analyte should be sufficient for a complete hydride atomization even in helium atmosphere.

In the end, the uncertainty of measured concentrations was estimated. First, there is some uncertainty of data taken from the literature: the ratio  $\sigma_{\text{Xe}}^{\text{TA}} / \sigma_{\text{O}}^{\text{TA}}$  is known with uncertainty 20% [1]. Quenching coefficients taken from various papers usually differ by less than 5% [1, 10, 11], Einstein coefficients for

spontaneous emission by 10% [2, 37]. Second, the experimental standard deviation of data obtained in one experiment was around 2%, which is illustrated by the figure 8. Consequently, reliability of measured trends seems to be relatively high, which can be demonstrated also in figures 10 and 11, where two measurements performed at similar or identical discharge conditions almost overlap. Finally, the most serious differences were observed between measurements performed at identical experimental conditions but in different days and analyzed with different calibration measurements of xenon fluorescence. These differences varied from 10% to 50%, which was, therefore, the most important limit of the accuracy of the absolute O concentration values.

#### 4. Conclusion

Concentration of atomic oxygen radicals in the plasma of DBD ignited at atmospheric pressure in mixtures of Ar + O<sub>2</sub> or Ar + H<sub>2</sub> + O<sub>2</sub> was measured by TALIF. For calibration of the fluorescence method, TALIF of xenon was used in a mixture of argon and a percent of xenon at atmospheric pressure. Advantageously, this calibration procedure was performed directly in the DBD atomizer without its exchange by any vacuum reactor and without necessity to place the DBD atomizer into any vacuum vessel. It was found that three-body collisions do not have significant effect on Xe\* quenching in the used Ar + Xe mixture at atmospheric pressure.

Atomic oxygen concentration in the DBD atomizer was in the order of  $10^{21} \text{ m}^{-3}$ , the oxygen dissociation degree varied in the range 0.001–0.01. Atomic oxygen concentration in the Ar + O<sub>2</sub> mixture was constant during the whole discharge period (42  $\mu\text{s}$ ) demonstrating that life-time of oxygen radicals is much longer. The measured concentration did not depend strongly on electric power delivered to the discharge if the power was sufficiently high and the visible discharge filled the whole reactor volume. Only at very low power when the discharge occupied only parts of the reactor, the atomic oxygen concentration strongly decreased with decreasing power.

The concentration of oxygen radicals dropped by an order of magnitude when hydrogen was added to the gas mixture. However, for O<sub>2</sub> flow rates higher than 10% of H<sub>2</sub> flow, i.e. even at strongly substoichiometric amount of O<sub>2</sub>, the O concentration at the inlet of gases was higher than the calculated H concentration, which demonstrates that at the beginning of the reaction zone plasma can have oxidative character even in an excess of molecular hydrogen. This is in agreement with fundamental change of analyte behavior in the HG-AAS preconcentration experiments when sufficient substoichiometric amount of O<sub>2</sub> is admixed to the Ar–H<sub>2</sub> flow. The atomic oxygen concentration was also decreased when argon was replaced by helium.

#### Acknowledgments

This research has been supported by the project CZ.1.05/2.1.00/03.0086 funded by European Regional Development

Fund, projects LO1411 (NPU I) and 7AMB14SK204 funded by Ministry of Education Youth and Sports of Czech Republic and by Czech Science Foundation under contracts GA13-24635S, 17-04329S and P206/14-23532S, by the Czech Academy of Sciences (project of international cooperation no. M200311202 and by Institute of Analytical Chemistry of the CAS, v. v. i. (Institutional Research Plan RVO: 68081715).

## References

- [1] Niemi K, Schulz-von der Gathen V and Döbele H F 2005 *Plasma Sources Sci. Technol.* **14** 375
- [2] van Gessel A F H, van Grootel S C and Bruggeman P J 2013 *Plasma Sources Sci. Technol.* **22** 055010
- [3] Knake N and Schulz-von der Gathen V 2010 *Eur. Phys. J. D* **60** 645
- [4] Reuter S, Niemi K, Schulz-von der Gathen V and Döbele H F 2009 *Plasma Sources Sci. Technol.* **18** 015006
- [5] Waskoenig J, Niemi K, Knake K, Graham L M, Reuter S, Schulz-von der Gathen V and Gans T 2010 *Plasma Sources Sci. Technol.* **19** 045018
- [6] Stancu G D, Kaddouri F, Lacoste D A and Laux C O 2010 *J. Phys. D: Appl. Phys.* **43** 124002
- [7] Meier U, Kohse-Höinghaus K and Just T 1986 *Chem. Phys. Lett.* **126** 567
- [8] Saxon R P and Eichler J 1986 *Phys. Rev. A* **34** 199
- [9] Bamford D J, Jusinski L E and Bischel W K 1986 *Phys. Rev. A* **34** 185
- [10] Niemi K, Schulz-von der Gathen V and Döbele H F 2001 *J. Phys. D: Appl. Phys.* **34** 2330
- [11] Bittner J, Kohse-Höinghaus K, Meier U and Just T 1988 *Chem. Phys. Lett.* **143** 571
- [12] Brandt S, Schütz A, Klute F D, Kratzer J and Franzke J 2016 *Spectrochim. Acta B* **123** 6
- [13] Dědina J and Tsalev D L 1995 *Hydride Generation Atomic Absorption Spectrometry* (Chichester: Wiley)
- [14] Zhu Z L, Zhang S C, Lv Y and Zhang X R 2006 *Anal. Chem.* **78** 865
- [15] Kratzer J, Boušek J, Sturgeon R E, Mester Z and Dědina J 2014 *Anal. Chem.* **86** 9620
- [16] Duben O, Boušek J, Dědina J and Kratzer J 2015 *Spectrochim. Acta B* **111** 57
- [17] Novák P, Dědina J and Kratzer J 2016 *Anal. Chem.* **88** 6064
- [18] Kratzer J, Zelina O, Svoboda M, Sturgeon R, Mester Z and Dědina J 2016 *Anal. Chem.* **88** 1804
- [19] Dvořák P, Talába M, Obrušník A, Kratzer J and Dědina J Concentration of atomic hydrogen in a dielectric barrier discharge measured by two-photon absorption fluorescence *Plasma Sources Sci. Technol.* submitted
- [20] Dědina J 2007 *Spectrochim. Acta B* **62** 846
- [21] Jenkins D R and Sugden T M 1971 Radicals and molecules in flame gases *Flame Emission and Atomic Absorption Spectrometry, Volume 1-Theory* ed J A Dean and T C Rains (New York: Marcell Dekker) pp 151–87
- [22] Dědina J 2011 Generation of volatile compounds for analytical atomic spectroscopy *Encyclopedia of Analytical Chemistry, Supplementary Volumes S1–S3* ed R A Meyers (Chichester, UK: Wiley) pp 897–936
- [23] Lu X, Naidis G V, Laroussi M, Reuter S, Graves D B and Ostrikov K 2016 *Phys. Rep.* **630** 1
- [24] Knake N, Reuter S, Niemi K, Schulz-von der Gathen V and Winter J 2008 *J. Phys. D: Appl. Phys.* **41** 194006
- [25] Kogelschatz U 2003 *Plasma Chem. Plasma Process.* **23** 1
- [26] Ambrico P F, Ambrico M, Šimek M, Colaianni A, Dilecce G and de Benedictis S 2009 *Appl. Phys. Lett.* **94** 231501
- [27] Voráč J, Dvořák P, Procházka V, Morávek T and Ráhel J 2015 *Eur. Phys. J. Appl. Phys.* **71** 20812
- [28] Ya Gerasimov G and Shatalov O P 2013 *J. Eng. Phys. Thermophys.* **86** 987
- [29] Hagelaar G J M and Pitchford L C 2005 *Plasma Sources Sci. Technol.* **14** 722
- [30] IST-Lisbon database, <http://lxcat.net>, (Retrieved:15-09-2015)
- [31] Subedi D P, Tyata R B, Shrestha R and Wong C S 2014 *AIP Conf. Proc.* **1588** 103
- [32] Trevisan C S and Tennyson J 2002 *Plasma Phys. Control. Fusion* **44** 2217
- [33] Whitehead C A, Pourmasr H, Bruce M R, Cai H, Kohel J, Layne W B and Keto J W 1995 *J. Chem. Phys.* **102** 1965
- [34] Bruce M R, Layne W B, Whitehead C A and Keto J W 1990 *J. Chem. Phys.* **92** 2917
- [35] Zurynková P, Dědina J and Kratzer J Trace determination of antimony by hydride generation atomic absorption spectrometry with analyte preconcentration/atomization in a dielectric barrier discharge (DBD) atomizer *Anal. Chim. Acta.* in preparation
- [36] Wei L, Yuan D, Zhang Y, Hu Z, Tan Z, Dong G and Tao S 2014 *Eur. Phys. J. D* **68** 17
- [37] Lemmon E W, McLinden M O and Friend D G 2014 Thermophysical Properties of Fluid Systems *NIST Chemistry WebBook* (Gaithersburg, MD: National Institute of Standards and Technology) (<https://doi.org/10.18434/T4D303>)